A N N U A L R E P O R T

2018

and list of publications

Bayerisches Forschungsinstitut
für Experimentelle Geochemie und Geophysik
Universität Bayreuth

Bayerisches Geoinstitut
Universität Bayreuth
95440 Bayreuth
Germany

Telephone: +49-(0)921-55-3700
Telefax: +49-(0)921-55-3769
e-mail: bayerisches.geoinstitut@uni-bayreuth.de
www: http://www.bgi.uni-bayreuth.de

Editorial compilation by: Florian Heidelbach and Petra Buchert
Section editors: Andreas Audétat, Tiziana Boffa Ballaran, Leonid Dubrovinsky, Dan Frost, Florian Heidelbach, Gregor Golabek, Tomoo Katsura, Hans Keppler, Catherine McCammon, Nobuyoshi Miyajima, Dave Rubie, Gerd Steinle-Neumann

Staff and guests of the Bayerisches Geoinstitut in **July 2018**:

Die Mitarbeiter und Gäste des Bayerischen Geoinstituts im **Juli 2018**:

first row, from left (1. Reihe, v. links) Caterina Melai, Dariia Simonova, Katherine Armstrong, Serena Dominijanni, Giacomo Criniti, Matteo Urgese, Anna Rebaza, Rong Huang, Fabian Wagle, Florian Heidelbach

second row, from left (2. Reihe, v. links) Stella Chariton, Greta Rustioni, Saiana Khandarkhaeva, Tiziana Boffa Ballaran, Catherine McCammon, Laura Cialdella, Dorothea Wiesner, Janina Potzel, Petra Buchert, Joana Polednia, Nicki Siersch, Jennifer Primocerio

third row, from left (3. Reihe, v. links) Anastasiya Iskrina, Tommaso Mandolini, Michaela Flanigan, Lisa Eberhard, Enrico Marzotto, Niccolò Satta, Katharina Marquardt, Caroline Bollinger, Heinz Fischer, Dan Frost, David Rubie, Sven Linhardt

fourth row, from left (4. Reihe, v. links) Florian Trybel, Kirsten Schulze, Ingrid Blanchard, Thomas Meier, Esther Posner, Hongzhan Fei, Tomo Katsura, Stefan Übelhack, Ulrich Faul, Svyatoslav Shcheka, Takahiro Yoshioka

back rows, from left (hintere Reihen, v. links) Alexander Kurnosov, Nobuyoshi Miyajima, Artem Chanyshev, Egor Koemets, Iuliia Koemets, Leonid Dubrovinsky, Takayuki Ishii, Timofey Fedotenko, Ulrich Böhm, Gerald Bauer, Egor Zakharchenko, Haihao Guo, Anna Spivak, Sergey Ovsyannikov, Kirill Vlasov, Gerd Steinle-Neumann, Lin Wang, Alexander Rother, Biao Wang, Andreas Audétat, Detlef Krauße, Johannes Buchen, Oliver Rausch, Jie Yao, Raphael Njul, Hans Keppler, Pierre Condaminé, Zhaodong Liu, Sumith Abeykoon, Jia Chang, Filippe Ferreira, Luca Ziberna, Taku Yutani

Absent (Es fehlten) Nicole Fischer, Holger Kriegl, Hauke Marquardt, Anke Potzel, Gerd Ramming, Romina Scharfenberg, Ulrike Trenz, Dmitry Bondar, Dmitry Druzhbin, Philipp Eichheimer, Gregor Golabek, Julia Immoor, Sylvain Petitgirard, Bertrand Rottier, Marcel Thielmann

Contents

Foreword

Progress in understanding the structure and dynamics of our planet is often closely related to advances in high-pressure technology. In recent years, Tomo Katsura has made great efforts to extend the capabilities of the multianvil laboratory at Bayerisches Geoinstitut. With the new IRIS press, it is now possible to routinely reach 35 GPa with anvils made of tungsten carbide. This technological development opens a new window into Earth's lower mantle. While previously multianvil experiments were largely limited to just the uppermost layer of the lower mantle, phase relationships and material properties can now be studied to much greater depth. We are therefore very pleased that the scientific achievements of Tomo Katsura were honoured by an ERC Advanced Grant, which he received in 2018. This is already the third ERC Advanced Grant awarded to BGI scientists, after previous awards to Dan Frost and Dave Rubie.

In the last year, the search procedure for a new professorship in Planetology was completed and we are very pleased that Audrey Bouvier from the University of Western Ontario in Canada has accepted the offer to join Bayerisches Geoinstitut on January 1, 2019. This success was made possible by a very generous offer from Bayreuth University, which included the construction of 120 m^2 new cleanrooms and laboratories for isotope geochemistry. The additional expertise in isotope geochemistry and cosmochemistry nicely complements the planetological research at Bayerisches Geoinstitut, which so far was mostly based on high-pressure experimentation and numerical modeling.

A major part of the scientific activities in 2018 was centered around our joint graduate school with Tohoku University on "Deep Earth Volatile Cycles", which is supported both by DFG and by the *Japanese Society for the Promotion of Science (JSPS)*. Several of our graduate students went to Sendai in Japan for up to six months in order to participate in research activities at Tohoku University. Chapter 3 of the current annual report contains results from various projects carried out within this joint graduate school. Volatiles, particularly H_2O and CO_2 are essential for melting in the mantle. Plate tectonics perhaps only works because of the "lubricating" effect of low-degree partial melts in the asthenosphere. A recently discovered new type of volcanism on the ocean floor, the so-called "petite-spot volcanoes" possibly taps such low-degree partial melts. The contribution by Yutani et al. on page 52 of this annual report describes the results from some exploratory experiments on the origin of these melts; the preliminary data seem to indicate that the source may contain phlogopite, which would suggest that the mantle below the volcanoes has experienced some previous metasomtic enrichment.

While only traces of volatiles are present in the normal mantle, magmas produced in subduction zones typically contain several weight percent of water. How this water was

transferred from the subducted slab to the zone of melting has been a subject of intense debate in the last years, with recent models favouring sediment melts as the trigger of melting in subduction zones. The main argument here used to be that aqueous fluids are "too dilute" to produce the trace element enrichment typically seen in arc magmas. The contribution by Greta Rustioni on page 59 shows that this is not so: If some NaCl is added to the fluid, the fluid/mineral partitioning of many trace elements increases by orders of magnitude due to the formation of chloride complexes. The resulting trace-element enrichment pattern has a striking similarity to that seen in arc magmas and therefore suggest that saline aqueous fluids, and not sediment melts, ultimately trigger magma formation in volcanic arcs – such as Japan.

On the behalf of my colleagues, I would like to thank the *Free State of Bavaria* as represented by the *Bavarian State Ministry of Science, Research and Art*, as well as the *Commission for High-Pressure Research in Geoscience* for their continuing support and strong commitment to the Bayerisches Geoinstitut. I would further like to thank the *President and Leadership of the University of Bayreuth* for their high regard of the profile field "High Pressure and High Temperature Research". We also gratefully acknowledge generous support from external funding agencies, in particular the *Alexander von Humboldt Foundation*, the *European Union*, the *German Science Foundation,* and the *Federal Ministry of Education and Research*, which continue to contribute greatly to the further development and success of the Geoinstitut.

Bayreuth, March 2019 Hans Keppler

Vorwort

Fortschritte in unserem Verständnis der Struktur und Dynamik unseres Planeten sind oft das Resultat von neuen Methoden der Hochdrucktechnologie. Tomo Katsura hat in den letzten Jahren sehr intensiv daran gearbeitet, die Möglichkeiten unseres Multi-Anvil-Labors zu erweitern. Mit der neuen IRIS-Presse können nun mit Wolframkarbid-Stempeln routinemäßig Drücke bis zu 35 GPa erreicht werden. Diese technologische Entwicklung öffnet ein neues Fenster in den unteren Erdmantel. Zuvor konnte man mit Multi-Anvil-Experimenten gerade noch die oberste Lage des unteren Erdmantels untersuchen; mit der neuen Technologie können nun Phasengleichgewichte und Materialeigenschaften bis zu sehr viel größeren Tiefen erforscht werden. Wir freuen uns daher, dass die wissenschaftlichen Leistungen von Tomo Katsura durch ein ERC Advanced Grant bestätigt wurden, das er im Jahr 2018 erhalten hat. Dies ist bereits das dritte ERC Advanced Grant an einen Wissenschaftler des BGI, nach früheren Verleihungen an Dan Frost und Dave Rubie.

Das Berufungsverfahren für eine neue Professur in Planetologie wurde im letzten Jahr abgeschlossen und wir freuen uns, dass Audrey Bouvier von der University of Western Ontario in Kanada den Ruf an das Bayerische Geoinstitut zum 1. Januar 2019 angenommen hat. Diese Berufung wurde ermöglicht durch ein überaus großzügiges Angebot der Universität Bayreuth, das unter anderem die Konstruktion von 120 m^2 neuer Reinsträume und Labore für Isotopen-Geochemie enthielt. Die zusätzliche Expertise in Isotopengeochemie und Kosmochemie ergänzt in perfekter Weise die planetologische Forschung am Bayerischen Geoinstitut, die bisher im Wesentlichen auf Hochdruckexperimenten und numerischer Modellierung beruhte.

Ein erheblicher Teil der wissenschaftlichen Aktivitäten in 2018 war Bestandteil unserer gemeinsamen Graduiertenschule über "Deep Earth Volatile Cycles" mit der Tohoku-Universität in Japan, die sowohl von der DFG als auch von der *Japanese Society for the Promotion of Science (JSPS)* gefördert wird. Mehrere Bayreuther Doktoranden reisten nach Sendai um an Forschungsprojekten der Tohoku-Universität mitzuarbeiten. Das Kapitel 3 des Jahresberichts enthält eine Reihe von Resultaten aus dem Graduiertenkolleg. Flüchtige Komponenten, insbesondere H_2O und CO_2 sind essentiell für die Schmelzbildung im Mantel. Möglicherweise funktioniert die Plattentektonik auf der Erde nur wegen der "Schmierwirkung" geringer Mengen von Schmelze in der Asthenosphäre. Ein vor kurzen entdeckter neuer Typ von Vulkanen auf dem Ozeanboden, die sogenannten "Petite-Spot-Vulkane" fördert möglicherweise solche Teilschmelzen aus dem Mantel. Der Beitrag von Yutani et al. auf Seite 52 dieses Jahresberichts beschreibt die Ergebnisse von einigen Experimenten zur Entstehung dieser Schmelzen; die vorläufigen Daten deuten darauf hin, dass der Mantel, aus dem diese Schmelzen stammen, Phlogopit enthält und daher wahrscheinlich durch Metasomatose chemisch verändert worden ist.

Während im normalen Mantel nur Spuren von flüchtigen Bestandteilen vorhanden sind, enthalten Magmen aus Subduktionszonen in der Regel mehrere Gewichtsprozent an Wasser. Wie dieses Wasser aus der subduzierten Platte in die Zone der Schmelzbildung im Mantel gelangt, wird gegenwärtig kontrovers diskutiert. Neuere Modelle gehen davon aus, dass Sediment-Schmelzen der eigentliche Auslöser für die Schmelzbildung im Mantel sind. Das Hauptargument hierfür war stets, dass wässrige Fluide "zu verdünnt" sind, um die typische Spurenelement-Anreicherung in Magmen von Subduktionszonen zu erzeugen. Der Beitrag von Greta Rustioni auf Seite 59 zeigt, dass dies nicht so ist: Sobald dem Fluid etwas NaCl zugefügt wird, erhöht sich der Fluid/Mineral-Verteilungskoeffizient vieler Spurenelemente um Größenordnungen. Grund hierfür ist wahrscheinlich die Bildung von Chlorid-Komplexen. Das resultierende Spurenelement-Anreicherungsmuster hat eine verblüffende Ähnlichkeit mit der Spurenelementhäufigkeit in Vulkaniten aus Inselbögen und zeigt, dass sehr wahrscheinlich salzhaltige Fluide (und nicht Sedimentschmelzen) der Auslöser für die vulkanische Aktivität oberhalb von Subduktionszonen sind – wie etwa in Japan.

Meine Kollegen und ich möchten dem *Freistaat Bayern*, vertreten durch das *Bayerische Staatsministerium für Wissenschaft, Forschung und Kunst*, und der *Kommission für Geowissenschaftliche Hochdruckforschung der Bayerischen Akademie der Wissenschaften* unseren Dank für ihre fortwährende Unterstützung des Bayerischen Geoinstituts aussprechen. Darüber hinaus möchten wir dem Präsidenten und der Hochschulleitung der Universität Bayreuth ausdrücklich für ihre zuverlässige und kontinuierliche Unterstützung des Profilfeldes 'Hochdruck- und Hochtemperaturforschung' danken. Wir sind auch für die großzügige Förderung durch externe Geldgeber dankbar, insbesondere der *Alexander-von-Humboldt-Stiftung*, der *Europäischen Union* und der *Deutschen Forschungsgemeinschaft*, die ebenfalls wesentlich zur Entwicklung und zum Erfolg des Bayerischen Geoinstituts beigetragen haben.

Bayreuth, im März 2019 Hans Keppler

1. Advisory Board and Directorship

1.1 Advisory Board

The *Beirat für Geowissenschaftliche Hochdruckforschung der Bayerischen Akademie der Wissenschaften* advises on the organisation and scientific activities of the institute. Members of this board are:

Prof. Dr. Gerhard BREY	Institut für Geowissenschaften der Johann Wolfgang Goethe-Universität, Frankfurt am Main
Prof. Dr. Ulrich CHRISTENSEN	Max-Planck-Institut für Sonnensystemforschung, Katlenburg-Lindau
Prof. Dr. Rudolf GROSS (Vice Chairman)	Walther-Meißner-Institut für Tieftemperatur-forschung (WMI), Garching
Prof. Dr. Rüdiger KNIEP	Emeritus, Max-Planck-Institut für Chemische Physik fester Stoffe, Dresden
Prof. Dr. Herbert PALME	Emeritus, Institut für Mineralogie und Geochemie der Universität zu Köln – Senckenberg Forschungsinstitut und Naturmuseum Frankfurt/M.
Prof. Dr. Markus RIEDERER (Chairman)	Julius-von-Sachs-Institut für Biowissenschaften, Würzburg
Prof. Dr. Ekhard SALJE, FRS, FRSA	Department of Earth Sciences, University of Cambridge
Prof. Dr. Christine THOMAS	Institut für Geophysik der Westfälischen Wilhelms-Universität Münster

The Advisory Board held a meeting in Bayreuth (27.04.2018).

1.2 Leadership

Prof. Dr. Hans KEPPLER (Director from 01.10.2018)
Prof. Dr. Dan FROST (Deputy Director from 01.10.2018)
Prof. Dr. Tomoo KATSURA

2. Staff, Funding and Facilities

2.1 Staff

At the end of 2018 the following staff positions existed in the Institute:

- Scientific staff: **15**
- Technical staff: **14**
- Administrative staff: **2**
- Administrative officer: **1**

During 2018, 49 scientific positions (455 months) were funded by grants raised externally by staff members of the institute. In addition 4 long-term scientific positions (38 months) were funded by the resources of the BGI Visiting Scientists' Programme (see Sect. 8) which also supported short-term visits for discussing future projects or presenting research results (see Sect. 5). 11 student assistants (83 months) were funded by externally raised grants. 8 scientists (63 months) were supported by personal grants or stipends.

2.2 Funding

In 2018, the following financial resources were available from the Free State of Bavaria:

- Visiting Scientists' Programme: 211.000 €
- Consumables: 519.000 €
- Investment funding: 60.000 €

The total amount of national/international external funding *("Drittmittel"*) used for ongoing research projects in 2018 was 3.580.000 € (Positions: 2.279.000 €; equipment, consumables and travel grants: 1.301.000 €).

	positions	**equipment, consumables, travel grants**	**total**
• AvH	81.000 €	34.000 €	115.000 €
• BMBF	136.000 €	178.000 €	314.000 €
• DFG	1.924.000 €	998.000 €	2.922.000 €
• EU	52.000 €	83.000 €	135.000 €
• Others	86.000 €	8.000 €	94.000 €
			3.580.000 €

(AvH = Alexander von Humboldt Foundation; BMBF = Federal Ministry of Education and Research; DFG = German Science Foundation; EU = European Union; Others: DAAD, Chinese Science Council, Japanese Society for the Promotion of Science, Swiss National Science Foundation)

In the following list only the BGI components of the funding are listed in cases where joint projects involved other research institutions. Principal investigators and the duration of the grants are listed in brackets. Total project funding refers to the funding over the entire duration of this project.

Funding institution	Project, Funding	Total Project Funding
BAdW	Bavarian Academy of Sciences research project (2016-2019) (H. Marquardt)	36.000 €
BMBF	05K16WCA (H. Keppler – 7/16-6/19) "Aufbau einer Hochdruckpresse vom Multi-Anvil-Typ an der Forschungs-Neutronenquelle FRM II in Garching" Total funding:	410.278 €
BMBF	05K16WC2 (T. Katsura – 7/16-6/19) "Erweiterung der Druckbereiche der In-Situ-Röntgen-beobachtung mit der Großvolumen-Hochdruckapparatur an der PETRA-III-Extension des Deutschen Elektronen-Synchrotrons DESY" Positions E 12-E 15: 214.882 € Consumables and travel funding: 298.197 € Equipment: 43.000 € Overhead: 111.216 €	667.295 €
DFG	BO 2550/7-2 (T. Boffa Ballaran, A. Woodland – 10/17-9/19) "Stabilities and properties of Mg, Al and Cr-bearing solid solutions of newly discovered Fe^{3+}-Fe^{2+} oxides at transition zone conditions: approaching geologically relevant compositions" Position: student assistant 7.500 € Consumables and travel funding: 7.000 € Overhead: 3.200 €	17.700 €
DFG	DU 393/9-2 (L.S. Dubrovinsky – 1/18-12/20) TP 7 'Chemische Reaktionen zwischen Karbonaten und pyrolitischem Erdmantel und Entstehung ultratiefer Diamanten', "Structures, properties and reactions of carbonates at high temperatures and pressures" Positions: E 13 (67 %), 36 months 132.800 € Consumables: 32.250 € Overhead: 36.300 €	201.350 €
DFG	DU 393/13-1 (L.S. Dubrovinsky – 4/17-3/20) "Mantel formende Materialien von Super Erden bei Statischen Drücken von über 500 GPa und hohen Temperaturen" Positions: E 13, 36 months 209.400 € student assistant 8.000 € Consumables: 27.750 € Overhead: 53.900 €	299.050 €

DFG	FR 1555/10-1 (D.J. Frost – 8/15-7/18) DFG SPP 1833 'Building a Habitable Earth' "Die Ermittlung des Mechanismus der frühzeitigen Oxidation des Erdinneren" Position: E 13 (75 %), 36 months 143.600 € Consumables: 22.250 € Overhead: 33.200 €	199.050 €
DFG	FR 1555/11-1 (D.J. Frost – 3/16-2/23) Gottfried Wilhelm Leibniz-Preis 2016	2.500.000 €
DFG	GRK 2156/1 (D.J. Frost, et al. – 4/16-10/20) Internationales Graduiertenkolleg "Deep Earth Volatile Cycles"	3.257.358 €
DFG	KA 3434/3-2 (T. Katsura – 7/18-6/20) "Dislocation recovery experiment of hydrous olivine as a function of water content and crystallographic orientation" Positions: E 13, 12 months 69.300 € E 13 (75 %), 12 months 48.100 € student assistant 5.000 € Consumables: 20.000 € Overhead: 31.300 €	173.700 €
DFG	KA 3434/8-1 (T. Katsura – 4/15-3/19) "Messung von Si-Selbstdiffusionskoeffizienten in Wadsleyit als Funktion des Wassergehaltes" Positions: E 13, 36 months 195.300 € student assistant 5.000 € Consumables and travel funding: 16.000 € Overhead: 43.300 €	259.600 €
DFG	KA 3434/9-1 (T. Katsura – 9/15-8/19) "Bestimmung des Drei-Phasen-Stabilitätsfelds des Postspinell-Übergangs in $(Mg,Fe)_2SiO_4$: Erörterung der extremen Schärfe der 660-km-Diskontinuität und deren Bedeutung für die chemische Struktur und die Dynamik des tiefen Erdmantels" Positions: E 13, 36 months 196.600 € student assistant 5.000 € Consumables and travel funding: 45.750 € Overhead: 49.500 €	296.850 €
DFG	KA 3434/11-1 (T. Katsura – 12/18-11/21) "Determining the water dissociation constant from the relationship between water solubility in ringwoodite and oxygen fugacity" Positions: E 13, 24 months 141.700 € Consumables: 23.500 € Overhead: 36.300 €	201.500 €

DFG	KA 3434/12-1 (T. Katsura – 10/18-09/20) "Determination of water partition coefficients between upper mantle minerals and melts as a function of pressure, temperature, and CO_2 content using a rapid quench cell in multi-anvil experiments" Positions: E 13, 24 months 142.700 € Consumables: 40.000 € Overhead: 40.200 €	222.900 €
DFG	KE 501/11-1 (H. Keppler – 2013-2018) "Electrical conductivity and dissociation of fluids in crust and mantle" Total funding:	267.800 €
DFG	KE 501/11-2 (H. Keppler – 2018-2020) "Electrical conductivity and dissociation of fluids in crust and mantle" Total funding:	209.600 €
DFG	KE 501/13-1 (H. Keppler – 2016-2018) "Nitrogen in the deep mantle" Total funding:	214.669 €
DFG	KE 501/15-1 (H. Keppler – 2017-2019) "Hochdrucklabore des Bayerischen Geoinstituts" Total funding:	371.878 €
DFG	KU 3447/1-1 (A. Kurnosov – 10/17-9/20) "Einkristall-Elastizität von Mars-Mineralen und ein flexibles CO_2 Laserheizsystem" Position: E 13, 36 months 217.700 € Consumables and travel funding: 15.250 € Overhead: 51.200 €	284.150 €
DFG	MA 4534/4-1 (H. Marquardt – 9/15-8/18) "Deformationsexperimente an (Mg,Fe)O Ferroperiklas bei hohen Drücken und gleichzeitig hohen Temperaturen" Position: E 13 (67 %), 36 months: 123.000 € Consumables: 33.850 € Overhead: 31.400 €	188.250 €
DFG	MA 4534/5-1 (H. Marquardt – 6/17-5/20) "Experimentelle Untersuchung von planetaren Eis-Verbindungen bei hohen Drücken mittels dynamisch-betriebener Diamantstempelzellen" Position: E 13 (75 %), 36 months: 145.700 € Consumables: 27.750 € Overhead: 38.200 €	211.650 €
DFG	MA 6287/3-1 (K. Marquardt, R. Dohmen – 9/15-8/18) "Elementverteilung in Geomaterial-Korngrenzen unter Berücksichtigung ihrer Geometrie" Positions: E 13 (67%), 36 months: 123.000 € student assistant 2.500 € Consumables: 26.445 € Overhead: 30.400 €	182.345 €

DFG	MA 6287/5-1 (S. Chakraborty, K. Marquardt, T. Fockenberg – 10/16-9/19) "Experimentelle Kalibrierung von Granat-Pyroxen Diffusionschronometrie für Anwendungen in terrestrische und planetare Proben" Position: student assistant 5.000 € Consumables: 5.000 € Overhead: 2.200 €	12.200 €
DFG	MA 6287/6-1 (K. Marquardt – 11/16-10/19) "Änderungen der Korngrenzcharakterverteilung in Olivin-dominierten Gesteinen als Funktion des Chemismus" Positions: E 13 (75 %), 36 months: 147.000 € student assistant 5.000 € Consumables, global funding: 45.030 € Overhead: 43.300 €	240.330 €
DFG	MC 3/20-1 (C.A. McCammon – 10/15-9/18) DFG FOR 2125 (CarboPaT) "Elastic properties of carbonates at high pressure and high temperature" Position: E 13 (66 %), 36 months: 120.600 € Equipment, consumables and travel funding: 32.250 € Overhead: 30.600 €	183.450 €
DFG	MC 3/20-2 (C.A. McCammon – 1/18-12/20) DFG FOR 2125 (CarboPaT) "Elastic properties of carbonates at high pressure and high temperature" Position: E 13 (67 %), 36 months: 132.800 € Equipment, consumables and travel funding: 27.750 € Overhead: 35.300 €	195.850 €
DFG	MC 3/21-1 (C.A. McCammon – 6/17-5/20) "Fe Spinübergang im Erdmantel: Einblicke durch Röntgen-Raman-Streuung und Röntgenabsorptionsspektroskopie" Position: student assistant (Bachelor) 9.482 € Equipment, consumables and travel funding: 6.000 € Overhead: 3.400 €	18.882 €
DFG	OV 110/1-3 (S.V. Ovsyannikov – 4/16-2/18) "Structural and electronic properties of sesquioxides at high pressures and temperatures: new forms, new insights and new possible applications" Position: E 13, 24 months 136.600 € Consumables and travel funding: 20.000 € Overhead: 31.300 €	187.900 €

DFG	OV 110/3-1 (S.V. Ovsyannikov – 9/18-8/20) "High-pressure synthesis and properties of novel simple oxides with unusual stoichiometries" Position: E 13, 24 months 141.600 € Consumables and travel funding: 30.250 € Overhead: 37.800 €	209.650 €
DFG	RU 1323/10-1 (D.C. Rubie – 1/17-12/19) DFG SPP 1833 'Building a Habitable Earth' "Entstehung und Entwicklung des Magmaozeans und Differentiation von Kern und Mantel während der Akkretion der Erde" Position: E 13, 36 months 206.700 € Consumables: 7.250 € Overhead: 42.800 €	256.750 €
DFG	STE 1105/12-1 (G. Steinle-Neumann, D.J. Frost, N. Tosi – 11/16-10/19) DFG SPP 1833 'Building a Habitable Earth' "Kristallisation des irdischen Magmaozeans: Thermo- und Geodynamik" Positions: E 13 (75%), 36 months 143.600 € student assistant 5.000 € Consumables: 8.250 € Overhead: 31.400 €	188.250 €
DFG	STE 1105/13-1 (G. Steinle-Neumann – 8/17-7/20) DFG through FOR 2440 (Matter Under Planetary Interior Conditions) "Thermodynamic properties of silicate solids and liquids and iron to the TPa range from *ab initio* calculations" Positions: E 13 (75%), 36 months 145.700 € student assistant 15.000 € Consumables: 7.750 € Overhead: 37.100 €	205.550 €
DFG	Emmy Noether-Programm (H. Marquardt – 2014-2019) "Structure and Elasticity of GeoMaterials at Extreme Conditions (GeoMaX)" Positions: group leader, E 14/E 15, 60 months: 375.400 € post doc, E 13, 60 months: 317.200 € 2 PhD students, E 13 (67%), 36 months: 264.400 € student assistant: 11.904 € Consumables, travel funding: 222.550 € Investments: 127.714 € Overhead: 184.400 €	1.503.568 €

EU	European Research Council (ERC) Advanced Grant No. 787 527 (T. Katsura – 10/18-9/23) "Chemistry and transport properties of bridgmanite controlling lower-mantle dynamics" ("UltraLVP") Positions (post docs): 860.144 € Travel funding: 187.380 € Equipment: 49.250 € Consumables: 997.722 € In-kind contributions: 24.000 € Overhead: 523.624 €	2.642.120 €
EU	European Research Council (ERC) Advanced Grant No. 290568 (D.C. Rubie – 5/12-4/18) "Accretion and Early Differentiation of the Earth and Terrestrial Planets" ("ACCRETE") Positions, consumables and travel funding:	1.826.200 €

2.3 Laboratory and office facilities

The institute occupies an area of

ca. 1350 m^2 laboratory space

ca. 480 m^2 infrastructural areas (machine shops, computer facilities, seminar room, library)

ca. 460 m^2 office space

in a building which was completed in 1994.

2.4 Experimental and analytical equipment

The following major equipment is available at the Bayerisches Geoinstitut:

I. High-pressure apparatus

15 MN/1500 tonne Kawai-type multianvil high-pressure apparatus (40 GPa, 2000 K)
6 x 8 MN/6x800 tonne independently acting-anvil press (25 GPa, 3000 K)
50 MN/5000 tonne multianvil press (25 GPa, 3000 K)
12 MN/1200 tonne multianvil press (25 GPa, 3000 K)
10 MN/1000 tonne multianvil press (25 GPa, 3000 K)
5 MN/500 tonne multianvil press (20 GPa, 3000 K)
5 MN/500 tonne press with a deformation DIA apparatus
5 piston-cylinder presses (4 GPa, 2100 K)
Cold-seal vessels (700 MPa, 1100 K, H2O), TZM vessels (300 MPa, 1400 K, gas), rapid-quench device
Internally-heated autoclave (1 GPa, 1600 K)
High-pressure gas loading apparatus for DAC

II. Structural and chemical analysis

1 X-ray powder micro-diffractometer
1 X-ray powder diffractometer with furnace and cryostat
2 automated single-crystal X-ray diffractometers
High-brilliance X-ray system
Single crystal X-ray diffraction with super-bright source
1 Mössbauer spectrometer (1.5 - 1300 K)
3 Mössbauer microspectrometers
2 FTIR spectrometers with IR microscope
FEG transmission electron microscope (TEM), 200 kV analytical, with EDS
FEG scanning TEM, 80-200 kV analytical, with 4-SDDs EDS and post-column energy filter (EFTEM/EELS)
FEG scanning electron microscope (SEM) with BSE detector, EDS, EBSD and CL
Dual beam device, focused ion beam (FIB) and FEG SEM. In situ easy-lift manipulator, STEM and EDS detector, and beam deceleration option
3 Micro-Raman spectrometers with ultraviolet and visible lasers
Tandem-multipass Fabry-Perot interferometer for Brillouin scattering spectroscopy
JEOL JXA-8200 electron microprobe; fully-automated with 14 crystals, 5 spectrometer configuration, EDX, capability for light elements
193 nm Excimer Laser-Ablation ICP-MS
Water content determination by Karl-Fischer titration
GC/MS-MS for organic analyses
Confocal 3D surface measurement system
1.4 Tesla sweepable ESR magnet
Solid state 300 MHz NMR spectrometer

III. *In situ* determination of properties

Diamond anvil cells for powder and single crystal X-ray diffraction, Mössbauer, IR, Raman, optical spectroscopy, NMR specroscopy, electrical resistivity measurements over 200 GPa
Facility for in situ hydrothermal studies in DAC
Externally heated DACs for in situ studies at pressures to 100 GPa and 1200 K
1-atm furnaces to 1950 K, gas mixing to 1600 K, zirconia fO2 probes
1-atm high-temperature creep apparatus
Gigahertz ultrasonic interferometer with interface to resistance-heated diamond-anvil cells
Freezing-heating stage for fluid inclusion studies
Impedance/gain-phase analyser for electrical conductivity studies
Apparatus for in situ measurements of thermal diffusivity at high P and T
Laser-heating facility for DAC
Portable pulsed laser heating system for DAC

The Geoinstitut is well equipped with machine shops, an electronic workshop and sample preparation laboratories. It also has access to the university computer centre.

3. Forschungsprojekte

3.1 Struktur und Dynamik der Erde und Planeten

Die terrestrischen Planeten im Sonnensystem entstanden über einen Zeitraum von etwa 100 Millionen Jahren. Moderne astrophysikalische Modelle deuten darauf hin, dass Planetesimale, die ersten Bausteine der Planeten, wenige Dutzend bis Hundert Kilometer große Körper waren. In diesen Planetesimalen war der Zerfall des kurzlebigen radiogenen Isotops ^{26}Al die dominante Wärmequelle. In primordialen Körpern war ^{26}Al größtenteils in Mineralen mit niedriger Schmelztemperatur konzentriert. Dementsprechend wurde vorgeschlagen, dass ^{26}Al in die erste Silikatschmelze gelangte und zur Oberfläche von Planetesimalen aufstieg und durch das Fehlen dieser Wärmequelle im Inneren keine Magmaozeane entstehen konnten. Die erste Studie untersucht mittels eines neuartigen Ansatzes, der petrologische Multi-komponenten-Reaktionen mit einem Zwei-Phasen-Schmelztransportmodell verbindet, unter welchen Bedingungen ^{26}Al-reiche Schmelzen zur Oberfläche aufsteigen konnten und wann es zur Entstehung von Magmaozeanen kommen konnte.

In der Folgezeit, als ^{26}Al größtenteils zerfallen war und durch Akkretion die Protoplaneten mindestens die Masse des Erdmondes erreicht hatten, wurde die Freisetzung kinetischer Energie durch Kollisionen von Bedeutung, um das Innere dieser Körper aufzuheizen. Jedoch ist die Simulation jeder einzelnen Kollision in der Entstehungsgeschichte eines terrestrischen Planeten sehr rechenintensiv. Deshalb wurde in der folgenden Studie eine Parametrisierung hergeleitet, so dass aus den Kollisionsparametern sowohl das Volumen als auch die Tiefe des jeweiligen Magmaozeans bestimmt werden kann. Dies kann dann verwendet werden, um sowohl das Verteilungsverhalten verschiedener Elemente zwischen Metall und Silikaten zu bestimmen, als auch um die frühe thermische Evolution von entstehenden terrestrischen Planeten zu studieren.

Sowohl astrophysikalische Beobachtungen als auch numerische Modelle zur Sternentstehung in jungen offenen Sternhaufen zeigen, dass ^{26}Al in der Galaxie sehr inhomogen verteilt ist. Dementsprechend sind die protoplanetaren Scheiben um junge Sterne in vielen Fällen völlig frei von ^{26}Al, in anderen Fällen wird das bis zu zehnfache der Anfangskonzentration von ^{26}Al in unserem Sonnensystem erwartet. Die dritte Studie kombiniert geodynamische Modelle, in denen der durch ^{26}Al verursachte Verlust von volatilen Bestandteilen aus Planetesimalen berechnet wird, mit Planetenentstehungsmodellen. In ausführlichen Berechnungen konnte gezeigt werden, dass der finale Wassergehalt eines neu entstandenen terrestrischen Planeten stark abhängt von der Anfangskonzentration an ^{26}Al. Dadurch lässt sich sowohl die geringe Masse an Wasser auf der heutigen Erde als auch auf den vor wenigen Jahren entdeckten TRAPPIST-1 Exoplaneten besser verstehen.

Die Resultate der NASA-Mission Kepler haben aufgezeigt, dass Supererden, terrestrische Planeten mit mehreren Erdmassen, den häufigsten Exoplaneten-Typ darstellen. Da der Druck- und Temperaturbereich im tiefen Inneren von Supererden experimentell noch nicht

zugänglich ist, verwendet die vierte Studie numerische Modelle, um Eisen unter diesen Druck- und Temperaturbedingungen zu studieren. Dadurch ist es möglich, Rückschlüsse zu ziehen, ob im Innern dieser Planeten ein flüssiger Eisenkern existieren kann, welcher ein schützendes Magnetfeld um den Planeten aufbauen könnte.

Nach dem Ende der Akkretion kühlten die terrestrischen Planeten ab und der anfängliche Magmaozean kristallisierte aus. Dies führte in der Erde zur Ausbildung eines festen Mantels. Der untere Mantel setzt sich größtenteils aus dem Mineral Bridgmanit und einer deutlich kleineren Menge an Ferroperiklas zusammen. Es ist momentan jedoch unklar, ob das zähflüssige Bridgmanit oder das rheologisch schwächere Ferroperiklas das Deformationsverhalten des unteren Mantels dominiert. Die folgende fünfte Studie simuliert die Deformation von Bridgmanit+Ferroperiklas-Gemischen auf der Mikroskala, um festzustellen unter welchen Bedingungen das Ferroperiklas ein verbundenes Netzwerk ausbilden und somit die Rheologie des unteren Erdmantels dominieren kann. Basierend auf diesen Resultaten kann zukünftig eine Parametrisierung entwickelt werden, um das Verhalten von Bridgmanit+Ferroperiklas in globalen Mantelkonvektionsmodellen besser zu beschreiben.

Von Deformationsprozessen im aktiven Erdinneren zeugen unter anderem Erdbeben. Dabei werfen tiefe Erdbeben mit Hypozentren in mehr als 300 km Tiefe bis heute Fragen auf, da sie nicht durch Sprödbruchprozesse erklärt werden können. Das numerische Modell in der folgenden Studie untersucht sowohl den Effekt von Reibungshitze als auch den von Korngrößenänderung als mögliche Erklärung tiefer Erdbeben. Die Resultate zeigen in der Tat, dass sich unter bestimmten Bedingungen wiederholt stark lokalisierte Scherbänder entwickeln können, deren Verhalten denen von sogenannten stillen Erdbeben ähnelt.

Ein anderer Prozess, der von der Aktivität im Erdinnern kündet ist Vulkanismus. Hierbei spielt die Permeabilität von Gesteinen eine wichtige Rolle beim Aufstieg von Schmelzen. Traditionell wird die Permeabilität von Gesteinen mittels Labormessungen ermittelt, jedoch ist dies im Fall sehr kleiner Porositäten nicht möglich. Die nächste Studie vergleicht die Resultate von Laborexperimenten mit numerischen 3D Modellen, die Computer-Tomographien als Ausgangspunkt für die Permeabilitätsberechnung verwenden. Die Resultate zeigen nicht nur eine gute Übereinstimmung zwischen beiden Methoden bei mittleren und hohen Porositäten, sondern demonstrieren weiterhin, dass die numerische Bestimmung der Permeabilität auch bei sehr kleinen Porositäten möglich ist.

3.2 Geochemie

Prozesse, die für die Bildung der Erde, den Ablauf der Plattentektonik und die geochemische Entwicklung der Kruste und des Erdmantels wichtig sind, haben Spuren in Gesteinen, Magmen und Flüssigkeiten hinterlassen. Die experimentelle Geochemie und Petrologie hat die Aufgabe, diese Spuren zu interpretieren, indem sie die Bedingungen ihres Ursprungs reproduziert oder die Fraktionierungsereignisse simuliert, durch die sie entstanden sind. Das

Problem ist, dass die Hinweise auf die kritischen Prozesse und die vorherrschenden Bedingungen immer knapper werden, je tiefer wir in das Innere der Erde oder weiter zurück in der Zeit gehen.

Der erste Abschnitt enthält eine Reihe von Berichten, die experimentelle Daten zur Interpretation geochemischer und petrologischer Beobachtungen liefern. In mehreren Studien werden auch natürliche Proben untersucht, um neue Einblicke in ihre Entstehung zu erhalten. Im ersten Bericht in diesem Abschnitt wird untersucht, wie sich Kohlenstoff zwischen dem kernbildenden Metall und dem Silikatmantel verteilt, während sich die Erde bildete und fraktionierte. Die wichtige Frage hier ist, warum so viel Kohlenstoff im Erdmantel geblieben ist, obwohl bisherige Studien zeigten, dass sich Kohlenstoff stark im Metall anreichert. Die neuen Experimente, die bei den extremen Drücken des unteren Erdmantels durchgeführt wurden, zeigen unter diesen Bedingungen jedoch eine drastische Abnahme der Präferenz von Kohlenstoff für metallisches Eisen. Kohlenstoff, der bei niedrigem Druck in das absinkende Metall fraktioniert wurde, würde daher in der Tiefe in den silikatischen Mantel zurück-diffundieren. Es folgt eine Studie zur Untersuchung der Verteilung stabiler Vanadium-Isotope zwischen kernbildendem Metall und Silikatschmelze. Der Erdmantel scheint im Vergleich zu seinen meteoritischen Bausteinen an schweren Vanadium-Isotopen angereichert zu sein, was ein Hinweis darauf sein könnte, dass leichte Vanadium-Isotope bevorzugt im Kern angereichert sind. Vorläufige Ergebnisse deuten darauf hin, dass dies unwahrscheinlich ist und dass die Erde im Vergleich zu Meteoriten tatsächlich eine andere Vanadium-Isotopensignatur enthält. Weitere Experimente bei höheren Drücken sind jedoch im Gange, um dies eindeutig zu klären.

Die nächsten drei Berichte untersuchen verschiedene Aspekte der Geochemie von Sulfidschmelzen. Gegen Ende der Kernbildung waren Sulfidschmelzen möglicherweise die Hauptagenzien für die Kernbildung, da die Sauerstofffugazität des Mantels zu steigen begann. Die erste Studie untersucht die Verteilung von Wasserstoff zwischen Sulfidschmelzen und H_2O-haltigen Silikatschmelzen, um zu testen, ob auf diese Weise Wasserstoff aus dem Mantel verloren gegangen sein könnte. Die vorläufigen Ergebnisse scheinen darauf hinzuweisen, dass Sulfidschmelzen Wasserstoff in Form von H_2O aufnehmen und daher den Redoxzustand des Mantels nicht beeinflussen. In den nächsten beiden Studien werden Sulfidschmelzen untersucht, weil sie die häufigsten Einschlüsse in Diamanten darstellen, was auch in den vier nachfolgenden Berichten thematisiert wird. In der Vergangenheit wurde angenommen, dass die Diamantbildung während der Metasomatose der subkratonischen Lithosphäre stattfindet, ein Prozess, der in gewisser Weise eine geochemische Sackgasse darstellt. Es ist jedoch jetzt erkannt worden, dass sich einige Diamanten (darunter auch einige besonders wertvolle), tatsächlich im tieferen konvektiven Mantel bilden. Solche Diamanten und ihre Einschlüsse stellen die einzigen Proben dar, die wir aus dem tiefen Mantel haben. Diamanten sind natürlich auch Zeitkapseln, die Schmelzen und Kristalle aus der Zeit der Diamantbildung konservieren. Die erste dieser Untersuchungen präsentiert eine vorläufige Analyse, ob der Sauerstoffgehalt von abgeschreckten Sulfidschmelzen zur Bestimmung der Bildungs-temperaturen verwendet werden kann. Die Ergebnisse sind vielversprechend, zumal es derzeit

keine andere Methode zur Bestimmung der Temperaturen der tiefen Diamantbildung gibt. Die nachfolgende Studie zeigt, dass Sulfidflüssigkeiten als Katalysator für die Keimbildung und das Wachstum von Diamanten wirken, eine Beobachtung, die zur Erklärung der Verbreitung von Sulfideinschlüssen in Diamanten beitragen kann und einen Mechanismus für die Diamantsynthese in natürlichen Mantelaggregaten bietet.

Der nächste Bericht von Ottersberg et al. untersucht einen anderen möglichen Mechanismus der Diamantbildung. Viele Einschlüsse in Diamanten, die sich in großer Tiefe gebildet haben, scheinen eine Reaktion zwischen partiellen Schmelzen aus Basalt und dem umgebenden Peridotit zu belegen. Experimente zeigen, dass sich in einer solchen Schmelzreaktionszone Diamanten bilden, wenn reduzierte CH_4-reiche Flüssigkeiten mit Mineralen in Kontakt kommen, die durch Schmelzreaktionen mit Fe^{3+} angereichert sind. Die darauf folgende Studie verwendet eine relativ neue Art von Synchrotron-Mössbauer-Spektroskopie, die das $Fe^{3+}/\Sigma Fe$-Verhältnis von relativ kleinen Proben ermitteln kann. Die Technik wird verwendet, um solche Verhältnisse in sehr chromreichen Spinellmineralen zu messen, die sowohl in Mantelgesteinen (Xenolithen) als auch in Diamanteinschlüssen vom Rand des Simbabwe-Kratons gefunden werden. Obwohl beide Arten von Proben durch die Extraktion großer Anteile an partieller Schmelze, die ebenfalls zur Abreicherung an Fe^{3+} führt, Cr-reich geworden sein müssen, weisen die Diamanteinschlüsse bemerkenswert hohe $Fe^{3+}/\Sigma Fe$-Verhältnisse auf, was wahrscheinlich auf eine Bildung der Diamanten aus relativ oxidierten Mantelflüssigkeiten schließen lässt. In der nächsten Studie wird die Geschichte eines diamantführenden Eklogits durch Untersuchungen von Reaktionen erhellt, die dessen Entstehungstiefe und den Oxidationszustand eingrenzen. Eklogite sind metamorphe Gesteine, die aus subduziertem ozeanischem Basalt gebildet wurden. Es wurde festgestellt, dass sich in diesem Gestein Diamanten während des Subduktionsprozesses aus Karbonat gebildet haben. Bevor das Gestein durch das Kimberlitmagma an die Oberfläche gebracht wurde, ist es im Mantel schrittweise in geringere Tiefen aufgestiegen, möglicherweise durch Pulse magmatischer Vorläufer. Die letzte Studie, die sich auf Diamanten bezieht, zielt darauf ab, den relativ hohen Oxidationszustand von Eisen in Majorit-Granateinschlüssen aus tiefen Manteldiamanten zu verstehen. Durch experimentelle Untersuchung der $Fe^{3+}/\Sigma Fe$-Verhältnisse solcher Einschlüsse sollte es möglich sein, den Oxidationszustand von diamant-bildenden Flüssigkeiten im tiefem Erdmantel zu verstehen. Im Gegensatz zu früheren Studien deuten die aktuellen Ergebnisse jedoch darauf hin, dass der Druck allein keinen wesentlichen Einfluss auf die Stabilisierung von Fe^{3+} in diesem Mineral hat und dass andere Mechanismen für die beobachteten $Fe^{3+}/\Sigma Fe$-Verhältnisse in den Einschlüssen gesucht werden müssen.

Die nächsten vier Studien untersuchen Mantelschmelzprozesse in der Erde bei schrittweise höheren Drücken. Die erste beschäftigt sich mit einer neu entdeckten Art von Mantel-schmelzbildung, dem sogenannten Petit-Spot-Vulkanismus. Petit-Spot-Vulkane sind, wie der Name vermuten lässt, klein und kommen auf dem Meeresboden weit weg von den Mittel-ozeanischen Rücken vor. In vielen Fällen treten sie auf, wenn ozeanische Platten beginnen, zu subduzieren. Die plausibelste Theorie ist, dass die durch die Biegung der Lithosphäre erzeugten Zugkräfte es ermöglichen, dass H_2O- und CO_2-haltige Mantelschmelzen aus der

darunter liegenden Asthenosphäre an die Oberfläche gelangen. In dieser Studie wird ein Modell verwendet, das die Auswirkungen der Olivinfraktionierung und der Entgasung flüchtiger Elemente berücksichtigt, um die primitive Zusammensetzung der Mantelschmelze zu bestimmen. Mit dieser Schmelzzusammensetzung werden dann Experimente durchgeführt, um die Bedingungen zu bestimmen, bei denen das Schmelzen zur Erzeugung des primitiven Magmas erfolgte. Vorläufige Ergebnisse deuten darauf hin, dass das Ausgangsgestein eines dieser Magmen das wasserhaltige Mineral Phlogopit enthielt, was wahrscheinlich darauf hindeutet, dass das Ausgangsgestein bereits durch vorherige Wechselwirkung mit wasserhaltiger Schmelze (Metasomatose) hydratisiert worden war. Die nächste Schmelzstudie zielt darauf ab, die Zusammensetzung einer sehr geringen Menge wasserhaltiger Schmelzen zu bestimmen, die in oder an der Grenzfläche der Mantelübergangszone der Erde vorhanden sein könnte. Im Mantel wurden langsame seismische Wellengeschwindigkeiten in Tiefen beobachtet, in denen nur die Anwesenheit von H_2O oder CO_2 zum Schmelzen führen könnte. Wenn Schmelzen tatsächlich für niedrige seismische Geschwindigkeiten verantwortlich sind, die in Tiefen von ~ 400 km beobachtet werden, könnte eine hohe Kompressibilität dazu führen, dass sie die gleiche Dichte haben wie die umgebenden Gesteine. Dies würde erklären, warum solche Schmelzen in dieser Tiefe bestehen bleiben und nicht aus dem Mantel aufsteigen. Experimente wurden durchgeführt, um die Zusammensetzung solcher Schmelzen zu bestimmen, die durch H_2O stabilisiert werden. Der nächste Schritt wird sein, zu untersuchen, ob diese Schmelzen tatsächlich im Mantel gravitativ stabil sind. Andererseits scheinen diese Schmelzzusammensetzungen den an der Oberfläche gefundenen kimberlitischen Magmen sehr ähnlich zu sein, die in diesen Tiefen gebildet werden. Die folgenden beiden Studien untersuchen das Schmelzen im unteren Mantel. Die erste untersucht Schmelzbildung in Gegenwart von H_2O, verwendet jedoch zwei Ausgangszusammensetzungen mit Eisen, das entweder vollständig im Fe^{3+}- oder im Fe^{2+}-Oxidationszustand ist. Ziel ist es, den Ursprung der Regionen mit niedriger seismischer Geschwindigkeit zu verstehen, die im oberen Teil des unteren Mantel beobachtet wurden. Interessanterweise zeigen die Ergebnisse, dass nur die stärker reduzierte Fe^{2+}-Zusammensetzung zu starkem Aufschmelzen führt, obwohl die Ursache für diesen Effekt noch nicht verstanden ist. Die abschließende Studie zum Mantelschmelzen zielt darauf ab, die Verteilung von Eisen während der Kristallisation eines tiefen Magmaozeans zu verstehen. Der Eisengehalt der Schmelze ist einer der Hauptfaktoren, die beeinflussen, ob eine Schmelze dichter als der umgebende Mantel sein kann. Dies könnte dazu führen, dass eine dichte Schmelzschicht an der Basis des Mantels erhalten bleibt. Multianvil-Experimente können die Bedingungen an der Basis des Mantels nicht erreichen, und Untersuchungen mit Diamantstempelzellen lieferten widersprüchliche Resultate. Durch die Entwicklung thermodynamischer Modelle für das Schmelzen auf der Grundlage von Experimenten bei geringerem Druck können Schmelzbeziehungen zuverlässiger extrapoliert werden, um die Ergebnisse von Experimenten bei höherem Druck zu interpretieren.

Die folgenden vier Studien behandeln die Rolle flüchtiger Komponenten in Subduktionszonen. Die Bildung von Serpentin hydratisiert die ozeanische Lithosphäre nicht nur, sondern

oxidiert sie auch. Natürliche Serpentine können ihr Eisen fast vollständig im Fe^{3+}-Zustand haben, aber bisher wurde in keinem Experiment die Auswirkung von Fe^{3+} auf die Serpentinitstabilität untersucht. In der ersten Studie erweist sich dieser Effekt als sehr gering. Andererseits zeigen die Ergebnisse, dass die Dehydratisierung von Serpentin aufgrund von Änderungen der Temperaturstabilität der Fe^{3+}-Komponente zu einer ziemlich starken Erhöhung der Sauerstofffugazität der subduzierenden Platte führen sollte. Dies könnte beispielsweise wichtige Auswirkungen auf das Verhalten von Schwefel in Subduktionszonen haben, der durch Oxidation zu Sulfat mobilisiert würde.

In den folgenden zwei Studien wird die Art der fluiden Phasen untersucht, die die angereicherte Spurenelement-Signatur in der Quellregion von Ozeanbogen-Magmen erzeugt. In der Vergangenheit wurde davon ausgegangen, dass wässrige Fluide, die durch Dehydratisierung von subduzierenden Platten erzeugt werden, diese angereicherte Signatur liefern. In neueren Studien stellte sich jedoch die Frage, ob die Konzentration von Spurenelementen in wässrigen Fluiden hoch genug ist, um dies zu erreichen, oder ob partielle Schmelzen aus subduzierten Sedimenten ein wahrscheinlicheres Medium dafür sind. Die Experimente in der ersten Studie zeigen jedoch überzeugend, dass die Erhöhung des Salzgehalts im Fluid die Konzentrationen genau jener Elemente, die in Ozeanbogen-Magmen angereichert sind, dramatisch erhöht, weshalb ein Beitrag durch Sediment-Schmelzen nicht mehr nötig ist. In der folgenden Studie wird auch die alternative Sedimentschmelzhypothese untersucht. Es wurden Experimente durchgeführt, um zu untersuchen, ob die schrittweise Reaktion silikatischer partieller Schmelzen mit dem darüberliegenden Mantel Magmen erzeugen kann, die in ihrer Zusammensetzung Inselbogen-Magmen ähneln. Die Ergebnisse zeigen, dass bei den Bedingungen an der Grenzfläche zwischen subduzierter Platte und Mantel ein solcher Prozess die gewünschten Schmelzzusammensetzungen nicht erzeugen kann. Die abschließende Studie im Zusammenhang mit der Subduktion untersucht das Verhalten von Karbonatgesteinen beim Eintritt in den reduzierten unteren Mantel. In Versuchen mit laserbeheizten Diamantstempelzellen reagierte $MgCO_3$ mit metallischem Fe, das aufgrund der geringen Sauerstofffugazität im unteren Mantel vorhanden ist. In den Proben scheint die Bildung von Fe_7C_3 darauf hinzuweisen, dass das Karbonat in Gegenwart von Eisenmetall reduziert wird; in einigen Proben gibt es jedoch Hinweise, dass eine Hochdruckphase von $MgCO_3$ bestehen bleiben kann.

Die letzten drei Beiträge in diesem Abschnitt befassen sich mit der Bildung von Erzlagerstätten vom Porphyr-Typ. Die erste ist eine umfangreiche petrologische Studie an zwei slowakischen Vulkanen, die mit mehreren kleinen Porphyr-Gold- und Kupferlagerstätten in Verbindung stehen. Ziel ist es zu untersuchen, ob das Au:Cu-Verhältnis dieser Erzlagerstätten bereits in den mineralisierenden Magmen vordefiniert war. Die Ergebnisse zeigen, dass dies eindeutig nicht der Fall ist und dass die Tiefe der Magma-Platznahme wahrscheinlich den stärksten Einfluss auf das Au:Cu-Verhältnis von porphyrartigen Lagerstätten hat. In der nächsten Studie werden die Kristallisationsbedingungen, flüchtige Anteile und Metallgehalte von mineralisierenden Magmen in sechs porphyrischen

Molybdänlagerstätten im Nordosten Chinas rekonstruiert, um die Bedingungen einzugrenzen, die zu Mo-Mineralisierung führen. Es zeigt sich, dass in den Schmelzen weder ungewöhnlich hohe Mo-Konzentrationen noch ungewöhnliche Wassergehalte erforderlich sind, und dass wiederum die Tiefe der Magma-Platznahme wahrscheinlich die wichtigste Rolle spielt. Der abschließende Beitrag in diesem Abschnitt ergänzt die vorherige Studie und ist eine petrologische Untersuchung von zwei nicht vererzten Intrusionen, die in größerer Tiefe (10-14 km) kristallisierten als typische porphyrische Mo-produzierende Intrusionen (4-8 km). Die Studie wurde durchgeführt, um das Verhalten von Mo bei tiefen Intrusionen zu bewerten. Es wurde festgestellt, dass Mo in diesen tiefen Graniten tatsächlich effizienter durch die austretenden Fluide extrahiert wurde, jedoch keine Strukturen entwickelt wurden, die einen fokussierten Fluidfluss und eine effiziente Mo-Abscheidung ermöglichten.

3.3 Mineralogie, Kristallchemie und Phasenübergänge

Die feste Erde besteht größtenteils aus Mineralen, d.h. natürlich gebildeten kristallinen Substanzen. Ihre chemische Zusammensetzung und Struktur bestimmen die Eigenschaften und das Verhalten unseres Planeten. Die Beiträge in diesem Kapitel untersuchen die strukturellen Veränderungen wichtiger Minerale der Erde unter verschiedenen äußeren Parametern wie Temperatur, Druck, Sauerstofffugazität und Wasserkonzentration. Ziel ist es, die Struktur des Inneren der Erde experimentell einzugrenzen und dieses Wissen zu nutzen, um die Bildungsprozesse innerhalb der Erde anhand der Analyse von natürlich gebildeten Mineralen zu entschlüsseln.

Die Festkörperdiffusion ist ein wichtiger Mechanismus für den chemischen Austausch in Mineralen und Gesteinen bei hoher Temperatur (und hohem Druck) und wird als geologischer Geschwindigkeitsmesser sowie als Geothermometer verwendet. Im ersten Beitrag dieses Kapitels wird der diffusive Austausch von Fe-Mg zwischen verschiedenen Pyroxenen experimentell untersucht, um dieses häufig verwendete Geothermometer zu verbessern. Erste Ergebnisse deuten darauf hin, dass die chemische Äquilibrierung auf einem anderen Weg erfolgt, als üblicherweise angenommen wird und nicht nur Interdiffusion beinhaltet, sondern auch die vollständige Umkristallisation von Körnern mit neuen Zusammensetzungen. In dem folgenden Bericht wurde der Einfluss der Wasserkonzentration auf die Bildung von Pargasit im oberen Erdmantel untersucht. Die Resultate zeigen, dass wassergesättigte Bedingungen erforderlich sind, um dieses Mineral zu bilden, während eine Wasseraktivität von 0,1 nicht ausreicht. Pargasit ist das wichtigste wasserhaltige Mineral in Gesteinen des oberen Mantels, und die Ergebnisse zeigen, dass seine Bildung auf besonders wasserreiche Zonen im oberen Mantel beschränkt ist, z. B. in der Nähe von subduzierenden Platten. Im dritten Beitrag wurde die Möglichkeit der Bildung von Phasen mit der allgemeinen Zusammensetzung $Ca_xAl_yFe_zO_w$ bei Drücken getestet, die der Mantelübergangszone und dem oberen Teil des unteren Mantels entsprechen. Eine zuvor unbekannte Phase mit der Zusammensetzung $Ca_2Al_6O_{11}$ wurde identifiziert und als potentiell im unteren Mantel vorhandene Struktur charakterisiert.

Das System Fe-O ist in der festen Erde von besonderer Bedeutung, da es aufgrund der unterschiedlichen Oxidationszustände von Eisen direkt mit der Sauerstofffugazität im Gestein korreliert. Die folgenden sechs Beiträge beziehen sich alle auf dieses Thema. Im ersten Bericht wurden das Stabilitätsfeld und die Struktur der Fe_5O_6-Phase bestimmt, die darauf hinweisen, dass es sich um eine stabile Phase entlang der Manteladiabate bis in die oberen Bereiche des unteren Mantels handeln könnte. Der folgende Beitrag untersucht die Substitution von etwas Fe^{2+} durch Mg^{2+} in den Phasen vom Fe-O-Typ und zeigt die Kristallstruktur von $Mg_{0.9}Fe_{8.1}O_{11}$, die bei 12 GPa und 1300 °C synthetisiert wurde. Im nächsten Bericht wird die Wechselwirkung von Bridgmanit $(Mg,Fe)(Al,Si)O_3$ mit der Sauerstofffugazität des unteren Mantels experimentell untersucht. Die Ergebnisse zeigen, dass das $Fe^{3+}/\Sigma Fe$-Verhältnis von Bridgmanit abhängig von der Sauerstofffugazität ist, und dass diese Abhängigkeit mit zunehmendem Al-Gehalt im Bridgmanit geringer wird. In dem folgenden Beitrag wird ein thermodynamisches Modell beschrieben, das die p, T und fO_2 Abhängigkeit des Fe^{3+}-Gehalts in Ferroperiklas auf der Grundlage einer Reihe von Experimenten im Bereich von 6-25 GPa und 1200-1800 °C eingrenzen soll, um die Bildungsbedingungen von Ferroperiklas-Einschlüssen in Diamanten besser bestimmen zu können. In der nächsten Studie wurde die Kristallstruktur von Fe_2O_3 bei extremen Drücken von bis zu über 200 GPa untersucht. Bei Raumtemperatur ist Fe_2O_3 bei diesen extremen Drücken stabil in der Post-Perowskit-Struktur, Aufheizung mithilfe von Lasern führt jedoch zu Sauerstoffverlust und zur Bildung von reduzierten Phasen mit unterschiedlichen Stöchiometrien.

Neben Fe-O-Zusammensetzungen sind auch Fe-O-H-Komponenten von großem Interesse, da ihre potenzielle Hochdruckstabilität einen Weg für eine tiefe Rückführung von Wasser in den Erdmantel bietet. Der neunte Beitrag dieses Kapitels konzentriert sich auf die Stabilität von δ-Phasentypen im System $AlOOH$-$FeOOH$-$MgSiO_2(OH)_2$, die bei 21 GPa und 1480 K synthetisiert werden konnten, wodurch sie als mögliche Mineralphasen für den Transport von Wasserstoff in den unteren Erdmantel geeignet wären. Wenn reines FeOOH in der Diamantstempelzelle Drücken ausgesetzt wurde, die einer Tiefe von 1800 km entsprachen, ergab sich ein Übergang von der Goethit- zur Pyrit-Struktur, wie im zehnten Bericht gezeigt. Aufheizung mit Laserlicht verursachte jedoch einen Verlust an Wasserstoff und Sauerstoff und die Bildung verschiedener Fe-O-Zusammensetzungen, was darauf hindeutet, dass reines FeOOH keine geeignete Phase für den Wasserstofftransfer in die Tiefe der Erde ist.

Der oberste Teil des festen Eisenkerns der Erde zeigt unerwartet niedrige seismische Scherwellengeschwindigkeiten relativ zu den aus mineralogischen Studien hergeleiteten Geschwindigkeiten. Ein möglicher Grund könnte der sogenannte Vorschmelzeffekt sein, der vorhersagt, dass Feststoffe in der Nähe ihres Schmelzpunkts eine signifikante Abnahme der elastischen Scherfestigkeit aufweisen. Im vorletzten Beitrag wurden Vorschmelz-Effekte in einem Neon-Einkristall nachgewiesen, der als Analogmaterial für Eisen unter extremen Bedingungen verwendet wurde. Eine Abnahme der elastischen Konstanten und der Anisotropie wurde in der Nähe des Schmelzpunkts bei ~ 7 GPa in einer Diamantstempelzelle beobachtet. Im vorletzten Beitrag dieses Kapitels wird die erste Strukturmessung der schwer

synthetisierbaren Wasser-Eis-X-Phase in der Diamantstempelzelle beschrieben. Mit Hilfe einer NMR-Mikrosonde wurde die Symmetrisierung der H-Bindung oberhalb von 60 GPa beobachtet. Im letzten Beitrag werden Einblicke in die Dehydratisierungsprozesse von Mineralien in chondritischen Meteoriten gegeben, die als älteste Proben unseres Sonnensystems gelten. Ziel ist es, die Auswirkungen von Impaktvorgängen auf die meteoritischen Grundkörper mit stufenweisen Aufheizungsversuchen zu rekonstruieren, um die ursprüngliche mineralogische Zusammensetzung dieser Meteoriten nach der Kondensation des Sonnennebels zu bestimmen. Die aus dieser Studie resultierenden Mineralzusammensetzungen können dann mit der Mineralogie von Proben verglichen werden, die von Missionen zu Kometen und Asteroiden zurückgebracht wurden.

3.4 Physikalische Eigenschaften von Mineralen

Vieles, was wir über den tieferen Teil des Erdmantels wissen, stammt aus der Seismologie, dem Studium der Schallwellenfortpflanzung durch das tiefe Innere der Erde. Durch Erdbeben angeregte elastische Wellen werden in der Erde gebrochen und reflektiert. Sie können dazu verwendet werden, das Erdinnere zu untersuchen und Informationen über die elastische Struktur und letztendlich die Physik und Chemie unzugänglicher Regionen bis zum Erdmittelpunkt zu liefern. Seismische Wellengeschwindigkeiten hängen von den Elastizitätsmodulen und Dichten der Materialien ab, durch die sich die Wellen ausbreiten. Beide Eigenschaften hängen wiederum von der Kristallstruktur und der chemischen Zusammensetzung der Mineralien ab, sowie vom Druck, der Temperatur und den Konfigurationen der einzelnen Mineralkörner, wie Korngröße und bevorzugte Kristall-orientierung. Die Eigenschaften der Korngrenzen zwischen den Mineralien sind besonders interessant, wenn die physikalischen und chemischen Eigenschaften von Einkristallen zur Abschätzung der Eigenschaften von ganzen Gesteinskörpern verwendet werden. Eine auf theoretischen Berechnungen basierende Protonendynamik ist unerlässlich, um ein besseres Verständnis des Verhaltens von Wasser / Eis in Innenräumen von Planeten und potenziell H_2O-dominierten Exoplaneten zu erhalten, auf die nur mit einem Computer zugegriffen werden kann.

In den ersten fünf Beiträgen werden die seismischen Wellengeschwindigkeiten von gesinterten polykristallinen Stishoviten, Einkristallen aus Antigorit und Phase E, Al-tragendem Akimotoit und $(Mg,Fe)CO_3$-Carbonaten untersucht. Experimente, die die Wellengeschwindigkeit direkt bestimmen, wurden entweder mit Laserlicht (Brillouin-Streuung im Gigahertz-Bereich) oder Ultraschallwellen (oft im Megahertz-Bereich) mit gleichzeitiger Dichtemessung als Funktion des Drucks (und der Temperatur) durchgeführt. Die Kombination von Geschwindigkeiten mit genauen Dichtedaten aus der Röntgenbeugung liefert Elastizitätsmodule, die mit seismischen Messungen oder den Ergebnissen von Hochfrequenzexperimenten verglichen werden können. Bei nicht transparenten Proben wie Fe-reichen Carbonaten können Schallgeschwindigkeiten mit Hilfe der nuklearen inelastischen Streuung gemessen werden.

Die nächsten beiden Beiträge befassen sich mit der Kompressibilität von Fe-haltigem Bridgmanit, dem am häufigsten vorkommenden Mineral im unteren Erdmantel. Unter den möglichen Kationensubstitutionen wurde die Fe^{3+}-Al-gekoppelte Substitution in Bridgmanit hervorgehoben. Chemische Variationen des Valenzzustands von Eisen und seiner Ortsverteilung in der orthorhombischen Perowskitstruktur kontrollieren weitgehend den Kompressionsmodul, und die Ergebnisse umfassen eine Abschätzung des Kompressionsmoduls des reinen $FeAlO_3$ -Endglieds.

Silikatgläser dienen häufig als Modelle für Silikatschmelzen, die im Erdmantel vorhanden sein können. Die Dichte von eisenhaltigen Silikatgläsern wurde mit Röntgenabsorptionstechniken in einer Diamantstempelzelle (DAC) bis zu 150 GPa gemessen. Bei 110 GPa wird eine plötzliche Zunahme der Dichte sowie eine Zunahme der Opazität der Probe beobachtet. Dieses Verhalten hängt wahrscheinlich mit einer Änderung des elektronischen Zustands von Eisen zusammen. Metastabile Siliziumdioxid-Hochdruck-polymorphe können auch als strukturelle Proxys für Silikatschmelzen im tiefen Mantel dienen. Einkristall-Röntgenbeugungsmessungen der Coesit-Kompression stellen bessere Bedingungen für die lokalen Strukturen von Silikaten und Silikatschmelzen bei tiefen Mantelbedingungen bereit.

Korngrenzdiffusion und anisotrope thermische Ausdehnung/Bruchbildung von Olivin-Bikristallen spielen eine wichtige Rolle bei der Bestimmung der Eigenschaften von Olivin-dominierten Gesteinen. Erstere kann die Mobilität inkompatibler Elemente steuern, die viele Seltene-Erden-Geothermometer auf der Grundlage von Verteilungskoeffizienten indirekt beeinflussen können, und letztere beeinflusst die Bildung eines miteinander verbundenen Permeabilitätsnetzwerks, das für die Mobilität und den Aufstieg von Magma wichtig ist.

Der letzte Beitrag beleuchtet mithilfe von *ab initio* Berechnungen die Protonendynamik in der Hochdruckphase Eis-VII. Mit zunehmendem Druck wird die O-H-O-Bindung kontinuierlich symmetrisiert, was letztendlich zur Umwandlung in die Phase Eis-X führt.

3.5 Fluide, Schmelzen und ihre Wechselwirkung mit Mineralen

Magmatische Aktivität in Subduktionszonen ist der Hauptmechanismus für das Wachsen der Kontinente in der jüngeren geologischen Vergangenheit. Wasserreiche Fluide oder eventuell auch Silikatschmelzen aus der subduzierten Platte verursachen hierbei die Aufschmelzung im darüber liegenden Mantelkeil. Daten aus magnetotellurischen Untersuchungen sind generell konsistent mit diese Modell; sie zeigen Bereiche erhöhter Leitfähigkeit, die möglicherweise auf elektrisch leitfähige Fluide oder Schmelzen im Mantel oberhalb der subduzierten Platte zurückzuführen sind. Die quantitative Interpretation solcher Daten war bisher jedoch immer schwierig, da elektrische Leitfähigkeitsmessungen von Fluiden bisher begrenzt waren auf Drücke unterhalb von 1 GPa. Der erste Beitrag in diesem Teil des Jahresberichts enthält neue Leitfähigkeitsdaten für NaCl-H_2O-Fluide bis zu 5 GPa. Diese Messungen wurden ermöglicht

durch die Entwicklung einer neuen Leitfähigkeitszelle für Piston-Zylinder-Experimente. In diese Zelle ist das Fluid im Porenraum von Diamantpulver zwischen zwei Elektroden eingeschlossen. Die Daten zeigen, dass bei hohem Druck aufgrund einer erhöhten Dissoziation von NaCl in Ionen die Leitfähigkeit generell ansteigt. Bereits sehr geringe Anteile von salzhaltigem Fluid im Gestein könnten die erhöhte Leitfähigkeit in Subduktionszonen erklären. Für die Modellierung der Leitfähigkeit eines derartigen Fluid-haltigen Gesteins benötigt man allerdings auch Daten über die Verteilung und Vernetzung der fluiden Phase in der Matrix. In einem weiteren Projekt wurde daher die elektrische Leitfähigkeit von Forsterit-Aggregaten mit einem geringen Fluid-Anteil gemessen. Im Laufe der Zeit näherten sich die gemessenen Leitfähigkeiten einem konstanten Wert, was darauf hindeutet, dass Gleichgewicht im Gefüge und in der Fluid-Verteilung im Gestein erreicht wurde. Die Beziehung zwischen Gesamt-Leitfähigkeit und Fluidverteilung soll im Detail mit Hilfe von Mikro-Röntgen-Tomographie weiter untersucht werden.

Die folgenden Kapitel in diesem Abschnitt des Jahresberichtes beschäftigen sich mit dem Verhalten von Wasser und Kohlenstoff, den beiden wichtigsten flüchtigen Komponenten im Erdinnern. Die Löslichkeit von Wasser in der Ringwoodit-Phase der Übergangszone des Mantels steht spätestens seit der Entdeckung eines wasserhaltigen Ringwoodit-Kristalls in einem natürlichen Diamanten im Fokus des Interesses. Der Wassergehalt von etwa 1 Gew. % in dieser natürlichen Ringwoodit-Probe stand in einem gewissen Gegensatz zu experimentellen Daten, wonach die Löslichkeit von Wasser in diesem Mineral bei realistischen Mantel-Temperaturen weit unter 1 Gew. % absinkt. Neue experimentelle Daten zeigen, dass die Wasserlöslichkeit in Ringwoodit in der Tat mit steigender Temperatur absinkt, der Effekt ist jedoch bei weitem nicht so stark, wie bisher angenommen wurde. Die nächsten beiden Beiträge beschäftigen sich mit dem Verhalten von Kohlenstoff in der frühesten Geschichte der Erde, als unser Planet überwiegend aufgeschmolzen war und sich der metallische Kern vom Magmen-Ozean getrennt hat. Es wird meist angenommen, dass während dieses Prozesses der größte Teil des Kohlenstoffs in den Kern gewandert ist. Neue Daten über die Löslichkeit von Kohlenmonoxid (CO) in Silikatschmelzen zeigen jedoch, dass unter gewissen, extrem reduzierenden Bedingungen die Löslichkeit von Kohlenstoff in Silikatschmelzen sehr gering ist, wodurch auch die mögliche Anreicherung von Kohlenstoff im Kern begrenzt wird. Neue Daten über die Diffusion von Kohlenstoff in flüssigem Eisen zeigen, dass die Gleichgewichts-Einstellung zwischen der Metallphase und dem Magmen-Ozean in relativ kurzen Zeiträumen erfolgte.

Die letzten beiden Beiträge in diesem Abschnitt beschäftigen sich mit der Dynamik magmatischer Systeme, in der frühen Erdgeschichte und heute. Messungen der Selbst-Diffusion von Si, O, Mg und Ca bis 25 GPa wurden benutzt, um das Viskositäts-Profil in einem tiefen Magmen-Ozean zu bestimmen. Ein Viskositäts-Maximum in einer Tiefe von 250 km wurde beobachtet. Eine weitere Studie beschäftigte sich mit der Kinetik von Magma-Gesteins-Wechselwirkung in der heutigen Erdkruste, die offenbar kontrolliert wird durch eine Kombination aus Diffusion und Konvektion.

3.6 Rheologie

Die Rheologie beschreibt in den Geowissenschaften u.a. die Fließeigenschaften von Mineralien und Gesteinen unter Druck- und Temperaturbedingungen, die dem (tiefen) Erdinneren entsprechen. Weiträumige Deformationsprozesse wie die globale Mantelkonvektion werden auf der Grundlage dieses Wissens verstanden. Aus diesen Gründen untersucht das Bayerische Geoinstitut die Rheologie von Mantelgesteinen durch experimentelle, analytische und rechnerische Verfahren. Alle Beiträge des Jahres 2018 bemühten sich jedoch um die Entwicklung analytischer Methoden. Im ersten Beitrag wurden Korngrenzcharakteristika von torsionsverformtem Olivinaggregaten mittels Elektronenrückstreuung untersucht, um den Einfluss von Korngrenzen auf das Deformationsverhalten herauszuarbeiten. Die zweite Untersuchung von Bollinger et al. analysierte auch Korngrenzen eines Olivinaggregats, jedoch unter Verwendung von Transmissionselektronenmikroskopie in Kombination mit Orientierungskartierungstechniken. Die dritte Studie von Sawa et al. untersuchte die Verdichtung poröser Germanat-Olivin-Polykristalle mithilfe der Rasterelektronenmikroskopie. Die Weiterentwicklung dieser Studien wird nützliche Informationen zur Untersuchung der Dynamik des Erdinneren liefern.

3.7 Materialwissenschaften

Das Bayerische Geoinstitut weist eine einzigartige Kombination an wissenschaftlicher Expertise, Hochdrucktechnologie sowie Probenanalytik auf, die es erlaubt, anspruchsvolle und komplexe physikalische und chemische Fragestellungen in den Materialwissenschaften zu bearbeiten. In diesem Jahresbericht werden Ergebnisse von Studien über ein weites Spektrum von Materialien vorgestellt: Fe_4O_5 Eisenoxid, mehrere Nitride sowie Yttrium Aluminium Granat (YAG). Der *in situ* Nachweis einer chemischen Reaktion von Eisen und Stickstoff zu FeN_4 bei 180 GPa im Beitrag b. stellt einen wichtigen Meilenstein in der Hochdruck-Materialwissenschaft dar.

Fe_4O_5 wurde im Jahr 2011 zum ersten Mal unter Hochdruck synthetisiert, und Proben konnten zu Raumbedingungen gebracht und entnommen werden. Mit dem Auftreten von Fe^{2+} und Fe^{3+} ist Fe_4O_5 ein Material, das eine Reihe interessanter chemischer und physikalischer Phänomene aufweist. Es ist auch deshalb Gegenstand einer fortlaufenden Serie von Beiträgen in den Jahresberichten des Bayerischen Geoinstituts. In diesem Jahr wird eine Studie vorgestellt, bei der die strukturellen und magnetischen Eigenschaften von Fe_4O_5 Einkristallen bei niedrigen Temperaturen untersucht wurden. Es zeigte sich hierbei, dass bei Temperaturen unter 150 K eine Reihe von Ordnungsübergängen in der Ladung auftreten, die dimere und trimere Ordnungen innerhalb der Eisenketten in der Struktur aufweisen und die für komplizierte inkommensurable Störungen in der Kristallstruktur verantwortlich sind.

Kristalle, die mehrere Stickstoffatome aufweisen, wie das oben angesprochene FeN_4, sind Gegenstand der folgenden drei Beiträge. Stickstoff-basierte Verbindungen haben ein großes

Potential als mögliche Materialien zur Speicherung von Energie, da durch den Übergang zwischen Einfach- und Dreifachbindungen viel Energie gespeichert und freigesetzt werden kann. Generell schließen sich ein hoher Stickstoffanteil in einem Material und dessen Stabilität aus, da viel Energie benötigt wird, um Mehrfachbindungen zu stabilisieren; der Energieeintrag durch hohen Druck bietet hier gegenüber klassischen chemischen Methoden einen großen Vorteil. Indem N_2 in der Diamantstempelzelle direkt mit Eisen, Rhenium und Schwefel eingebracht wurde, haben Wissenschaftler am Bayerischen Geoinstitut mehrere neue Stickstoff-haltige Kristalle synthetisiert. Die sich ergebenden Kristalle von FeN_4, $ReN_8 \cdot xN_2$ und SN_2 wurden auf ihre Struktur hin untersucht. $ReN_8 \cdot xN_2$ ist hierbei von besonderem Interesse, da hier Stickstoff zusammen mit Rhenium nicht nur das poröse Netzwerk bildet, sondern als N_2-Molekül auch als Gastphase in den Poren auftritt.

Die Diffusion entlang von Korngrenzen in polykristallinen Materialien spielt eine große Rolle in den Ingenieurwissenschaften und in der Geologie, da sie zahlreiche Prozesse beeinflusst. Für Laserkristalle wie YAG bestimmt die Diffusion von Nebenbestandteilen die Effizienz und Lebensdauer des Lasers. Hier wird die Diffusion von Lanthan, Eisen, Magnesium und Titan entlang von geometrisch gut bestimmten Korngrenzen in YAG untersucht. Die Konzentration dieser Nebenbestandteile an Korngrenzen beeinflusst deren Auftreten in YAG und damit dessen Materialeigenschaften.

3.8 Methodologische Entwicklungen

Ein wichtiges Ziel des Bayerischen Geoinstituts sind methodische Entwicklungen, die die Forschung in den Erd-, Planeten- und Materialwissenschaften fördern und verbessern werden. Ein naheliegendes Ziel ist es, hier den Bereich der experimentell erreichbaren Druck- und Temperaturbedingungen zu erhöhen. Ebenso wichtig ist die Entwicklung experimenteller Techniken zur genauen Messung physikalischer Parameter in Hochdruckexperimenten und zur Charakterisierung der Struktur, Zusammensetzung und anderer Eigenschaften von Proben unter extremen Bedingungen. Weitere Bereiche umfassen die Entwicklung von Methoden zur Analyse der chemischen Zusammensetzung von sehr kleinen Proben und zur Quantifizierung der Mikrostrukturen von deformierten Mineralen und anderen Materialien. Schließlich sind methodische Entwicklungen, die die Ergebnisse numerischer Modelle verbessern, von erheblicher Bedeutung, zum Beispiel für das Verständnis der Konvektionsdynamik des Erdinneren und anderer Planeten. Die zehn Beiträge dieses Abschnitts behandeln viele dieser Aspekte.

Die ersten fünf Beiträge dieses Abschnitts befassen sich mit der weiteren Entwicklung der Diamantstempelzelle (DAC), die zum Erreichen von Drücken verwendet wird, die wesentlich höher sind als in der Multianvil-Presse. In Kombination mit der Aufheizung durch Laser ermöglicht die DAC das Erreichen von Druck-Temperatur-Bedingungen, die im Erdmittel-punkt herrschen. Sie ist daher für experimentelle Untersuchungen im tiefen Mantel und im

Kern der Erde unerlässlich. Der erste Beitrag beschreibt neue Entwicklungen, um die Struktur sehr kleiner Proben bei hohem Druck in einer Diamantstempelzelle mittels Kernspinresonanzspektroskopie (NMR) zu untersuchen. NMR ist eine wichtige Technik, die in den Erdwissenschaften routinemäßig verwendet wird, um die Struktur von Mineralien und Gläsern unter Raumbedingungen zu untersuchen. Normalerweise sind recht große Proben erforderlich. Aufgrund der hier beschriebenen Entwicklungen können nun sehr kleine Proben *in situ* bei extrem hohen Drücken untersucht werden. Ein weiteres Problem bei der geringen Größe von DAC-Proben (typischerweise nur 3-4 μm bei Drücken über 200 GPa) besteht darin, dass die Beheizung mit Lasern oft einen Bereich beeinflussen kann, der viel größer ist als die Probe. Der zweite Beitrag beschreibt die Entwicklungen, um einen stark fokussierten Laserstrahl mit einem Durchmesser von nur 5 μm zu erhalten. Dies führt zu einer deutlich verbesserten Genauigkeit bei der Messung der Probentemperatur. Der folgende Beitrag befasst sich mit der Untersuchung von Wassereis bei hohen Temperaturen in der Diamantstempelzelle, um die äußeren Schichten der Riesenplaneten Uranus und Saturn zu verstehen. Solche Experimente sind schwierig zu realisieren, da H_2O in DAC-Experimenten mit den metallischen Dichtungen reagiert und Wasserstoff freisetzt, der zum Versagen der Diamantstempel führen kann. Eine Lösung für dieses Problem besteht darin, die Probe schnell zu komprimieren und aufzuheizen, während gleichzeitig Röntgenbeugungsdaten erfasst werden. Ein weiteres Problem bei der DAC besteht darin, dass die Zelle in einigen Experimenten gedreht werden muss (z. B. bei Einkristall-Röntgenbeugung), was zu einer Fehlausrichtung der Probe in Bezug auf Röntgenstrahlen und Laserstrahlen führen kann. Dieses Problem wurde durch die Neugestaltung der Diamantstempel mit einem runden Tisch (DART-Stempel) gelöst.

Die Sauerstofffugazität (oder das chemische Potenzial von Sauerstoff) ist ein kritischer Parameter, der das Ergebnis vieler Experimente an eisenhaltigen Systemen bestimmt. Es ist daher unabdingbar, die Sauerstofffugazität in Experimenten bei hohen Drücken und Temperaturen bestimmen zu können. Nachfolgend werden zwei neue Methoden beschrieben, um dies zu tun. Das erste Verfahren verwendet eine metallische Fe-Ir-Legierung in einer DAC-Probe als Sensor für die Sauerstofffugazität. Im zweiten Fall wurde die Sauerstofffugazität als Funktion von Druck und Temperatur für den Ru-RuO_2-Puffer bestimmt.

Im folgenden Beitrag werden technische Entwicklungen beschrieben, die eine Analyse der Konzentrationen der Elemente Schwefel und Chlor in kleinen Schmelzeinschlüssen mittels Laser-Ablation-Massenspektrometrie mit induktiv gekoppeltem Plasma (LA-ICP-MS) ermöglichen. Andere Analyseverfahren erfordern typischerweise große homogene Proben, wenn diese Elemente analysiert werden und sind daher für Schmelzeinschlüsse ungeeignet. Der nächste Beitrag befasst sich mit der Erforschung der Rheologie gesteinsbildender Minerale. Die Verwendung einer Kombination mehrerer Techniken wird zur Herstellung von Proben deformierter Minerale zur Untersuchung im Transmissionselektronenmikroskop (TEM) beschrieben. Dieser Ansatz führt dazu, dass sehr spezifische Mikrostrukturen für TEM-Untersuchungen ausgewählt werden können.

Die letzten beiden Beiträge beschreiben einige Entwicklungen in der numerischen Modellierung. Die erste befasst sich mit der Bestimmung der Permeabilität von Gesteinen mit niedriger Porosität unter Verwendung eines numerischen Ansatzes (die Permeabilität ist sehr schwierig experimentell zu messen, wenn die Porositäten niedrig sind). Im zweiten (und letzten Beitrag dieses Abschnitts) werden die Auswirkungen der unterschiedlichen rechnerischen Gitterauflösung und -geometrie auf die Ergebnisse numerischer Modelle der Mantelkonvektion und der daran gekoppelten Plattentektonik untersucht.

3. Research Projects

3.1 Earth and Planetary Structure and Dynamics

The terrestrial planets formed within roughly 100 million years after the start of the solar system. Modern astrophysical theories indicate that planetesimals had sizes ranging from a few dozen to hundreds of kilometers. The decay of the short-lived radiogenic isotope ^{26}Al was the primary heat source for these planetesimals. In primordial bodies ^{26}Al was primarily stored within silicate minerals with low melting temperatures. Based on this it has been proposed that ^{26}Al was partitioned early on into silicate melt and ascended towards the surface; thus the removal of the heat source would impede the formation of a magma ocean. The first contribution uses a novel approach combining multi-component petrological reactions with a two-phase magma transport model to determine under which conditions ^{26}Al-rich melt was transported towards the surface and under which conditions magma oceans could develop.

Later on, after ^{26}Al went extinct and accreting protoplanets reached at least lunar mass, the release of kinetic energy due to collisions became an important heat source for the forming terrestrial planets. The simulation of each of these impact events taking place during terrestrial planet accretion is computationally expensive. For this purpose the second contribution develops a parameterization, so by knowing the impact parameters both the volume and the depth of the forming magma ocean can be determined. This parameterization can be used to predict the partitioning behaviour of elements between metal and silicates and also to study the early thermal evolution of forming terrestrial planets.

Both astrophysical observations and numerical models of star formation in young open star clusters show that ^{26}Al is inhomogeneously distributed throughout the galaxy. Thus in many cases the protoplanetary disks around young stars are devoid of ^{26}Al, while in some cases the initial concentration of ^{26}Al is up to ten times higher than that in the early solar system. The third study combines geodynamical models of volatile loss from planetesimals caused by ^{26}Al decay with planet formation models. Extensive calculations showed that the final mass of water on a newly formed terrestrial planet is dependent on the initial concentration of ^{26}Al. Using these results we can better understand why both Earth and the recently discovered TRAPPIST-1 exoplanets are rather dry.

NASA's Kepler mission showed that Super-Earths, terrestrial planets with several Earth masses, are the most common type of exoplanets. The pressure and temperature conditions in the deep interior of such Super-Earths are not yet accessible to laboratory experiments. Thus the fourth contribution uses numerical models to study iron under these conditions. Based on this it is possible to determine whether a liquid iron core is viable in the interior of these planets, which is of fundamental importance for the existence of a protective magnetic field.

After the end of accretion the terrestrial planets started to cool down and the magma ocean crystallized. This led to the formation of a solid mantle. The Earth's lower mantle is mostly

made of bridgmanite and smaller quantities of ferropericlase. At the moment it remains unclear whether bridgmanite or the less viscous ferropericlase controls lower mantle deformation. The next contribution presents numerical experiments simulating the deformation of a bridgmanite+ferropericlase mixture on a microscale in order to determine under which conditions an interconnected ferropericlase network can be established that will control lower mantle rheology. Based on these results it will be possible to derive a parameterization enabling a better description of the behaviour of bridgmanite+ferropericlase in global-scale mantle convection models.

Among other phenomena, earthquakes are witness to deformation processes in the Earth's active interior. Deep earthquakes with hypocenters at more than 300 km depth still raise questions since they cannot be explained by brittle failure processes. The numerical model described in the sixth contribution considers both shear heating and grain size evolution as a potential explanation for deep earthquakes. The results demonstrate that under certain conditions strongly localized shear bands can form periodically whose behaviour is comparable to those of so-called silent earthquakes.

Another process related to Earth's internal activity is volcanism. Rock permeability is important for melt ascent processes. Traditionally rock permeability is measured in laboratory experiments; however this is not viable in case the porosity is very low. The final contribution compares the results of laboratory experiments with those of numerical 3D simulations that employ computer topography data to calculate permeability. Both methods show good agreement for intermediate and high porosities and the results demonstrate that it is viable to use numerical methods to determine the permeability for very small porosities.

a. *Magma ascent in planetesimals: Control by grain size (G.J. Golabek, T. Lichtenberg/ Oxford, T. Keller/Stanford, R.F. Katz/Oxford and T.V. Gerya/Zurich)*

Rocky planetesimals in the early solar system melted internally and evolved chemically due to radiogenic heating from ^{26}Al. Here we quantify the parametric controls on magma genesis and transport using a coupled petrological and fluid mechanical model of reactive two-phase flow. We find the mean grain size of silicate minerals to be a key control on magma ascent. For grain sizes larger than ≈1 mm, melt segregation produces distinct radial structure and chemical stratification. This stratification is most pronounced for bodies formed at around 1 Myr after Ca,Al-rich inclusions (CAIs). These findings suggest a link between the time and orbital location of planetesimal formation and their subsequent structural and chemical evolution.

According to our models, the evolution of partially molten planetesimal interiors falls into two categories. In the magma ocean scenario, the whole interior of a planetesimal experiences nearly complete melting, resulting in turbulent convection and coremantle differentiation by the rainfall mechanism. In the magma sill scenario, segregating melts gradually deplete the deep interior of the radiogenic heat source. In this case, magma may form melt-rich sills beneath a cool and stable lid, while core formation would proceed by percolation.

Our findings (see Fig. 3.1-1) suggest that grain sizes prevalent during the internal-heating stage governed magma ascent in planetesimals. Regardless of whether evolution progresses toward a magma ocean or segregated magma sills, our models predict that temperature inversions due to rapid ^{26}Al redistribution are limited to bodies formed earlier than ≈1 Myr after CAIs. We find that if grain size was smaller than ≈1 mm during peak internal melting, only elevated solid-melt density contrasts (such as found for enstatite chondrite compositions) would allow substantial melt segregation to occur.

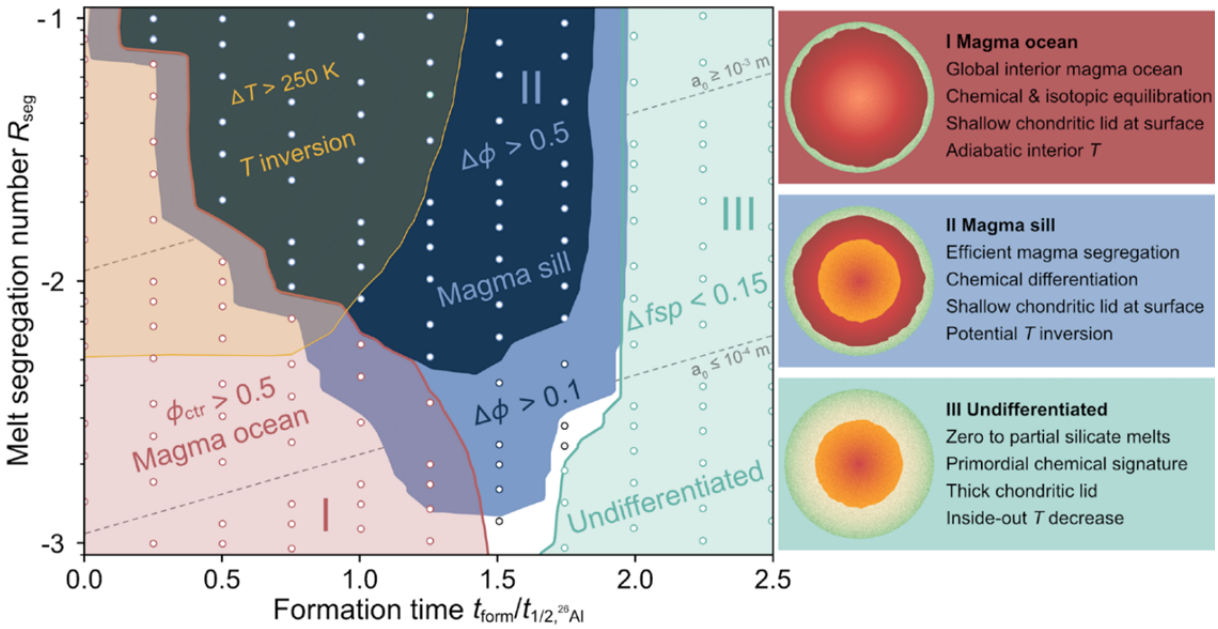

Fig. 3.1-1: Melt segregation regimes and potential temperature inversions during planetesimal evolution.

b. *The formation and evolution of magma oceans during the accretion of terrestrial planets (M. Nakajima/Rochester, D.J. Bower/Bern, D.C. Rubie and G.J. Golabek)*

The terrestrial planets of our solar system (Earth, Mars, Venus and Mercury) accreted during the first 10-100 million years of solar system history through collisions with other smaller planetary bodies. The energy of such collisions was often extremely high especially because of high impact velocities that were on the order of 10-20 km/second. In the case of Earth, the final giant impact is believed to have been a collision with a planetary embryo, with a mass approximately that of Mars, that resulted in the formation of Earth's Moon.

A major consequence of collisions between planetary bodies is a drastic increase in temperature due to the conversion of kinetic energy and potential energy to heat. This results in extensive melting and the formation of deep magma oceans. In extreme cases, the entire mantle of a target body could melt and form a magma ocean 2000-3000 km deep. Such melting greatly facilitates the formation of the metallic core of a planet because liquid iron-

rich metal can separate very efficiently from liquid silicate and sink to the growing core because of the metal's relatively high density. Chemical equilibration between segregating metal and silicate ultimately determines the chemical compositions of the mantle and core. For example, siderophile (metal-loving) elements, such as Ni, Co, W and Mo, partition strongly into liquid metal and are therefore depleted from the mantle during core formation. The extent of such depletion depends on the pressure-temperature conditions under which metal and silicate equilibrate which, in turn, depend on the depth of the magma ocean. In order to quantify this effect in models of planetary accretion and core-mantle differentiation, we are determining the extent and depth of melting caused by giant impacts as a function of impact parameters (*e.g.*, mass of the impactor, impact velocity, impact angle etc.). In addition, we are determining the rate at which magma oceans cool, crystallize and therefore decrease in depth in order to be able to model the entire melting history of a planet during its accretion.

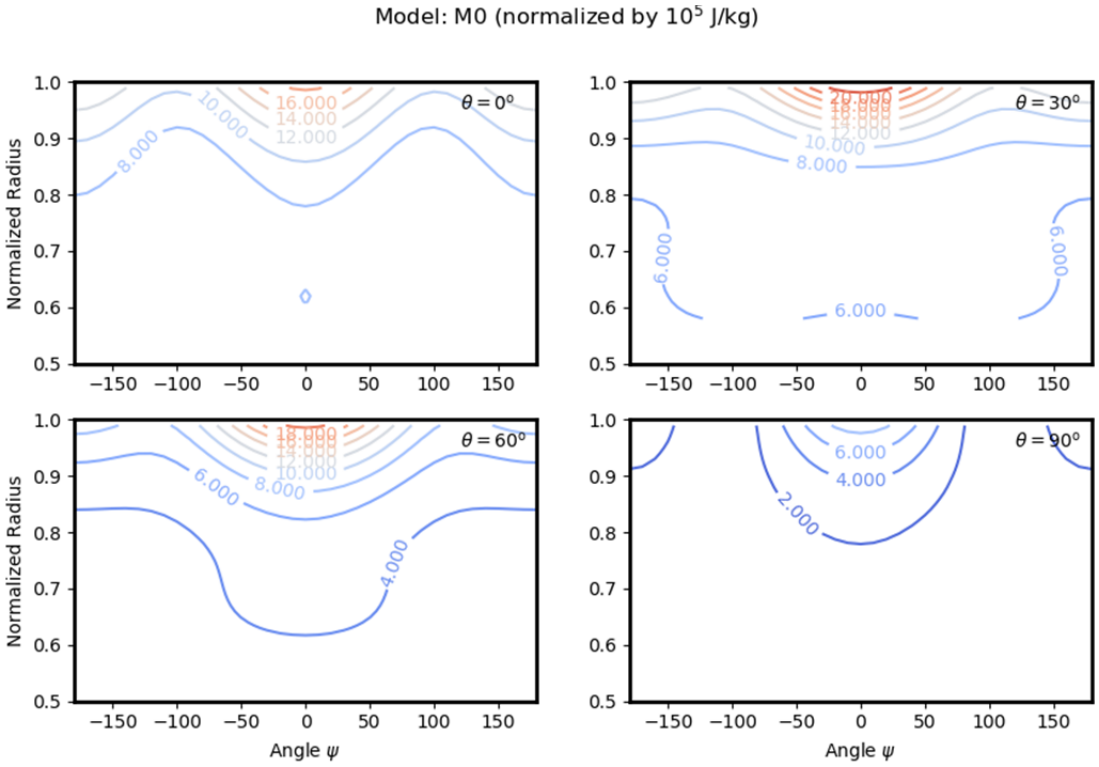

Fig 3.1-2: Internal energy contours of the mantle normalized by 10^5 J/kg. Θ is the impact angle where 0° is a head-on impact and 90° is a grazing impact; ψ is the angle from the most intensely heated region of the mantle. The y-axis indicates the radial distance from the center of the planet normalized by the planet's radius. Regions with normalized internal energy values greater than 5.0 are molten in this example.

We are developing scaling laws that describe the volume of melt in a planetary mantle that is created by an accretional collision. The scaling laws are based on more than 100 impact simulations using a smoothed-particle hydrodynamics (SPH) code. We have determined (1) the impact-induced melt volume of the mantle as a function of the impact angle, impact

velocity, and the impactor-to-total mass ratio, and (2) how the heat is distributed within the mantle following the impact (Fig. 3.1-2). By combining these results, we can determine the lateral extent of the magma ocean as well as its depth. The resulting parameterization of the results will make it possible to model the pressure-temperature conditions of metal-silicate equilibration for every accretional impact in an N-body accretion simulation and thus to model the early chemical evolution of the mantle and core more realistically than has been done previously.

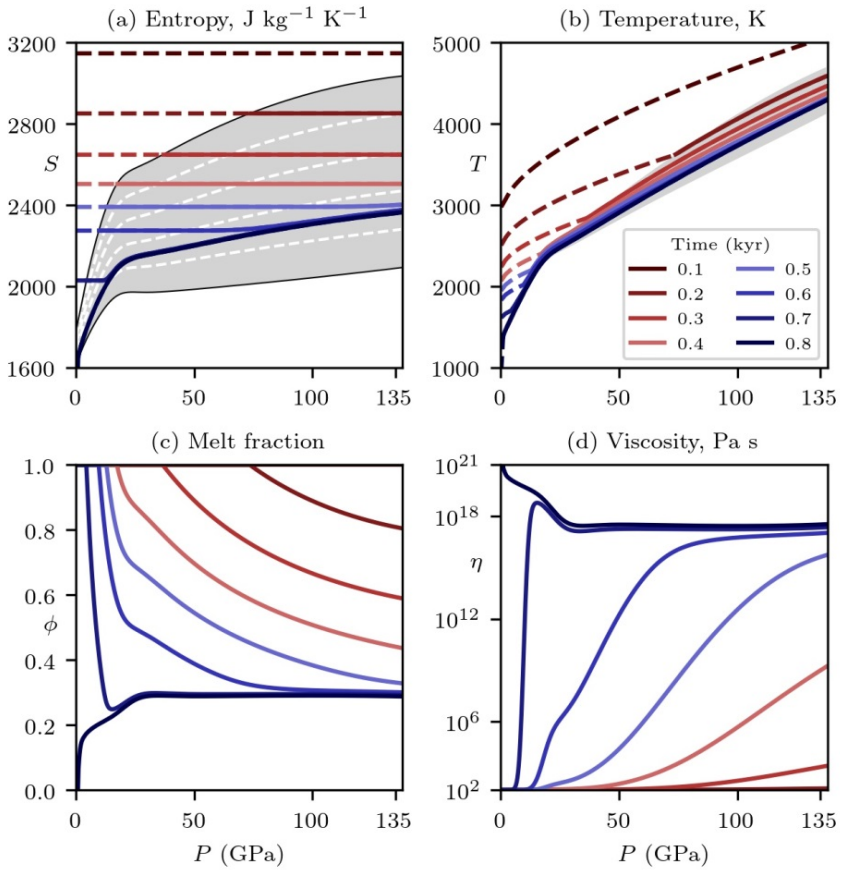

Fig. 3.1-3: Evolution of a magma ocean as a function of pressure (depth) over the time period 0.1-0.8 kyr. The surface and core-mantle boundary are at 0 and 135 GPa, respectively, and the mantle is initially completely molten at 0 kyr (not shown). (a) Entropy. The mixed phase region (melt + crystals) is coloured grey and is bounded by the liquidus above and solidus below. Melt fraction contours are plotted every 0.2 units and are denoted by white dashed lines. Lines are solid for the mixed phase and dashed for the pure liquid. (b) Temperature, (c) Melt fraction, and (d) Viscosity.

As a magma ocean cools, its depth decreases with time. This means that the metal delivered by the accretion of small differentiated bodies (planetesimals) during the cooling period and before the next giant impact will equilibrate with silicate liquid at progressively decreasing pressures and temperatures. In order to take account of this effect, we are developing parameterizations of magma ocean evolution during cooling and crystallization. We track the evolution of a magma ocean using the published interior evolution model ``SPIDER''. This

model solves the energy balance in a partially molten mantle by considering heat transport by convection, conduction, and separation and mixing of melt and solid phases (Fig. 3.1-3). From this model, we extract the maximum temperature-pressure conditions in a magma ocean as a function of time (Fig. 3.1-4), values of which can then be used in geochemical partitioning models. We are modelling a suite of magma ocean crystallization scenarios for different planetary and core-mantle radii and surface heat fluxes. The results can then be

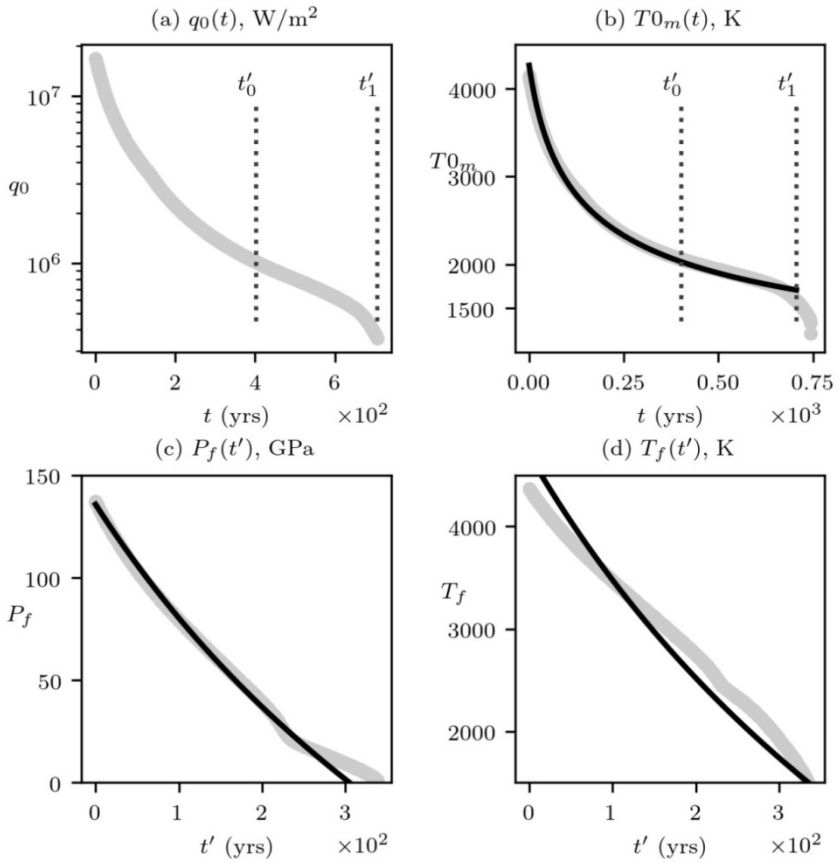

Fig. 3.1-4: Evolution of magma ocean properties with time based on a black body cooling model (*i.e.*, in the absence of an insulating atmosphere). (a) Surface heat flux. (b) Surface temperature. (c) Maximum pressure (*i.e.*, at the base of the magma ocean). (d) Maximum temperature (*i.e.*, at the base of the magma ocean. Time t is defined from the start of the model when the entire mantle is completely molten. The time at which the magma ocean at the core-mantle boundary has crystallized to a melt fraction of about 40 % is denoted by t'_0. The time offset between t'_0 and t'_1 is shown in (a) and (b) where $t = t'_1$ is the time at which the magma ocean depth is zero – which is taken to be the case when the melt fraction close to the surface has decreased to below about 40 %. Numerical output from SPIDER is plotted as light grey lines and the analytical fits are shown as black lines.

consolidated into a parameter space that spans the entire growth phase of the proto-Earth. For all cases, we consider bottom-up crystallization in which the liquidus and solidus temperatures increase monotonically with pressure. An analytic model is devised to provide

fits to the numerical results, and thus provide a convenient parameterization for use in coupled accretion and geochemical partitioning models.

c. *Gradual desiccation of rocky protoplanets from ^{26}Al-heating (G.J. Golabek, T. Lichtenberg/Oxford, R. Burn/Bern, M.R. Meyer/Ann Arbor, Y. Alibert/Bern, T.V. Gerya/ Zurich and C.A. Mordasini/Bern)*

The formation and distribution of Earth-like planets remains poorly constrained. However, stochasticity during accretion and the variety of exoplanet compositions favor rocky worlds covered in thick volatile ice layers as the dominant family of terrestrial analogues, deviating from the water-poor inner-Solar system planets. Here, we demonstrate the power of ^{26}Al, a short-lived radioisotope abundant in the early Solar system, to control the water content of terrestrial exoplanets.

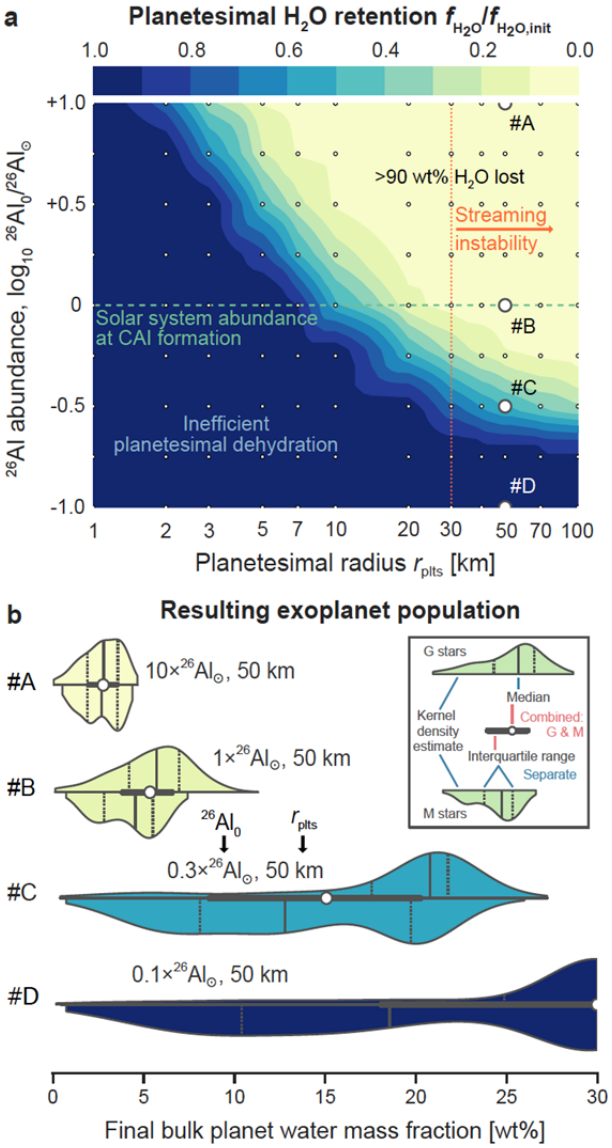

Using numerical models of planet formation, evolution, and interior structure, we generate synthetic planet populations that are subject to a varying degree of ^{26}Al-heating during accretion. We show that planet bulk water fraction and radius are anti-correlated with the host system's ^{26}Al levels (see Fig. 3.1-5). This yields a system-wide correlation of bulk abundances, and is consistent with the location-independent scarcity of water within the TRAPPIST-1 planets. The generic sensitivity of exoplanet observables on primordial ^{26}Al inferred from our models suggests two distinct classes of rocky exoplanets: high-^{26}Al systems form small, water-depleted planets, those devoid of ^{26}Al form ocean worlds, with the mean planet radii deviating by up to ≈ 10 %.

Fig. 3.1-5: (a) Water retention in planetesimals subject to a varying degree of ^{26}Al heating. (b) Bulk planet water abundances f_{H2O} in exoplanet populations with M_{planet} = 0.1–10 M_{Earth} and $f_{H2O} > 0$, formed with fixed $^{26}Al_0$ and planetesimal radius r_{plts}.

d. *Liquid iron equation of state to the terapascal regime from ab initio simulations (F. Wagle and G. Steinle-Neumann)*

The observation of a significant number of exoplanets with multiple Earth masses and an average density similar to that of the terrestrial planets in our solar system (super-Earths) has raised questions about their habitability and internal structure which are closely interlinked. An important factor for creating and maintaining an atmosphere – conducive for habitability – is an internally generated dynamo. This requires a liquid portion of a metallic, most likely iron-based core, of which thermodynamic properties at extreme *P-T* conditions are of interest.

We present a thermodynamic model for liquid iron, based on *ab-initio* molecular dynamics simulations which is applicable to 2 TPa and beyond 10,000 K, conditions that are relevant in the cores of super-Earths. By combining *ab-initio* results for *V-T-P* with a thermodynamically self-consistent correction scheme for the Helmholtz potential, we anchor our equation of state at well-constrained experimental values for density, bulk modulus and melting temperature at ambient pressure, where *ab-initio* results show poor agreement (Fig. 3.1-6).

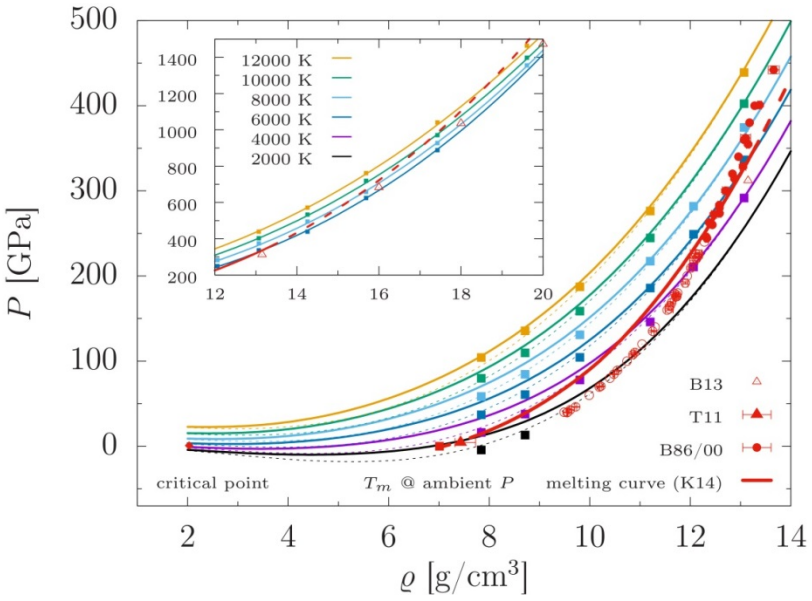

Fig 3.1-6: Pressure as a function of density for liquid iron along different isotherms for 2-14 g/cm³ in the main panel and 12-20 g/cm³ in the inset. Squares represent our *ab-initio* molecular dynamics results, the dashed lines an uncorrected equation of state fit, and solid lines the corresponding isotherms after correction. Experimental data are shown in red, for the critical point and the melting temperature at ambient pressure. High-pressure data are from one large volume press experiment by Tateyama *et al.* (2011; Phys. Chem. Miner. 38: 801) (T11) and along the Hugoniot from dynamic compression experiments of Brown & McQueen (1986; JGR 91: 7485) and Brown *et al.* (2000; J. Appl. Phys. 88: 7485) (B86/00), where filled symbols indicate the shock Hugoniot in the liquid stability field. The melting curve from the thermodynamic model (solid red curve, extrapolated for guidance) by Komabayashi (2014; JGR 119: 4164) and *ab-initio* computations by Bouchet *et al.* (2013; Phys. Rev. B 87: 094,102) (B13) have been included for comparison.

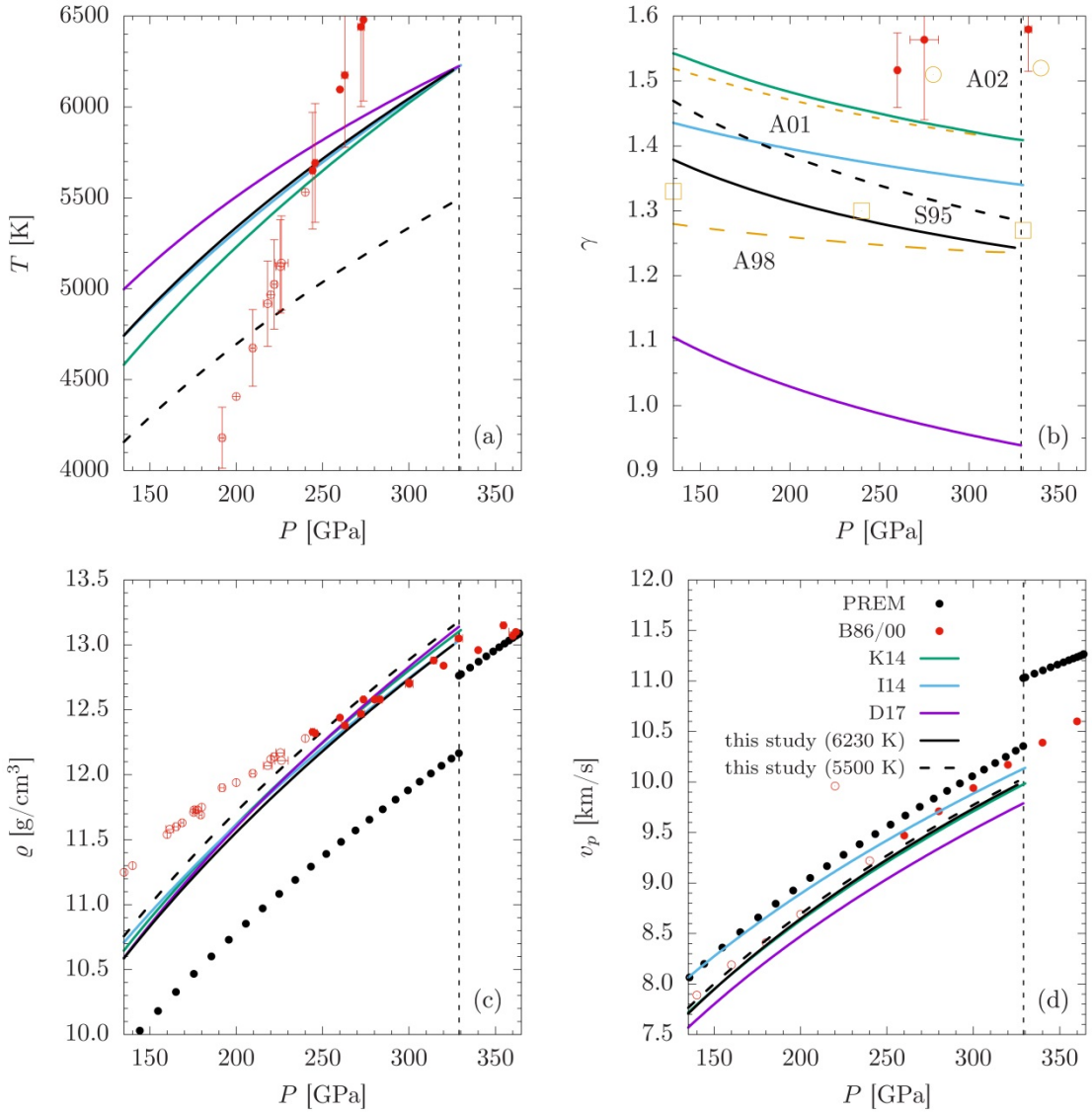

Fig 3.1-7: (a) Temperature, (b) Grüneisen parameter γ, (c) density and (d) acoustic wave velocity v_P as functions of pressure in the Earth's outer core for our thermodynamic model of liquid Fe (black lines) and other models reported in the literature (solid lines): Komabayashi (2014; JGR 119: 4164), Ichikawa *et al.* (2014; JGR 119: 240) and Dorogokupets *et al.* (2017; Sci. Rep. 7: 41,863), labeled K14, I14 and D17, respectively. The isentropes are fixed at the melting point of iron (T_m=6,230 K) at the Earth's inner core boundary (P=330 GPa, vertical dashed line) from the model of Komabayashi (2014; JGR 119: 4164) and properties in panels (b)-(d) are evaluated along the respective temperature profile. For our model we include profiles that account for a melting point depression of ~ 700 K, starting at 5,500 K at the inner core boundary (dashed line). Black dots show the seismic reference model PREM by Dziewonski & Anderson (1981; PEPI 25: 297). Values for γ from *ab-initio* computations by Alfè *et al.* (2001; Phys. Rev. B 64: 045,123) and Alfè *et al.* (2002; EPSL 195: 91) (A01/A02) and thermodynamic considerations by Stacey (1995; PEPI 89: 219) and Anderson (1998; PEPI 198: 179) (S95/A98) are included for comparison. Red circles show data from dynamic compression experiments of Brown & McQueen (1986; JGR 91: 7485) and Brown *et al.* (2000; J. Appl. Phys. 88: 7485) (B86/00), where filled symbols indicate the liquid stability field along the shock Hugoniot.

We explore the performance of properties based on our corrected Helmholtz energy and various previously published thermodynamic models for liquid iron over a wide range of conditions, including both low and high-pressure conditions. The correction term significantly improves the agreement of computed properties with experiments for density and acoustic velocity, as well as thermodynamic models that are based on an assessment of the phase diagram at ambient and moderate pressure. This shows how *ab-initio* molecular dynamics simulations can be used at par with other thermodynamic techniques, making our model suitable as a baseline at conditions of the interior in small planetary bodies. For conditions of the Earth's core, densities from the various models are similar and consistent with shock compression data, but higher-order derivatives (acoustic velocities and Grüneisen parameter) show significant differences (Fig. 3.1-7).

Evaluated along a core-temperature profile in Kepler-36b, differences in density from various models are negligible, for core mass they do not exceed 2 %, showing robust extrapolation of all equation of state models. The robustness of the different formulations of iron equations of state at conditions of the cores of super-Earths is encouraging in the sense that it will allow for a meaningful inversion of first order planetary structure (*e.g.*, core radius ratio) once relevant astronomical observations become available.

e. *From topology to rheology: Layer formation in bridgmanite-ferropericlase mixtures (M. Thielmann, G.J. Golabek and H. Marquardt/Oxford)*

The rheology of the lower mantle is dominated by its main constituents bridgmanite and ferropericlase, their relative importance is however still unclear. Ferropericlase is thought to have a particularly large impact on lower mantle rheology in case it forms networks of interconnected weak layers due to deformation. The exact nature of this interconnection process is still not fully understood, yet it is needed in order to be able to conduct quantitative mantle convection simulations.

When deformed, two-phase aggregates exhibit heterogeneous deformation patterns, which depend on the rheological contrast between the different phases and their distribution within the rock. The effective properties of such heterogeneous mixtures have received a significant amount of attention in the past, but the considered mixtures typically consisted of a matrix with inclusions with distinct shapes such as circles or ellipses.

Here we use a numerical-statistical approach to gain insight into the relationship between phase distribution topology and effective rheology. To this end, we prescribe the distribution of weak phases using random fields and deform the resulting structures in numerical simple shear experiments (see Fig. 3.1-8). The usage of random fields allows us to prescribe a more realistic topology of the weak phase and to investigate its effect on bulk properties as well as stresses, strain rates and pressures.

Simulations results show that the effective rheology of a two-phase aggregate can be described using a combination of the two-point cluster function of the aggregate and an analytical solution which i) links the two-phase cluster function to the effective rheology and ii) describes the evolution of this function through time. This provides us with the means to implement the deformation of two-phase media into large-scale mantle convection codes.

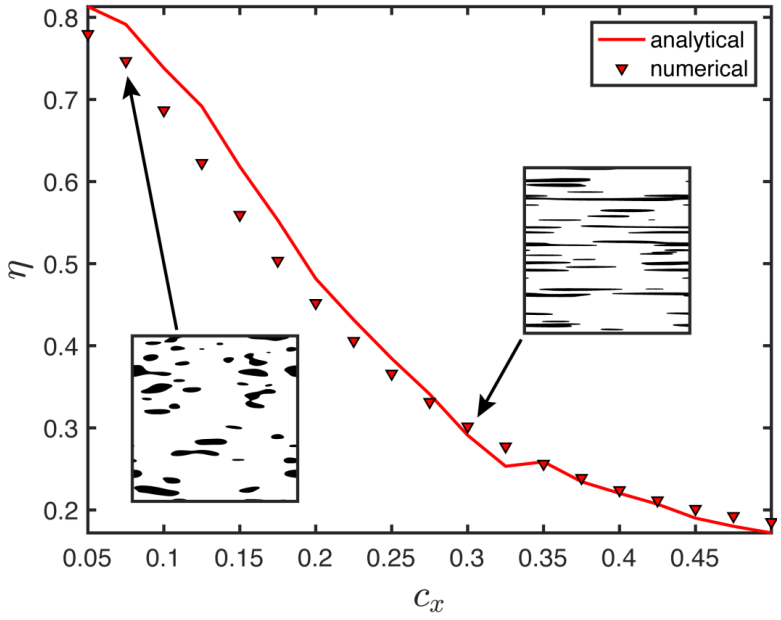

Fig. 3.1-8: Effective normalized viscosity of a random binary medium as a function of correlation length. The binary medium consists of a strong matrix and 10 % weak inclusions with a 100 times lower viscosity. Numerical results (denoted as symbols) represent the average of 5000 simulations. Insets show example binary distributions.

f. *Deep superslow earthquakes and ductile shear zone formation (M. Thielmann; in collaboration with T. Duretz/Rennes)*

The nucleation and rupture mechanisms of deep earthquakes are still incompletely understood. One of the mechanisms that has been proposed to generate deep earthquakes is shear heating. However, the stresses required for this mechanism to work are quite large. Previous work has shown that grain size reduction prior to thermal runaway may facilitate this process. In this project, we investigate the feedback loop between grain size reduction and shear heating using fully coupled thermomechanical numerical models.

The governing equations of viscoelastic deformation, shear heating and grain size reduction are solved using a fully staggered discretization and an adaptive implicit time stepping scheme. Nonlinearities are treated using Picard iterations with their convergence being determined through the nonlinear residuals of velocity, pressure, grain size and temperature.

Results from 2D simple shear simulations confirm previous results from 1D models and show that grain size reduction precedes thermal runaway and also facilitates its occurrence (see Fig. 3.1-9). Under certain conditions, we observe the propagation of a progressively localizing shear band, where velocities at the shear band tip resemble a classical double couple geometry. Due to the strong localization, stresses are strongly focused at the rupture tip, exceeding values of 1 GPa. We also observe that ductile shear band formation and propagation exhibits a periodic behaviour, with distinct rupture events. Peak velocities in these events become progressively larger, while event durations decrease. During those events, maximum rupture velocities reach values of about 4 m/yr, with event durations of about 5 years. The observed events are thus reminiscent of silent earthquakes, albeit exhibiting slower rupture velocities and larger event durations, which is why we term them superslow earthquakes. These superslow earthquakes may be precursors of more rapid events such as megathrust earthquakes as they weaken the ductile part of the slab, which may result in increased stresses at shallower levels.

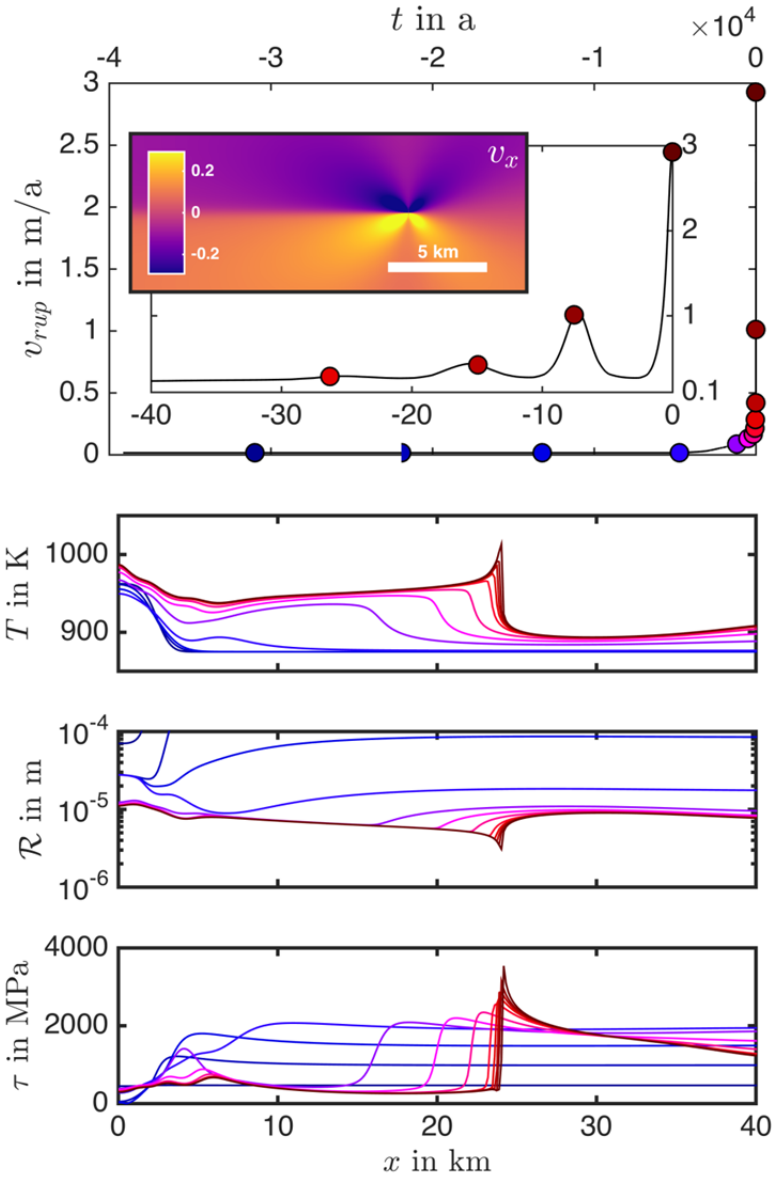

Fig. 3.1-9: Example of shear zone propagation in a multiphysics simulation conducted with a modified version of M2Di. Top: Temporal evolution of the rupture velocity, with insets showing a zoom on the last 40 years and the horizontal velocity field. The colored circles denote the times at which a horizontal profile through the shear zone is extracted (shown in the bottom three plots). Bottom: Profiles of temperature, grain size and stress through the shear zone at selected times.

g. *A numerical and experimental study on permeability of porous media (P. Eichheimer; W. Fujita, S. Okumura, M. Nakamura and T. Nakatani/Sendai; M. Thielmann and G.J. Golabek)*

Micro permeabilites on pore scales and their related geometric parameters play an important role in several geological fields like hydrogeology and volcanology. The measurement of permeabilities in porous media still remains challenging. Experimental measurements often lack precision at low porosities as the permeability is below the detection limit. Numerical modelling can help to accurately compute permeabilities from a calculated velocity field of the given porous media. In this study we measure permeabilities of simple porous media consisting of glass bead assemblies, which are sintered using a piston cylinder at 710 °C and atmospheric pressure. The glass beads have an average diameter of 1 mm and different porosities are synthesized by changing the run time inside the piston cylinder (*e.g.*, longer time results in smaller porosities).

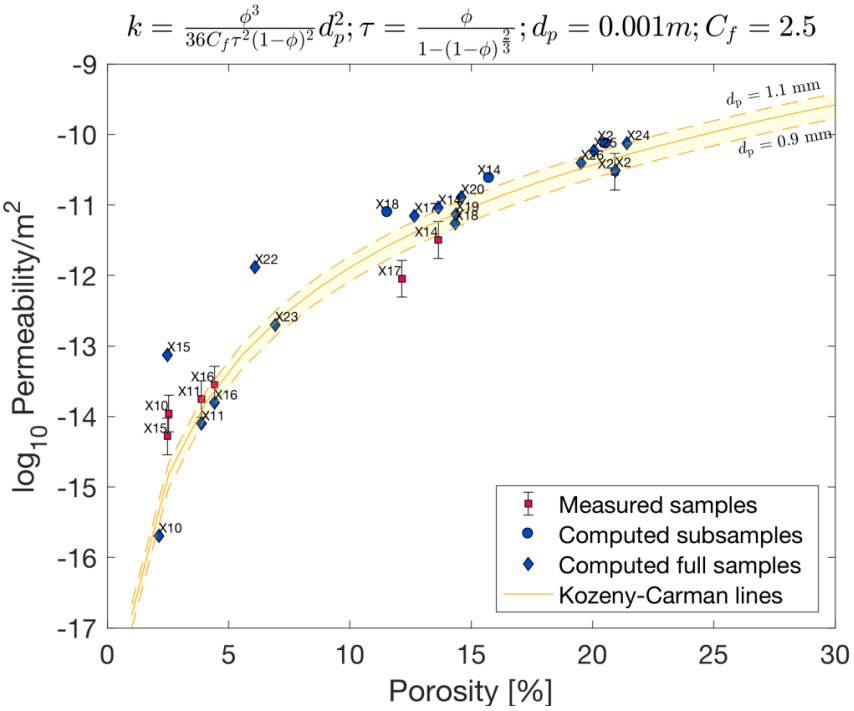

Fig. 3.1-10: Summary of the computed and measured permeabilities obtained from the synthetic porous media. The shown curve represents a Kozeny-Carman relation for grain diameters of 0.9-1.1 mm.

The permeability of the samples is measured experimentally with the usage of a flow meter, whereas the numerical permeability is computed using computer tomographic images (micro-CT) with the 3D finite difference code LaMEM. The permeabilities measured in the laboratory show a good agreement with the Cozeny- Karman relation. Furthermore the numerical results are in good agreement over a wide range of porosities (see Fig. 3.1-10). The obtained porosity/permeability relation can be used as a benchmark and shows that numerical

models are able to reproduce experimental measured permeabilities accurately. Furthermore a huge advantage of using numerical modelling is that the computed velocity field can be used to analyze several geometric relevant parameters, which influence permeability like critical porosity, tortuosity and specific surface area.

3.2 Geochemistry

Processes important to the formation of the Earth, the operation of plate tectonics and the geochemical evolution of the crust and mantle have left imprints on rocks, magmas and fluids that contain information on how these mechanisms operated. Experimental geochemistry and petrology is tasked with interpreting these imprints usually by reproducing the conditions of their origin or simulating the fractionation events that created them. The problem is that as we go deeper into the interior or further back in time, the evidence for the critical processes and the prevailing conditions becomes increasingly scarce. It is therefore essential that experimental scientists stay informed about new discoveries that push the frontiers in natural observations in both depth and time. Similarly the results of experiments can provide guidance as to what features may be important in newly discovered samples.

In this section, in addition to a number of reports that provide experimental data to interpret geochemical and petrological observations, several studies also examine natural samples to obtain new insights into their formation that can be used to place tighter constraints on Earth processes. The first report in this section is a study on how carbon partitioned between core-forming metal and the silicate mantle as the Earth formed and fractionated. The important issue here is to explain why so much carbon was left in the Earth's mantle, because existing studies show that carbon should have partitioned strongly into the metal that would have formed the core. The experiments, which have been performed at the extreme pressures of the Earth's lower mantle, offer an intriguing answer here because they show a dramatic decrease in the preference of carbon for iron metal at these conditions. Carbon that partitioned into descending metal at low pressure would, therefore, have partitioned back into the mantle at depth. This is followed by a study to examine the partitioning of stable isotopes of vanadium between core forming metal and silicate melt. The Earth's mantle appears to be more enriched in heavier isotopes of vanadium compared to its meteoritic building blocks, which might be an indication that light vanadium isotopes partitioned preferentially into the core. Although some preliminary results suggest this is unlikely and that the Earth simply incorporated a different vanadium isotopic signature compared to meteorites, further experiments at higher pressures are underway to clarify this.

The next three reports examine different aspects of the geochemistry of sulphide liquids. Towards the end of core formation sulphide melts may have been the main agents of core formation as the oxygen fugacity of the mantle started to rise. The first study examines the partitioning of hydrogen between sulphide melt and H_2O-bearing silicate melt to investigate whether hydrogen could have been lost from the mantle in this way, and thus drive the mantle to be richer in oxygen. The results, although not unequivocal, seem to indicate that sulphide partitions hydrogen in the form of H_2O rather than H itself and its loss would, therefore, not affect the redox state of the mantle. The next two studies examine sulphide liquids in relation to the fact that they form the dominant type of inclusion found in diamonds, which is also a theme in the four subsequent reports. In the past diamond formation was considered to occur during metasomatism of the subcratonic lithosphere, a process which is somewhat of a

geochemical cul-de-sac. It is now recognized, however, that some diamonds, including some of the most highly valued, actually form in the deeper convecting mantle. Such diamonds and their inclusions provide the only samples we have from the deep mantle and their formation processes become, therefore, much more important as they characterize events that take place during the deep mantle carbon cycle. Diamonds are also of course time capsules that preserve melts and crystals from the time of diamond formation, unlike the mantle rocks in which they are found that continuously equilibrate with incoming melts and fluids. The first of these studies presents a preliminary analysis of whether the oxygen content of quenched sulphide melts can be used to determine temperatures of formation. The results are promising, particularly as there is currently no other method for determining temperatures of deep diamond formation. The following study shows that sulphide liquids act as a catalyst for diamond nucleation and growth, an observation that may help to explain the prevalence of sulphide inclusions in diamonds and provides a mechanism for diamond synthesis within natural mantle assemblages.

The next report by Ottersberg *et al.* also examines a potential diamond formation mechanism which is implied by the fact that many deep diamond inclusions seem to have formed from a reaction between partial melts from basaltic rocks and surrounding peridotite rocks. Experiments to simulate this situation show that diamonds do tend to form within such a melt reaction zone, most likely as reduced CH_4-rich fluids come into contact with minerals enriched, through melt reaction, in ferric iron. The following study uses a fairly new type of Mössbauer spectroscopy based at a synchrotron facility that can measure the ferric/ferrous iron ratio of relatively small samples. The technique is employed to measure such ratios in very chrome-rich spinel minerals that are found in both mantle rocks (xenoliths) and as diamond inclusions in samples from the edge of the Zimbabwe craton. Although both types of samples must have become Cr-rich as a result of the extraction of large degrees of partial melt that should have left the samples also depleted in ferric iron, the diamond inclusions reveal remarkably high ferric iron concentrations, which probably indicates that the diamonds formed from relatively oxidised mantle fluids. In the next study the history of a diamond-bearing mantle eclogite rock is teased apart by examining reactions that constrain the depth and oxidation state at which certain features formed. Eclogites are metamorphic rocks which likely form from oceanic basalt that has been subducted into the mantle. Diamonds are found to have formed in this rock from carbonate during the subduction process, but before the rock was brought to the surface by erupting kimberlite magma it seems to have been brought to successfully shallower levels in the mantle, possibly by precursor magmatic pulses. The final study that relates to diamonds is aimed at understanding the relatively high oxidation state of iron found in majoritic garnet inclusions recovered from deep mantle diamonds. By experimentally studying how the ferric/ferrous iron ratios of such inclusions vary with pressure, it should be possible to understand the oxidation state of deep mantle diamond-forming fluids. In contrast to previous studies, however, the current results indicate that pressure alone does not have a significant effect on stabilising ferric iron in this mineral, implying that other mechanisms for the observed ferric iron enrichments in the inclusions need to be sought.

The next four studies examine mantle melting processes in the Earth at successively higher pressures. The first deals with a newly discovered type of mantle melting setting called petit-spot volcanism. Petit spot volcanos are small as the name suggests, and occur on the ocean floor far from mid ocean ridges, in many cases close to the point where oceanic slabs start to bend as they enter subduction zones. The most plausible theory is that tensile forces created as the lithosphere bends allow H_2O and CO_2-bearing mantle melts from the underlying asthenosphere to reach the surface. In this study a model that accounts for the effects of olivine crystal fractionation and volatile degassing is used to determine the primitive composition of the mantle melt. Experiments are then performed on this melt composition to determine the conditions at which melting took place to produce the primitive magma that occurred. Preliminary results indicate that the source rock for one of these magmas contained the hydrous mineral phlogopite, which probably indicates that the source rock had already been hydrated by previous interaction with hydrous melt, in a process known as metasomatism. The next melting study aims at determining the composition of a very small degree of hydrous melts that might be present in or at the top of the Earth's transition zone. Slow seismic wave velocities have been observed in the mantle at depths where only the presence of H_2O or CO_2 could lead to melting. If melts are indeed responsible for low seismic velocities observed at depths of ~400 km, then high melt compressibility might lead to them having the same density as the surrounding rocks. This would explain why such melts might persist at this depth and not rise out of the mantle. Experiments are used to determine the composition of such melts stabilised by the presence of H_2O and the next step will be to examine whether such melts could indeed be neutrally buoyant in the mantle. On the other hand the melt compositions seem to be very similar to kimberlitic magmas found at the surface, which if formed at these depths, cannot of course be neutrally buoyant. The following two studies examine melting at lower mantle conditions. The first examines melting in the presence of H_2O but employs two mantle starting compositions with iron either all in the ferric or all in the ferrous state. The aim is to also understand the origin of low seismic velocity regions that have been observed at the top of the lower mantle. Intriguingly, the results indicate that only the more reduced ferrous iron composition leads to extensive melting, although the cause of this effect is not yet understood. The final study on mantle melting is aimed at understanding the partitioning of iron during the crystallisation of a deep magma ocean. The iron content of the melt is one of the main factors influencing whether a melt could be denser than the surrounding mantle, which could have led to a dense melt layer being preserved at the base of the mantle. Although multianvil experiments cannot reach the conditions at the base of the mantle, diamond anvil cell studies that do reach these conditions are in poor agreement. By developing thermodynamic models for melting based on more constrained lower pressure experiments, melting relations can be more reliably extrapolated to interpret the results of higher pressure experiments.

The following four studies address a number of aspects concerning the role of volatile components in subduction zones. The first of these examines how the ferric iron content of serpentine depends on oxygen fugacity. The formation of serpentine not only hydrates the

oceanic lithosphere but also oxidises it. Natural serpentines can have almost all of their iron in the ferric state but to date no experiments have examined the effect of ferric iron on serpentine stability. In this study this effect is shown to be quite minimal. On the other hand the results show that due to changes in the stability of the ferric iron component with temperature, the dehydration of serpentine should lead to a quite sharp increase in the oxygen fugacity of the subducting slab. This could, for example, have important effects on the behaviour of sulphur in subduction zones, which would be mobilised by oxidation to sulphate.

In the following two studies the nature of the agent that produces the enriched trace element signature in the source of arc magmas is examined. In the past it was considered that fluids produced by dehydration of subducting slabs provide this enriched signature but more recent studies have questioned whether fluid trace element concentrations are high enough to achieve this or whether partial melts of subducting sediments are a more likely agent. The experiments in the first study show convincingly, however, that raising the salinity of fluids dramatically increases the concentrations of exactly those elements that are enriched in arc sources, removing the need for slab melt contributions. In the following study the alternative sediment melting hypothesis is also examined. Experiments are performed to examine if the stepwise reaction of silicic partial melts with the overlying mantle could produce magmas that are compositionally similar to arc magmas. The results indicate that at the conditions prevailing at the slab-mantle interface, such a process cannot produce the desired melt compositions. The final study related to subduction examines the fate of carbonate rocks as they enter the reduced lower mantle. In laser heated diamond anvil experiments $MgCO_3$ is reacted with metallic Fe, which is considered to be present in the lower mantle due to the low prevailing oxygen fugacity. In the recovered samples the formation of Fe_7C_3 seems to indicate that the carbonate is reduced in the presence of iron metal, but in some samples there is evidence that a high-pressure phase of $MgCO_3$ may persist.

The last three contributions in this section deal with the formation of porphyry-type ore deposits. The first is an extensive petrological study on two Slovakian volcanoes that are associated with several small porphyry gold and copper deposits. The objective is to examine whether the Au:Cu ratio of porphyry-type ore deposits was already predefined in the mineralizing magmas. The results demonstrate that this is clearly not the case, and that the depth of magma emplacement has probably the strongest influence on the Au:Cu ratio of porphyry-type deposits. In the next study the crystallization conditions, volatile contents and metal contents of mineralizing magmas in six porphyry molybdenum deposits in northeast China are reconstructed in a search for the conditions that produce porphyry Mo mineralization. It is found that neither unusually high Mo concentrations nor unusual volatile contents are required in the melts, and that it is again the depth of magma emplacement that likely plays the most important role. The final contribution in this section is complementary to the previous study, and is a petrological examination of two barren intrusions that crystallized at greater depth (10-14 km) than typical porphyry Mo-producing intrusions (4-8 km). The study is performed to evaluate the behaviour of Mo in deep intrusions. It is found that in these

deep granites, Mo was actually more efficiently extracted by the exsolving fluids, but no structures developed that allowed focused fluid flow and efficient Mo deposition.

a. *Metal-silicate partitioning of carbon during Earth's differentiation (I. Blanchard, E. Jennings/London, S. Petitgirard/Zurich; I. Franchi and X. Zhao/Milton Keynes and D.C. Rubie)*

Carbon is an element of great importance in the Earth, because it is intimately linked to the presence of life at the surface, and, as a light element, it may contribute to the density deficit of the Earth's iron-rich core. The Earth's core consists mostly of iron, alloyed with ~ 5 % Ni and ~ 10 % light elements (Si, O, S and/or C) in order to explain the density that is inferred from seismology. The composition of this iron alloy is closely linked to the conditions that occurred during the formation of the core in terms of *P*, *T*, and chemistry. While the partitioning of Si, O and a range of siderophile elements has been studied over a wide range of *P–T* conditions, little is known about the behaviour of carbon during Earth's differentiation, which involved the separation of metal from silicate in deep magma ocean environments. Carbon is siderophile at low pressures and temperatures, as shown by a very high metal-silicate partition coefficient ($D^{\text{met-sil}} > 100$). Based on this behaviour, it should be stored mainly in the Earth's core. Nevertheless, we still observe the existence of carbon at the surface, stored in crustal rocks and associated with the presence of life, and in the mantle, as shown by the exhumation of diamonds. The presence of carbon in the crust and mantle could be the result of the arrival of carbon during late accretion, after the process of core formation ceased, or because of a change in its metal–silicate partitioning behaviour at the conditions of core formation (*e.g.*, $P > 40$ GPa and $T > 3500$ K). Previous studies reported metal–silicate partitioning of carbon based on experiments using large volume presses up to 8 GPa and 2473 K maximum. The aim of this study is to extend this database to conditions of core-mantle differentiation in a deep magma ocean. We carried out experiments using the laser-heated diamond anvil cell apparatus (LH-DAC) in order to cover a wide range of *P-T* conditions (49-71 GPa and 3600-4000 K). Extending the study of carbon solubility in molten iron to such conditions is fundamental to better constraining the thermodynamics of its metal-silicate partitioning during core formation processes. Knowing the contribution of core formation processes in producing the current concentration of carbon in the bulk silicate Earth (BSE) will help to address the amount that has been subsequently added by the late veneer after core formation finished.

Our starting material consisted of a basaltic glass synthesised using an aerodynamic levitation furnace and subsequently polished down to 20 microns thickness. The samples were then machined with a femtosecond laser to obtain small discs 80-100 microns in diameter. We used a piston cylinder apparatus to synthesise ^{13}C doped iron carbide that was then crushed and used as the metal component in our experiments. We loaded two silicate discs of identical

composition into the LH-DAC so that they encapsulated the metal to limit the thermal gradient. We first pressurized the cells to the target pressure and then heated the samples using a double-sided laser heating system. High temperatures were maintained for tens of seconds, which is sufficient to achieve thermodynamic equilibrium given the small sample size and high temperatures of our experiments. Recovered run products were prepared using a Focused Ion Beam instrument (FIB) to obtain a sample 3 microns thick and consisting of two distinct phases (metal and silicate) that are each < 5-10 µm across. They were welded to a TEM grid prior to making EPMA measurements of major element concentrations (see Fig. 3.2-1, a typical run product). We synthesized a Fe_3C standard with a piston-cylinder in order to analyze the composition of our carbides with EPMA. To assess the quantity of carbon that is dissolved in the quenched silicate melt of each of our runs, we used a nanoSIMS facility, at the open University, Milton Keynes, UK. We synthesized two basaltic glasses doped in ^{13}C to be used as nanoSIMS standards, along with two meteorites (D'Orbigny and ALV981-R23) for which the ^{12}C and ^{13}C abundances are known.

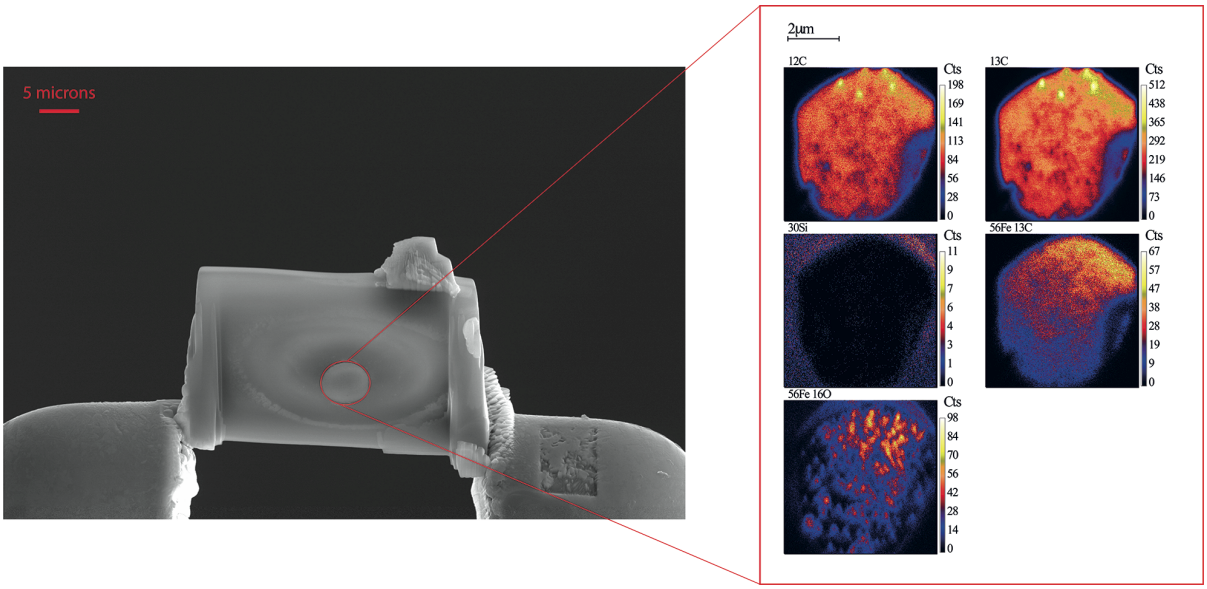

Fig. 3.2-1: Backscattered electron image (left) of a typical recovered run produced at 49 GPa and 3600 K. On the right, ion-probe images of the metallic part of the sample obtained using the nanoSIMS facility.

Our experimentally derived carbon metal-silicate partitioning coefficient are about two order of magnitude lower than those obtained at lower P-T conditions; which means that the metal-silicate partition coefficient of carbon decreases with increasing pressure and temperature. We also observe that the presence of oxygen and silicon in the metallic phase does not affect C partitioning. The next step in this study is to derive a thermodynamic model that can unite both low and high P-T experiments, in order to explain the behaviour of carbon during core-mantle differentiation.

b. *Vanadium stable isotope fractionation in the Earth's interior (D. Novella/Cambridge, J. Prytulak/Durham, J. Maclennan/Cambridge and D.J. Frost)*

The stable isotopic composition of transition metals such as vanadium hold much promise as emerging tools for investigating a wide breadth of geological processes. Studying the vanadium stable isotopic composition of terrestrial and extra-terrestrial material can inform us on the environment and mechanisms of formation of the Earth and the solar system. For example, vanadium isotopic compositions enriched in the lighter isotope (^{50}V over ^{51}V) are expected for material that received high-energy irradiation closer to the sun. To interpret V isotope data, however, knowledge about terrestrial processes that can cause variation is required. Potential isotopic fractionation during core formation is one such fundamental process to be considered.

The vanadium isotopic composition of the bulk silicate Earth is slightly heavier (*i.e.*, richer in ^{51}V) than chondrites, suggesting possible isotopic fractionation during core formation. Previous metal-silicate experiments at 1.5 GPa and 1650 °C lack resolvable vanadium isotopic fractionation between silicate glasses (the mantle) and metal alloys (the core), arguing against core formation as the cause of the observed V stable isotope disparity. These data therefore suggest a scenario where Earth formed with a deficit in high energy material irradiated during the early stages of the solar system and support the hypothesis that Earth is not formed only by chondritic material. However, vanadium isotope experimental data are scarce and the possible effect of pressure, temperature, oxygen fugacity (fO_2) and chemical composition have not been to date investigated.

Against this background, more experimental data are needed to determine the V isotope fractionation factor between metal and silicate melt phases to assess core formation as a driver of vanadium isotope fractionation. Therefore, we performed a series of high-pressure (HP) and high-temperature (HT) experiments at 1-3 GPa and up to 1750 °C using a multianvil apparatus, which provides relatively large sample volume and fast quenching conditions. The experiments employed different bulk compositions designed to account for the effect of chemistry on isotopic fractionation and also to set different fO_2 conditions.

Upon quenching the HP-HT experiments, silicate glasses formed in equilibrium with metal alloys that simulated core formation conditions. These phases are easily distinguished in the experimental charge and will be treated following chemical separation routines to purify V. The vanadium isotopic composition of samples will be measured via multi collector inductively coupled plasma mass spectrometry. The results from this study will directly address whether core formation can account for the origin of the terrestrial-extraterrestrial offset in stable vanadium isotopes. The experiments also have the potential to calibrate the metal-silicate isotope fractionation factor in terms of composition and oxygen fugacity.

c. *Measurements of H in FeS melts and the oxidation of the Earth's upper mantle through the accretion of water (K. Armstrong, S. Abeykoon, P. Condaminé, H. Bureau/Paris, C.A. McCammon and D.J. Frost)*

The Earth's upper mantle today exhibits an oxygen fugacity that is about 5 log units higher than that expected during accretion and core-mantle separation. Oxidation of the mantle must have happened towards the end of core formation or soon after because the oldest magmas seem to come from a mantle that had a similar oxidation state to the mantle today. One way that this could have happened is through reaction with water-bearing material late in accretion through the reaction $2FeO + H_2O = Fe_2O_3 + H_2$. For this to operate efficiently, however, hydrogen needs to be removed from the mantle as the mantle is being oxidized or its presence would simply reverse the reaction. This could for example occur at the surface, but the time scale of mixing with the entire mantle and the fact that H would be diluted with other gases probably makes this inefficient. There is significant evidence that late in the Earth's accretionary history, as a global magma ocean cooled towards crystallisation, it exsolved liquid FeS sulphide (the Hadean matte), which sank to the core. If this sulphide melt dissolved hydrogen then it could have led to oxidation of the mantle.

A series of experiments were performed to examine the partitioning hydrogen between liquid sulphide and molten silicate. The starting material was a synthetic mid-ocean ridge basalt composition with between 0.1 and 0.4 wt. % H_2O added as hydroxides and FeS. Fe metal was added to some experiments to change the oxygen fugacity. Silicate and sulphide were placed in a graphite inner capsule, which was in turn sealed in a welded AuPd outer capsule. Experiments were performed at 3 GPa and superliquidus temperatures in a 500 tonne multianvil press with an 18/11 assembly. Hydrogen contents of the silicate glasses and quenched sulphide liquids were measured using elastic recoil detection analysis (ERDA), at the nuclear microprobe facility at CEA Saclay, France. Oxygen fugacities were determined from the $Fe^{3+}/\sum Fe$ ratios of the silicate glasses.

Although the FeS liquid quenched to an assemblage of crystalline phases, by keeping the total H content relatively low the aim was to stay below the H solubility threshold of the quenched phases. No bubbles were observed in the texture of the sulphide to indicate H loss on quenching and the H contents ranged from 0.2-0.6 at. %. As shown in Fig. 3.2-2 the partition coefficients were determined over a range of oxygen fugacities that spanned most of the range over which the mantle must have oxidized after core formation. The sulphide/silicate partition coefficient for H shows no oxygen fugacity dependence, which would seem to indicate that H dissolved in the sulphide in the same form as in the silicate *i.e.*, dominantly as H_2O. Under such conditions sulphide could not assist H_2O in the oxidation of the mantle by removing H. However as also shown in Fig. 3.2-2 (right) the H partition coefficient shows a weak dependence with silicate melt H_2O content. This may be an indication that a threshold in the amount of H that the quenched sulphide phases can host has been reached, which could lead to an underestimation of the partition coefficient. Further work is ongoing to identify the solubility threshold of H in quenched sulphide assemblages.

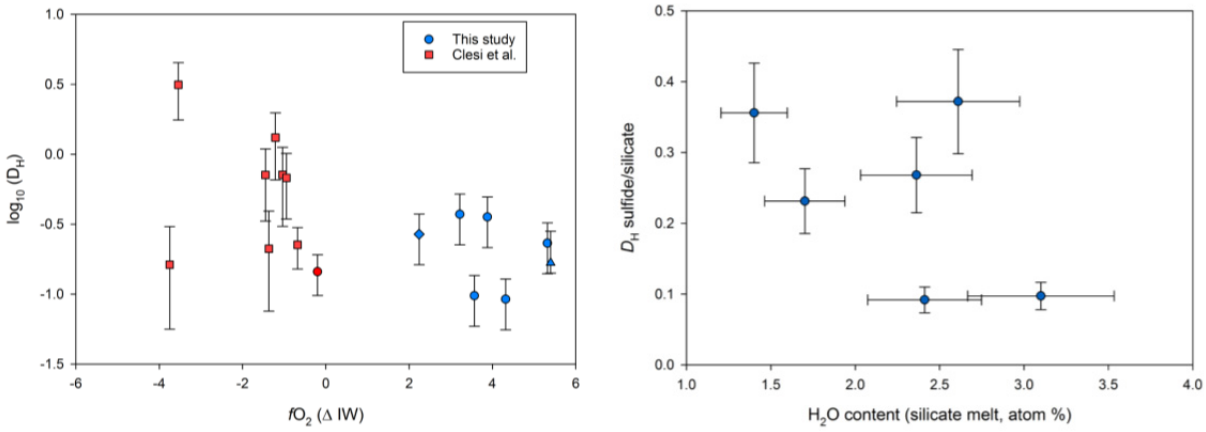

Fig. 3.2-2: (Left) Sulphide/silicate partition coefficient for hydrogen as a function of oxygen fugacty normalised against the iron-wustite buffer (IW). Results for sulphide from this study (blue symbols) are plotted with those from a previous study on iron metal/silicate (red squares, Clesi *et al.* (2018) Science Advances 14, DOI: 10.1126/sciadv.1701876). Blue diamond, 1573K, circles, 1673 K and triangle 1823 K. (Right) Sulphide/silicate H partition coefficient as a function of the melt H_2O content. If the quenched sulphide phases reach a threshold in soluble H, then D_H would drop as the melt H_2O content increases. This is in broad agreement with the data.

d. *The oxygen content of sulphide inclusions as a potential geothermometer (S. Abeykoon, D.J. Frost and V. Laurenz)*

Understanding the conditions at which xenoliths and xenocrysts are formed is important for reconstructing mantle geotherms and understanding the thermal events that lead to geochemical fractionation. Sulphide inclusions formed through the crystallization of sulphide melts are found in many xenoliths but they form the most common type of inclusion in diamonds. A geothermometer based on sulphide inclusion compositions would be particularly useful for determining diamond formation temperatures as there is currently no way of reliably achieving this for sub lithospheric diamonds.

Experiments indicate that oxygen partitions into sulphide melts and although sparse some measurements of natural sulphides from mantle xenoliths indeed show measurable and in some cases relatively high oxygen concentrations. In this study we are conducting a systematic experimental investigation of oxygen partitioning between mantle sulphides and silicate minerals at high pressures and temperatures. A series of multianvil experiments were conducted to equilibrate a fertile peridotite (KLB-1) mixture with molten sulphide (FeS) at pressures between 3-11 GPa and temperatures of 1300-1700 °C. The effects of pressure, temperature, oxygen fugacity and composition (both silicate and sulphide) have been investigated. Oxygen fugacity was determined in some experiments by saturating the sulphide in Ir to produce a separate Ir-Fe metal alloy, for which the Fe content is a function of oxygen fugacity. The electron microprobe is used to analyse the major element composition of the run products.

In a preliminary set of experiments we found oxygen concentrations in the quenched sulphide up to an equivalent of approximately 12 wt. % FeO at mantle temperatures. Moreover, the content of oxygen in the sulphide is found to be not controlled by fO_2 or fS_2, which is in disagreement with previous experimental studies conducted at ambient pressure conditions. The experiments indicate that the oxygen concentration in sulphide is mainly controlled by the FeO concentration in coexisting silicates in addition to the temperature. In order to fit the date and account for the FeO dependence we define an end member equilibrium between olivine, pyroxene and FeO in the sulphide melt, *i.e.*,

$$\underset{olivine}{Fe_2SiO_4} = \underset{orthopyroxene}{FeSiO_3} + \underset{sulphide\ melt}{FeO}$$

The standard state Gibbs free energy change (ΔG^0) at equilibrium is,

$$\Delta G^o = -RT \ln \frac{a_{FeO}^{sulfide}\ a_{FeSiO_3}^{ferrosilite}}{a_{Fe_2SiO_4}^{fayalite}}$$

Figure 3.2-3 shows values of ΔG^0 calculated using the experimental data and employing known activity composition relations for the silicates but ideal mixing for the sulphide melt. The variation in ΔG^0 with temperature is of sufficient magnitude to make a useful thermometer, however, in order to apply it to natural samples the effects of Ni and Cu also need to be examined.

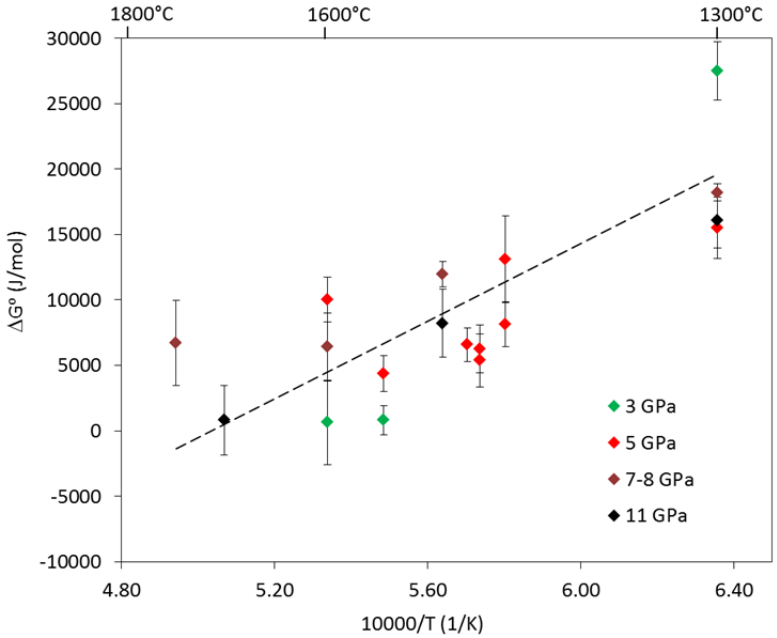

Fig. 3.2-3: The ΔG^0 for FeO dissolution in sulphide melt determined from individual experiments, plotted as a function of the inverse temperature. The dashed line is the calculated fit using the experimental data. Errors were propagated from the 1σ standard deviation in the sulphide X_{FeO} concentration.

e. *The growth of diamonds from mantle sulphides (C. Melai, D.J. Frost and T. Boffa Ballaran)*

Inclusions in diamonds provide direct insight into the chemistry of diamond-forming domains of Earth's mantle and allow a better understanding of the recycling of volatiles through the Earth's interior. The wide range of mineral, fluid and melt inclusions observed in natural diamonds probably reflects heterogeneity in the diamond forming media and confirms the complexity of diamond nucleation and growth processes. One of the most common types of inclusions found in diamonds are sulphides although the direct connection between the diamond forming reaction and the presence of sulphides is not at all clear. Diamond formation is kinetically inhibited in the region of the graphite to diamond equilibrium phase transition so a catalyst is required, probably even in the Earth, to instigate diamond formation under these conditions.

The aim of this study is to experimentally investigate diamond nucleation from sulphide melts using multianvil experiment without the addition of a diamond seeds. The purpose is threefold. Firstly, to examine whether sulphides indeed act as a medium for diamond formation. Second to produce diamonds from a medium that can be in equilibrium with mantle assemblages such that partition coefficients including those of N and C isotopes can be determined between diamond and silicate minerals and melts and thirdly to examine whether it is possible to capture fluid or solid inclusions in synthetically grown diamonds. Fe-Ni-S alloy, adipic acid and graphite are loaded into olivine or MgO single crystal capsules and experiments are run between 6 and 10 GPa at 1250-1500 °C. After the experiments samples are sectioned and polished for analysis with SEM, Raman and infra-red spectrscopy. Figure 3.2-4 shows an experiment from 10 GPa and 1500 °C performed for 5 hours, which

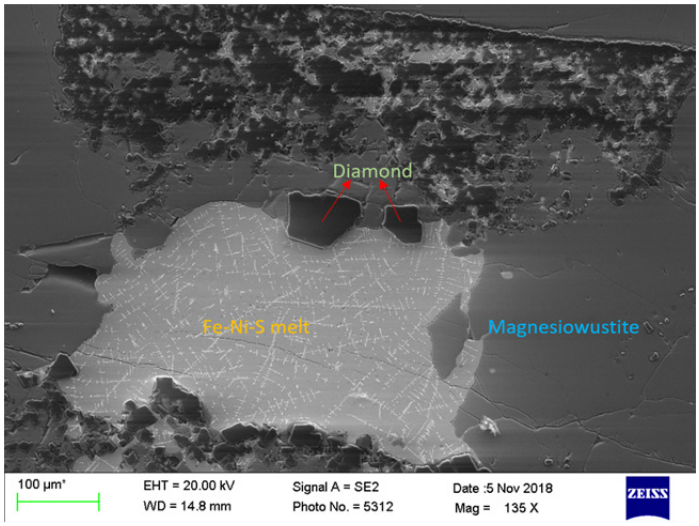

Fig. 3.2-4: SEM image of a run product from 10 GPa and 1500 °C performed in an MgO single crystal capsule. Diamonds have formed with several that remained in contact with the Fe-Ni-S melt pool growing to > 50 µm. Bright pentlandite quench crystals can be seen inside the melt pool. The surrounding matrix is magnesiowustite that has formed from the interaction of the Fe in the starting material with the capsule itself.

shows diamond nucleation and growth from sulphide melt. The diamonds are up to 0.1 mm in length and are easily separated from the charge. They contain sulphide inclusions but spectroscopic analyses find no evidence for the presence of fluid inclusions even though adipic acid should have broken down to form H_2O and CH_4 in the experiment. The diamonds have very low N contents.

f. *Formation of sublithospheric diamond and pyroxenite in Earth's upper mantle (N. Ottersberg/Bochum, C. Beyer/Bochum and D.J. Frost)*

Majoritic garnet inclusions in diamond, originating from depths exceeding 300 km, show a strong similarity with pyroxenite and eclogite lithologies, whereas, peridotitic garnets are absent at these depths. This implies that there is a potential link between the formation of diamond and its host lithology. Here we put this hypothesis to the test and examine whether the redox-reaction of a methane-dominated C-O-H fluid with ferric iron-rich eclogitic/pyroxenitic majoritic garnet is a factor in the formation of diamond.

We performed multianvil experiments at 10 GPa and 1300 to 1400 °C with a double capsule setup. The outer capsule contained a solid-state oxygen buffer and the inner capsule contained a layer of synthetic peridotite and eclogite. Stearic acid was used as a C-O-H fluid source. The recovered charges are composed of recrystallized peridotite, a well distinguishable pyroxenite reaction layer and a partially reacted melt layer. The pyroxenite layer is produced as eclogite partial melt reacts with the peridotite. In a similar set of experiments at 8 GPa we modified this setup by releasing the stearic acid after the formation of pyroxenite by employing a third capsule, fabricated from gold, which we can melt by a short increase in temperature. We also replaced the eclogite with different glasses (basaltic to dacitic) to create the pyroxenite layer. With this setup we observed diamond formation in the reaction layer and in the melt layer (Fig. 3.2-5). As steric acid was the only C-source, and it produces CH_4 and H_2O, it is likely that the diamond formed through the oxidation of CH_4 possibly by reduction of ferric iron that was concentrated in and by the partial melt.

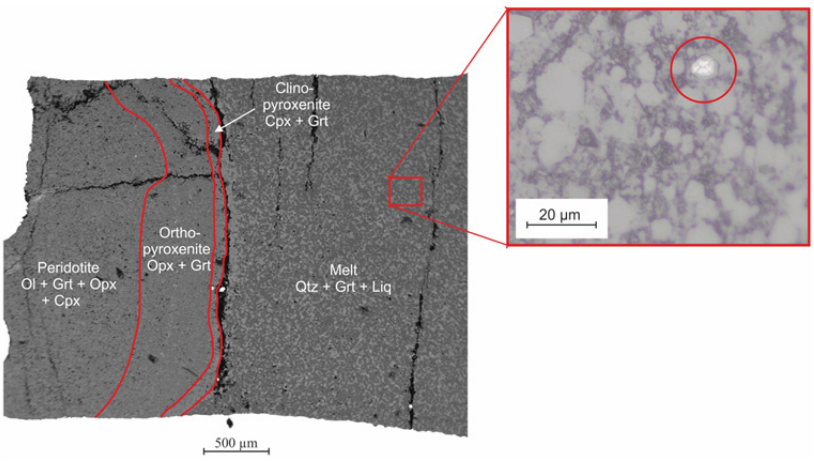

Fig. 3.2-5: Backscattered electron image of an experimental run at 7.5 GPa and 1320 °C. The red lines indicate the different layers and their mineral assemblage. The inset shows a diamond of ~ 8 µm which seems to have formed through the oxidation of a more reduced fluid containing CH_4.

g. *A synchrotron Mössbauer study of Mg-chromite-bearing xenoliths and diamonds from the Murowa kimberlite, Zimbabwe (L. Ziberna, V. Cerantola/Hamburg, S. Milani/Milano, G. Bulanova/Bristol, C. Smith/Bristol, A.I. Chumakov/Grenoble, L. Faccincani/Padova, C. Melai and D.J. Frost)*

The oxidation state of the Earth's upper mantle during the Archean is still poorly understood. Mantle xenoliths and rare mineral inclusions in diamonds from cratonic areas are the only direct samples that can be used to investigate how deep redox processes operated during this Eon. What hampers their use is the difficulty in accurately quantifying the oxidation state of Fe at the scale of the inclusions in diamonds and within synthetic mantle assembages used to calibrate oxygen barometers. Among peridotitic inclusions in diamonds worldwide, Mg-chromite is one of the most abundant (ca. 30 %) and since its crystal structure can accommodate both Fe^{2+} and Fe^{3+}, it potentially holds relevant information about the redox state of its source rock during or before diamond formation. In this study, we investigate a suite of Mg-chromite-bearing harzburgite and dunite mantle xenoliths and primary inclusions in diamonds from the Murowa kimberlite (Zimbabwe). These samples are rare examples of pristine, highly refractory mantle fragments that most likely represent the residua of the high-degree melting events that occurred during the Archean.

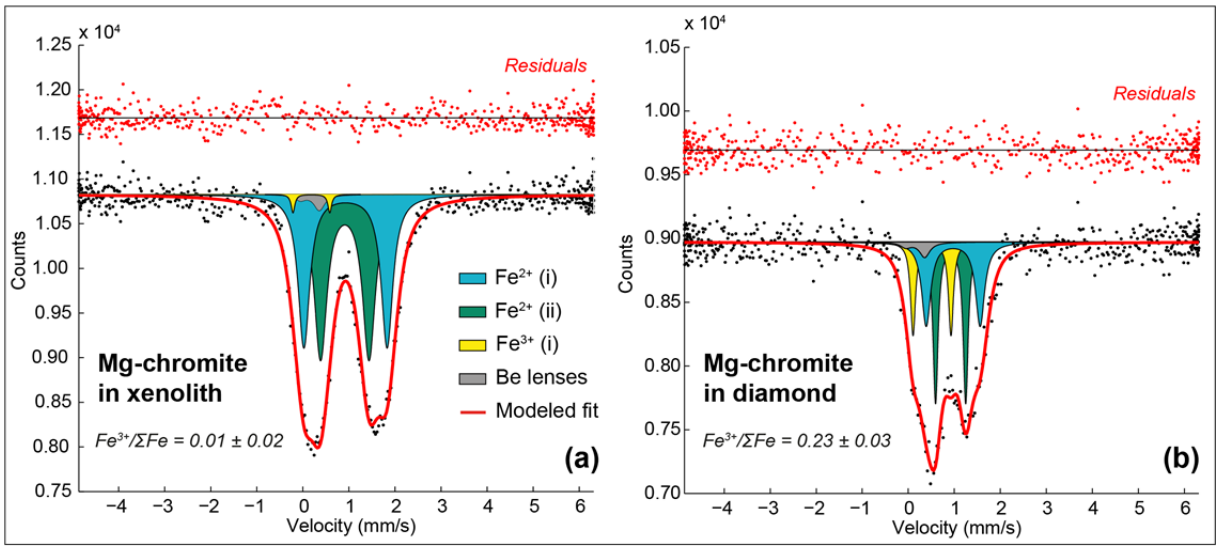

Fig. 3.2-6: Mössbauer spectra obtained for Mg-chromites in (a) mantle xenoliths and (b) diamond inclusions.

The average modal composition of mantle xenoliths, which show textures from coarse granular to porphyroclastic, is 84 vol. % olivine, 10 % orthopyroxene, 4 % clinopyroxene and 1 % Mg-chromite. Mineral inclusions in diamonds, on the other hand, are 33 % chromite, 31 % sulfide, 28 % olivine, 4 % orthopyroxene, 3 % garnet and < 1 % clinopyroxene. Electron microprobe analyses have been carried out on both xenoliths and inclusions in diamonds. The results show very high Mg# [$Mg/(Mg+Fe_{tot})$] for olivine and orthopyroxene in both xenoliths

and diamonds (0.92-0.95) and variable Cr_2O_3 in Mg-chromites, in the range 20-65 wt. % for the xenolith samples and 61-66 wt. % for the diamond inclusions. ^{57}Fe Mössbauer analyses, mainly focused on the Mg-chromites, have been performed using the synchrotron Mössbauer source (SMS) available at the Nuclear Resonance beamline ID18, ESRF, Grenoble. Fitting results for Mg-chromites were obtained using Lorentzian shape doublets, two for Fe^{2+} and one for Fe^{3+}. Values of $Fe^{3+}/\Sigma Fe$ were calculated based on relative area ratios of the doublets and were corrected for the recoil-free fractions. Estimated uncertainties in $Fe^{3+}/\Sigma Fe$ vary between 0.02 and 0.04. The main results show that $Fe^{3+}/\Sigma Fe$ ratios in Mg-chromites in mantle xenoliths are significantly lower than the Mg-chromites included in diamonds (0.02-0.08 vs. 0.08-0.26; *e.g.*, Fig. 3.2-6). With the exception of one sample, the combination of microprobe analyses and Mössbauer spectroscopy suggest that the Mg-chromites are stoichiometric and that Cr is present only as Cr^{3+}.

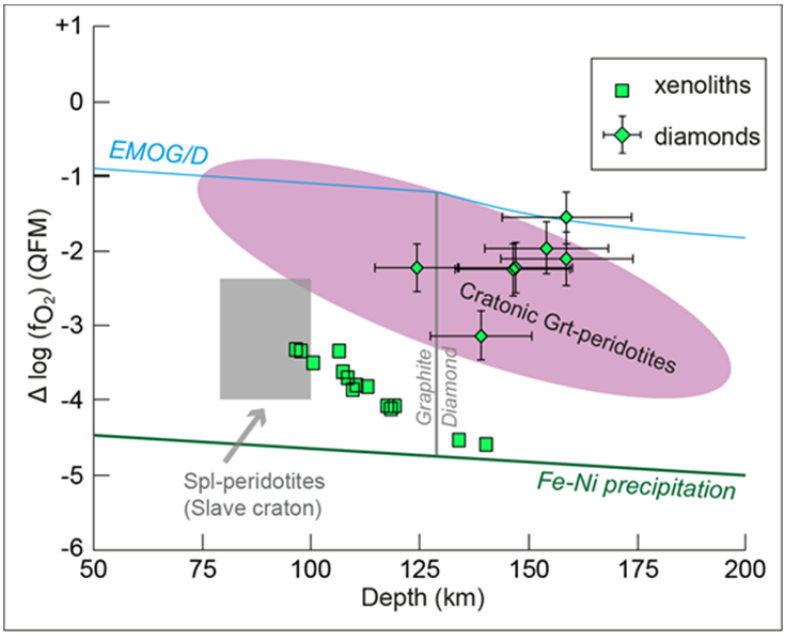

Fig. 3.2-7: Oxygen fugacity (normalized to the Quartz-Fayalite-Magnetite buffer) for the xenoliths and inclusions in diamonds from the Murowa kimberlite, using the oxygen barometer of Ballhaus *et al.* (1991). For the inclusions in diamonds, each data point represents one single Mg-chromite inclusion and error bars represent the range derived from multiple calculations using a set of olivine compositions from the same diamond suite, assuming equilibrium with orthopyroxene. Temperatures were calculated using the olivine-spinel thermometer of Ballhaus *et al.* (1991) and depths were extrapolated from a 40 mW/m^2 geotherm. EMOG/D, Fe-Ni precipitation and the field of garnet peridotites are after Stagno *et al.* (2013, Nature 493, 84). Data for the Slave Craton are from McCammon & Kopylova (2004, Contrib. Mineral. Petrol. 148, 55).

A set of oxygen barometers have been applied to both the xenolith and diamond inclusion suites. The results for calculations using the oxybarometer of Ballhaus *et al.* (1991; Contrib. Mineral. Petrol. 107, 27) are reported in Fig. 3.2-7. Mantle xenoliths record low oxygen

fugacities (fO_2) approaching the Fe-Ni precipitation curve (Δlog fO_2 QFM -3.3 to -4.5), whereas Mg-chromites in diamonds show distinctively higher values of fO_2 (Δlog fO_2 QFM -1.1 to -3.3). The latter are consistent with the range of fO_2 determined for some high-density fluids included in diamonds (Weiss *et al.*, 2018; Earth Planet. Sci. Lett. 491, 134). Application of other oxygen barometers (*e.g.*, Miller *et al.*, 2016, J. Petrol. 57, 1199) produces values that are systematically higher by ~ 1 log unit for all the samples, but still show the same relative difference between inclusions in diamonds and mantle xenoliths. On the one hand, the higher fO_2 values recorded by inclusions in diamonds are consistent with a model of diamond formation in which the diamond-forming fluids are more oxidized than the ambient refractory mantle. On the other hand, the low oxygen fugacity recorded in the pristine, ultra-depleted mantle xenoliths from Murowa suggests that during the Archean a relevant portion of the upper mantle might have been considerably more reduced than the more commonly studied cratonic garnet peridotites.

h. *Redox history of a carbon-bearing eclogite from Roberts Victor, South Africa (C.A. McCammon, S. Misra and D. Jacob/North Ryde)*

The pressure-temperature history of rocks can often be deciphered from compositional variations in their constituent minerals, while ferric iron variations can reveal the redox history of the rocks. Recent calibration of both a geobarometer and oxybarometer for eclogite (see BGI Annual Reports 2012 and 2013) enables the history of an enigmatic eclogite from Roberts Victor, South Africa to be determined. The enigmatic hand specimen, Rovic-124, shows three distinct layers over a scale of only a few cm: zone A6 has a garnet to clinopyroxene (cpx) ratio of 90:10 and contains diamonds, zone A3 has a garnet to cpx ratio of 60:40 and contains graphite, while zone A1 has a 50:50 ratio of garnet to cpx and contains no carbon at all. What is the origin of the layering? What conditions did the eclogite experience during its history? How do they relate to the forms of carbon in the rock? To answer these questions, we undertook a combined Mössbauer and electron microprobe study of the rock and applied thermodynamic models to determine temperature, pressure and oxygen fugacity.

Thick sections were cut from each of the three zones in the hand specimen with 500 μm thickness and polished on both sides. The sections were mounted on stiff plastic sheets so that Mössbauer spectra could be collected for roughly 25 garnet and cpx grains in each zone. The gamma-ray beam was collimated using a 500 μm diameter hole in lead foil placed on the grain to be measured. Afterwards the sections were mounted on glass slides and carbon coated so that electron microprobe analysis could be made on the same grains (Fig. 3.2-8). Temperatures, pressures and oxygen fugacities were calculated based on thermodynamic models with major element compositions from the electron microprobe and ferric iron from Mössbauer spectroscopy.

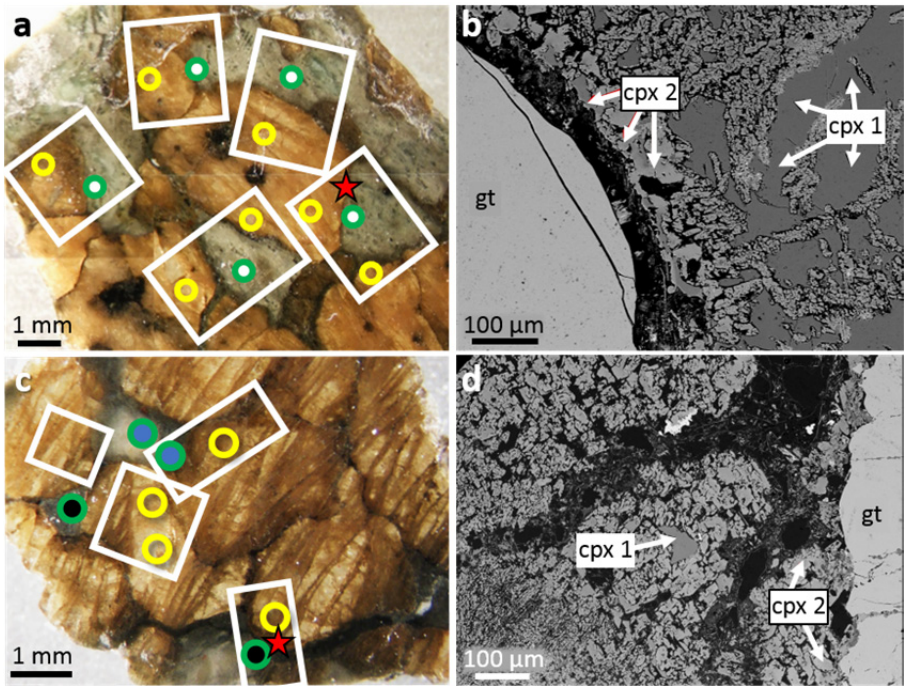

Fig. 3.2-8: Optical and backscattered images of Rovic-124 zones A3 (a, b) and A6 (c, d). The red stars mark the positions where the backscattered images were taken and the white boxes indicate the regions examined using the electron microprobe. Mössbauer spectra were collected over the 500 µm spots marked by circles, where the colours indicate the phase and range of $Fe^{3+}/\Sigma Fe$ (in brackets): yellow – garnet (0.02-0.04); green with white fill – cpx (0.14-0.17); green with blue fill – cpx (0.18-0.20); green with black fill – cpx (0.21-0.23). The two distinct types of cpx are indicated on the backscattered images.

Our data show that garnet compositions are uniform across all zones, while there are two distinct compositions of cpx with different textures (Fig. 3.2-8). The temperatures calculated for garnet-cpx 1 and garnet-cpx 2 pairs are similar (1000 to 1200 °C), while pressures are higher for garnet-cpx 1 pairs (3 to 4.5 GPa) compared to those for garnet-cpx 2 pairs (1.5 to 2.5 GPa). The oxygen fugacities calculated for all garnet-cpx pairs are similar (-1.0 to -2.5 relative to the fayalite-magnetite-quartz buffer), although cpx 2 has higher $Fe^{3+}/\Sigma Fe$ (0.21 to 0.23) compared to cpx 1 (0.14 to 0.17) (Fig. 3.2-8).

These results suggest the following scenario. Zonal layering was likely inherited from the gabbro protolith, which was already proposed in the literature based on isotopic studies. Zones A3 and A6 were carbonated, which stabilised diamond following subduction to > 150 km depth. Partial exhumation to around 100 km depth led to graphite formation in zone A3, but preserved diamond metastably in zone A6. Further exhumation to around 60 km depth combined with metasomatism stabilised a slightly more oxidised cpx, but fluids were sufficiently reducing to maintain carbon as graphite or diamond. Finally, the rock was rapidly exhumed by the Roberts Victor kimberlite, which preserved the compositions already existing in the garnet and cpx generations.

i. *Ferric iron in majorite between 13 and 20 GPa in mafic and ultramafic compositions: Towards a thermodynamic model for iron partitioning in majorite (C. Beyer/Bochum, R. Myhill/Bristol, C.A. McCammon and K. Marquardt)*

Knowledge of the oxidation state of iron in mantle minerals under different conditions is needed in order to determine the stability ranges of redox-sensitive phases, such as diamonds, sulphides and carbonatitic melts. Garnet is particularly important, as it is a major component of the deep upper mantle and mantle transition zone and can potentially accept ferric iron on its octahedral site (a khoharite component). However, there is competition for this site in the form of Al (pyrope component), MgSi (a majorite component) and AlSi (Na-majorite component), amongst others. The interaction between these different components at high pressure is poorly understood.

In this study, we conducted multianvil experiments at 14, 17 and 20 GPa under iron-saturated, Mo – MoO_2 and Re – ReO_2 buffered conditions using a double-capsule design. Starting materials were reduced glasses of basaltic, peridotitic and Martian mantle compositions. After quenching, run products were analysed by EPMA. $Fe^{3+}/\Sigma Fe$ ratios in garnet and coexisting clinopyroxene were analysed using Mössbauer spectroscopy and electron energy loss spectroscopy. An example for the variation of ferric iron with pressure is given in Fig. 3.2-9.

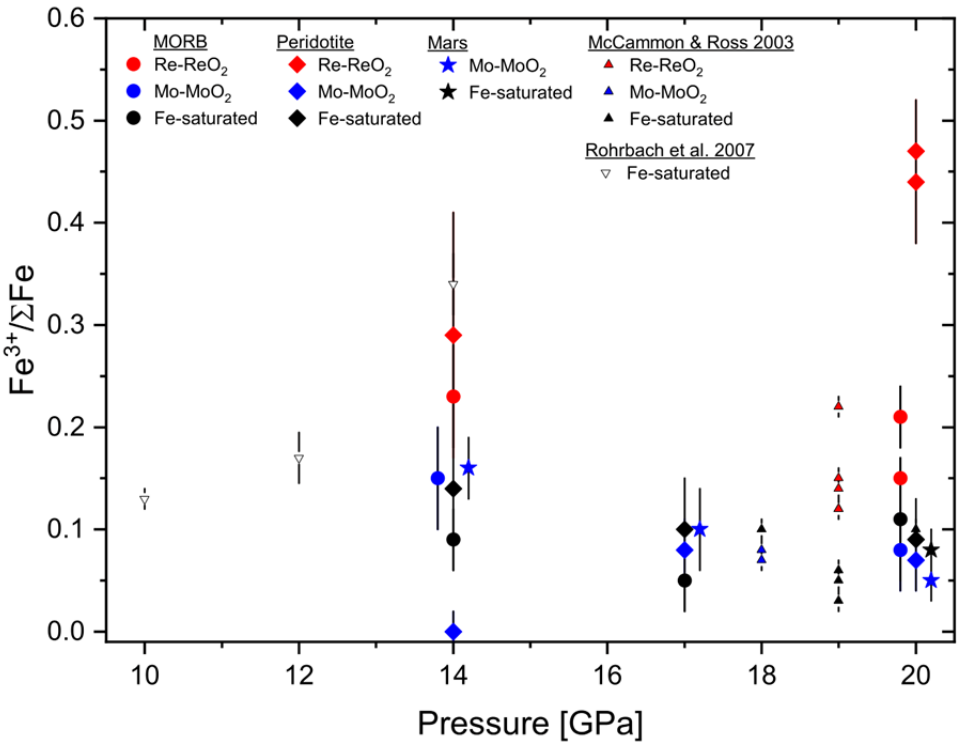

Fig. 3.2-9: $Fe^{3+}/\Sigma Fe$ ratio of majoritic garnet as a function of pressure and fO_2. Results from the previous studies of Rohrbach *et al.* (2007; Nature 449, 456) and McCammon & Ross (2003; Phys. Chem. Min. 30, 206) are shown for comparison.

Using the results from these experiments together with previous studies, we create a new high-pressure solution model for garnet with both majorite and ferric iron components. We will apply this model to majoritic inclusions in diamonds to determine the conditions of their formation and the compositions of fluids that potentially affected the local availability of oxygen.

j. *Multiple saturation conditions of "direct ascent" petit-spot magmas (T. Yutani and N. Hirano/Sendai; P. Condaminé, C.A. McCammon and D.J. Frost)*

The asthenospheric mantle and in particular the seismic low-velocity zone must play an important role in plate tectonics. Although the geochemical and petrological properties of the asthenosphere are essential to understand the surface environment of terrestrial planets, the nature of the asthenosphere is still enigmatic because we have never gained samples from the oceanic asthenosphere directly. Petit-spot volcanism, which mainly produces small submarine knolls, is a new-type of monogenic volcanic activity discovered at the beginning of the 21st century. Because of the age and eruption setting of the petit-spot sea knolls (the eruption age is much younger than surrounding crustal rocks), it is proposed that petit-spot magma has been generated inside the asthenospheric mantle far from mid ocean ridges in many cases close to subduction zones. These magmas almost certainly contain crucial information on the asthenosphere. Petrographical and geochemical data on petit-spot alkaline basalts, however, suggests that previously reported petit-spot samples from the Northwest Pacific Ocean have undergone some degree of fractional crystallization of olivine and/or clinopyroxene etc. and have also assimilated surrounding lithospheric mantle. Thus, their chemical composition may be considerably modified before eruption. On the other hand, the samples newly collected from three isolated knolls show strongly primitive geochemical characteristics such as low-silica, high alkali and high volatile element contents.

These petit-spot magmas, which are potentially derived via a "direct ascent" with minimal lithospheric interaction, show relatively primitive geochemical characteristics such as high alkaline content and high Zr/Hf ratio. Although they do not seem to have undergone assimilation with surrounding mantle peridotite during ascent, they do contain significant olivine phenocrysts and have relatively high vesicularities (around 15 vol. %), implying that they have undergone olivine-fractional crystallization and degassing of volatile components such as H_2O and/or CO_2.

We calculated H_2O and CO_2 contents of three "direct ascent" petit-spot samples from the NW Pacific plate before degassing by assuming closed system degassing and using the measured H_2O and CO_2 contents in the glass, as shown in Fig. 3.2-10. The calculated volatile contents of H_2O and CO_2 are 2.0-2.4 wt. % and 1.0-5.0 wt. % respectively. Chemical compositions of olivines that would be in equilibrium with the melt are calculated from partition coefficients of Mg, Fe, Mn and Ni between olivine and melt. According to our calculations, the Mg, Fe, Mn and Ni compositions of olivines would reach those expected for mantle peridotite if ~ 25 mol. % of olivine fractionation had occurred, as shown in Fig. 3.2-11.

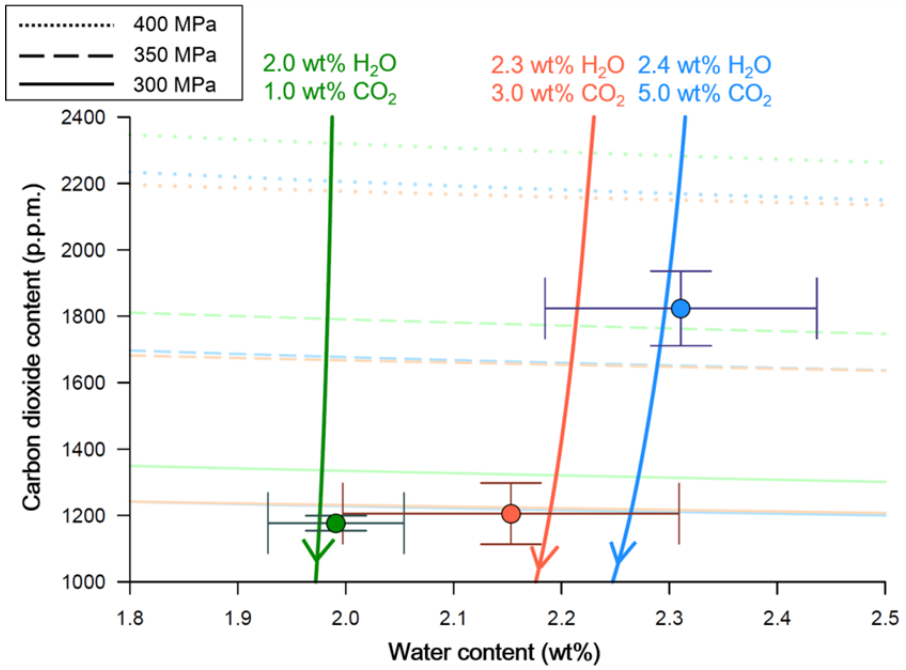

Fig. 3.2-10: Circles are H_2O and CO_2 contents of the glass samples analyzed by SIMS. Arrows are expected degassing paths for each samples. Pale coloured dotted, dashed and solid lines indicate solubilities of H_2O and CO_2 mixture for respective chemical compositions of the petit-spot basalts at 1200 °C.

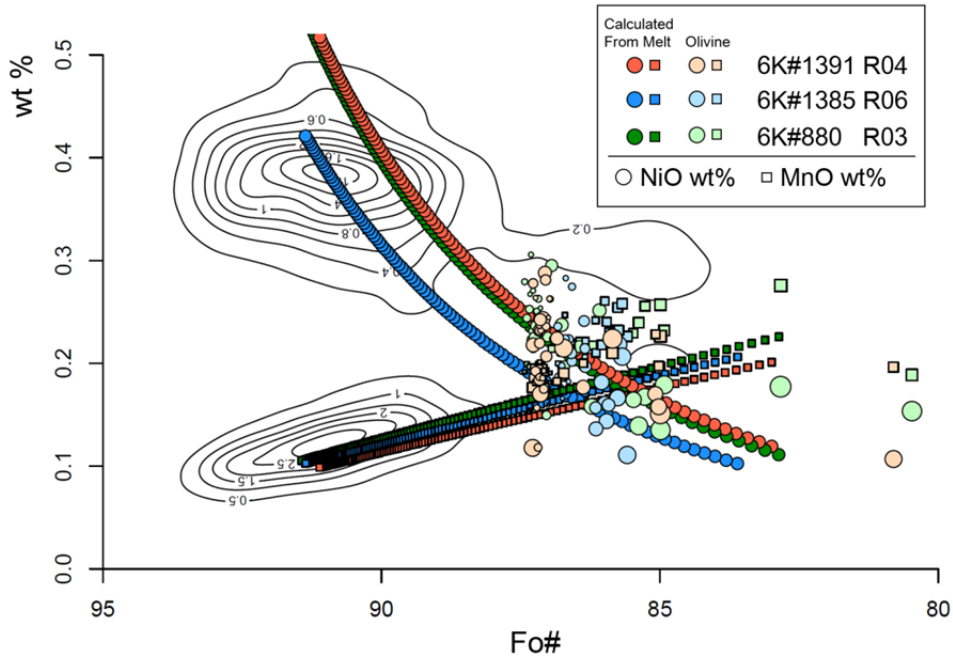

Fig. 3.2-11: Pale coloured symbols indicate compositions of olivine phenocrysts in the petit-spot basalts analysed by EPMA. The bigger symbols are analyses taken closer to the crystal rim, which clearly shows evidence for olivine fractionation. Contours indicate the frequency at which "mantle olivine" compositions are found.

Multiple saturation experiments are now being performed using the primary compositions of the "direct ascent" petit-spot magmas in order to determine the P-T conditions at which the magmas formed and the lithologies with which the melts are in equilibrium. This is being investigating using piston cylinder experiments. Although we have not yet found the conditions of multiple saturation, we have identified that phlogopite is in equilibrium with one of the primary melts at 1300 °C and 2.8 GPa. That implies that the liquidus phase assemblage of the primary melt is a phlogopite peridotite, which may imply a metasomatic source for the magmas.

k. *Kimberlite from incipient melting of the mantle transition zone? (P. Condaminé and D.J. Frost)*

The mantle transition zone (410-660 km) is often proposed to be an important water repository in the Earth's mantle and a low velocity layer attributed to the presence of a partially (low-degree) molten hydrated layer has been suggested to exist atop the 410 km discontinuity where it may reside due to neutral melt buoyancy. Previous studies have indeed proposed that ascending ambient mantle may undergo hydrous partial melting as it rises out of the transition zone at 410 km owing to a decrease in the H_2O storage capacity of olivine compared to wadsleyite. The buoyancy of such a melt layer *i.e.*, its density compared to the surrounding mantle will be controlled by its chemical composition. On the other hand, ringwoodite inclusions in diamonds brought to the surface by kimberlite magmas may support the presence of deep-rooted melts that can ascent to the Earth's surface. To date no experimental study has examined the possible composition of low-degree melts at transition zone depths or their associated buoyancy. Here we determine the incipient melt composition of a peridotite assemblage at mantle transition zone conditions in order that we can ultimately asses its buoyancy.

Multianvil experiments have been performed at 17 GPa and 1600 °C using a natural KLB-1 peridotite. Because extracting incipient melt at high pressure (> 3 GPa) is almost impossible for current experimental petrology, iterative sandwich experiments are required to study ‘low-degree' melts. A high proportion of glass (50-70 wt. %) is added to the peridotite to ensure melt pool separation. Large degrees of melt make the determination of melt H_2O contents by mass balance more accurate.

The initial first guess melts composition results in significant reaction with the peridotite assemblage due to disequilibrium. However by analysing the resulting melt composition a second guess melt is produced which should be closer to equilibrium with the peridotite. After 6 iterative experiments, a melt was produced that was in equilibrium with a typical peridotite assemblage containing wadsleyite, garnet and pyroxene. As shown in Fig. 3.2-12 it was possible to saturate a large melt pool for which the H_2O content can be accurately determined by mass balance with a transition zone assemblage. While almost all the inserted melt

composition was recrystallizing during previous iterations, nearly all the melt is still present at the end of the experiment in the last iterations, indicating near-equilibrium conditions. The melt is strongly silica-undersaturated (34 wt. % SiO_2) together with high amounts of MgO (27 wt. %) and CaO (13 wt. %) while being depleted in Al_2O_3 (1 wt. %). These features are nearly identical to kimberlite rocks from group I. Further experiments will allow us to better constrain whether such incipient melts could remain neutrally buoyant on top of the transition zone or whether they should rise up to the surface as kimberlite-like volcanism. SIMS measurements of minerals will then allow us to provide for the first time partition coefficients for water at mantle transition zone conditions.

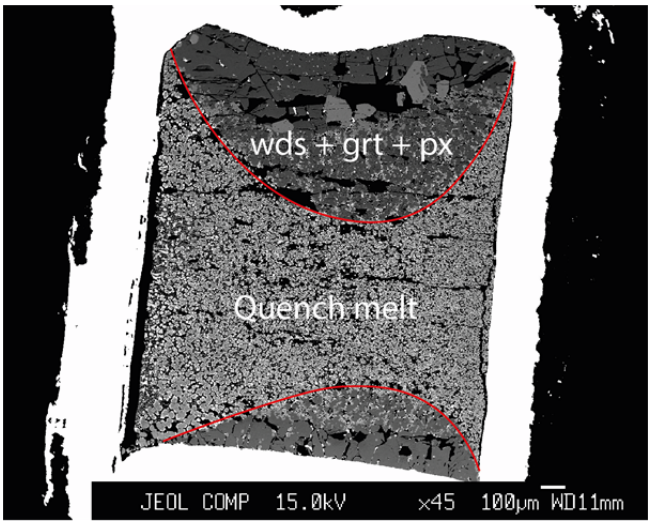

Fig. 3.2-12: Backscattered electron image showing the last iterative experiment at 17 GPa. The melt coexists with wadsleyite (wds), garnet (grt) and a high-Ca pyroxene (px).

l. *Melting experiments on hydrous peridotite at top of the lower mantle conditions (A. Nakajima, T. Sakamaki and A. Suzuki/Sendai)*

Compared to minerals of the lower mantle, which have the potential to host of the order of 0.1-0.2 wt. % H_2O, mantle transition zone minerals have a much larger water-hosting capacity of about 1-2 wt. % H_2O and could thus embody a large "water reservoir" inside the Earth. Water-rich material descending into the lower mantle could, therefore, instigate dehydration melting at the top of the lower mantle. This hypothesis is supported by seismological observations, which indicate a low-velocity anomaly at the top of the lower mantle. To better constrain the melting conditions in this region, high-pressure melting experiments are required. Focusing also on the effect of redox conditions (the valence of iron in the system), we have conducted melting experiment at high pressure and temperature.

Pressure and temperature conditions were 26 GPa and 1600-2000 °C, respectively. To achieve high pressures, a Kawai-type multianvil press was used and a 7/3 high-pressure

assembly. The composition of the starting material was peridotite with 2 wt. % H_2O. One material was made with all iron as Fe_2O_3 while a second contained iron as FeO. The two types of starting material were filled into gold capsules and put into the same high-pressure cell assembly. The samples were compressed to 26 GPa, then heated to desired temperature, and kept there for 10-120 minutes. The recovered samples were analysed using a field emission-scanning electron microscope and energy dispersive X-ray spectrometry.

Fine quench crystals plus glass were observed in the reduced sample recovered from 2000 °C. Figure 3.2-13 shows a picture of the sample. This result implies that reduced, hydrous peridotite containing 2 wt. % H_2O can be molten under conditions compatible with the top of the lower mantle. On the other hand, no quenched crystals or glass were observed in the oxidized sample at the same P-T conditions. This suggests that variations in the redox conditions at the top of lower mantle can control mantle melting.

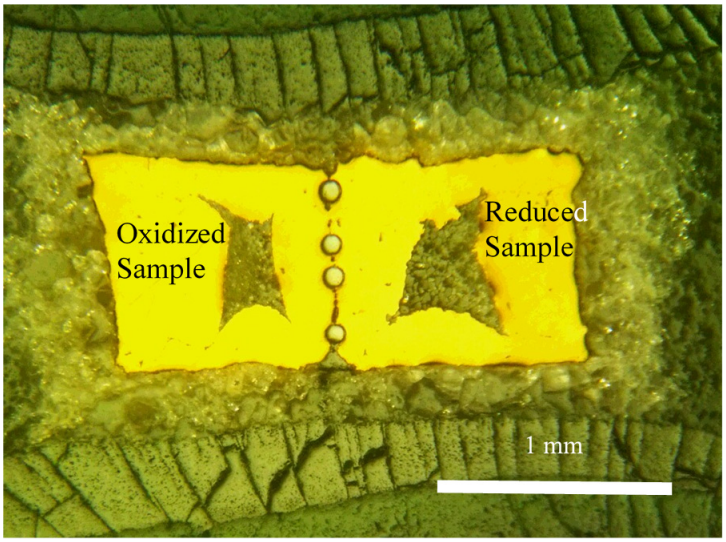

Fig. 3.2-13: A reflected light microscope photograph of a polished experimental section recovered from 26 GPa and 2000 °C showing both gold capsules surrounded by an MgO sleeve and the $LaCrO_3$ furnace.

m. *Towards melting relations in the MgO-FeO-SiO_2 system at lower mantle conditions from multianvil experiments (J. Yao, D.J. Frost, G. Steinle-Neumann, Z. Liu, H. Fei and L. Ziberna)*

During crystallization of the terrestrial magma ocean, phase relations for bulk silicate Earth composition govern the dynamic regime of the solidifying portion of the mantle. The phase on the liquidus, *i.e.*, the mineral that first crystallizes from the melt, is of particular importance, as it determines the density balance between silicate liquid and the forming crystallites, as well as the initial temperature profile in the mantle when its dynamic regime transitions from turbulent to solid-state convection. Phase relations in the MgO-SiO_2 system

have been explored by multianvil experiments and computations up to pressures of the Earth's lower mantle, but the influence of FeO on the phase relations is not sufficiently explored to date.

Based on limited work on peridotite composition, FeO is expected to lower the liquidus temperature and partition into the melt, strongly affecting the density difference between the melt and mineral phase on the liquidus. We investigate these two aspects in a series of multianvil experiments along the $MgSiO_3$-$FeSiO_3$ compositional join at 25 GPa, *i.e.*, the pressure at the top of Earth's lower mantle. Experiments in the Sumitomo press are performed for starting compositions of $Mg_{0.9}Fe_{0.1}SiO_3$, $Mg_{0.8}Fe_{0.2}SiO_3$, $Mg_{0.7}Fe_{0.3}SiO_3$ and $Mg_{0.5}Fe_{0.5}SiO_3$, with a 7/3 cell assembly and rhenium capsules. Scanning electron microscope imaging of the recovered capsules (Fig. 3.2-14) show coexisting solid and melt. In all samples, bridgmanite occurs as the liquidus phase, similar to previous experiments for peridotite-like compositions.

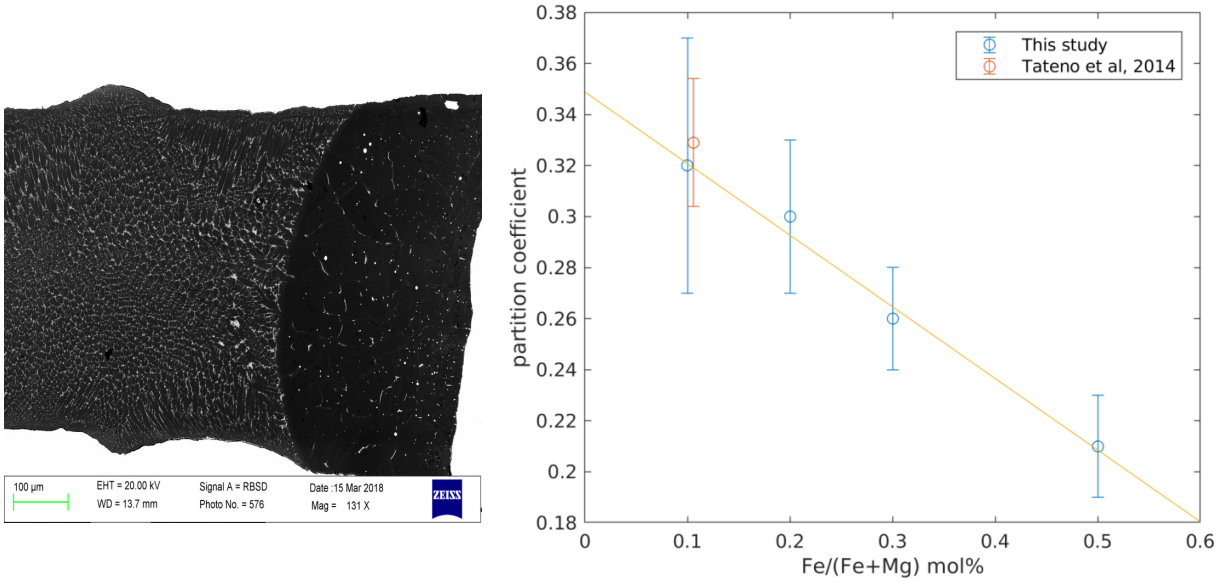

Fig. 3.2-14: (Left) Back-scattered electron image of a recovered mult-anvil capsule with an $Mg_{0.9}Fe_{0.1}SiO_3$ sample heated to 2800 K at 25 GPa. The sample has experienced partial melting due to a small temperature-gradient, with typical melt quench texture on the left side. The melt coexists with bridgmanite (dark field on the right side), the phase on the liquidus. (Right) Equilibrium constant for Fe-partitioning between bridgmanite and coexisting melt as a function of iron content of the initial composition. For comparison we have included a data point by Tateno *et al.* (2014; JGR 119: 4684)

From the chemical analysis of the coexisting liquid and solid by electron microprobe, we calculate the equilibrium constant for Fe-distribution as $K_D = \left(X_{Fe}^{solid}/X_{Mg}^{solid}\right)/\left(X_{Fe}^{liquid}/X_{Mg}^{liquid}\right)$, with $X_A^{solid/liquid}$ the molar fraction of element A in the solid and liquid, respectively. For peridotite-like starting compositions with $Fe/Fe+$

Mg$\sim$0.1 our value of $K_D \sim 0.32$ is similar to previously published results, but K_D decreases in a quasi-linear fashion with Fe-content in the starting composition to values of $K_D \sim 0.2$ for $Mg_{0.5}Fe_{0.5}SiO_3$.

n. *The role of oxygen fugacity in subduction zone dehydration processes and carbonate mineral stability (L. Eberhard, D.J. Frost and C.A. McCammon)*

Serpentinisation is not only the main mechanism through which the oceanic lithosphere absorbs and subducts H_2O but the process also leads to oxidation of the lithosphere through the formation of magnetite and ferric iron in serpentine minerals and the release of hydrogen. This is a very important redox process with implications for both the crust and mantle. Recently, for example, the release of hydrogen in this way by the Archean continental crust was proposed as a mechanism which could have delayed the oxygenation of the atmosphere. Although studies of serpentinites show that the $Fe^{3+}/\Sigma Fe$ ratio can vary from 0.1 to 0.8 no thermodynamic data exist for the ferric iron serpentine end member and almost nothing is known about the effect of the ferric iron component on the stability of serpentinites. Significant disagreements between studies of the stability field of serpentine might be explained, for example, by differences in ferric iron concentrations. Changes in the partitioning of ferric iron with pressure could also lead to redox reactions with surrounding minerals, particularly carbonates.

In this study we focus on the stability of antigorite at subarc conditions as a function of fO_2 and bulk rock carbonate content. Experiments are performed in a multianvil apparatus over the antigorite stability field. Natural serpentinites are used as starting materials with initially high (0.6, Liguria) and low (0.3, Zermatt) $Fe^{3+}/\sum Fe$ ratios. In some experiments calcium carbonate is added to simulate the subduction of ophicarbonates and examine how dehydration influences carbonate stability. Iridium metal was added to some nominally unbuffered experiments to allow the oxygen fugacity to be determined, where as in other experiments the oxygen fugacity was fixed using powders of Ru + RuO_2 and Re + ReO_2 distributed throughout the sample. $Fe^{3+}/\sum Fe$ ratios of antigorite in the recovered samples are measured using Mössbauer spectroscopy.

During experiments run for approximately 3 days it was possible to change the $Fe^{3+}/\sum Fe$ ratios of the starting materials to both higher and low ratios. As shown in Fig. 3.2-15 a wide range of ratios were achieved across a significant range of oxygen fugacity. Experiments were performed at 500 °C which is inside the stability field of antigorite, but also at 550-600 °C where antigorite starts to dehydrate. What is particularly intriguing is that the dependence between the $Fe^{3+}/\sum Fe$ ratio and the oxygen fugacity seems to be very dependent on this temperature change, with $Fe^{3+}/\sum Fe$ ratios decreasing sharply at the same oxygen fugacity as dehydration commences. This behaviour should cause the oxygen fugacity within subducting lithosphere to increase as dehydration takes place. On the other hand the stabilisation of ferric

iron in antigorite at high oxygen fugacities appears to have a minimal effect on the temperature of dehydration.

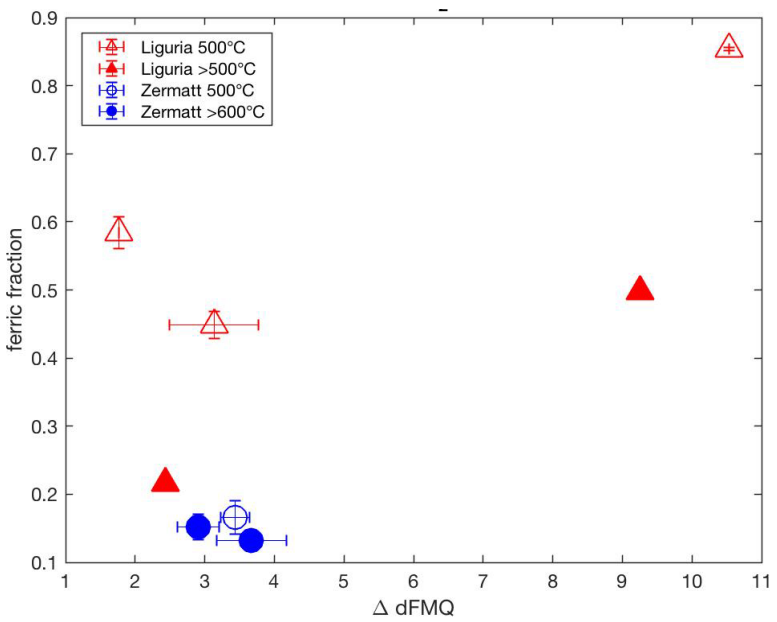

Fig. 3.2-15: $Fe^{3+}/\sum Fe$ ratios of antigorite samples as a function of oxygen fugacity normalised to the fayalite-magnetite-quartz (FMQ) oxygen buffer.

o. *Experimental constraints on the role of fluids in subduction zone magma generation (G. Rustioni, A. Audétat and H. Keppler)*

Understanding of the formation of arc magmas is fundamental to better constrain the origin of the continental crust and the cycling of volatiles in subduction zones. Current models agree that these magmas are produced by partial melting of the mantle wedge, but the composition and nature of the slab-derived, mobile phase that metasomatizes the mantle and causes melting is still controversial. Originally, the metasomatizing agent was proposed to be an aqueous fluid released by the breakdown of hydrous minerals contained in the slab. More recently, alternative models have been proposed that involve a hydrous melt produced by direct melting of subducted sediments to explain the trace element enrichment observed in arc magma. In some of these studies it was argued that hydrous fluids may be "too dilute" to produce this trace element enrichment. However, this argument may not be valid if the effect of Cl on the trace element solubility in aqueous fluids is taken into account.

The influence of fluid salinity on the partitioning behaviour of trace elements between aqueous fluids and eclogitic minerals at subduction zone conditions was investigated by piston cylinder experiments conducted at 4 GPa and 800 °C. The initial composition of the fluids ranged from pure water to 15 wt. % of NaCl, covering the most common salinities observed in subduction zone fluids. A MORB glass was used as starting material, which

produced in all experiments an eclogitic mineral assemblage consisting of omphacite, garnet and accessory kyanite and rutile. A diamond powder layer was also added in the central part of the capsule to provide a pore network in which the fluid was able to equilibrate during the experiments. Accordingly, it is reasonable to assume that any solid phase present in this "diamond trap" represents a fluid component that precipitated upon quenching. It is therefore possible to directly obtain the original composition of the fluid at high pressure and temperature by analyzing the diamond layer with Laser-Ablation Inductively-Coupled-Plasma Mass-Spectrometry (LA-ICP-MS). Also the composition of the minerals was analyzed by LA-ICP-MS in order to calculate trace elements fluid/eclogite partition coefficients (Fig. 3.2-16).

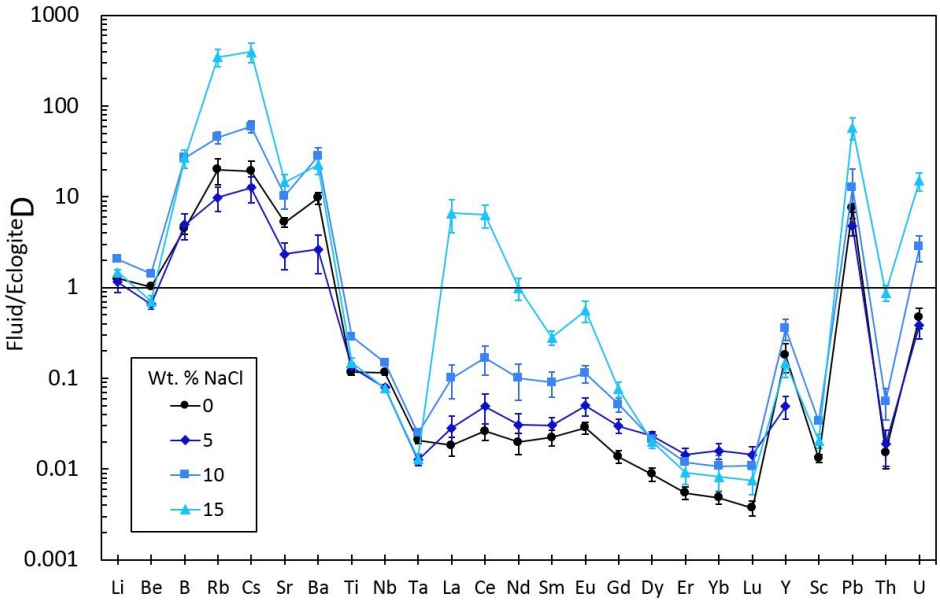

Fig. 3.2-16: Fluid/eclogite partition coefficients from four diamond trap experiments conducted at 4 GPa and 800 °C with different initial fluid salinity.

The results show that fluid salinity strongly enhances trace element solubility. This effect is particularly pronounced for Large-Ion Lithophile Elements (LILE) and Light Rare Earth Elements (LREE), for which the fluid/mineral partition coefficients may increase up to three orders of magnitude. Moving towards Heavy Rare Earth Elements (HREE) the partitioning behaviour seems to be less affected by the addition of Cl, and the High-Field Strength Elements (HFSE) solubilities show no significant dependency on fluid salinity. These observations are in perfect agreement with features typically observed in arc magmas, such as the relative enrichment in fluid-mobile elements like Rb and the negative Nb-Ta anomaly. Overall, this study shows that Cl-bearing aqueous fluids are an efficient carrier of trace elements at subduction zone conditions and that they can explain the development of the characteristic trace element signature of arc magmatism. It is therefore suggested that slab-derived saline fluids are the main metasomatizing agent, and that slab melting of sediments is a process of only local importance.

p. *Multiple episodes of metasomatism of the sub-arc mantle by slab partial melt: Insights into intermediate to hot subduction zones (A.M. Rebaza, A. Mallik/Providence and S.M. Straub/ Palisades)*

Subduction-related magmas have distinct major and trace element compositions compared to lavas from other tectonic settings, such as, high-water contents, and relative enrichments of fluid-mobile LILEs and LREEs. Although subducted sediments have similar incompatible trace element patterns, it remains unclear whether arc magmas inherited their specific trace element signature from recycled sediments or from other processes.

In this study, we explore the possibility of producing the compositional range of arc magmas by assuming a scenario where multiple episodes of metasomatism occur at the slab-mantle interface. A natural rhyolite, JR-1 (0.7 wt. % trace of the following elements added: Sc, V, Co, Ni, Cu, Zn, Ga, Ge), and a synthetic KLB-1 composition (10 wt. % H_2O added) were the starting materials employed to be representative of the initial composition of the hydrous slab-derived partial melt and the mantle wedge, respectively. The water content of JR-1 (123 ppm) was measured with FTIR-technique. The experiments were carried out at a pressure (P) of 3 GPa for periods of 7 to 9 days, using a piston cylinder device. P and H_2O content were kept constant, while temperature (800 °C and 950 °C) and the rock:melt ratio were varied. A double-capsule-setup of Au_{80}-Pd_{20} was used and filled with the same starting material with the aim to minimize H_2O and Fe loss (Fig. 3.2-17). Mass balance calculations were employed to obtain the respective residual bulk composition in each experiment and to estimate the mass proportions of the phases. In the first experiments KLB-1 and the JR-1 melt were mixed in different ratios (75:25 wt. % or 50:50 wt. %). These experiments produced a reacted melt (melt 1) and a solid residue (R1). A second set of experiments reacted R1 with JR-1 in different ratios (75:25 or 50:50) to produce reacted melt 2 and a second residue (R2). In a third set of experiments R2 was reacted with JR-1 (75:25 or 50:50) to produce reacted melt 3 and a third residue (R3).

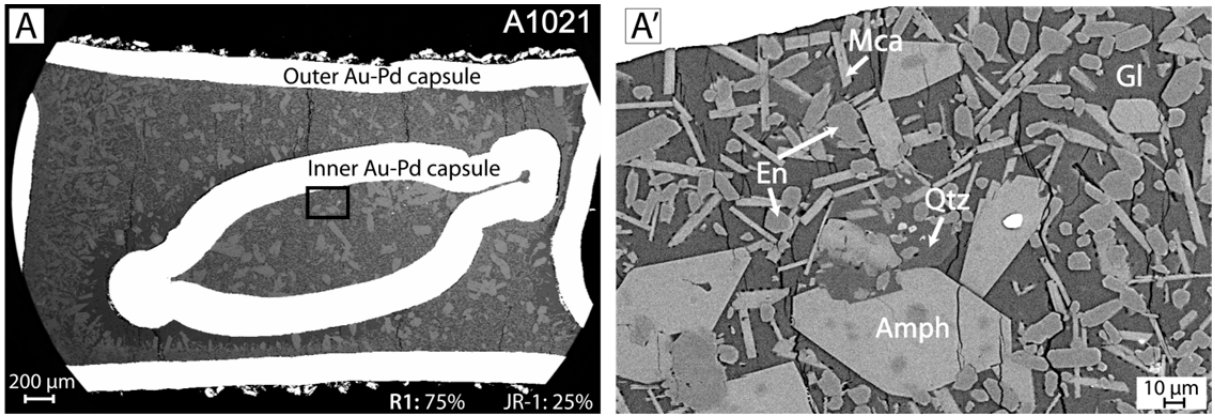

Fig. 3.2-17: SEM photomicrographs of the experimental run product of run A1021, which was performed at 3 GPa and 800 °C (10 wt. % H_2O). (A) Image of the double-capsule setup; (A') Magnified image of the area marked in A. Mca: mica; En: enstatite; Qtz: quartz; Amph: amphibole; Gl: glass.

Electron microprobe analyses (EMPA) of the experimental products show that the progressively reacted melt preserves its rhyolitic composition (72 to 80 wt. % SiO_2) and shows increasing concentrations of alkalis and aluminium. The melts produced at 800 °C and a rock:melt ratio of 75:25 follow a similar trend for alkalis and alumina as natural arc lavas found in the Pacific Ring of Fire (Fig. 3.2-18). The alkali elements (Na_2O and K_2O) in the melts are supplied by the occurrence of abundant K-mica, amphiboles, Na-pyroxenes, and by the new influx of hydrous rhyolitic partial melt rich in alkalis. However, the experimental rhyolitic melts are depleted in MgO, CaO, and FeO relative to erupted arc magmas, suggesting that these elements, in a natural case, may be supplied by the interaction with the hotter mantle wedge (> 1200 °C) in their later ascent through the mantle wedge. The study of trace element abundances by means of LA-ICP-MS may help to further constrain this model of magmatic differentiation and to examine whether this process of multiple metasomatism can preserve the trace element signature observed in natural arc lavas.

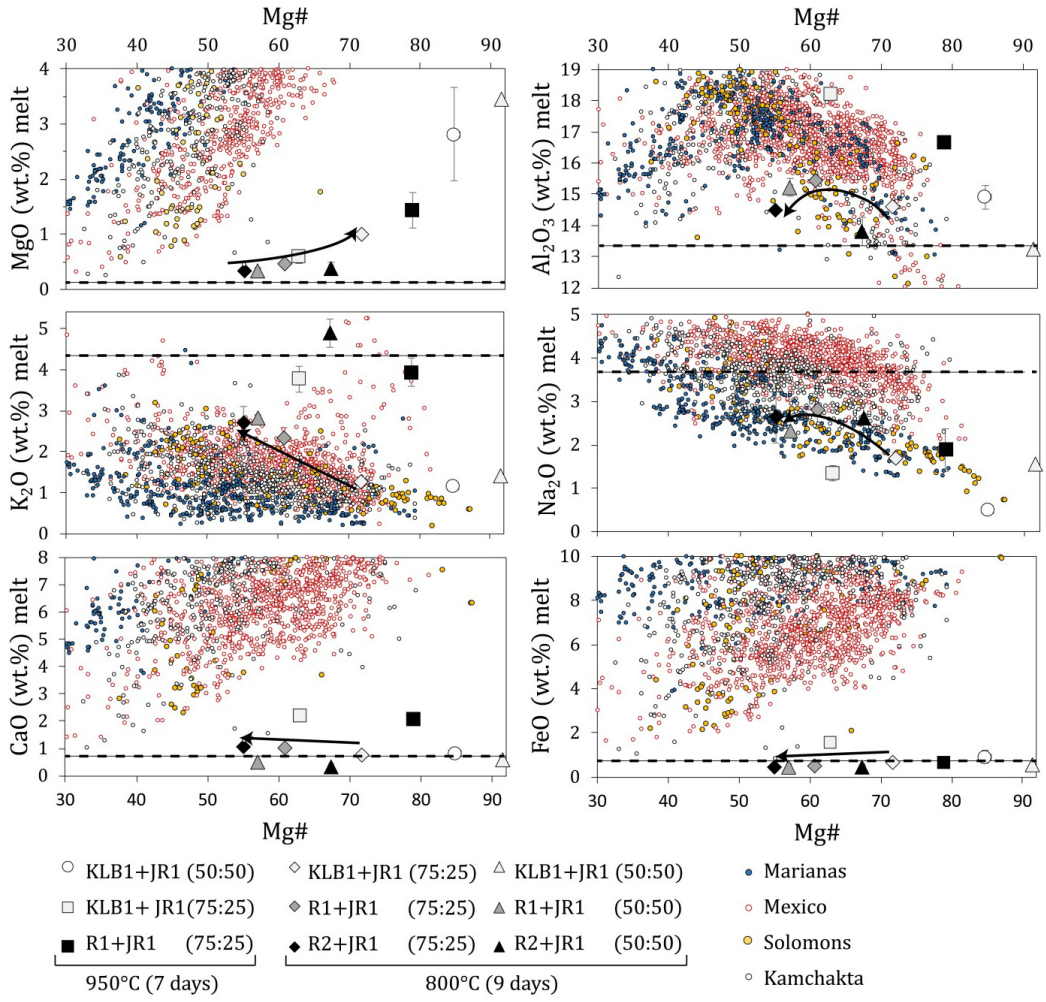

Fig. 3.2-18: Mg#-major element diagrams for the 9 experiments performed at 3 GPa and at temperatures of 950 °C and 800 °C with two rock-melt ratios of 75:25 and 50:50. The major elements of the experimental melts are normalized to 100 %. Dashed horizontal line corresponds to the JR-1 element oxide concentration. The continuous black arrow indicates the direction of evolution for the set of experiments at 800 °C with a ratio of rock-melt 75:25.

q. *The stability of $MgCO_3$ under iron-saturated lower mantle conditions (F. Maeda/Sendai, N. Miyajima, S. Kamada/Sendai, N. Hirao/Hyogo, S. Petitgirard/Zurich, C.A. McCammon, D.J. Frost and S. Khandarkhaeva; T. Sakamaki and A. Suzuki/Sendai)*

Knowledge of the nature of potential carbon hosts in the Earth's deep interior is crucial for understanding the global carbon cycle from the Earth surfaces to its core. Carbonates are oxidized carbon-bearing components of subducted and deeply subducted slabs in the Earth's interior. $MgCO_3$ (magnesite) in particular has been considered to be stable down to the lowermost mantle because both its melting and decarbonation temperature are higher than the mantle geotherm. Furthermore, magnesite has been reported to transform to several $MgCO_3$ high-pressure polymorphs under deep lower mantle conditions, which can enhance its preservation. On the other hand, reduced conditions in the lower mantle can stabilize metallic iron and lead to the breakdown of $MgCO_3$ to diamond or iron-carbide through reactions involving iron. It is therefore of interest to investigate the stability limit of $MgCO_3$ at P–T–fO_2 conditions corresponding to the lower mantle.

We investigated the reaction between $MgCO_3$ and Fe under lower mantle conditions by combining synchrotron X-ray diffraction (XRD) techniques and a transmission electron microscope (TEM). The lower-mantle P–T–fO_2 conditions were simulated using a laser-heated diamond anvil cell (LHDAC) incorporating a micro-iron capsule. The high P–T experiment was conducted at ~ 100 GPa and 1720-2150 K at beamline BL10XU of SPring-8 using ~ 30-keV monochromatic X-rays. The total heating duration was 157 minutes. The sample was recovered from the LHDAC to ambient conditions and observed using a TEM operated at 200 kV at BGI. The TEM lamella was prepared using a focused ion beam (FIB) system. Qualitative chemical analysis and elemental mapping were also conducted by combining energy dispersive X-ray spectroscopy (EDXS) with a scanning TEM. Powders of natural magnesite ($Mg_{0.994}Ca_{0.003}Fe_{0.003}CO_3$) from Bahia in Brazil and reagent-grade MgO were loaded into a miniature iron capsule (~ 15 μm in diameter and 7 μm in thickness) fabricated from iron foil (Inset in Fig. 3.2-19a). This micro-iron capsule was used in order to decrease thermal gradients in the sample chamber and to achieve reducing conditions below the iron-wustite fO_2 buffer. The iron capsule was surrounded by an MgO pressure medium in the sample chamber.

The diffraction pattern in Fig. 3.2-19 was acquired at 113(1) GPa and room temperature after laser heating at 2150(80) K for 37 minutes. Fe_7C_3 was observed as a product of the reaction between $MgCO_3$ and Fe. Several diffraction peaks are not from orthorhombic or hexagonal Fe_7C_3 and can be explained by $P\bar{1}$ triclinic carbonate, which is one of the high-pressure polymorphs of $MgCO_3$. The TEM image of the recovered sample shows that the iron capsule became severely deformed at high pressure (Fig. 3.2-20a). The inside of the capsule appears to be divided into Fe-rich and Fe-poor zones based on the TEM image and element maps (Fig. 3.2-20). Fe-C compounds and diamond are observed as carbon hosts in the Fe-rich and Fe-poor zones, respectively. EDXS analysis shows no evidence of carbonates in the capsule. The

difference between XRD and TEM results regarding carbonate existence could be caused by variations in the carbonate distribution in the capsule due to severe deformation of the capsule. Otherwise, the diffraction peaks from high-pressure carbonate may arise from other unknown phases: some SiO_2 contamination was detected by EDXS in the capsule and hence the diffraction patterns could reflect silicates phases. The formation of diamond is possibly related to a reaction between $MgCO_3$ and SiO_2 to produce bridgmanite and diamond, which could occur even at higher fO_2 conditions than those expected for the direct breakdown of magnesite to diamond.

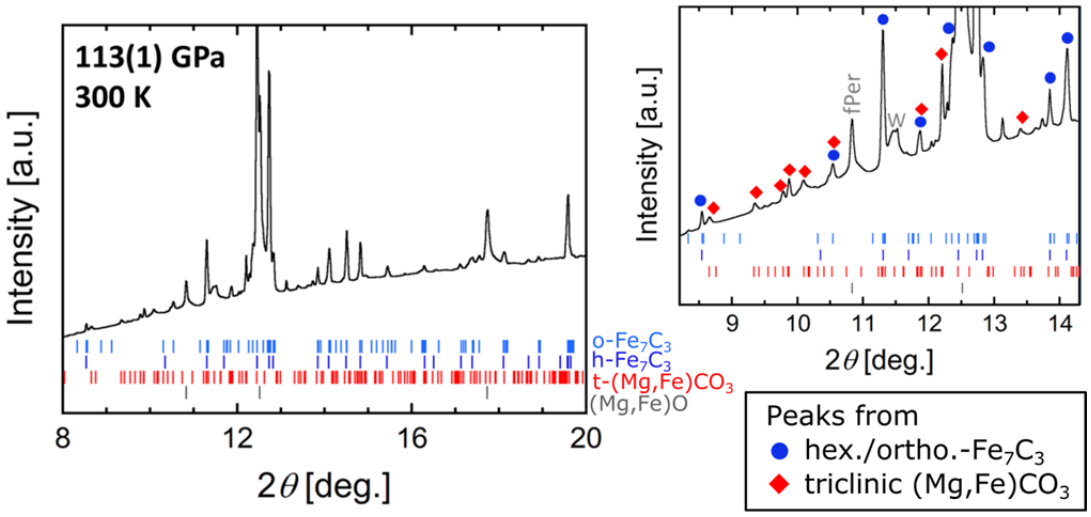

Fig. 3.2-19: Synchrotron XRD pattern acquired at 113 GPa and room temperature after laser heating at 2150 K. The abbreviations are as follows: o-Fe_7C_3: orthorhombic Fe_7C_3; h-Fe_7C_3: hexagonal Fe_7C_3; t-$(Mg,Fe)CO_3$: triclinic high-pressure carbonate. An enlarged region is shown on the right.

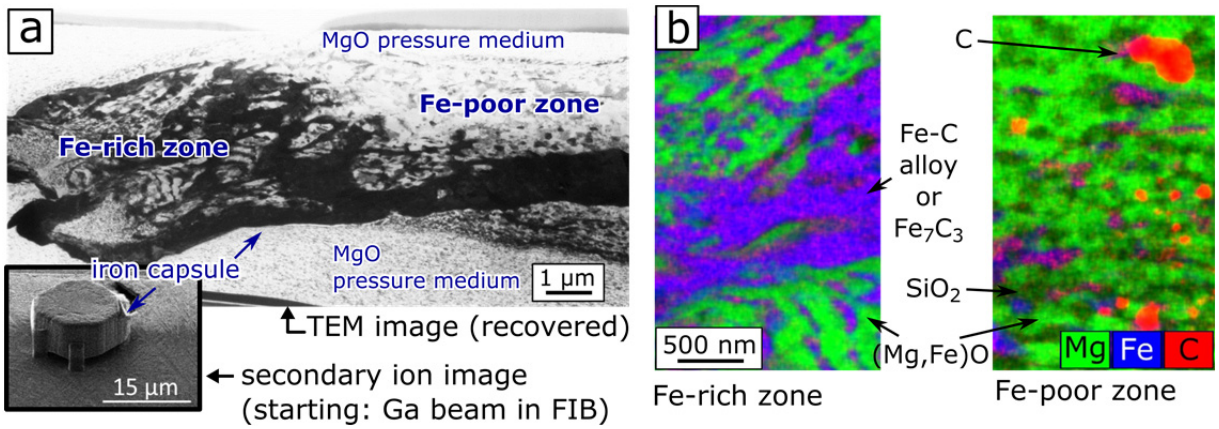

Fig. 3.2-20: (a) TEM image of the recovered sample, and secondary ion image of the starting capsule (inset). The latter was acquired using a Ga ion beam when making the capsule using the FIB. (b) Elemental map acquired using STEM-EDXS, showing Fe-rich and Fe-poor zones within the recovered sample.

r. *Are there magmatic controls on the Cu/Au ratio of porphyry-type ore deposits? (B. Rottier and A. Audétat; P. Koděra and J. Lexa/Bratislava)*

Most of the world's supply of Cu, Mo, and Au stems from porphyry-type ore deposits. Porphyry-type ore deposits are found in subduction and post-subduction settings where magmatism is abundant, but only a small fraction of these magmas generate porphyry deposits. The factors controlling the fertility (*e.g.*, the capacity to form a deposit) of a magmatic system is a long-standing research subject. It is thought that the mineralization potential of magmatic systems is to a large degree acquired within the crust. Among the potential factors, magmatic sulphide saturation is proposed to have either a negative or a negligible impact on the fertility. Magmatic sulphides strongly sequester chalcophile elements such as Cu, Au, Ag, PGEs, Se, and Te, resulting in a strong depletion of these elements in the residual melt upon differentiation. Therefore, removal of such sulphides through the formation of cumulate rocks should strongly reduce the magma fertility. However, magmatic sulphides could simply act as an intermediate, neutral storage medium, from which ore metals are subsequently remobilized either by sulphur under-saturated melts or by magmatic volatiles. Sulphide saturation appears to be a common, if not unavoidable mechanism during the evolution of arc magmas. In addition, several studies suggest that the Cu/Au ratio of the mineralizing fluids and of the bulk ores of porphyry deposits are also controlled by crystallization/dissolution of magmatic sulphides. However, even if the scientific community is becoming increasingly aware of the potential role of magmatic sulphides, only few studies are focused on this subject, mainly because of the difficulty to recognize and to accurately quantify magmatic sulphides.

This project is focused on two adjacent volcanoes located in Slovakian volcanic field in Central Europe that belong to the Carpathians arc: the Jarovie and the Štiavnica volcanoes (Fig. 3.2-21). The Jarovie volcano hosts several small Au porphyry deposits characterized by extremely low Cu/Au molar ratios (< 3100). The Štiavnica volcano hosts a small Au porphyry deposit (Beluj) and also a more classical Cu-Au porphyry deposit (Zlatno) that has a Cu/Au molar ratio of ca. 12500. For both volcanoes we studied pre-, syn-, and post-ore volcanic and intrusive rocks (around 60 samples in total). Temperature, pressure, and oxygen fugacity of these magmas were constrained by using a variety of geothermobarometers and oxybarometers. In addition, the composition of unexposed silicate melt (n=407) and sulphide inclusions (n=243) trapped in the different phenocrysts forming these rocks were determined by LA-ICP-MS.

The obtained data suggest that both volcanoes were fed by transcrustal crystal mush systems, where differentiation, crystallization, and stagnation of the magmas occurred mainly in a shallow crustal chamber (1-3 kbar). Both volcanoes are characterized by a relatively low oxygen fugacity ΔNNO $\pm$ 0.5 and were sulphide saturated during their entire history, which means that that the attainment of sulphide saturation in the magma chambers did not suppress the fertility of the two magma systems. Another important outcome of this study is that the

Cu/Au molar ratios of the porphyry deposits were not already preset in the magmas, but were apparently acquired during the hydrothermal stage. The results further demonstrate that not only oxidized but also reduced magmas are able to form Au and Cu-Au porphyry deposits. The contrasting Cu/Au ratios of the porphyry deposits in the Štiavnica volcano appear to be controlled by the emplacement depths of the ore-related intrusive bodies, which themselves are controlled by the dynamics of the upper crustal magma chamber. The Au porphyry deposits formed at shallow depth (< 1.5 km), and the ore-related intrusive rocks display strong evidence of mixing with mafic magma sourced from a lower crustal reservoir as indicated by the occurrence of mafic amphibole and clinopyroxene, and of magmatic garnet. This mixing took place in the upper crustal chamber (1-3 kbar) and occurred only shortly before the emplacement of the mixed magma at shallow level (< 0.5 kbar), indicating that the mixing triggered the emplacement of these magmas. The result was the exsolution of hot fluids at shallow pressure, which apparently was the key to form Au porphry deposits. In contrast, the intrusion that produced the Zlatno Cu-Au porphyry deposit was emplaced at greater depth (~ 1 kbar) and does not show any evidence for magma mixing. It formed when the upper crustal chamber was cooler (~ 750 °C) and fluid saturated. In this case, the emplacement of the ore-related intrusion is thought to have been triggered by the exsolution and accumulation of fluids in the upper crustal chamber. The Cu/Au ratio of porphyry-type ore deposits thus seems to be linked to the temperature and emplacement depth of the causative intrusions, factors which control the physical and chemical properties of the hydrothermal fluids.

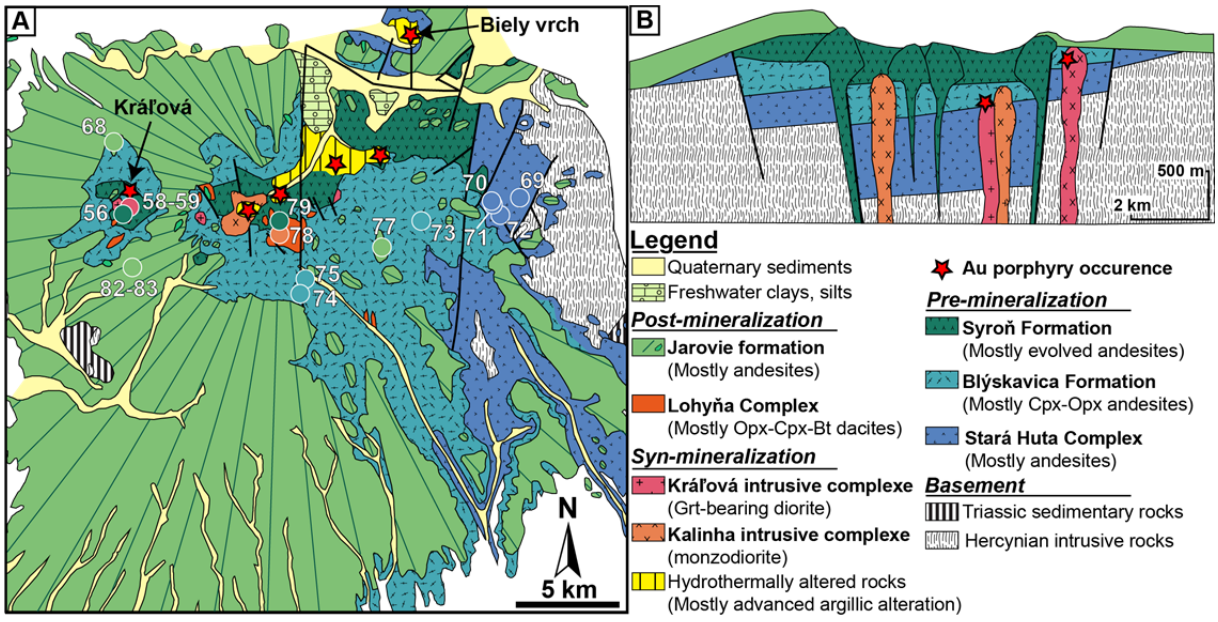

Fig. 3.2-21: A) Simplified geological map of the Jarovie volcano (modified from Konečný *et al.*, 1998; Geological Survey of Slovak Republic) and location of the studied samples and the main Au porphyry occurrences. B) Schematic cross-section of the Jarovie volcano showing the graben structure (modified from Koděra *et al.*, 2014; Geology 42: 495-498.)

s. *Geochemistry and crystallization conditions of magmas related to porphyry Mo mineralization in northeastern China (H.G. Ouyang and A. Audétat)*

In the past tens of years, China has emerged as the country with the largest Mo reserves in the world (8.3 Megatons). However, most Chinese porphyry Mo deposits are difficult to classify using the existing classification schemes. Although much has been learned about the genesis of Climax-type porphyry Mo deposits through the analysis of melt inclusions, relatively little is known about the nature of the mineralizing melts in Chinese porphyry Mo deposits. Furthermore, it is not certain whether the model of volatile transport in convecting magma columns that has been proposed for Climax-type porphyry Mo deposits is applicable also to Chinese porphyry Mo deposits because corresponding key information on the geochemistry and crystallization conditions of magmas from Chinese porphyry Mo deposits are missing. In this study we aim to close this gap by characterizing the major element-, trace element-, and volatile element content of melt inclusions from eight syn-mineralization and two pre-mineralization magmatic units in six porphyry Mo deposits in northeastern China (Aolunhua, Hashitu, Lanjiagou, Songbei, Wanbaoyuan, Yangjiazhangzi).

All of the analysed melt inclusions are high-silica rhyolitic in composition. Those melts that most closely approach the composition of bulk magmas are 1-2 times more evolved than average granite, containing 2-11 ppm Cs and 150-390 ppm Rb, except for those from Hashitu, which contain 10-28 ppm Cs and 200-500 ppm Rb (Fig. 3.2-22). In the Rb vs Y + Nb tectonic discrimination diagram the melt compositions straddle along the border between the field of syn-collisional granites and the fields of volcanic arc, and within-plate granites. All melts are rather Mo-poor, with most values falling between 1 and 7 ppm. Fluorine concentrations in the ore-forming melts were considerably lower than in those that formed Climax-type deposits, with the melt inclusions from Hashitu containing max. 0.4 wt. % F and the others < 0.1 wt. %. Water contents are high in the fertile magmas at Hashitu and Yangjiazhangzi (5.0-7.0 wt. % H_2O), and slightly lower at Wanbaoyuan (4.0-5.2 wt. % H_2O).

Based on zircon saturation thermometry combined with TitaniQ thermobarometry, ore-forming intrusions tend to record lower crystallization temperatures than cogenetic barren intrusions in the same deposit (695-720 °C vs. 729-789 °C at Yangjiazhangzi; 708-711 °C vs. 739-758 °C at Lanjiagou; and 695-715 °C vs. 698-771 °C at Wanbaoyuan), whereas recorded pressures are similar. At Hashitu, both ore-related and barren intrusions record similar *P-T* conditions (740-770 °C and 1.0-2.0 kbar, vs. 730-760 °C and 1.0-2.8 kbar), and log fO_2 was around QFM+0.7. Calculated magma viscosities for the ore-related magmas at Hashitu, Yangjiazhangzi, and Wanbaoyuan are 4.3-5.1 Pa s, 4.9-5.6 Pa s, and 5.8-6.1 Pa s, respectively (Fig. 3.2-23), which is at the lower end of the values published for non-mineralized magma systems.

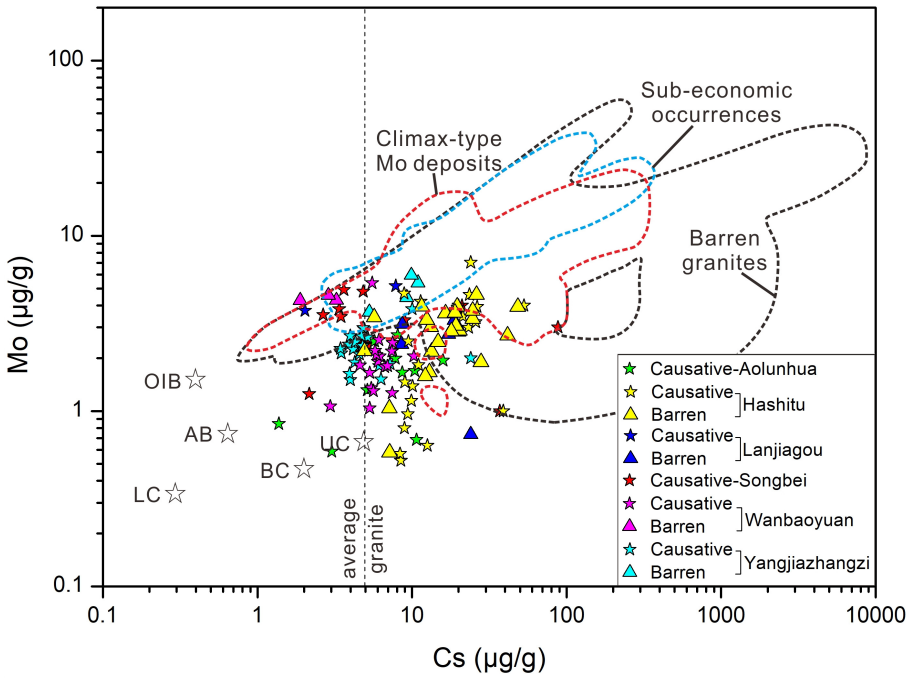

Fig. 3.2-22: Molybdenum vs. Cs concentrations in melt inclusions from the porphyry Mo deposits in this study, compared to melt inclusion data from Climax-type porphyry Mo deposits, sub-economic occurrences, and barren granites.

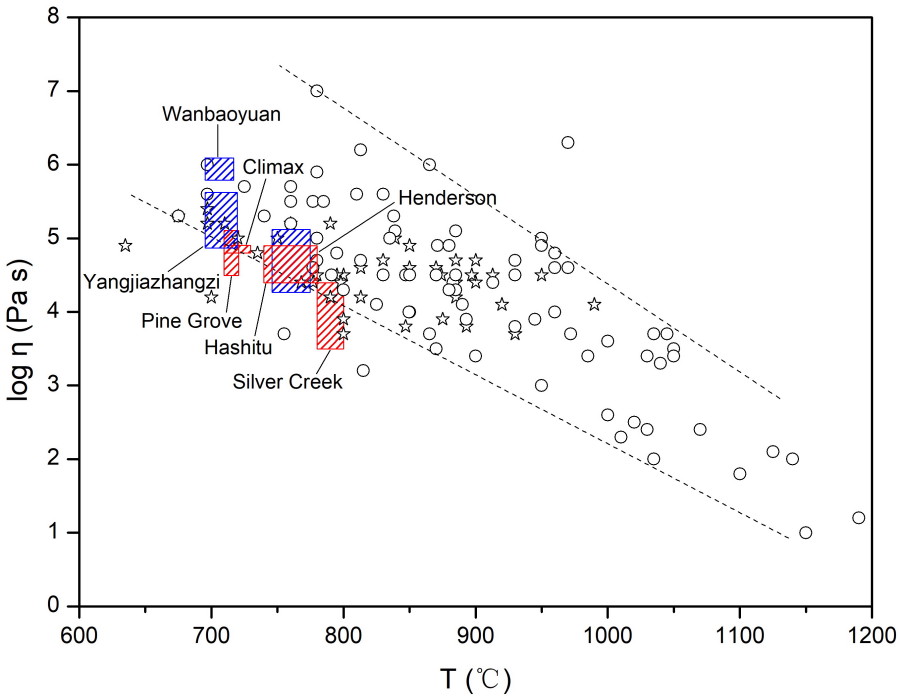

Fig. 3.2-23: Estimated viscosities of the melt inclusions from the samples in this study (blue boxes) compared to estimates for melt viscosities in Climax-type porphyry deposits (red boxes). The pre-eruption magma viscosities of extrusive mafic to felsic magmas (circles) and intrusive magmas (stars) are shown for comparison. The dotted lines indicate the upper and lower limits of the viscosity of extrusive mafic to felsic magmas.

The results of this and previous studies suggest that porphyry Mo deposit formation requires neither unusually high Mo concentrations in the silicate melt nor in the exsolving fluids, nor does it require unusually high F concentrations. The oxygen fugacity of the magma does not seem to be a critical factor either. What is common to all types of porphyry Mo deposits is (i) the presence of structures that led to focused fluid flow (stockwork veining or breccia pipes), (ii) that the mineralizing magmas were mostly rhyolitic in composition, and (iii) that the magmas were fluid-saturated at the time of intrusion. The key to porphyry Mo formation thus likely lies in the factors that control the segregation of evolved, fluid-saturated melts from larger precursor plutons and those that control the efficiency of fluid focusing into smaller rock volumes. Potential factors include the depth of magma emplacement, the shape of the intrusive body, the nature of the country rock, the tectonic stress regime, the magma viscosity, and the magma chamber dynamics (*e.g.*, replenishment events).

t. *The behaviour of Mo during the crystallization of deep-seated plutons: A melt and fluid inclusion study (J. Chang and A. Audétat)*

Recent melt inclusion studies suggest that the ore-forming magmas of Climax-type porphyry Mo deposits were not particularly enriched in Mo compared to similarly evolved magmas in barren and subeconomic systems. Efficient extraction of fractionated residual melts and their accumulation in the apical part of large, middle- to upper crustal magma chambers (> 5 km below the surface) was proposed to be the most important requirement for the formation of economic deposits in the shallow crust (2-5 km). H_2O ± F contents could have played a crucial role in efficient crystal-melt segregation by controlling melt viscosity. As the H_2O solubility in silicate melts strongly depends on pressure, the emplacement depth of magma chambers may have a strong influence on the ore-forming potential. In this study, we performed petrographic studies and quantitative analyses of melt- and fluid inclusions in quartz phenocrysts, matrix quartz, granophyric quartz and pegmatitic quartz from the top of the barren Mineral Mountain and Spirit Mountain granite plutons in southwestern USA.

Microthermometric results of fluid inclusions coexisting with melt inclusions at Mineral Mountain suggest that the top of the granite pluton crystallized at a temperature of 650-670 °C and a pressure of 2.8-3.1 kbar (corresponding to a depth of 10-12 km based on an average upper crustal density of 2.7 g/cm^3). These results are consistent with estimations derived from zircon saturation thermometry (640-710 °C) and Ti-in-quartz thermobarometry (2.4-3.8 kbar) at Mineral Mountain. Similarly, samples from the top of the Spirit Mountain Pluton returned zircon saturation temperatures of 640-750 °C and Ti-in-quartz pressures of 2.6-4.1 kbar. Electron microprobe analyses of re-homogenized melt inclusions from both granite plutons suggest that the melt inclusions contain 6-8 wt. % H_2O, < 0.9 wt. % F and < 0.3 wt. % Cl. The high H_2O content in silicate melts confirms the relatively deep crystallization conditions of these plutons.

Interestingly, variously evolved melt inclusions from both plutons contain constant or slightly decreasing Mo contents with increasing degree of magma fractionation (the latter approximated by Cs contents), which contrasts with the generally increasing Mo concentrations observed in shallower granites (*e.g.*, Treasure Mountain Granite, Rito del Medio Pluton, and Stronghold Granite; Fig. 3.2-24). Quantitative modeling results suggest that the lack of Mo enrichment in the residual melts at Mineral Mountain and Spirit Mountain is due to the relatively high crystallization pressure of these magmas, as the extraction efficiency of Mo into the exsolving fluid phase depends critically on the melt water content. Whether or not fluid exsolution from such relatively deep plutons can have any influence on the Mo mineralization potential at shallower levels is not yet clear at the moment.

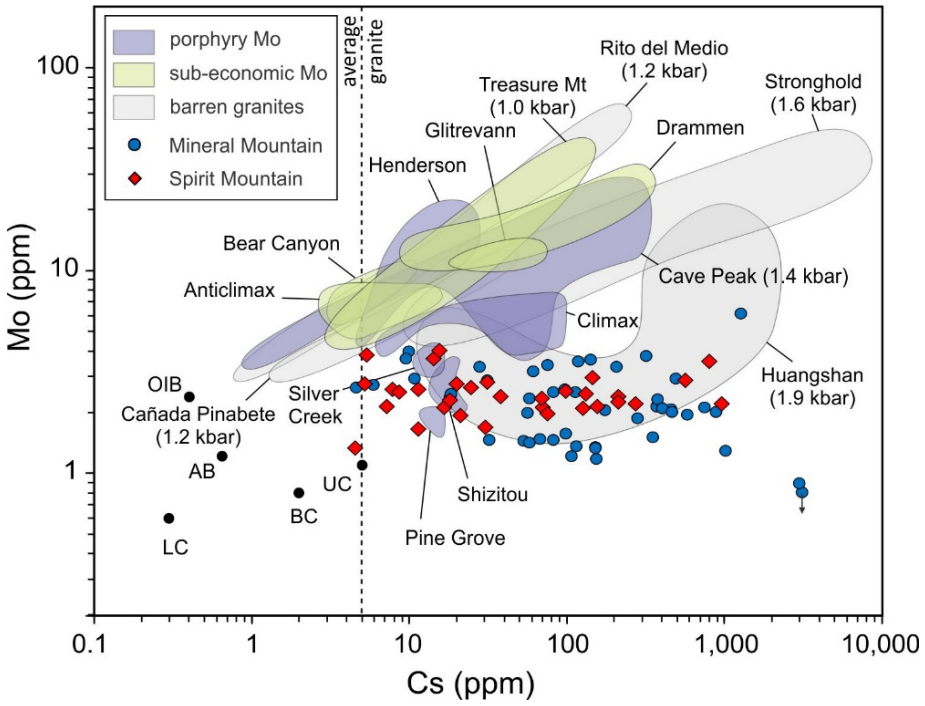

Fig. 3.2-24: Cs vs. Mo systematics of melt inclusions from Mineral Mountain and Spirit Mountain, compared to similar data obtained from variously mineralized other plutons. Pressures in parentheses were estimated from coexisting melt inclusions and fluid inclusions in miarolitic cavities at the top of the plutons. Notice the lack of Mo enrichment with increasing degree of magma fractionation at Mineral Mountain and Spirit Mountain.

3.3 Mineralogy, Crystal Chemistry and Phase Transformations

The solid Earth largely consists of minerals, *i.e.*, naturally formed crystalline substances. Their chemical composition and structure determine the properties and the behaviour of our planet. The contributions in this chapter investigate the structural changes of important Earth minerals under varying external parameters such as temperature, pressure, oxygen and water fugacity. The goal is to experimentally constrain the structure of the deep Earth's interior and to use such knowledge to decipher the evolution processes inside the Earth from the analysis of naturally occurring minerals.

Solid state diffusion is an important mechanism for chemical exchange in minerals and rocks at high temperature (and pressure) and it is used as a ratemeter as well as an indicator of temperature. In the first contribution of this chapter the diffusive exchange of Fe-Mg between different pyroxenes is experimentally investigated with the aim to improve this commonly used geothermometer. First results indicate that chemical equilibration occurs by a different route than commonly assumed involving not only interdiffusion but the complete recrystallization of grains with new compositions. In the following report the influence of water fugacity on the formation of pargasite in the upper mantle was investigated, yielding that saturated water conditions are necessary to form this hydrous mineral whereas a water fugacity of 0.1 was not sufficient. Pargasite is the main carrier of water in upper mantle rocks and the results indicate that its formation is restricted to particularly water-rich zones in the upper mantle, *e.g.*, in the vicinity of subducting slabs. In the third contribution the possibility of forming phases with the general composition $Ca_xAl_yFe_zO_w$ was tested at pressures corresponding to the mantle transition zone and upper lower mantle; a previously unknown phase with the composition $Ca_2Al_6O_{11}$ has been identified and characterized as a structure potentially present in the lower mantle.

The Fe-O system is of particular importance in the solid Earth since, due to the different oxidation states of iron, it directly interacts with the oxygen fugacity in the rock. The following six contributions are all related to this topic. In the first report the stability field and structure of the Fe_5O_6 phase was determined, indicating that it could be a stable phase along the mantle adiabat into the upper portions of the lower mantle. The following contribution explores the substitution of some of the Fe^{2+} by Mg^{2+} in the Fe-O-type phases and presents the crystal structure of $Mg_{0.9}Fe_{8.1}O_{11}$ synthesized at 12 GPa and 1300 °C. In the next report the interaction of bridgmanite $(Mg,Fe)(Al,Si)O_3$ with the oxygen fugacity of the lower mantle is explored experimentally. The results show that the $Fe^{3+}/\sum Fe$ ratio of bridgmanite is not independent of oxygen fugacity, but the gradient of this dependence become flatter with increasing Al content in bridgmanite. The following contribution reports a thermodynamic model aimed at constraining the P, T, fO_2 dependence of ferric iron in ferropericlase based on a set of experiments in a range of 6-25 GPa and 1200-1800 °C to shed light on the formation conditions of ferropericlase diamond inclusions. The crystal structure of Fe_2O_3 at extreme pressures of up to over 200 GPa was explored in the next study. At room temperature Fe_2O_3 is stable in the post-perovskite structure at these extreme pressures, laser heating however leads to oxygen loss and the formation of more reduced phases with different stoichiometries.

Besides Fe-O compositions also Fe-O-H components are of great interest since their potential high-pressure stability offers a pathway for deep recycling of water into the Earth's mantle. The ninth contribution of this chapter focuses on the stability of δ phase-type structures in the system AlOOH-FeOOH-$MgSiO_2(OH)_2$ which could be synthesized at 21 GPa and 1480 K, making them viable candidate minerals for transporting water (or better H) into the lower mantle. Pressurizing pure FeOOH in the diamond anvil cell to pressures corresponding to 1800 km depth yielded a transition from goethite to pyrite-type structure as shown in the tenth report. Laser heating however caused loss of hydrogen and oxygen and the formation of various Fe-O compositions, indicating that pure FeOOH is not a suitable candidate phase for hydrogen transfer into the deep Earth.

The uppermost part of the Earth's solid iron core shows unexpectedly low seismic shear velocities with respect to those predicted from mineralogical studies. A possible reason might be the so-called pre-melting effect, which predicts that solids close to their melting point display a significant decrease in elastic shear strength. In the third to last contribution, pre-melting effects have been demonstrated in a single crystal of Neon which has been used as an analogue material for iron at extreme conditions. A decrease in elastic constants and anisotropy has been observed near the melting point at ~ 7 GPa in a diamond anvil cell. The second to last contribution in this chapter reports the first synthesis of the elusive water ice X phase in the diamond anvil cell. With the help of a NMR microprobe the symmetrization of the H bond has been observed above 60 GPa. The final contribution presents insights about dehydration processes of minerals in chondritic meteorites which are considered to be the oldest material of our solar system. The aim is to reconstruct the effects of impact processes on the meteoritic parent bodies with stepped heating experiments in order to determine the pristine mineralogical composition after the condensation of the solar nebula. The resulting mineral compositions from this study can then be compared with the mineralogy of samples brought back from missions to comets and asteroids.

a. *Mechanism of element exchange between solid phases – a case study using Fe-Mg exchange between ortho- and clinopyroxenes (J. Primocerio, S. Chakraborty and T. Fockenberg/Bochum, in collaboration with K. Marquardt)*

Knowledge of temperatures and durations of geological processes play an important role in our understanding of the Earth's history. Pyroxenes and Garnets are mineral groups that are found frequently in terrestrial and extraterrestrial rocks, and their diffusive properties have been used widely for the determination of temperatures and durations of geological processes. The nature of element partitioning and diffusion in these minerals is however difficult to ascertain due to the complexity of the interactions involved. Recent technological developments such as the ability to produce thin films of silicates using pulsed laser deposition (PLD) and to analyse chemical concentrations as well as structural features on submicron scales (*e.g.*, analytical transmission electron microscopy, ATEM) now make it possible to determine coefficients of element diffusion and partitioning with better precision.

Our aim is to study the partitioning and diffusion of Fe-Mg in the garnet – pyroxene system using both PLD and ATEM. So far, we have carried out experiments using orthopyroxene – clinopyroxene pairs at high pressures (15 kbar) in a piston cylinder apparatus and at room pressure in gas mixing furnaces at temperatures between 900 and 1200 °C. Graphite or AuPd capsules as sample containers were used for the control of oxygen fugacity. The pyroxenes were present either as mixtures of pre-synthesised powders, or as thin films deposited on polished sample surfaces of natural pyroxene cubes of different compositions.

Our initial experiments have already revealed that the cation exchange in this system proceeds as a multistep process. It is generally assumed that the compositions at the interface between the two pyroxene solid phases attain equilibrium instantaneously, and then the bulk of the crystals equilibrate by diffusion. Our observations indicate that the samples follow a different path toward equilibrium. Element exchange is coupled with recrystallization and grain growth whereby the rim composition evolves only partially toward the equilibrium composition, followed by diffusion to some extent until the grain recrystallizes to a new composition. The process is repeated until the equilibrium composition is attained. This gives rise to grains with a full range of compositions between the initial and the final equilibrium composition with each individual grain appearing homogeneous or only weakly chemically zoned (Fig. 3.3-1). This behaviour has important implications for the evaluation of closure temperatures, apparent temperatures calculated from geothermometers, and calculations of cooling rates and residence times in geospeedometry. Further experiments are in progress to quantify this process.

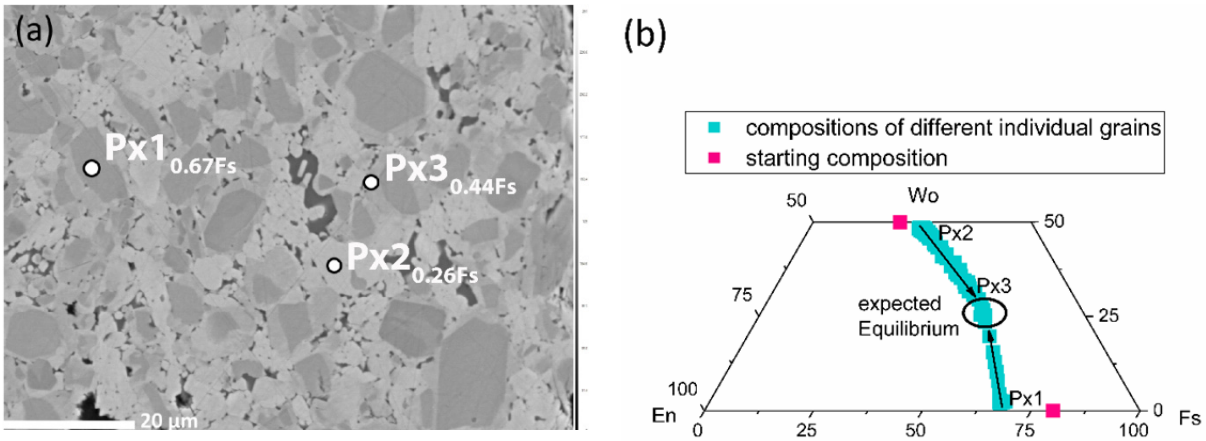

Fig. 3.3-1: a) BSE image of an experimental sample where pyroxenes of two compositions (shown by red squares in Fig. 3.3-1b) were annealed at 15 kbar and 900 °C for 168 h in a graphite capsule. The run product shows grains of different compositions (different brightness) – three of them have been labelled as examples: Px1: $En_{30}Fs_{67}Wo_3$, Px2: $En_{25}Fs_{26}Wo_{49}$ and Px3: $En_{23}Fs_{44}Wo_{33}$. b) Complete array of compositions (blue squares) measured across different grains all of which were homogeneous or only very weakly zoned (*e.g.*, see BSE image in Fig. 3.3-1a). The expected equilibrium composition is shown as a black ellipse.

b. *Pargasite stability in the upper mantle at H_2O-undersaturated conditions (M. Putak Juriček and H. Keppler)*

Amphibole is the most commonly occurring hydrous mineral in mantle xenoliths. The majority of upper mantle amphiboles have compositions close to the pargasite end-member. Previous experimental work has demonstrated that pargasite stability is sensitive to variations in bulk alkali and water content of the starting material. A comparison among studies using starting materials with different bulk alkali contents shows that addition of more alkali leads to stabilization of pargasite at higher *P* and *T*. The effect of water on amphibole stability is instead not so straightforward. At H_2O-saturated conditions, alkali elements partition strongly into aqueous fluid and thus become less available for the crystallization of amphibole. As a result, amphibole appears to become stable at higher *P* and *T* when less H_2O is added to the starting material. This observation led to the hypothesis that pargasite may be more ubiquitous in the upper mantle than previously thought and that it may be an important water-storing phase at depths to approximately 100 km. However, most of the previous work focused on pargasite stability at H_2O-saturated conditions, where pargasite and other nominally anhydrous phases coexist with an aqueous fluid during experiments. Since such environments are likely not representative of the 'ambient' upper mantle, which is believed to contain only several hundred ppm of H_2O, this study was undertaken to determine pargasite stability at H_2O-undersaturated conditions.

Because of the high specific surface area of powders, adsorption of atmospheric H_2O on fine-grained starting materials prevents attaining H_2O-undersaturation by simply adding small amounts of water to the sample. Instead, H_2O-undersaturated conditions may be precisely controlled by diluting the water in the sample with another component. Under such conditions, solid phases are expected to coexist with a low water activity fluid throughout the experiment. As molecular nitrogen is mostly insoluble in upper mantle minerals it can be reliably used to adjust the water activity of the fluid to a desired low value. A series of experiments were performed in an end-loaded piston cylinder apparatus. The samples for H_2O-undersaturated experiments were prepared by adding silver azide (AgN_3) and brucite to a synthetic peridotite mixture. During experiments AgN_3 thermally decomposes to metallic silver and molecular nitrogen while brucite dehydrates to introduce water to the sample. The amount of water was kept constant in all experiments (1 wt. %) and the molar fraction of water in the N_2-H_2O fluid was then adjusted to the desired value by weighing an appropriate amount of AgN_3. In H_2O-saturated experiments, no silver azide was added to the peridotite mixture. The duration of experiments was up to 10 days, depending on *P*, *T* and X_{H2O} of the fluid, to ensure equilibration. Experimental products were analysed using electron microprobe.

Preliminary results show that pargasite is not stable in equilibrium with fluids diluted to X_{H2O}=0.1 at pressures above 1 GPa. In comparison, at H_2O-saturated conditions, the pargasite stability field can extend to pressures of 4 GPa and above 1100 °C, depending on bulk alkali

and water contents (Fig. 3.3-2). The combined results of experiments at X_{H2O}=0.1 and X_{H2O}=1 suggest that pargasite can exist only in regions of the upper mantle which have been affected by fluids with high water activity, such as areas in the vicinity of subduction zones. The 'ambient' nominally anhydrous upper mantle, better represented by experiments at H_2O-undersaturated conditions, is not expected to contain pargasite.

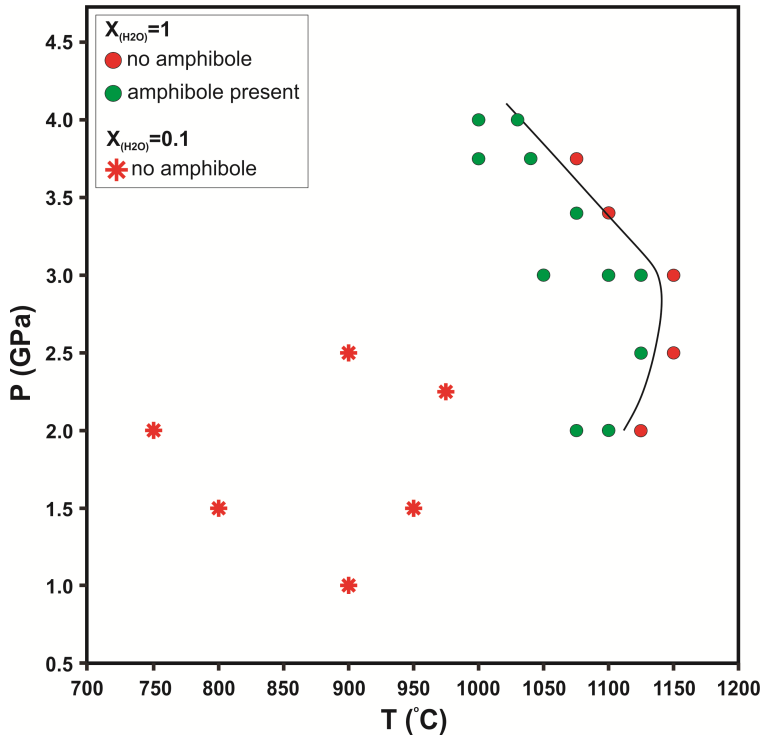

Fig. 3.3-2: Stability field of pargasite under H_2O-saturated conditions (X_{H2O}=1) compared to results from experiments at H_2O-undersaturated (X_{H2O}=0.1) conditions which did not produce any pargasite at any of the pressures and temperatures conditions investigated so far.

c. *Synthesis and crystal structures of Ca aluminates under the conditions of the Earth's transition zone and lower mantle (A. Iskrina/Moscow, A. Spivak/Chernogolovka; A. Bobrov, N. Eremin and E. Marchenko/Moscow, in collaboration with L.S. Dubrovinsky)*

Aluminium is one of the most abundant elements in the Earth crust and mantle. It is incorporated in major rock-forming minerals, including pyroxenes, garnets and bridgmanites. Moreover in alumina-rich xenolites and in metamorphic rocks it is present as spinel, $MgAl_2O_4$, or spinel solid solutions. Theoretical simulations indicate that spinel and post-spinel phases $Ca(Al,Fe)_2O_4$ may be energetically favorable at the conditions of the Earth's mantle. However, the system CaO-Al_2O_3($\pm Fe_2O_3$) is still poorly constrained experimentally, so the aim of this work was to synthetize and to structurally characterize the crystalline phases with general composition $Ca_xAl_yFe_zO_w$.

Experiments were carried out using a high-pressure device MavoPress LPRU 1200-555/50 with toroidal anvils at a pressure of 6 GPa and at temperatures of 1000 to 1200 °C for 3 to 11 hours, as well as using 1000-t and 1200-t Kawai-type multianvil presses at pressures of 15, 18 and 24 GPa, and at 1600 °C for 1 hour. Three different phases have been obtained in these synthesis experiments: $CaAl_2O_4$ (space group *Pnma*), $Ca(Al,Fe)_2O_4$ (space group *Pnma*), and a new, previously unknown phase $Ca_2Al_6O_{11}$ (space group $P4_2/mnm$). The structure and the stoichiometric formula of $Ca_2Al_6O_{11}$ were identified by means of single crystal X-ray diffraction. All phases were investigated by optical microscopy, SEM, Raman spectroscopy and microprobe analysis.

d. *Stability of Fe_5O_6 and related Fe-oxides (A.B. Woodland and L. Uenver-Thiele/ Frankfurt/M., in collaboration with T. Boffa Ballaran and T. Ishii)*

The simple Fe-O system is fundamental for understanding many geochemical processes. At high pressures and temperatures corresponding to conditions of the lower upper mantle and transition zone, magnetite breaks down to the assemblage Fe_4O_5 + hematite. The recent synthesis of Fe_5O_6 increases the complexity of the phase relations in the Fe-O system. Having a lower $Fe^{3+}/\sum Fe$ than Fe_4O_5 (0.4 rather than 0.5 for Fe_4O_5), Fe_5O_6 is arguably more relevant for the relatively reducing conditions of the Earth's deep mantle. This study was undertaken to determine the *P-T* stability of Fe_5O_6.

Experiments were performed at 8-28 GPa and 900-1600 °C, with run products characterized by powder diffraction and microprobe. Fe_5O_6 has a jet-black colour with a vitreous luster (Fig. 3.3-3). The low-pressure stability limit of Fe_5O_6 lies near 9 GPa over a large range of temperature, which is similar to that reported for Fe_4O_5. At lower pressures, the stable assemblage is magnetite + wustite. A low-temperature phase boundary exists where Fe_5O_6 is replaced by the assemblage of Fe_4O_5 + wustite. This boundary has a rather steep *P-T* slope such that the stability field of Fe_5O_6 tends to pinch out to higher pressure. However, Fe_5O_6 remains stable up to at least 28 GPa, indicating that it could be a stable phase along the mantle adiabat into the upper portions of the lower mantle.

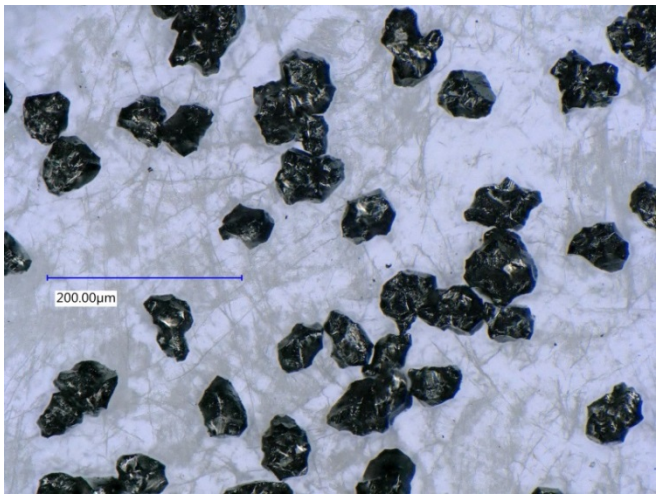

Fig. 3.3-3: Reflected light micrograph of crystals of Fe_5O_6 synthesised at 28 GPa and 1500 °C.

Depending on the overall oxidation state, Fe_5O_6 can coexist with either wustite or Fe_4O_5. However, an additional phase with $Fe^{2+}{}_5Fe^{3+}{}_4O_{11}$ stoichiometry can coexist with Fe_5O_6 instead of Fe_4O_5 over a limited *P-T* range. This phase possesses a structural stacking sequence and $Fe^{3+}/\sum Fe$ (0.44) that is intermediate between Fe_4O_5 and Fe_5O_6, and as a result exhibits a reduction in symmetry from orthorhombic (*Cmcm* space group) to monoclinic (*C2/m* space group). The occurrence of $Fe^{2+}{}_5Fe^{3+}{}_4O_{11}$ is further evidence for much more complicated phase relations in the Fe-O system at pressures above ~ 10 GPa, with a sequence of different phases being stable as a function of the bulk oxidation state.

e. *Synthesis and crystal structure of Mg-bearing Fe_9O_{11} (T. Ishii; L. Uenver-Thiele, A.B. Woodland and E. Alig/Frankfurt/M. and T. Boffa Ballaran)*

The Fe-O system is fundamental for understanding redox processes operating in the Earth's interior. Recent experimental studies have revealed several new mixed-valence Fe-oxides to be stable at high pressures and temperatures, such as the orthorhombic-structured phases $Fe^{2+}{}_2Fe^{3+}{}_2O_5$ and $Fe^{2+}{}_3Fe^{3+}{}_2O_6$. and the monoclinic-structured $Fe^{2+}{}_3Fe^{3+}{}_4O_9$. It has been also demonstrated that Fe_4O_5 and Fe_7O_9 form solid solutions with the Mg end-members such as $Mg_2Fe_2O_5$ and $Mg_3Fe_4O_9$, suggesting possible existence of complicated Mg-Fe oxides in the deep mantle. We synthesized a new Mg-Fe oxide with a composition of $Mg_{0.9}Fe_{8.1}O_{11}$. We report the synthesis and crystal structure of $Mg_{0.9}Fe_{8.1}O_{11}$ obtained using the Rietveld method.

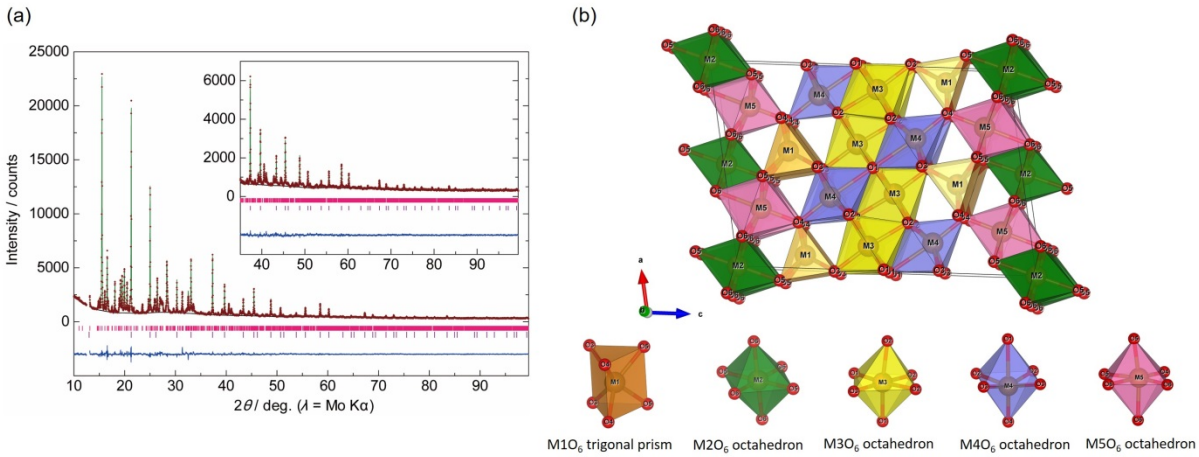

Fig. 3.3-4: (a) Diffraction pattern of $Mg_{0.87}Fe_{8.13}O_{11}$ (red crosses). The Rietveld structural refinement and refined background are reported as green and black curves, respectively. The difference between calculated and observed intensities is reported as blue curve. Tick marks indicate the Bragg peak positions for the two phases present in the diffraction pattern, *i.e.*, $Mg_{0.87}Fe_{8.13}O_{11}$ (top marks) and silicon standard (bottom marks). The inset illustrates the high 2θ region with an expanded intensity scale. (b) Structural model obtained from the Rietveld analysis for $Mg_{0.87}Fe_{8.13}O_{11}$.

A novel Mg-bearing iron oxide $Mg_{0.87(1)}Fe^{2+}_{4.13(1)}Fe^{3+}_4O_{11}$ was synthesized at 12 GPa and 1300 °C using a large volume press. Rietveld structural analysis was conducted with a high-resolution X-ray diffraction pattern collected at ambient conditions with an *in house* system at the University of Frankfurt. The crystal structure, which has one oxygen trigonal prism site and four octahedral sites, was found to be isostructural with $Ca_2Fe_7O_{11}$ (Fig. 3.3-4). The unit-cell lattice parameters are: a = 9.8441(5) Å, b = 2.8920(1) Å, c = 14.1760(6) Å, β = 99.956(4)°, V = 397.50(3) Å, and Z = 2 (monoclinic, $C2/m$). Mg and Fe cations are disordered on the trigonal prism site and on two of the four octahedral sites, and the remaining Fe is accommodated at the other two octahedral sites. The present structure is closely related to the other recently discovered Fe oxide structures, *e.g.*, Fe_4O_5 and Fe_5O_6, by distortion derived either from incorporation (Fe_4O_5) or removal (Fe_5O_6) of an edge-shared FeO_6 single octahedral chain in their structures. The present synthesis at deep upper mantle conditions and the structural relationships observed between various novel Mg-Fe oxides indicate that a series of different phases become stable above 10 GPa and that their relative stabilities (Fe^{2+}/Fe^{3+}) must be controlled by oxygen fugacity.

f. *The composition of bridgmanite at the redox conditions of the lower mantle (R. Huang, T. Boffa Ballaran, C.A. McCammon, N. Miyajima and D.J. Frost)*

The dominant phase of the lower mantle $(Mg,Fe)(Si,Al)O_3$ bridgmanite is a relatively complex solid solution due to the presence of both ferric and ferrous Fe and the fact that trivalent Fe^{3+} and Al^{3+} cations can be incorporated on both cation sites with various states of local ordering. Furthermore previous studies have shown that the Fe^{3+} content of Al-bearing bridgmanite can reach relatively high proportions even at oxygen fugacities consistent with the presence of metallic iron. The variation in the Fe^{3+} content of bridgmanite as a function of composition and oxygen fugacity (fO_2) is important for determining the redox state of the lower mantle, which in turn influences C-O-H fluid speciation and may have influenced the redox state of the mantle as a whole during core formation. Such information is also important for determining mineral models for the lower mantle in order to compare seismic velocity-depth profiles for specific lower mantle compositions. Moreover, transport properties of the lower mantle are likely to be influenced by trivalent cation contents and distributions in the constituent minerals. In spite of its importance, however, the variation in the Fe^{3+} content of bridgmanite as a function of composition and oxygen fugacity (fO_2) is still poorly understood. In this study, we are investigating the relationship between the $Fe^{3+}/\sum Fe$ content in bridgmanite and oxygen fugacity in addition to characterizing the partitioning of Fe^{3+} between the A and B sites of the bridgmanite structure as a function of bulk Fe and Al content.

Samples of $(Mg,Fe)(Si,Al)O_3$ bridgmanite were synthesized in multianvil runs at a pressure of 25 GPa and at temperatures between 1700 ~ 2000 °C. Different fO_2 conditions during the synthesis experiments were obtained by adding to the starting materials either Fe powder or hematite with different amounts of water together with redox sensitive alloys, which allowed the fO_2 to be calculated. In the run products Fe or Fe-Ir alloy or Fe_4O_5 were found to coexist with bridgmanite and a wide range of fO_2 values between IW-1 to IW+5 were achieved. The

bridgmanite samples were characterized by means of microprobe analysis and Mössbauer spectroscopy or electron energy loss spectroscopy.

Figure 3.3-5 shows how the $Fe^{3+}/\sum Fe$ ratio of bridgmanite increases with fO_2 for a fixed bridgmanite Al content. In all samples the total Fe content remains relatively constant at 0.1-0.12 cations per three oxygen formula unit. Even for Al free bridgmanite at conditions of Fe-metal saturation, the ferric iron content is approximately 10 % of total iron. This marks a deviation from low-pressure minerals such as spinel which contain effectively no ferric iron at the same relative oxygen fugacity. As the Al content of bridgmanite is increased its ferric iron content at a given oxygen fugacity also increases. The ferric iron content is therefore not independent of oxygen fugacity but the gradient of this dependence becomes flatter with increasing Al content. We are currently deriving a thermodynamic model to fully describe this dependence which will be essential for interpreting the results from further experiments performed at higher pressures. The average upper mantle has a ferric iron content of the order of 3 %, which implies that even in the absence of Al, the oxygen fugacity of the lower mantle would be at conditions of iron metal saturation. If we consider that the bulk oxygen content of the mantle as a whole is constant and we ignore the redox effects of volatile species such as carbon, then iron metal would be forced to disproportionate at the top of the lower mantle. The amount of iron metal produced in a lower mantle assemblage would be a function of the Al content of bridgmanite and would increase from 0.3 wt. % to 0.9 wt. % as the Al content increases from 0 to 0.1 cations per formula unit.

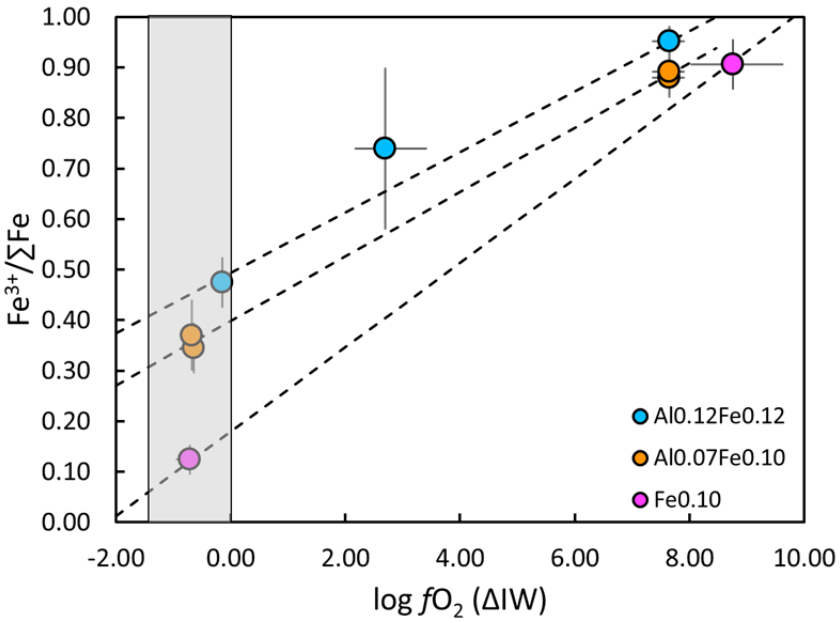

Fig. 3.3-5: The ferric iron content of brigdmanite as a function of oxygen fugacity normalised to the iron-wustite oxygen buffer. The different trends represent three different Al contents in the bridgmanite samples having, however, the same total Fe content of 0.1-0.12 cations per formula unit. The grey shaded region shows the oxygen fugacity where Fe-Ni alloy would precipitate, which marks the lowest plausible value for the lower mantle.

g. *Pressure, temperature and oxygen fugacity dependence of ferric iron content in ferropericlase (C. Melai, D.J. Frost, T. Boffa Ballaran and C.A. McCammon)*

Ferropericlase comprises one of the more common types of inclusions in sub-lithospheric diamonds, which form in the convecting mantle below the lithosphere. Although it was initially proposed that such inclusions must have formed in the lower mantle, further analyses have shown that their individual compositions cover almost the entire range of the Fe/(Fe+Mg) solid solution implying formation in some cases within very Fe-rich assemblages. One possibility is that the inclusions form through oxidation of iron metal, however, in many instances exsolution of an Fe^{3+} rich phase such as magnetite has been observed. In most studies where TEM investigations were made excess Fe^{3+} rich exsolutions were identified. Ferropericlase-magnesiowustite inclusions are most likely some of the deepest available samples from the mantle and they potentially provide the most tangible evidence for deep mantle processes. To interpret their formation conditions and the conditions under which exsolution of Fe^{3+} richer phases must have occurred, however, we need experimental information on how the stability and composition of such oxide inclusions change with pressure, temperature and oxygen fugacity.

The stability field of (Fe,Mg)O and the exsolution of Fe^{3+} rich phases has recently been shown to be more complicated at high pressure due to the formation of mixed valence iron oxides such as Fe_4O_5 and Fe_5O_6. As shown in Fig. 3.3-6 for the end member Fe-O system,

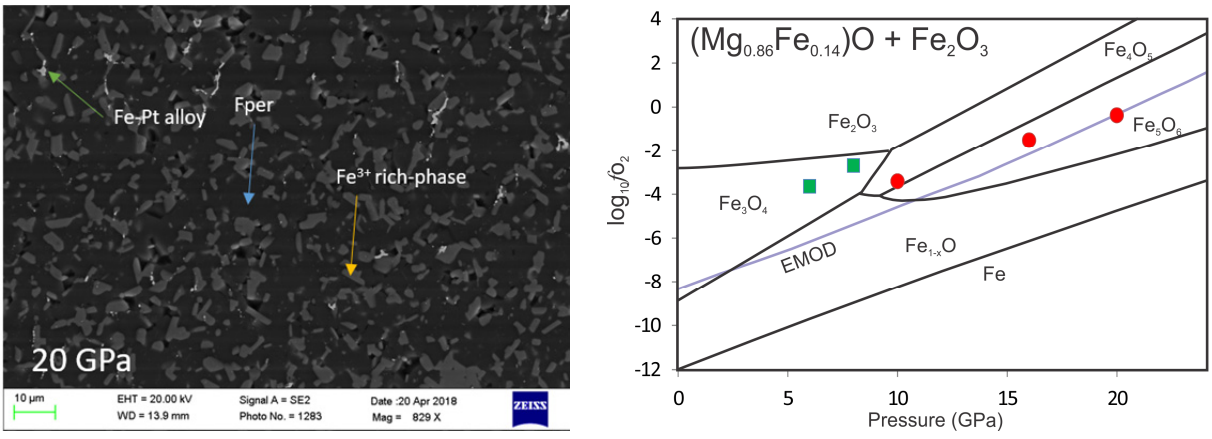

Fig. 3.3-6: Left: SEM image of a run product recovered from an experiment performed at 20 GPa and 1200 °C. Ferropericlase coexists with an Fe^{3+}-rich $Mg_2Fe_2O_5$-Fe_4O_5 solid solution. Right: Calculated oxygen fugacities at which $(Mg_{0.86}Fe_{0.14})O$ coexists with an Fe^{3+}-rich phase at 1200 °C. Green symbols indicate coexisting magnetite-magnesioferrite while red symbols indicate $Mg_2Fe_2O_5$-Fe_4O_5 solid solution. The background solid black lines show the stability of phases in the end-member Fe-O system, while EMOD indicates the equilibrium enstatite + magnesite = olivine + diamond which defines the diamond stability field. This curve takes into account phase transitions of olivine at higher pressures.

$Fe_{1-x}O$ should breakdown at high oxygen fugacity to form Fe_2O_3 magnetite at pressures below 10 GPa, while, at higher pressures, the breakdown product should be Fe_5O_6. The questions we address in this project using thermodynamic modelling and experimental measurements are: at what conditions do the Mg-bearing solid solutions of these new iron oxide phases become stable and what is, therefore, the maximum $Fe^{3+}/\Sigma Fe$ ratio of (Fe,Mg)O?

Multianvil experiments were performed in a range of 6-25 GPa and 1200-1800 °C using a starting composition of $(Mg_{86}Fe_{14})O$ plus 20 % Fe_2O_3. Pt powder was added to the experiments to act as a redox sensor and minor amounts of Ni, Cr, Mn and Na were also added. Samples were then analysed with scanning electron microscope (SEM), electron microprobe, Mössbauer Spectroscopy, X-ray diffraction and transmission electron microscopy (TEM).

In the recovered experiments ferropericlase coexists with magnetite-magnesioferrite solid solution up to 10 GPa and with $Mg_2Fe_2O_5$-Fe_4O_5 solid solution at higher pressures. The Fe/(Fe+Mg) ratios of both oxides is approximately 0.7 whereas the ferropericlase ratio remained close to that of the starting material. In all experiments the oxygen fugacities could be determined from the equilibrium:

$$\underset{\textit{Fe-Pt alloy}}{2Fe} + O_2 = \underset{\textit{ferropericlase.}}{2FeO} \qquad [1]$$

Below 10 GPa the oxygen fugacity could also be determined from the equilibrium:

$$\underset{\textit{ferropericlase}}{6FeO} + O_2 = \underset{\textit{magnetite-magnesioferrite}}{2Fe_3O_4} \qquad [2]$$

In the calculation of the oxygen fugacity a ferropericlase model in the FeO-$Fe_{2/3}O$-MgO system was employed and exchange of Mg and Fe^{2+} in magnetite was accounted for. The resulting oxygen fugacites from both equilibria at 6 and 8 GPa are within 0.1 log units of each other and are plotted in Fig. 3.3-6. Given the good agreement between both equilibria, we then calculated the oxygen fugacities for the higher pressure assemblages using only equilibrium [1]. Diamond can only be stable at oxygen fugacities below the EMOD curve indicated in Fig. 3.3-6. The results therefore indicate that magnetite-magnesioferrite solid solutions should not be in equilibrium with ferropericlase inclusions in the diamond stability field. At 20 GPa an assemblage containing $Mg_2Fe_2O_5$-Fe_4O_5 solid solution would be in equilibrium with ferropericlase just inside the diamond stability field. The results indicate that the exsolution of Fe^{3+} rich phases observed in ferropericlase inclusions in diamond occurred potentially in the transition zone or deeper. Further experiments to explore the effects of varying Fe/(Fe+Mg) ratio and temperature are underway.

h. *Single-crystal X-ray diffraction studies of Fe_2O_3 at pressures over 200 GPa (S. Khandarkhaeva, M. Bykov, T. Fedotenko/Bayreuth, E. Koemets, N.A. Dubrovinskaia/ Bayreuth and L.S. Dubrovinsky, in collaboration with E. Bykova/Hamburg and P. Sedmak/Grenoble)*

Hematite (α-Fe_2O_3) is one of the major components of banded iron formations (BIFs) and other iron ore deposits. Deposited in the world's oceans, BIFs may be recycled as part of the ocean floor through the subduction down to the core-mantle boundary. Therefore, structural studies of iron oxides under extreme *P-T* conditions contribute to our understanding of processes occurring deep inside the Earth. At the same time knowledge of the chemistry of the Fe-O system at ultra-high pressures is important for modelling properties of the Earth's core. The complex behaviour of simple Fe_2O_3 under high pressure has been demonstrated in a number of recent studies using single-crystal X-ray diffraction and synchrotron Mössbauer spectroscopy. It was found that decomposition of Fe_2O_3 (and Fe_3O_4) at high-pressure and high-temperature (HPHT) conditions leads to crystallization of unusual Fe_5O_7 and $Fe_{25}O_{32}$ compounds, whereas at lower pressures mixed oxides such as Fe_4O_5, Fe_5O_6, and Fe_7O_9, appear to be stable depending on oxygen fugacity. Iron oxide phases forming a homologous series nFeO·$m$$Fe_2O_3$ may, therefore, play a significant role in oxygen cycling in deep planetary interiors.

Here we report the results of *in situ* single-crystal X-ray diffraction studies of Fe_2O_3 at conditions relevant to the Earth's core-mantle boundary and outer core. Diffraction experiments were conducted at the materials science (nano-) beamline ID11 at the European Synchrotron Radiation Facility (ESRF), Grenoble, France (Frelon4M detector; λ = 0.3092 Å and 0.30996 Å; spot size $0.3^x0.3$ μm^2 and $0.45^x0.45$ μm^2, respectively). Single crystals of α-Fe_2O_3 were loaded in BX-90 diamond anvil cells equipped with diamond anvils with 40-μm culets. The maximum pressures achieved in two different experiments were 187(2) GPa and 213(1) GPa. Pressure conditions in the DAC experiments were estimated using the 3rd order Birch–Murnaghan equation of state of Re. Pulsed laser heating up to 3000 K was performed using a portable double-sided pulsed laser heating system developed at the Bayerisches Geoinstitut. Temperatures were determined using the grey body approximation of Planck's law.

Single crystal XRD studies show that HP PPv-phase of Fe_2O_3 (η-Fe_2O_3) exists up to 213(2) GPa, its crystal structure was refined with a discrepancy factor R1=7.1% (Fig. 3.3-7d). Laser heating resulted in partial decomposition of η-Fe_2O_3 with formation of new iron oxides with monoclinic symmetry (space group *C2/m*): $Fe_{13}O_{19}$ (a=18.9445(18) Å, b=2.5297(13) Å, c=9.393(11) Å, β=117.57°(3)) and $Fe_{19}O_{27}$ (a=19.001(3) Å, b=2.5464(16) Å, c=13.932(3) Å, β =121.57°(2)). Both crystal structures were solved and refined with R1=5.9% and R1=9.5%, respectively (Fig. 3.3-7a, b). At 187(2) GPa we observed a HP-phase of Fe_3O_4 with the distorted Th_3P_4-type structure (space group $I4_1/amd$, a=5.576(2) Å, c=5.622(2) Å), which was refined with R1=4.0% (Fig. 3.3-7c). At 213(2) GPa two Fe_3O_4 polymorphs with orthorhombic

structures were found: one had a distorted $CaTi_2O_4$-type structure (space group *Pnma*, *a*=7.991(3) Å, *b*=2.5965(5) Å, c=8.384 (2) Å, R1=5.3%) and the other a distorted $CaFe_2O_4$-type structure (space group *Pnma*, *a*=7.796(5) Å, *b*=2.4369(6) Å, *c*=9.1831(19) Å, R1=9.9%) (Fig. 3.3-7e, f). All these chemical transformations of η- Fe_2O_3 occur upon release of oxygen.

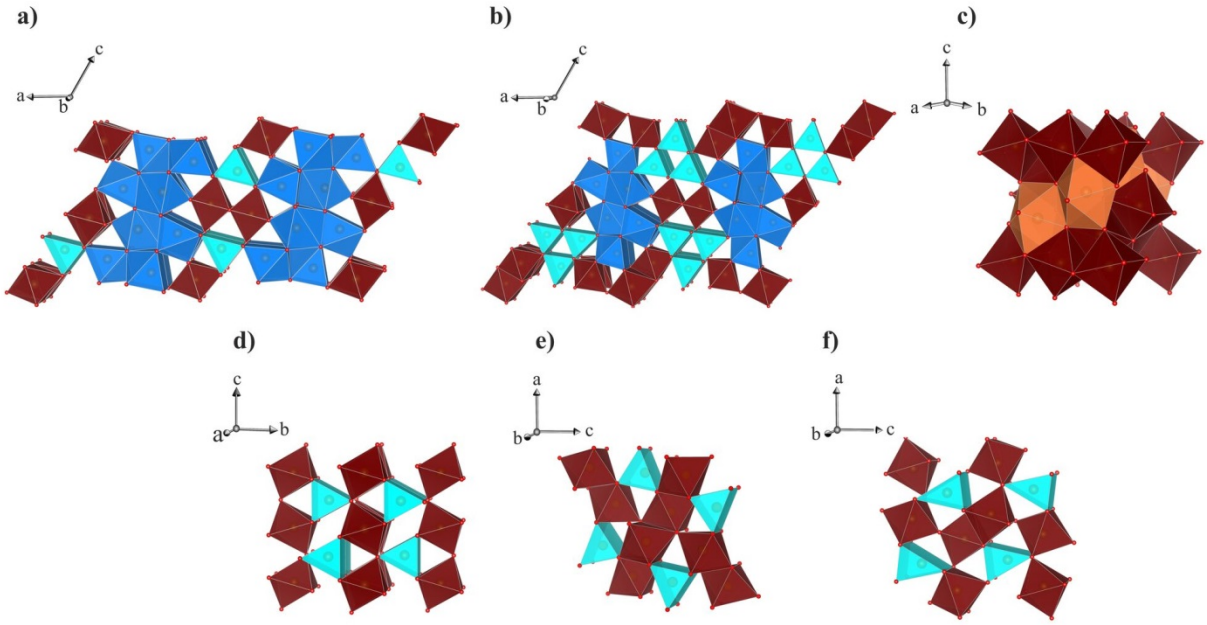

Fig. 3.3-7: Crystal structures of iron oxide phases observed at 187(2) and 213(1) GPa before and after laser heating: a) $Fe_{13}O_{19}$, b) $Fe_{19}O_{27}$, c) Fe_3O_4 with a distorted Th_3P_4-type structure, d) HP η-Fe_2O_3 (PPV-type structure), e) Fe_3O_4 with a distorted $CaTi_2O_4$-type structure, and f) Fe_3O_4 with a distorted $CaFe_2O_4$-type structure.

i. *Single crystal X-ray structure study of δ-phase AlOOH-FeOOH-$MgSiO_2(OH)_2$ (T. Ishii, I. Ohira/Washington, T. Kawazoe/Higashi-Hiroshima, T. Boffa Ballaran, A. Suzuki/Sendai and E. Ohtani/Sendai)*

δ-AlOOH is a hydrous phase stable in the hydrous sediment component of slabs subducted into the mantle transition zone and lower mantle and as such may play an important role in the Earth's deep water cycle. This phase likely forms a solid solution with ε-FeOOH (space group $P2_1nm$) and $MgSiO_2(OH)_2$ (space group *Pnnm*). The Fe, Mg and Si substitution may affect the physical and chemical properties of δ-AlOOH, therefore knowledge of the mechanism of cation substitution in the AlOOH-FeOOH-$MgSiO_2(OH)_2$ solid solution is of fundamental importance for understanding the water cycle into the deep mantle. In this study, we conducted a structural analysis of the δ-phase AlOOH-FeOOH-$MgSiO_2(OH)_2$ solid solution by means of single crystal X-ray diffraction.

Single crystals of pure δ-AlOOH, δ-(Al,Fe)OOH and δ-(Al,Fe,Mg,Si)OOH with Fe, Mg and Si components up to about 10 mol. % were synthesized at 21 GPa and 1480 K for 4 h using a

Kawai-type multianvil apparatus. X-ray diffraction experiments were conducted at BGI using a HUBER four-circle diffractometer for accurate unit-cell lattice parameter determination following the eight-positions centering method and an Xcalibur diffractometer with a CCD detector for full intensity data collections. The structure determination of each synthetic crystal was performed using the SHELXL-97 program. The atomic occupancies of the octahedral sites were constrained using the chemical composition determined using an electron microprobe operating in wavelength-dispersive mode. All Fe was considered as ferric iron.

The space group of δ-AlOOH ($P2_1nm$) remains unchanged by the substitution of Al by Fe, whereas addition of only ~ 1 mol. % of $MgSiO_2(OH)_2$ component is sufficient to change the space group to *Pnnm* (Fig. 3.3-8) already at room pressure. Since it has been reported that also pure δ-AlOOH undergoes a phase transformation to a *Pnnm* phase above 7 GPa, we can expect that δ- phases coexisting with mantle minerals in the deep mantle have only *Pnnm* space group.

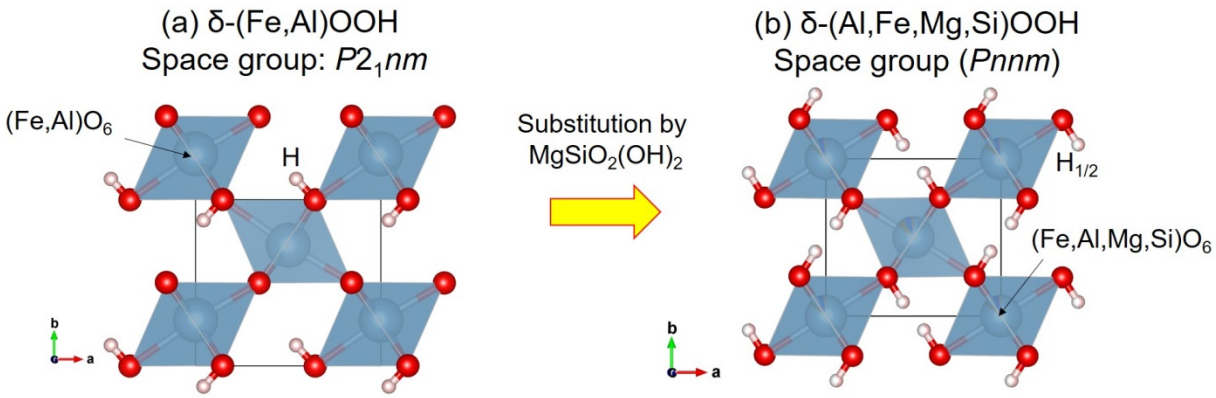

Fig. 3.3-8: (a) Crystal structures of δ-phases with space groups of (a) $P2_1nm$ and (b) *Pnnm*.

j. *Novel iron oxides obtained from goethite (FeOOH) decomposition at HP-HT conditions (E. Koemets and M. Bykov; G. Aprilis and T. Fedotenko/Bayreuth; S. Chariton, S. Khandarkhaeva, I. Koemets, M. Thielmann, N.A. Dubrovinskaia/Bayreuth and L.S. Dubrovinsky)*

Water and water-bearing species have a strong impact on numerous processes of the Earth's interior. The presence of water affects the chemical and physical properties of mantle minerals, changes melting temperatures, sound velocities and viscosity of materials causing different global phenomena such as, for example, arc volcanism and plate tectonics. Thereby, the deep Earth's regions enriched with water directly influence our planet's geodynamics and geochemistry. Still, the mechanisms of water circulation between geospheres remain poorly understood.

Recent studies suggest that goethite present in Banded Iron Formations (BIFs) may transfer some quantities of water to the deep Earth's interior via subducting slabs. It was reported that goethite may remain stable in the sinking slab until it reaches the base of the lower mantle. By means of *in situ* powder X-ray diffraction (XRD) it was revealed that, at pressures corresponding to the depths of ~ 1500-1800 km and at moderately high temperatures, goethite undergoes a phase transition to form a novel stable pyrite-type phase FeO_2H_x with $0 \leq x \leq 1$ (Py-phase). Thus, goethite and in particular its HP pyrite-type form may be a candidate for water and/or hydrogen transfer and storage in the lower mantle and at the core-mantle boundary.

Using laser-heating in diamond anvil cells we performed a series of experiments to investigate goethite stability at *P-T* conditions of subducting slabs. By means of *in situ* single-crystal XRD in diamond anvil cell (DAC) we observed decomposition of goethite and formation of known (such as ι-Fe_2O_3, η-Fe_2O_3, the high-pressure orthorhombic form of Fe_3O_4, and Fe_5O_7), and of novel iron- oxygen compounds. Structure solution and refinement of the XRD intensity data of these unknown phases show that these are an orthorhombic Fe_7O_{10} and a hexagonal non-stoichiometric phase $Fe_{6.31}O_9$. Our results suggest that FeOOH cannot be preserved in subducted slabs at conditions of the Earth's lower mantle.

k. *Pre-melting in Neon: Dramatic changes observed in elastic anisotropy (M.G. Pamato, L. Vočadlo, D.P. Dobson and I.G. Wood/London, in collaboration with A. Kurnosov and T. Boffa Ballaran)*

Seismological models of the Earth's inner core do not agree with mineralogical models constructed using both *ab initio* simulations and laboratory experiments. The latter, in fact, predicts shear-wave velocities up to 30 % greater than the observed geophysical values. A possible explanation for the mismatch in shear wave velocities was recently proposed on the basis of *ab initio* calculations which showed a dramatic and non-linear softening of the elastic constants of *hcp*-iron at 360 GPa, just before melting ($T/T_m > 0.96$, where T_m is the melting temperature). This was interpreted as a "pre-melting" effect, associated with the formation of defects in the structure of *hcp*-iron. However, to date, computer calculations are the only studies on pre-melting effects in a metal directly applicable to the Earth's inner core. Therefore, the question we would like to answer is: are these effects real or just an artefact from super-heating in the computer simulations? In the context of planetary cores, it is essential to systematically investigate such phenomena for iron and relevant iron alloys over a range of pressures and temperatures (*P-T*) at inner core conditions. However, measuring the pressure dependence of pre-melting effects under such conditions, to the required precision, is extremely challenging – indeed prohibitively so at present.

In this study, therefore, we have carried out high-pressure experiments at more experimentally accessible conditions. We have investigated the elastic properties of single-crystals of neon (Ne) prior to melting. Ne is an ideal initial test material since it crystallises in a simple face-centred cubic structure and is easily modelled using classical potentials or ab initio methods. In addition, the compressibility of Ne is large and the temperature range required is within the

capabilities of externally heated diamond anvil cells, so pressures and temperatures close to the melting point can be readily achieved. Ne was loaded using a high-pressure gas loading device in a diamond anvil cell with a large opening angle of 80° and Almax- Böhler type diamond anvils with culets of 500 µm in diameter. A specially designed internal resistive heater was placed around the diamonds for the high-temperature measurements. A single crystal of Ne, completely filling the interior of the pressure chamber, was grown by increasing slowly the pressure on a seed crystal, which coexisted with the liquid Ne at P = 4.6 GPa and room temperature. After the single-crystal was obtained, the elastic constants, sound velocities, anisotropy, and the crystal orientation were determined at each pressure and temperature by combining Brillouin scattering measurements with X-ray diffraction at BGI. Measurements were made upon heating the sample from ~ 7 GPa at room temperature up to melting (7.9 GPa and 410 K), following an isochoric trace as the thermal expansion of the pressure vessel material is much smaller than that of the solidified gas.

If pre-melting in this system occurs, we expect to observe a non-linear softening of the elastic constants and velocities just before the melting temperature. Ne appears to have a non-linear behaviour not only in sound velocities and shear modulus but also in elastic anisotropy (Fig. 3.3-9). For cubic crystals, the elastic anisotropy is given by $A = 2C_{44}/(C_{11}-C_{12})$; for isotropic

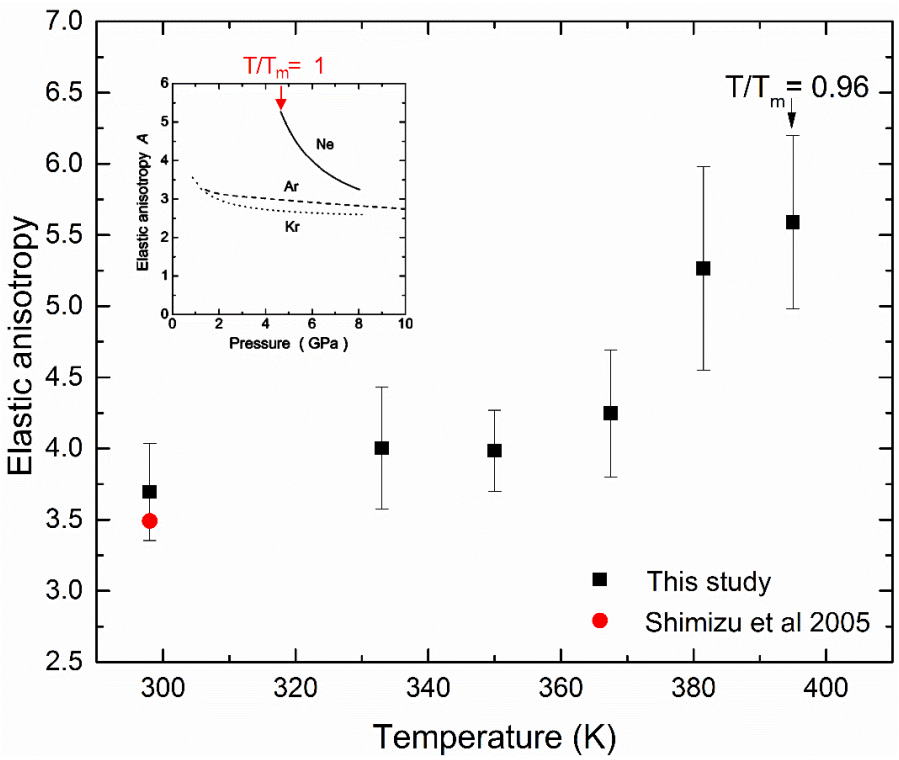

Fig. 3.3-9: Elastic anisotropy of solid Ne as a function of temperature showing remarkable behaviour close to melting, together with literature results (Shimizu *et al.* 2005, Phys. Rev. B 71, 014108) at the same conditions (7 GPa and room temperature). For comparison the inset shows the elastic anisotropy as a function of pressure at room temperature as determined in the mentioned study; similarly to our study the anisotropy is larger as T/T_m approaches 1.

materials A = 1 and thus the shear modulus C_{44} = (C_{11}−C_{12})/2. Our results show that the behaviour of Ne is remarkable: the anisotropy increases from A = 3.7 at room temperature to A= 5.7 at 395 K (T/T_m = 0.96). A similar behaviour has been reported in the literature (inset in Fig. 3.3-9), where the anisotropy at room temperature is largest (A = 5.27) close to melting (T/T_m = 1) at 4.6 GPa, but decreases rapidly to A = 3.62 at 7 GPa.

The outermost part (~ 200 km) of the Earth's inner core, corresponding to the region which is closest to T_m, shows stronger anisotropy than the innermost inner core. This has been interpreted as a change in flow regime between the outermost and innermost inner core but, if similar pre-melting effects occur in *hcp* materials, it could just be a pre-melting effect causing the CPO in the outermost inner core to become visible to seismic anisotropy observations.

l. *Proton Nuclear Quantum Effects and Hydrogen Bond Symmetrisations (T. Meier, S. Khandarkhaeva, F. Trybel and L.S. Dubrovinsky)*

One of the most elusive effects in high-pressure sciences is the proposed transition from hydrogen disordered IceVII, a high-pressure ice polymorph forming at pressures above 2 GPa, to the hydrogen ordered phase ice X. Since its prediction 46 years ago by Wilfried Holzapfel a large number of different studies have been involved trying to detect the hydrogen bond symmetrisation and as a consequence the transition from Ice VII to Ice X. Under reduction of the average oxygen-oxygen distance, *i.e.*, under increasing pressure, the energy barrier of the symmetric double potential well describing the hydrogen bond (H-Bond) will be modulated, leading to increasing tunnel probabilities, and thus tunnel frequencies υ_T, of the proton residing in either of both non-distinguishable energy minima (the high barrier hydrogen bond regime, HBHB). At higher pressures, υ_T increases and the probability density of the protonic wave function delocalizes, or smears out across the double potential well (the strong hydrogen bond regime, LBHB). Under further compression, the energy barrier completely diminishes and the protons localize in the symmetric mid-point of the H-Bond (the symmetric hydrogen bond regime, SHB). While this scenario is widely acknowledged in the theoretical physics community, experimental evidence is still sparse and highly controversial due to the fact that most of the established experimental methods like X-ray or neutron diffraction, Raman or IR spectroscopy are not very sensitive to hydrogens or are not feasible at very high pressures.

Using our recently developed NMR technique at BGI, it was possible to follow the protons response to this energy barrier modulation and to observe the full pressure dependence of the induced so-called nuclear quantum effects (NQEs). The experimental data of our ^{1}H-NMR experiments up to 90 GPa are summarised in Fig. 3.3-10. It has been shown that NMR can be used to quantify the relative amount of protons tunneling across the H-Bond's energy barrier. As can be seen in Fig. 3.3-10c, with increasing pressure more and more protons become delocalised, reaching a maximum at about 60 GPa. At higher pressures, the H-bonds

symmetrisation occurs, leading to a localization of the protons. Chemical shift analyses even showed that all three regimes, HBHB, LHBH as well as SHB can be probed by NMR, settling a decade long debate in condensed matter and high-pressure physics.

These NQEs are thought to be universal and potentially detectable in other materials stabilised by H-bonds. Recent experiments demonstrated that this is indeed the case in δ–AlOOH, with the HBHB to LBHB transition at about 10 GPa and the symmetrisation of the hydrogen bond at 15 to 17 GPa.

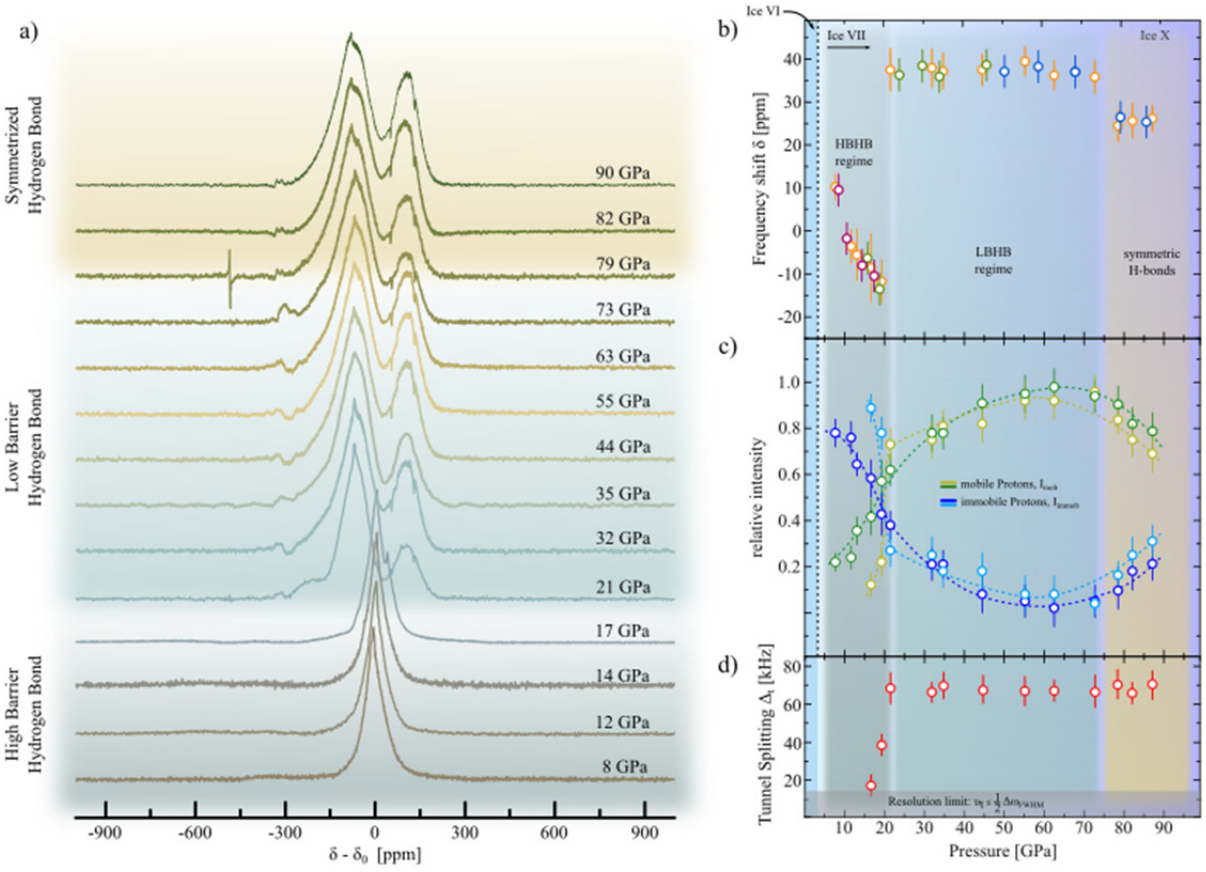

Fig. 3.3-10: Summary of high field data collected at 9.3 T; a) Proton NMR signals of ice from 8 to 90 GPa; b) chemical shifts relative to a water sample at ambient conditions; c) Intensities from localised and tunneling protons d) tunnel splitting up to 90 GPa.

m. *Spectral and mineralogical studies using heated and dehydrated carbonaceous chondrites (M. Matsuoka and T. Nakamura/Sendai, in collaboration with N. Miyajima)*

Carbonaceous chondrites represent some of the most pristine matter having a composition close to that of the Sun. Since they are undifferentiated meteorites, they are thought to have been subjected only to minor heating on their parent bodies. However, many carbonaceous chondrites that have been found in Antarctica appear to have experienced heating and

dehydration after aqueous alteration before they fell on Earth. In order to estimate the heating and dehydration processes occurring on their parent bodies, it is essential to clarify the spectral, chemical, and mineralogical changes due to heating. Moreover, a data base of Vis-IR spectra of well characterised mineralogies belonging to naturally-heated carbonaceous chondrites may help to better understand spectral data obtained from ongoing sample return missions (*e.g.*, JAXA Hayabusa2, NASA OSIRIS-REx).

Spectral and mineralogical analyses were performed using nine naturally-heated and dehydrated carbonaceous chondrite samples which were classified into heating stages (HS) from I to IV in terms of their mineralogical properties based on X-ray diffraction analysis results. *In situ* heating of samples at 120-400 °C was performed during spectral measurements and efficiently removed terrestrial absorbed water and part of rehydrated water from chondrite samples. Reflectance spectra of unheated HS-I samples show a positive slope in Vis- IR range and large 0.7- and 3-μm absorption bands. The 0.7-μm band appears in HS-I sample spectra only. With increasing heating, (1) the Vis-IR slope decreases, (2) the 3-μm band becomes shallower, and (3) the Christiansen feature and Reststrahlen bands shift toward longer wavelength.

TEM/EDX analyses showed a compositional difference between the matrix containing "tochilinite cronstedtite intergrowth (TCI)" (Pignatelli *et al.*, 2016, MAPS, 51, 785) of unheated chondrites, and the matrix of heated chondrites; the matrix of strongly-heated chondrites consists of tiny olivine, low-Ca pyroxene, and Fe- and Ni-rich metallic grains mostly smaller than 100 nm in diameter (Fig. 3.3-11), instead of Fe-rich serpentinites and tochilinite observed in the HS-I chondrite. The matrices of strongly heated chondrites show a similar average chemical composition to that of HS-I, but the former consists of Mg-rich anhydrous silicates such as olivine and silicate as well as Fe- and Ni-rich metal grains. Comparison in the chemical composition of matrix minerals between HS-I and HS-IV samples suggests that metallic FeNi-rich grains formed from Fe provided by Fe-rich hydrous silicates such as cronstedtite and tochilinite enriched in HS-I chondrite matrices, and Ni from Ni-bearing tochilinite, and then the remnants become Fe-poor anhydrous silicates such as Mg-rich olivine and pyroxene during heating process. The Ni contents of metal grains probably depend on the availability of nearby tochilinite as a source mineral.

In this study, the mineralogical and chemical changes of naturally-heated carbonaceous chondrites due to heating on their parent bodies are described as follows: (i) [HS-I to II] Hydrous minerals such as Fe-rich serpentinites (*e.g.*, cronstedtite decomposes at 470 °C) and tochilinite (decomposes at ~ 245 °C; Tonui *et al.*, 2002, AMR, 15, 35) became amorphous and decomposed. (ii) [at HS-IV] Submicron-size secondary anhydrous silicates were formed as heating proceeded. The anhydrous silicates are ranging in composition from Mg-rich olivine to pyroxene. (iii) [at HS-IV] Metal grains generally enriched in Fe suggest that metal grains could be formed from Fe-bearing hydrous silicates, and the remnants formed Mg-rich anhydrous silicates as dehydration of hydrous minerals proceeded (Fig. 3.3-11). (iv) [HS-I to

IV] In terms of organic contents, with continued heating carbon was depleted progressively by oxidation to CO/CO_2 based on previous results of heating experiments using the Murchison meteorite. All the processes listed above possibly contribute to changes of spectral features. It is indicated that the Vis-IR spectral slope decreases mainly due to decomposition of hydrous minerals, and the 0.7- and 3-μm band weakening proceed with progress of dehydration of hydrous minerals and formation of FeNi metal grains and secondary anhydrous silicates.

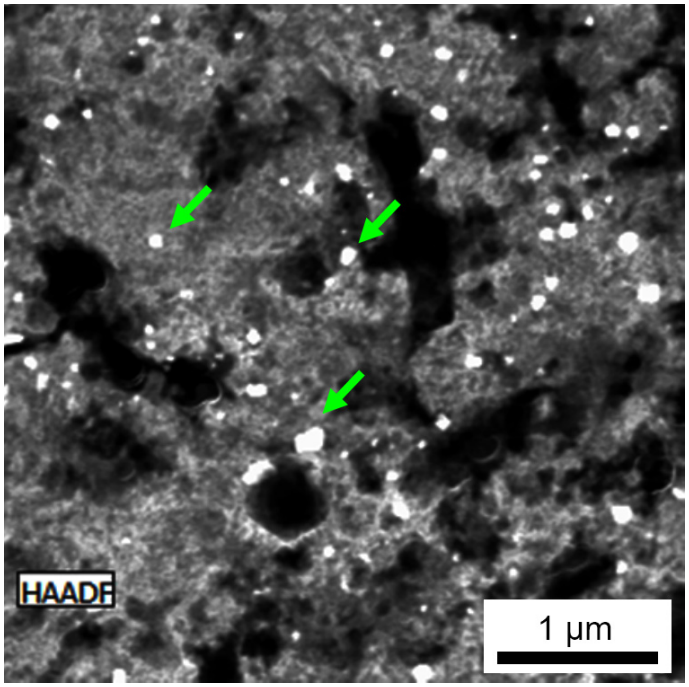

Fig. 3.3-11: HAADF-STEM image of matrices in Dhofar 735, classified as HS-IV sample. Small reflective grains (< 100 nm) indicated by arrows are observed in the entire region of the FIB sections.

3.4 Physical Properties of Minerals

Much of what we know about the deeper part of Earth's mantle comes from seismology: the study of sound waves passing through Earth's deep interior. Elastic waves excited by earthquakes are refracted and reflected within Earth and can be used to probe its depth and provide information on the elastic structure and ultimately the physics and chemistry of inaccessible regions down to the very centre of Earth. Seismic wave velocities depend on the elastic moduli and densities of the materials through which waves propagate. Both properties depend in turn on the crystal structure and chemical composition of the constituent minerals as well as on pressure, temperature and the configurations of individual grains such as grain size and crystal preferred orientation. The properties of grain boundaries between constituent minerals are of particular interest when the physical and chemical properties of single crystals are used to estimate properties of bulk rocks. Proton dynamics based on theoretical calculations are indispensable for obtaining a better understanding of the behaviour of water/ice for planetary interiors and potential H_2O-dominated exoplanets that we can access only on a computer.

The first five contributions investigate seismic wave velocities of sintered polycrystalline stishovite, single crystals of antigorite and phase E, Al-bearing akimotoite and $(Mg,Fe)CO_3$ carbonates. Experiments that directly constrain wave velocities were conducted using either laser light (Brillouin scattering, in the gigahertz range) or ultrasonic sound waves (often in the megahertz range) with simultaneous density measurements as a function of pressure (and temperature). Combination of velocities with precise density data from X-ray diffraction yields elastic moduli that can be compared with seismic measurements or the results of high-frequency experiments. In the case of non-transparent samples such as Fe-rich carbonates, sound velocities can be measured using nuclear inelastic scattering.

The next two contributions address the compressibility of Fe-bearing bridgmanite, the most abundant mineral in the Earth's lower mantle. Among the possible cation substitutions, Fe^{3+}-Al-coupled substitution in bridgmanite has been highlighted. Chemical variations of the valence state of iron and its site distribution in the orthorhombic perovskite structure largely control the bulk modulus, and results include an estimation of the bulk modulus of the pure $FeAlO_3$ endmember.

Silicate glasses often serve as proxies for silicate melts that may be present in Earth's mantle. The density of iron-bearing silicate glasses has been measured up to 150 GPa using X-ray absorption techniques in a diamond anvil cell (DAC). At 110 GPa a sudden increase in density as well as an increase in the opacity of the sample is observed. This behaviour is likely related to a change in the electronic state of iron. Metastable silica high-pressure polymorphs can also serve as structural proxies of silicate melts in the deep mantle. Single-crystal X-ray diffraction measurements of coesite compression provide better constraints on the local structures of silicates and silicate melts at deep mantle conditions.

Grain boundary diffusion and anisotropic thermal expansion/fracturing of olivine bicrystals play an important role in determining properties of olivine-dominated rocks. The former can control the mobility of incompatible elements, that can indirectly affect many REE-geothermometers based on partitioning, and the latter affects the formation of an interconnected permeability network important for magma ascent.

The final contribution highlights *ab initio* calculations of proton dynamics in high-pressure ice-VII. With increasing pressure, the O-H-O bond continuously symmetrises to form ice-X, a process that continues to be of great interest in the completion of the transformation to the symmetric ice-X phase.

a. *High-pressure elasticity of sintered polycrystalline stishovite: Effect of grain size and anisotropy on Brillouin scattering spectra (J. Buchen, H. Marquardt/Oxford, K. Schulze, A. Kurnosov, A. Chaudhari, S. Speziale/Potsdam and N. Nishiyama/Hamburg)*

High pressures in Earth's mantle may stabilise dense polymorphs of silica in SiO_2-rich rocks. Subducted oceanic crust may sink into the lower mantle where the original basalt would transform to a phase assemblage that is dominated by bridgmanite but contains up to 20 vol. % stishovite. Detecting SiO_2-rich rocks in Earth's lower mantle using seismology would help to better constrain the bulk composition of the mantle and to trace deep material cycles. In this context, stishovite stands out as it undergoes a ferroelastic phase transition at high pressure that may strongly influence the elastic properties of crystalline SiO_2 and may impose a specific signature on seismic waves that interact with SiO_2-rich rocks in the lower mantle. We performed high-pressure X-ray diffraction and Brillouin spectroscopy experiments on sintered polycrystalline stishovite and found that the elastic response of sintered polycrystalline SiO_2 deviates from observations on powders and single crystals, in particular at pressures close to the ferroelastic phase transition.

A focused ion beam was used to cut circular disks from a double-sided polished platelet of sintered polycrystalline stishovite with an average grain size 165 nm. These disks were 13 μm thick and loaded into diamond anvil cells. In each loading, a ruby sphere was placed next to the stishovite disk for pressure determination. We used neon as pressure-transmitting medium. X-ray diffraction patterns were collected along a compression path up to 73 GPa at beamline ID15 at the European Synchrotron Radiation Facility (ESRF, Grenoble). Unit cell parameters were extracted from diffraction patterns using Le Bail refinements. Shear wave velocities were derived from a total of 13 Brillouin scattering spectra that were recorded at pressures up to 60 GPa at Brillouin spectroscopy setups located at Deutsches Elektronen-Synchrotron (DESY, Hamburg) and Bayerisches Geoinstitut (BGI, Bayreuth).

The ferroelastic phase transition from tetragonal stishovite to orthorhombic $CaCl_2$-type SiO_2 results in a clear splitting of the tetragonal **a** axis into the orthorhombic **a** and **b** axes. We

located the phase transition around 46 GPa. In addition to the lattice distortion, we observed a kink in the volume compression curve at the phase transition that indicates a drop in the bulk modulus of sintered polycrystalline SiO_2 at the phase transition. We further analysed the pressure evolution of the unit cell parameters using Landau theory to predict the impact of the phase transition on the elastic properties of sintered polycrystalline SiO_2. While Landau theory predicts substantial softening of the shear modulus around the phase transition, shear wave velocities derived from Brillouin spectroscopy on sintered polycrystalline stishovite do not show the predicted reduction, but rather increase throughout the relevant pressure range (Fig. 3.4-1a). To resolve this apparent contradiction, we used the elastic properties predicted by Landau theory to model the sampling of individual grains by Brillouin spectroscopy and the effect on observed sound wave velocities of a polycrystalline sample (Figs. 3.4-1a and 1b). We found that average sound wave velocities derived from Brillouin spectra of polycrystalline samples can deviate from aggregate sound wave velocities in a systematic way. Large grain sizes and strong acoustic anisotropy are expected to amplify this deviation as observed here in the vicinity of the ferroelastic phase transition from stishovite to $CaCl_2$-type SiO_2. While the differences in shear wave velocities predicted by Landau theory and derived from Brillouin spectra can partly be explained by this sampling bias, polycrystalline silica appears to be stiffer than predicted close to the ferroelastic phase transition.

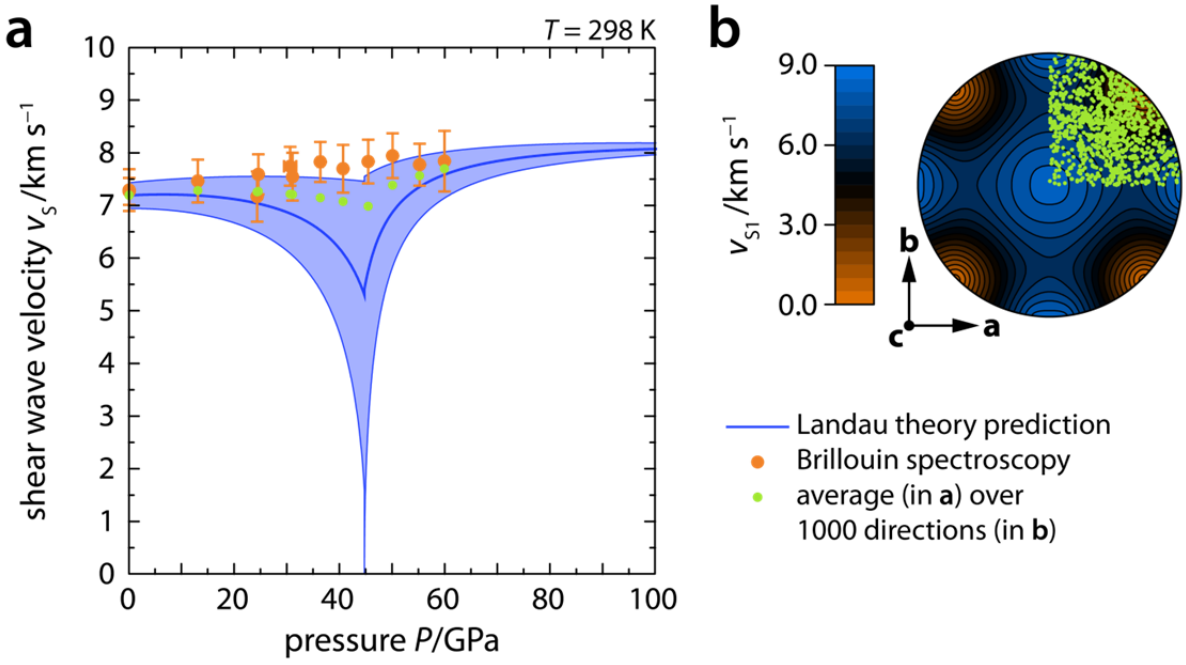

Fig. 3.4-1: a) Aggregate shear wave velocities of SiO_2 across the ferroelastic phase transition from stishovite to $CaCl_2$-type SiO_2. Shading indicates Voigt (upper) and Reuss (lower) bounds on the Landau theory prediction (Voigt-Reuss-Hill average). b) Equal-area projection of the slower shear wave velocity (S1) in a stishovite single crystal at the ferroelastic phase transition (45 GPa, 298 K). Green dots show 1000 random directions that were used to model the observed average shear wave velocities shown in a). Note that observed and modelled shear wave velocities disagree at pressures close to the phase transition.

b. *Single-crystal elasticity of natural antigorite studied using Brillouin spectroscopy (N. Satta, H. Marquardt/Oxford, A. Kurnosov, T. Boffa Ballaran, S. Speziale/Potsdam and G. Capitani/Milan)*

Water-bearing minerals are transported into Earth's mantle though subduction of hydrated oceanic lithosphere. A large amount of structural water (~ 13 wt. %) can be stored in altered olivine and pyroxenes that form serpentine group minerals. Antigorite, a monoclinic phyllosilicate, is the high-pressure/high-temperature form of serpentine and is stable down to 180-200 km depth. When antigorite eventually breaks down, it releases fluids that migrate into the overlying mantle wedge. This fluid flow is thought to reduce mantle viscosity and trigger arc magmatism and earthquakes within subduction zones, linking antigorite breakdown to global-scale geological events. Knowledge of the amount and distribution of antigorite in subduction zones is crucial to quantifying water reservoirs in subduction regions and their implications for mantle dynamics. Previous works have suggested that antigorite could be mapped using seismology; hence studies of the elasticity of antigorite have recently been performed using both experiments and computational methods. However, an accurate determination of its single-crystal elastic properties has been hampered by the scarcity of samples suitable for experiments and their fragility.

The goal of our project is to determine all 13 individual elastic components of the elastic stiffness tensor of antigorite through Brillouin scattering measurements at ambient conditions on double-sided polished samples. We are using natural samples that have been previously chemically and structurally characterised using a series of analytical techniques already described in the literature. Three crystals were optically selected and double-sided polished to a final thickness of about 30 μm. Using Brillouin spectroscopy, we are determining acoustic wave propagation velocities along different crystallographic directions. The combination of measured acoustic wave velocities, densities and crystallographic orientations of these three platelets can be included in a least square fitting procedure based on Christoffel's equations to constrain the complete elastic stiffness tensor. So far, acoustic velocities have been probed in several crystallographic orientations at ambient condition in two out of three platelets (Fig. 3.4-2).

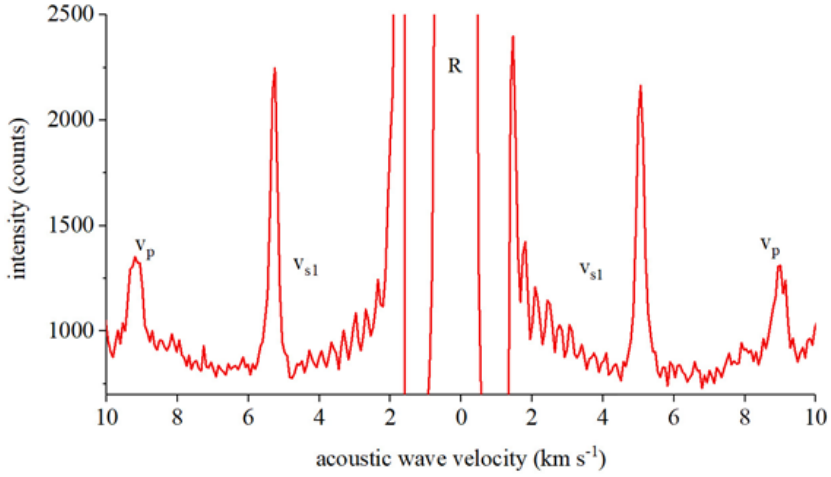

Fig. 3.4-2: Representative Brillouin spectrum of antigorite single crystal at ambient conditions. Labelled peaks are associated with inelastic anti-Stokes and Stokes scattering by longitudinal (V_P) and transversal (V_{S1}) modes. The peak arising from elastically scattered light is indicated by "R".

c. *Elasticity of iron-bearing phase E single crystals from Brillouin scattering measurements and implications for the mapping of "water" in Earth's mantle (N. Satta, H. Marquardt/Oxford, A. Kurnosov, J. Buchen, T. Kawazoe/Hiroshima and T. Boffa Ballaran)*

Through plate tectonics, water-containing minerals are transported into Earth's interior by subduction processes. At larger depths, water can be stored in Dense Hydrous Magnesium Silicate (DHMS) phases. Among the many DHMSs, phase E is known to have both low bulk modulus and density. These two physical parameters are of particular importance in a seismological context because, together with the shear modulus, they control the propagation velocities of seismic wave in a solid material. Despite this importance, however, phase E shear elastic properties have not yet been measured, hindering the quantification of phase E abundance at depth through interpretation of seismic velocity heterogeneities detected by seismological investigations.

We investigated for the first time the full single crystal elastic properties of phase E. Two optically clear iron-bearing phase E crystals were selected, double-sided polished and investigated using Brillouin spectroscopy to probe acoustic wave velocities along several crystallographic directions at ambient conditions. We used the electron microprobe, Mössbauer spectroscopy and single-crystal X-ray diffraction to accurately determine the density of our material. We determined all six non-independent components of the elastic stiffness tensor, employing a least squares fit procedure based on the Christoffel equation (Fig. 3.4-3). This procedure requires the density and a database of acoustic wave velocities along determined crystallographic directions. We found that phase E has very low aggregate acoustic velocities, significantly lower than other mantle minerals. We modelled acoustic

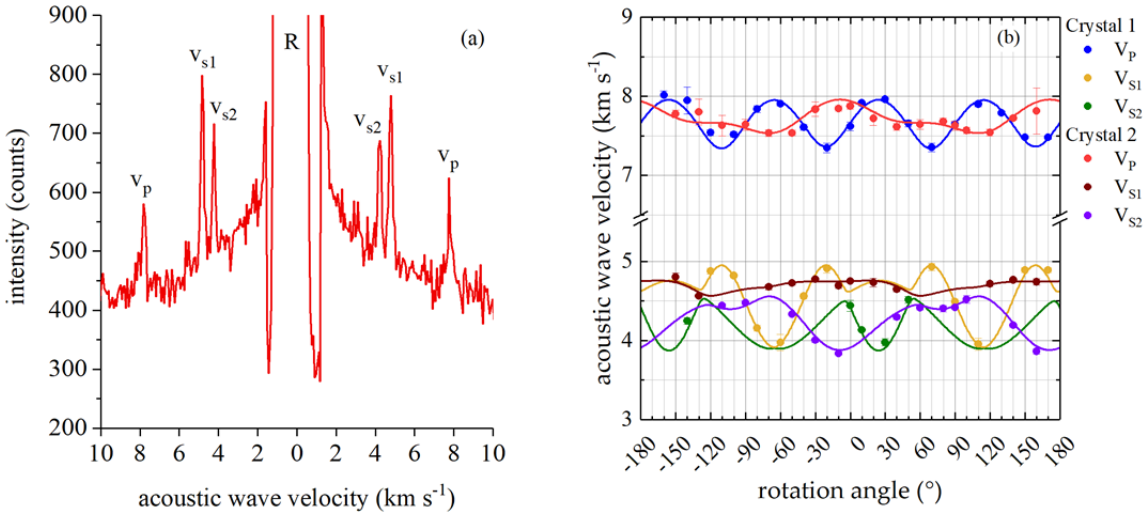

Fig. 3.4-3: a) Representative Brillouin spectrum of iron-bearing phase E. Labelled peaks arise from inelastic anti-Stokes and Stokes scattering by longitudinal (V_P), transversal fast (V_{S1}) and transversal slow (V_{S2}) acoustic modes. The peak associated with elastically scattered photons is marked with "R"; b) Measured (circles) and modelled (curves) acoustic wave velocities resulting from a least squares fit of the Christoffel equation as a function of the rotation angle.

wave velocities propagating through dry and hydrous mantle rocks at ambient conditions to evaluate the potential influence of a small amount of phase E in subduction regions. Our results show that phase E can strongly influence the propagation of seismic waves, reducing their velocity and producing seismologically detectable seismic velocity heterogeneities in subducting slabs. Our finding could be used to improve the interpretation of seismic tomography images and facilitate "seismic mapping of water" in Earth's mantle. We anticipate that our study could be the starting point for future high-pressure and high-temperature experiments to quantitatively predict the role of phase E under more realistic mantle conditions.

d. *The effect of Al on the acoustic wave velocities of akimotoite (N.C. Siersch, T. Boffa Ballaran, Z. Liu, T. Ishii, D.J. Frost and T. Katsura, in collaboration with Y. Wang and T. Yu/ Argonne)*

Akimotoite, a $MgSiO_3$ polymorph, may be present at pressures between 22 and 24 GPa at temperatures lower than the mantle geotherm, conditions that are possible when cold slab material is subducted into the lower mantle and stagnates and/or accumulates at the 660 km discontinuity. In this scenario, akimotoite may play a key role in resolving the discrepancy between globally observed seismic velocities and velocities calculated using the elastic properties of the two main minerals present at the base of the transition zone, ringwoodite and majoritic garnet. The elastic properties of the $MgSiO_3$-akimotoite end-member have been studied recently; however since slab material contains harzburgite and MORB material that is rich in Al, understanding the effect of Al substitution on the wave velocities of akimotoite is crucial for reproducing the transition zone velocity structure. To this end ultrasonic measurements on Al-rich akimotoite have been performed.

Two samples for each starting material containing 2.5 mol. % Al_2O_3 and 20 mol. % Al_2O_3 components were synthesized at 27 GPa and 800 °C for 1 hour in the IRIS-15 multianvil apparatus installed at BGI. All four well-sintered samples were carefully investigated using a micro-focus X-ray diffractometer equipped with a Co tube (λ=1.79026 Å) to confirm the formation of pure akimotoite. Further analyses using scanning electron microscopy and the electron microprobe were performed to determine the chemical composition of each sample and a grain size around 1 µm. To perform ultrasonic measurements at high pressure, the samples were polished into disks with perfectly parallel faces and inserted into modified 10/4 cell assemblies. Re foil heaters were used with laser cut windows to enable measurement of densities using *in situ* synchrotron X-ray diffraction and sample lengths using X-ray radiography. A D-type thermocouple was used to monitor the temperature. $LiNbO_3$ transducers that were suitable for producing and detecting P- and S-waves simultaneously were glued with a small amount of epoxy onto one truncation of an TF05 anvil polished to mirror quality. High-pressure/high-temperature experiments were performed up to 25 GPa and 800 °C at the 13 ID-D beam line of the Argonne Photon Source using an ultrasonic system to collect compressional and shear wave velocities of the different akimotoite compositions at each pressure and temperature point.

Figure 3.4-4 shows that the incorporation of Al into the akimotoite structure (blue and black circles) clearly reduces both the compressional and shear wave velocities relative to the $MgSiO_3$ akimotoite end-member (red circles). This is surprising since the Al_2O_3 end-member corundum (green circles) has much faster wave velocities than akimotoite. This behaviour suggests a large non-ideality in the akimotoite-corundum system. We note, however, that even taking into account the wave velocity reduction due to Al substitution, both compressional and shear wave velocities of akimotoite remain faster than those of majoritic garnet (purple circles).

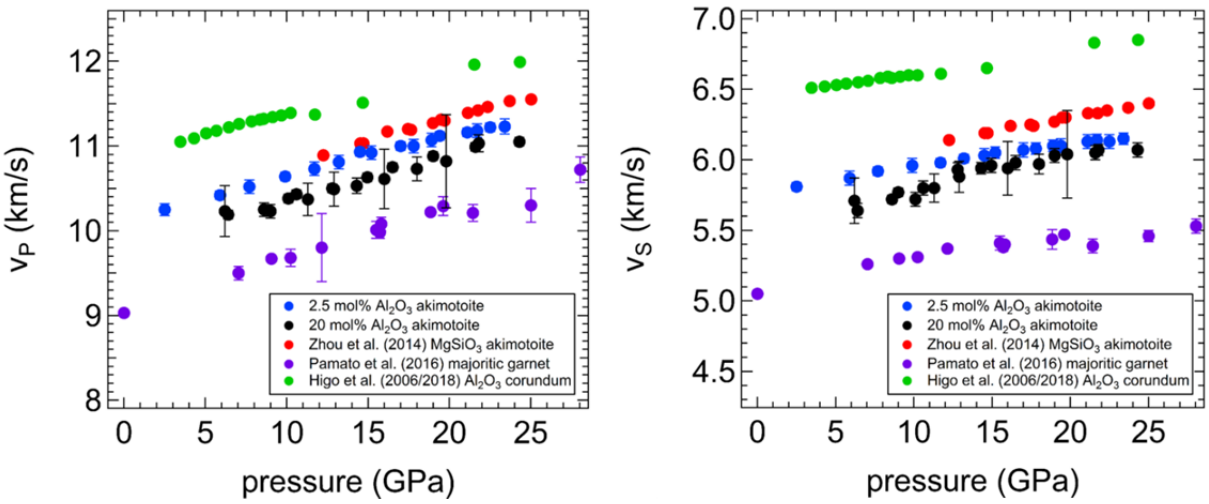

Fig. 3.4-4: Compressional and shear wave velocities versus pressure of two Al-bearing akimotoite compositions compared to data from the literature: $MgSiO_3$-akimotoite (Zhou *et al.*, PEPI, 228, 97-105, 2014), Al_2O_3-corundum (Higo *et al.*, PEPI, 159, 276-285, 2006; Higo *et al.*, Rev. Sci. Inst, 89, 014501, 2018) and majoritic garnet (Pamato *et al.*, EPSL, 451, 114-124, 2016).

e. *The seismic detectability of carbonates in Earth's mantle (S. Chariton, C.A. McCammon, D. Vasiukov/Bayreuth, M. Stekiel/Frankfurt/M., V. Cerantola/Grenoble, I. Kupenko/Münster, G. Aprilis and T. Fedotenko/Bayreuth, E. Koemets, A.I. Chumakov/Grenoble and L.S. Dubrovinsky)*

For over a decade carbonates have been proposed to be a major carrier of carbon into Earth's mantle. Natural samples support this theory, including diamond inclusions and mantle xenoliths, but such samples from great depths are rare, and thus an experimental approach has been traditionally used to study carbonate systems. However, seismological observations may also have information as to which C-bearing accessory phases are abundant in the mantle, how they influence dynamic processes and whether we can quantify them. To use seismic information, it is first necessary to determine elastic properties of carbonates at pressures and temperatures relevant to Earth's mantle.

Nuclear Inelastic Scattering (NIS) is a useful technique to study lattice dynamics and determine sound velocities of Fe-bearing samples. Here we present our results on sound velocities in the $FeCO_3$-$MgCO_3$ system. According to previous studies, carbonates with ferromagnesian composition are expected to persist in Earth's deep mantle following their subduction. We performed NIS measurements on synthetic $FeCO_3$ and $(Mg_{0.74}Fe_{0.26})CO_3$ samples using panoramic diamond anvil cells to generate pressures up to ~ 66 GPa and a double-sided laser-heating system to obtain temperatures up to ~ 1800 K. The ^{57}Fe enriched samples were synthesized using a multianvil apparatus at BGI and NIS measurements were performed at the Nuclear Resonance beamline, ID18 at the European Synchrotron Radiation Facility (ESRF), France. We made a complementary compressibility study of the two samples using single-crystal X-ray diffraction (SCXRD) at the ID15b beamline, ESRF.

Sound velocities increase gradually on cold compression at pressures that correspond to shallow lower mantle depths (*i.e.*, < 45 GPa) (Fig. 3.4-5 top). Our Mg-rich carbonate sample has nearly 19 % higher velocity than the Fe end-member, in good agreement with previous studies that used methods different from NIS. We also investigated the effect of the Fe^{2+} spin transition that is complete above 50 GPa. The sudden volume collapse of FeO_6 octahedra that follows Fe spin-crossover is associated with a substantial velocity increase (Fig. 3.4-5 top), where Debye velocities increase by ~ 19 % and ~ 9 % for $FeCO_3$ and $(Mg_{0.74}Fe_{0.26})CO_3$, respectively. During *in situ* laser heating of $FeCO_3$ at pressures and temperatures relevant to transition zone depths, the velocities appear similar to those of the original sample at room temperature (Fig. 3.4-5 top). On the other hand, laser-heating of siderite at higher pressures produces a dramatic velocity drop (Fig. 3.4-5 top). According to previous studies, $FeCO_3$ thermally decomposes to form high-pressure Fe_3O_4 (Bbmm) at the pressure-temperature conditions of our NIS experiments.

We determined the primary and shear wave velocities of our samples using the Debye velocities from NIS and the density and bulk modulus values from SCXRD. By comparing the V_S values of three carbonate compositions based on our NIS measurements with the PREM model (Fig. 3.4-5 bottom) and considering that $(Mg_{0.85}Fe_{0.15})CO_3$ is the most realistic composition for the Earth's mantle and that the present seismic resolution limit is close to 1 %, we have estimated the amount of CO_2 wt. % that needs to be present in the subduction slab in order to induce a 1 % velocity drop at various depths. At shallow depths (~ 300 km) carbonates will be undetectable by geophysical methods since their velocity contrast to other upper mantle lithologies is negligible. At greater depths (~ 1450 km) the contrast is more intense, however our laser-heating experiments suggest that Fe-oxides may play a more important role in the velocity profiles of the lower mantle compared to carbonates. Considering that up to 80 wt. % of subducted CO_2 is estimated to return to the atmosphere through degassing processes, we conclude that nearly 22 wt. % of CO_2 would be needed in the subduction slab in order to detect a 1 % shear wave velocity decrease compared to non-carbonated lithologies at transition zone to lower mantle depths. A few subduction trenches have such high CO_2 contents, namely Guatemala, Peru and Colombia. These regions are therefore of high interest for future geophysical surveys looking for carbonates in the deep Earth.

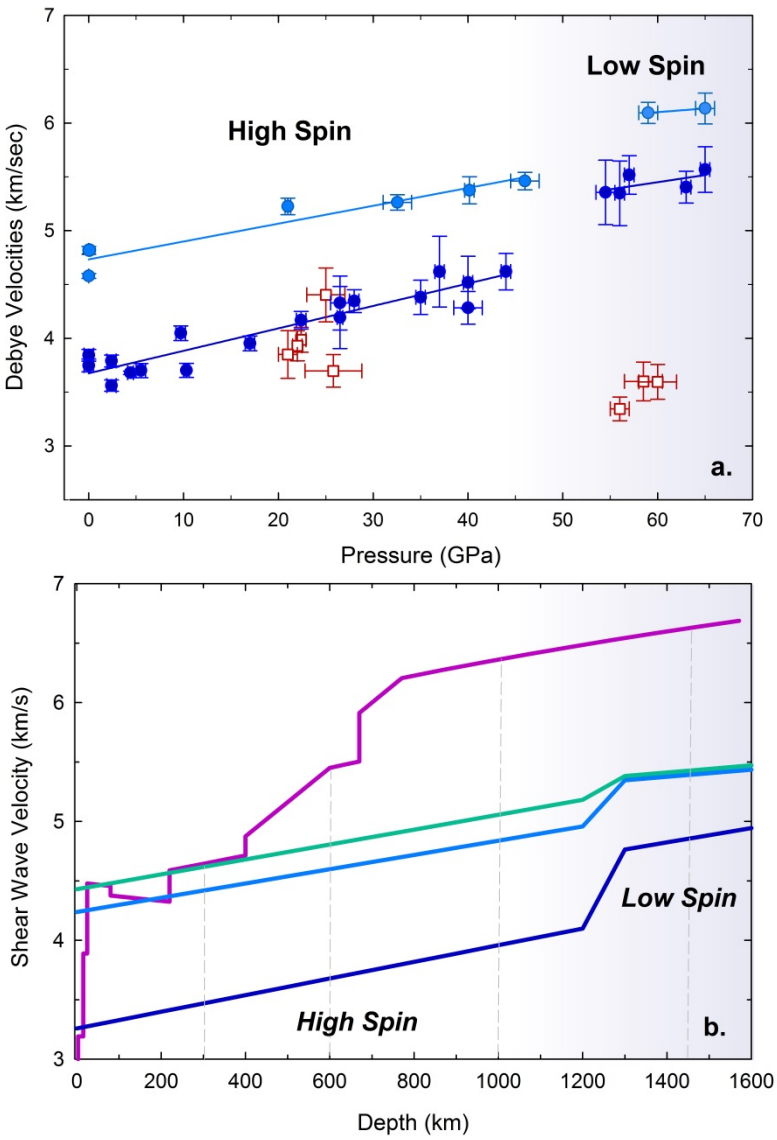

Fig. 3.4-5: top) Debye sound velocities of siderite and Fe-bearing magnesite with increasing pressure. Dark blue: $FeCO_3$, light blue: $Mg_{0.74}Fe_{0.26}CO_3$, red: $FeCO_3$ during laser heating. bottom) Shear wave velocities (VS) of the PREM model (magenta) compared to our modelled carbonate compositions as a function of depth (dark blue: $FeCO_3$, light blue: $Mg_{0.74}Fe_{0.26}CO_3$, green: $Mg_{0.85}Fe_{0.15}CO_3$). The effect of temperature is not taken into account in this plot (see text for details).

f. *Compressibility of Fe^{2+}-bearing bridgmanite single crystals (M. Urgese, R. Huang, A. Kurnosov, T. Boffa Ballaran and D.J. Frost)*

Over the past decades, the compressibility of pure $MgSiO_3$ bridgmanite has been extensively studied because of its expected major influence on properties of Earth's lower mantle based on its abundance. Several studies have also been performed to document the effect of cation substitution on physical properties of bridgmanite, although discrepant results have been reported. Among the possible cation substitutions, those involving Fe are of particular importance because iron may be responsible for mantle heterogeneities. Some consensus appears to have been reached in high-pressure single crystal X-ray diffraction studies that show an increase in compressibility of bridgmanite with increasing Fe^{3+}-Al coupled substitution. The effect of Fe^{2+}, however, is more difficult to constrain due to the likely presence of some Fe^{3+} even in bridgmanite samples synthesised at reduced conditions.

We studied two bridgmanite samples that were accurately characterised using single-crystal X-ray diffraction, scanning electron microscopy, electron microprobe analysis and Mössbauer spectroscopy. The Fe^{3+}-Al coupled substitution is identical for both samples (0.04 $Fe^{3+}AlO_3$ content) and they differ uniquely in their Fe^{2+} content, one being very low (0.01 atoms per formula unit) and one being much larger (0.12 atoms per formula unit). Single-crystal structural refinements of crystals selected from the two bridgmanite samples showed a larger orthorhombic distortion, *i.e.*, a larger octahedral tilting, with respect to the end-member $MgSiO_3$, with the more Fe^{2+}-rich sample having a smaller distortion than the other crystal. We conclude that the orthorhombic distortion increases even for a very small amount of Fe^{3+}-Al coupled substitution, but decreases with increasing Fe^{2+} content likely due to the slightly larger size of Fe^{2+} compared to Mg.

To study the compression of bridgmanite, we loaded two thin crystals, one for each composition, into the same diamond anvil cell together with a ruby chip for pressure calibration and Ne as a pressure-transmitting medium. Unit-cell lattice parameters were measured at different pressures up to 15 GPa. No significant difference was observed in the compressibility of the two samples (Fig. 3.4-6) and a Birch-Murnaghan equation of state used to fit the P-V data showed identical bulk moduli for the two samples within uncertainty and no change with respect to the $MgSiO_3$ bridgmanite end-member.

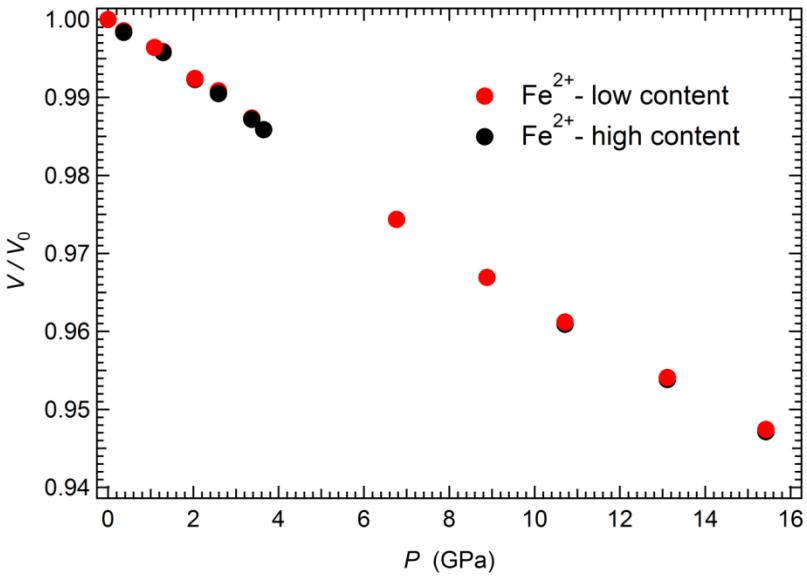

Fig. 3.4-6: Pressure variation of the unit cell volume of Fe^{2+}-bearing bridgmanite normalised to room pressure values.

g. *Compressibility of $Fe_{0.5}Mg_{0.5}Al_{0.5}Si_{0.5}O_3$ bridgmanite at pressures up to 60 GPa (I. Koemets, Z. Liu, E. Koemets, T. Katsura and L.S. Dubrovinsky, in collaboration with M. Hanfland/Grenoble)*

Bridgmanite is widely considered to be the most abundant mineral in Earth's lower mantle, so its properties largely control the rheology of this region. Chemical variations in bridgmanite

may be an important factor that could help to explain observed lower mantle heterogeneities; hence a large number of studies have focused on the behaviour of bridgmanite at mantle conditions. Studies of silicate end-members have also become a subject of great interest.

Crystalline material with composition $Fe_{0.5}Mg_{0.5}Al_{0.5}Si_{0.5}O_3$ was synthesised in a Kawai-type multianvil apparatus (IRIS-15) at Bayerisches Geoinstitut. The starting material was reagent-grade oxides of MgO, SiO_2, and Al_2O_3 with a nominal bulk composition of 50 mol. % $MgSiO_3$ + 50 mol. % $FeAlO_3$. Quench experiments were performed at 27 GPa and 2000 K after heating for 20 hours. The phase recovered at ambient conditions crystallises in a $LiNbO_3$-type structure (space group $R3c$, with a = 4.8720(6) Å, c = 12.898(2) Å, V =265.14(8) Å^3), and almost all iron in the sample is ferric within detection limits. Recovered crystals were compressed up to 60 GPa in a BX90-type diamond anvil cell with 250 µm culet Bueler-Almax diamonds. We used rhenium as a gasket material and neon as a pressure-transmitting medium. At each pressure point, we collected single crystal X-ray diffraction data at beamline ID15 at the European Synchrotron Radiation Facility (ESRF), Grenoble.

Upon compression, the $LiNbO_3$-structured phase transforms to a distorted perovskite structure with space group $Pnma$ at pressures of 5 to 10 GPa. The bicapped prism (A-site) is occupied by Fe and Mg (0.5/0.5) and the octahedral B-site is occupied by Al and Si (0.5/0.5). Fitting the pressure-volume data with a second order Burch-Murnaghan equation of state gives V_0 = 171.2(2) Å^3 and K_0 = 221(3) GPa (Fig. 3.4-7a). This measurement, together with previously reported bulk moduli for Al, Fe-bearing bridgmanite, allows us to estimate the bulk modulus of the pure $FeAlO_3$ end-member (Fig. 3.4-7b).

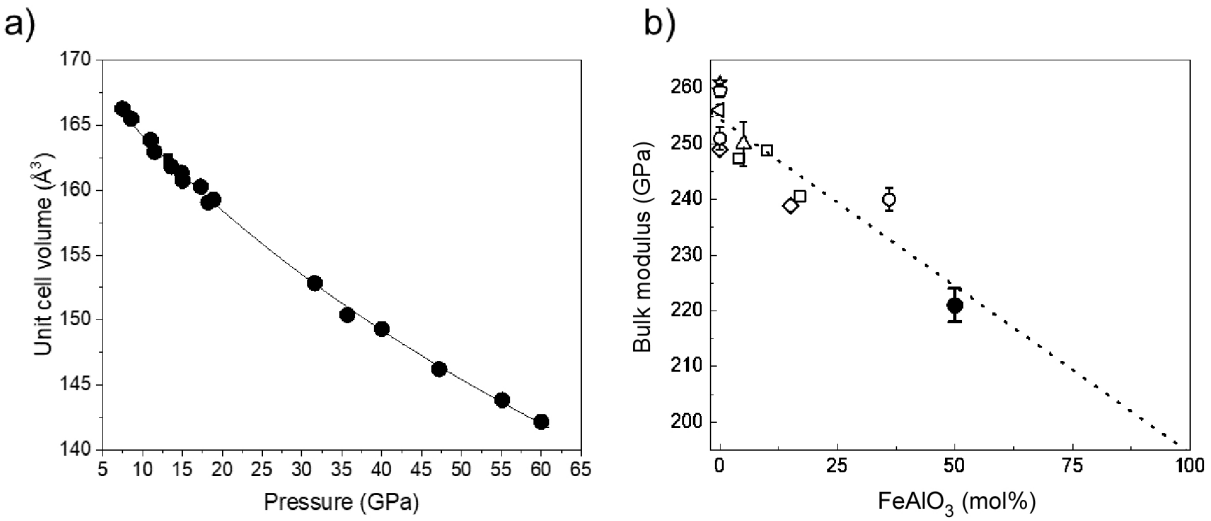

Fig. 3.4-7: a) Unit cell volume versus pressure for $Fe_{0.5}Mg_{0.5}Si_{0.5}Al_{0.5}O_3$ bridgmanite. Experimental points were obtained in different experimental runs and fitted with a second order Birch-Murnaghan equation of state (solid line). b) Bulk moduli of Fe,Al-bearing bridgmanite solid solutions as a function of $FeAlO_3$ content. A linear fit (dashed line) to the value from this study (solid circle) and data from the literature (open symbols) gives an estimate for K_0 for end-member $FeAlO_3$ of 194(8) GPa.

h. *Density of iron-rich bearing glass up to 150 GPa (S. Petitgirard, I. Kupenko/Münster, I.E. Collings/Grenoble, E. Jennings, I. Blanchard, W.J. Malfait/Zürich, M. Cotte and A.W. Johannes/Grenoble, D.J. Frost, L.S. Dubrovinsky and D.C. Rubie)*

The density contrast in Earth's lower mantle is the main parameter that controls the entrainment and settlement of matter. During early Earth's formation, tremendous amounts of melt could have been generated due to large planetary impacts such as the moon-forming impact and accumulated on top of the core-mantle boundary, facilitating the formation of a deep basal magma ocean. The key parameter that controls a potential density crossover of solid and melt is the iron content and its influence on melts at high pressure. In order to measure the density of amorphous silicate glass as an analogue for melt at these conditions, we developed a unique technique using the X-ray absorption method in a diamond anvil cell.

Our previous results showed that the densities of $MgSiO_3$ and SiO_2 glasses could be similar to their crystalline phases at pressures of the deep lower mantle. Recently we extended the data to iron-bearing $Mg_{0.7}Fe_{0.3}SiO_3$ glass up to 150 GPa in measurements performed at the European Synchrotron Radiation Facility (ESRF) in Grenoble. At 110 GPa we observed a sudden increase in density as well as an increase in the opacity of the sample (Fig. 3.4-8). This behaviour strongly suggests that a change related to iron takes place, leading to an increase of density of the glass and melt. We conclude that iron-rich magmas could densify at pressures above 110 GPa. Further work is planned using synchrotron Mössbauer source spectroscopy on the same composition to investigate the electronic structure of iron at such conditions to unravel the mechanisms behind the density increase.

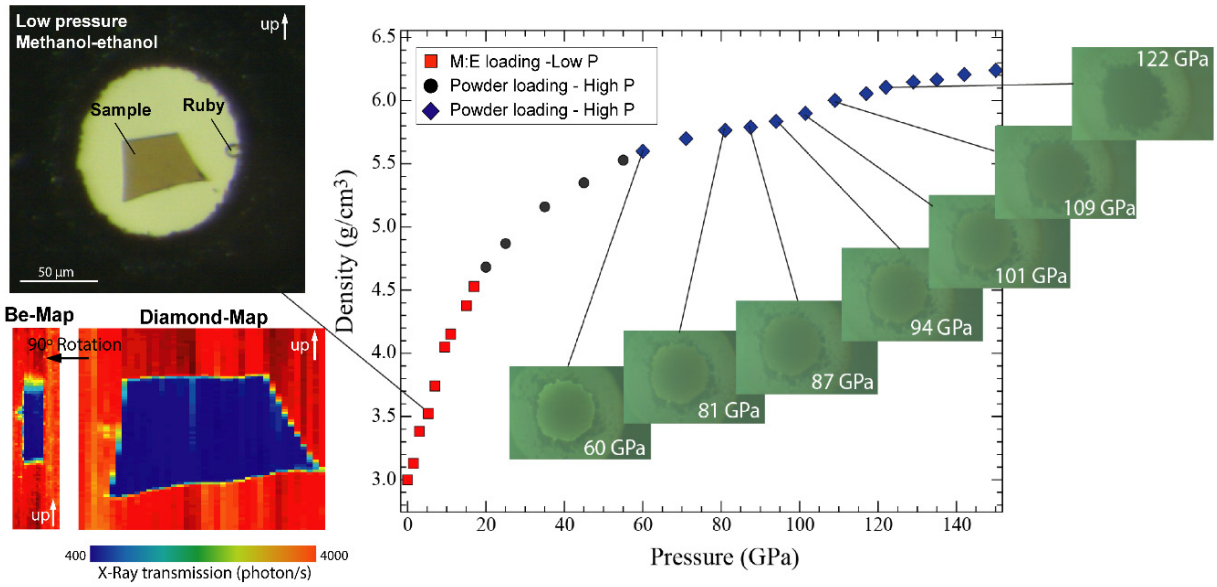

Fig. 3.4-8: Density of $Mg_{0.7}Fe_{0.3}SiO_3$ glass at high pressure. Left: sample image at low pressure in a methanol:ethanol (M:E) mixture, with the corresponding X-ray absorption maps of the sample through the Be gasket (lower left) and diamonds (lower right). Right: high-pressure data with sample images up to 150 GPa. At 110 GPa the density increases by ~ 5 % and the sample becomes opaque.

i. *Metastable silica high-pressure polymorphs as structural proxies of deep Earth silicate melts (E. Bykova/Hamburg, M. Bykov, A. Černok, N.A. Dubrovinskaia/Bayreuth, L.S. Dubrovinsky, J. Tidholm and S.I. Simak/Linköping, O. Hellman/Pasadena, M. Belov and I. Abrikosov/Moscow, H.-P. Liermann/Hamburg, M. Hanfland/Grenoble, C. Prescher/Köln and V.B. Prakapenka/Argonne)*

Modelling of processes involving deep Earth liquids requires information on their structures and compression mechanisms. However, knowledge of the local structures of silicates and silica (SiO_2) melts at deep mantle conditions and their densification mechanisms is still limited. A convincing method to obtain structural models of non-crystalline silica material is to compare (or fit) experimental total scattering data with pair distribution functions of known crystalline phase(s). So far, however, no crystalline phases are known that are able to describe features of the total scattering data of silica and/or silicate glass (acting as proxies of melt) at high pressure.

Here we apply single-crystal X-ray diffraction in diamond anvil cells in order to study SiO_2 phases that appear on compression of coesite as well as their high-pressure behaviour. Several independent experiments were performed at different synchrotron radiation facilities at pressures over 70 GPa. Previously we reported structural transformations to coesite-II and coesite-III at pressures above 20 and 25 GPa, respectively. On compression beyond ~ 30 GPa, a new set of reflections indicates the presence of a new triclinic (space group *P*-1) phase that we called coesite-IV, with lattice parameters distinctly different to any known for other coesite-derived polymorphs. Upon further compression, the reflections of coesite-IV split and a new triclinic (space group *P*-1) phase, coesite-V, emerges. Above ~ 50 GPa, only coesite-V is found. The structure of coesite-IV has *tetra*-, *penta*- and *hexa*-coordinated silicon, while the structure of coesite-V has only *penta*- and *hexa*-coordinated silicon (Fig. 3.4-9). The structures of coesite-IV and coesite-V may be considered as a three-dimensional framework of face- and edge-sharing octahedra with the empty space filled by SiO_5 and SiO_4 (in coesite-IV) or only SiO_5 (in coesite-V) polyhedra (Fig. 3.4-9). The presence of face-sharing octahedra, a structural element never observed or even expected in silica, silicates or glasses, violates Pauling's third rule. Our results suggest that possible silicate liquids in Earth's lower mantle may have complex structures, making them more compressible compared to previously considered models.

We found that pair-distribution functions calculated for coesite-IV and coesite-V indeed closely reproduce experimental data reported recently for compressed silica glass and molten basalt (Fig. 3.4-10). Moreover, above 45 GPa the densities of coesite-IV and coesite-V coincide with the density of silica glass within measurement uncertainty. These observations are strong arguments in support of analogous atomic arrangements in compressed silica glass (and molten basalt) and in coesite-IV or coesite-V. The presence of "unconventional" structural elements like SiO_5 polyhedra and face-sharing octahedra in silicate melts would decrease their density and, even more important, cause a drop in their bulk sound velocity (by about 10 % over a 100-GPa pressure range). If silicate liquids with such properties are present in the lower mantle, they should be seismically detectable.

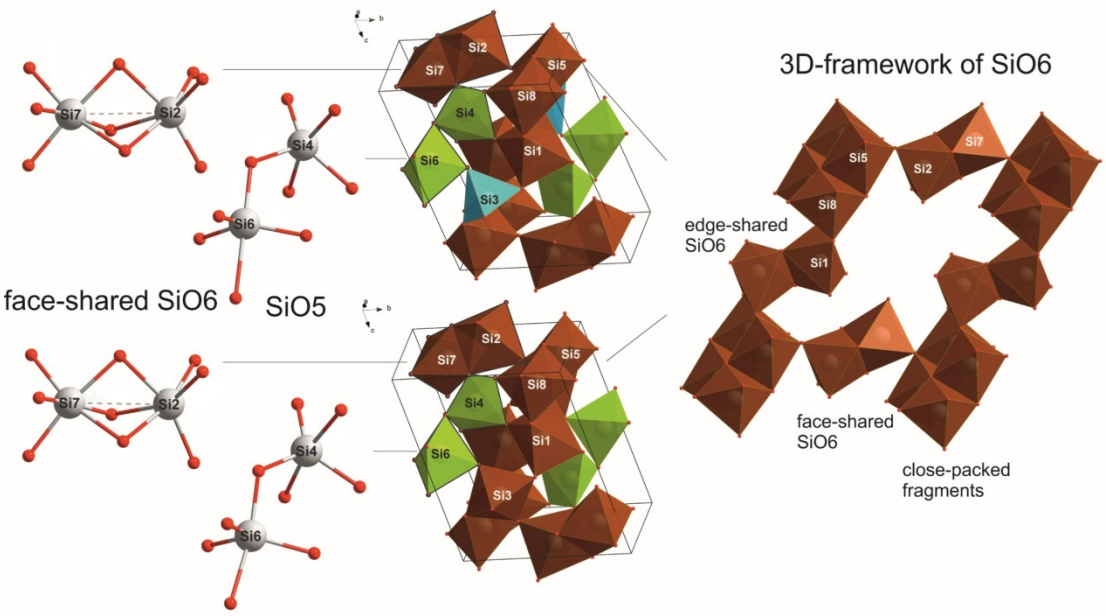

Fig. 3.4-9: Crystal structures of coesite-IV (upper) and coesite-V (lower). Left: ball and stick models representing polyhedral building blocks of coesite-IV and coesite-V (two SiO_6 octahedra sharing a face; two SiO_5 polyhedra sharing a corner). Middle: polyhedral models of coesite-IV and coesite-V (SiO_6 octahedra are brown, SiO_5 polyhedra are green; SiO_4 tetrahedra are blue). Right: Fragment of the structures that are similar for both coesite-IV and coesite V, showing a 3D framework of SiO_6 octahedra.

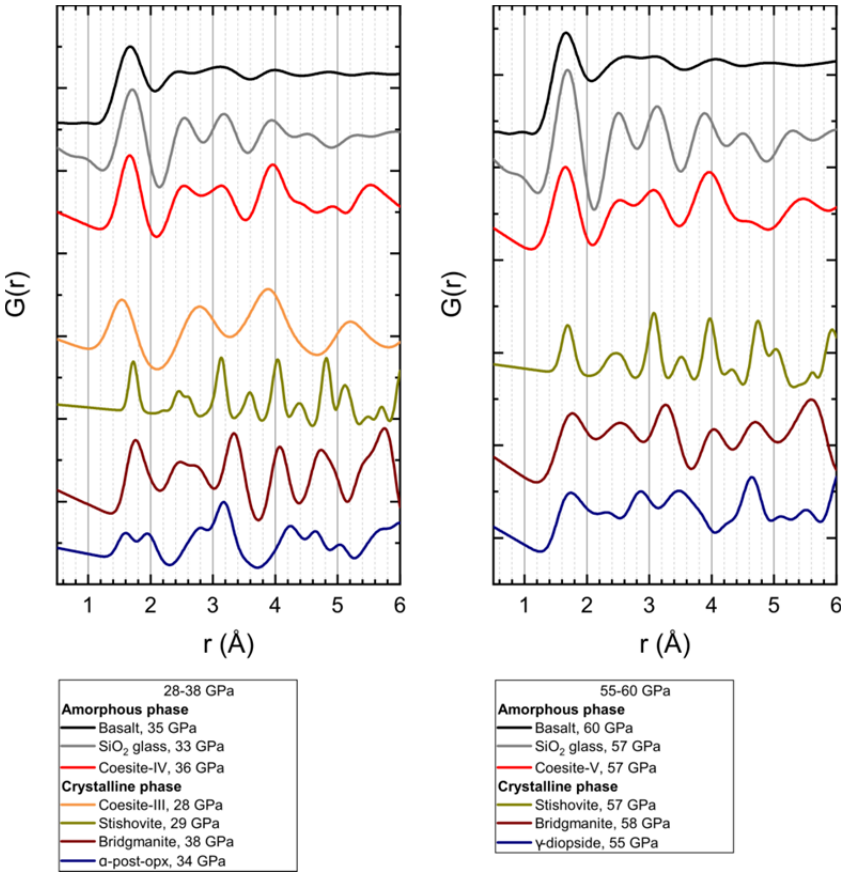

Fig. 3.4-10: Pair distribution functions of silica and silicate phases. Pair-distribution functions calculated for silica polymorphs and silicates are compared with those for basalt and silica glass measured at different pressures: left, in the range from 28 to 38 GPa; right, in the range from 55 to 60 GPa.

j. *Lutetium grain boundary diffusion and accompanying segregation along different grain boundary geometries in forsterite (J. Polednia, R. Dohmen/Bochum and K. Marquardt)*

The mobility of incompatible elements such as rare earth elements (REEs) in olivine grain boundaries plays an important role in mantle rocks because: 1) incompatible elements and isotopes can be fractionated by grain boundary diffusion and thus affect geochemical signatures, and 2) REE mobility along olivine grain boundaries can indirectly affect REE-geothermometers (for example, the REE-in-two-pyroxene thermometer) when applied to olivine-rich rocks. REE-thermometers can be applied correctly only when equilibrium between different, co-existing REE-containing minerals is achieved. The diffusion length of elements along grain boundaries controls the chemical equilibration between non-touching grains and is governed by grain boundary diffusion and grain boundary segregation. Only a few grain boundary diffusion studies on polycrystalline olivine aggregates have been performed, and grain boundary diffusion is far from being understood. We have therefore investigated the diffusion and segregation characteristics of lutetium along different forsterite grain boundaries. Lutetium is a heavy REE and is considered to be incompatible in olivine.

We produced two high angle grain boundaries (HAGBs) and one low angle grain boundary (LAGB) from synthetic forsterite (space group *Pbnm*) using the direct wafer bonding method, and characterised the grain boundaries according to the following scheme: angle[rotation axis]/(contact planes). The advantages of using pure forsterite are the good crystal quality and a well-defined contaminant-free chemistry. We synthesized a 90° HAGB 90°[001]/(100)&(010) (one of the most abundant grain boundaries in undeformed olivine-bearing rocks), a symmetric 60°[100]/(011) HAGB, and a 10°[010]/(5° off 100) LAGB. Diffusion anneals were performed in a gas mixing furnace at temperatures of 1000-1300 °C under controlled fO_2 at the fayalite-quartz-magnetite buffer. Element concentrations were mapped using energy dispersive X-ray spectroscopy in scanning transmission electron microscopy mode.

Volume and grain boundary diffusion coefficients, and the segregation factor D_{vol}, D_{gb}, and s, were determined by fitting a numerical diffusion model to the data: at 1300 °C, $D_{\mathrm{vol}}^{[011]}$ yields 1.5×10^{-15} m^2/s and $D_{\mathrm{vol}}^{[\sim c]}$ yields 2.0×10^{-15} m^2/s, while at 1200 °C, $D_{\mathrm{vol}}^{[011]} = D_{\mathrm{vol}}^{[\sim c]} = 1.1\times10^{-15}$ m^2/s. The product sD_{gb} was determined for the 10° and 60° grain boundary samples to have a preliminary value of at least 1×10^{-11} m^2/s at the above mentioned temperatures. Preliminary results show that no grain boundary diffusion anisotropy between the LAGB and the 60° grain boundary was observed. However, for the 90° GB, a higher grain boundary diffusivity compared to the 60° and the 10° grain boundary is expected due to the larger atomic distances.

k. *Anisotropic thermal expansion and thermal fracturing of olivine bicrystals: Pathways for magma flux at mid-ocean ridges (J. Polednia, J. Buchen and K. Marquardt)*

Anisotropic thermal expansion of olivine crystals may result in the accumulation of stress in olivine-dominated rocks in the vicinity of oceanic spreading centres. Thermally-induced stress is significantly larger than the stress caused by depressurisation. Thermal fracturing therefore controls the formation of an interconnected permeability network for magma ascent. In this study, we demonstrate how bicrystal experiments can provide insight to the fracture behaviour of polycrystalline olivine aggregates resulting from thermal expansion anisotropy.

We made bicrystals of i) San Carlos olivine and ii) synthetic forsterite using the direct wafer bonding method and characterised the grain boundaries with following scheme: angle[rotation axis]/(contact planes). We synthesised two 90° grain boundaries from San Carlos olivine and forsterite grain boundaries: 90°[001]/(100)&(010) and 90°[001]/(001) − the two most abundant grain boundaries in undeformed olivine-bearing rocks. We also produced a symmetric forsterite 10°[010]/(5° off 100) low angle grain boundary and a symmetric 60°[100]/(011) grain boundary for comparison. Fractures formed during heating and especially cooling at rates of 30 K/h in the temperature ranges 298 to 1373 K and 298 to 1873 K for San Carlos olivine and forsterite, respectively. After cooling, the bicrystals were characterised using reflective and transmitted light microscopies as well as transmission electron microscopy (TEM) and high resolution TEM.

Our results showed that cracks do not necessarily propagate along grain boundaries. Instead, characteristic fracture patterns with fractures perpendicular to the grain boundary plane developed in the non-symmetric 90° grain boundary bicrystals. These fractures have characteristic distances of approximately 100-200 µm and are oriented parallel to the crystallographic **a** and **b** axes. Millimetre-sized bicrystals with symmetric grain boundaries did not show thermal fracturing. We used the fracture distances to derive thermal stresses, strain energies, critical grainsizes, and fracture surface energies. Our results suggest that intense thermal cracking across non-symmetric grain boundaries in olivine may reduce the grainsize of olivine-dominated rocks and increase the permeability of rocks in the vicinity of magma chambers at mid-ocean ridges.

l. *Proton dynamics in high-pressure ice-VII from density functional theory (F. Trybel, G. Steinle-Neumann and T. Meier)*

The recent discovery of an ice-VII inclusion in diamond from the transition zone in Earth's mantle (410-660 km) highlights the importance of this high-pressure phase of water for planetary interiors, including icy satellites of Jupiter and Saturn in our solar system and potentially H_2O-dominated exosolar planets. At pressures above ~ 2 GPa, water crystallises as ice-VII in a cubic structure, defined by a bcc arrangement of oxygens with two possible proton positions along the diagonal O-O directions that are occupied randomly. The

energetically lowest configuration is achieved if two hydrogens are coordinated to one oxygen (conforming to the ice rules). With increasing pressure, the O-H-O bond continuously symmetrises to form ice-X at ~ 70 GPa at room temperature, a process that continues to be of great interest in high-pressure physics and chemistry.

Proton disorder in ice-VII that violates the ice rules can trigger the occurrence of a double-well potential along the O-O direction, significantly changing during high-pressure symmetrisation. The double-well character of the potential provides an opportunity for protons to tunnel, as recently observed in nuclear magnetic resonance experiments in a diamond anvil cell.

Using Kohn-Sham density functional theory-based methods, we explored the double-well potential by directly sampling the proton position along the diagonal O-O direction in the disordered bcc configuration. Investigating the potential as a function of the proton displacement (Fig. 3.4-11) revealed the following behaviour: with increasing compression, the barrier and the width of the double-well decreases and thereby encourages proton tunnelling. At lattice constants < 2.9 Å (~ 45 GPa) the double-well character is lost, but a broad minimum with high proton mobility persists. This can be interpreted as the onset of the transformation to ice-X. Further compression leads to a stronger localisation of the minimum, and an extrapolation of results predicts a full localisation for pressures over 120 GPa, corresponding to the completion of the transformation to the symmetric ice-X phase.

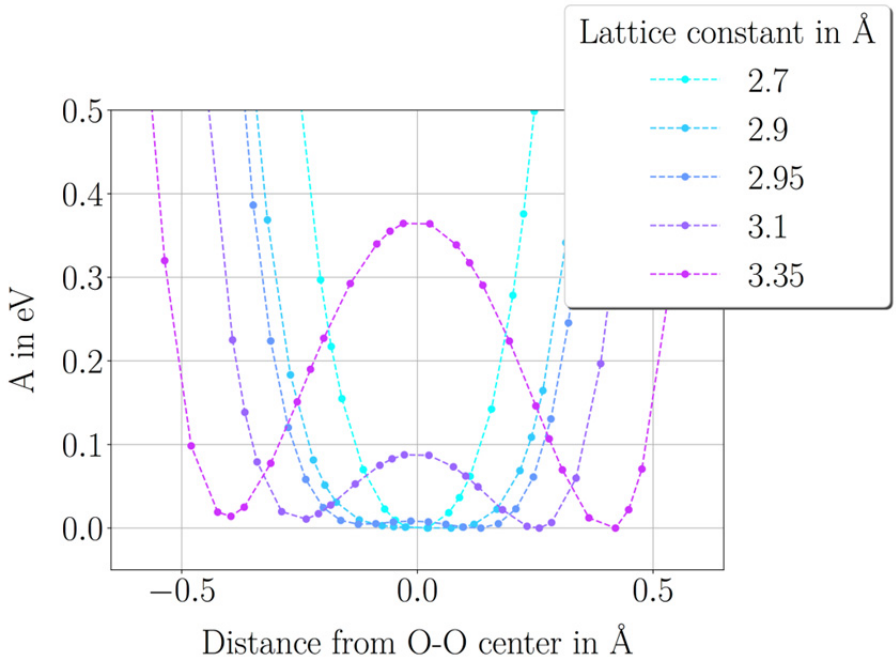

Fig. 3.4-11: Potential of proton positions along the O-O direction of the double-well structure of ice-VII for different lattice constants *l*. The potentials are vertically shifted so that the energy minimum is zero at each lattice constant. With increasing compression, the distance of the minima from the centre of the potential and the depth of the well decrease until *l*=2.9 Å where the double-well character disappears.

3.5 Fluids, melts and their interaction with minerals

Magma formation in volcanic arcs above subduction zones is the main mechanism for the growth of continental crust today. It is widely believed that aqueous fluids and possibly silicate melts released from the subducted slab trigger melting in the mantle wedge. Data from magnetotelluric surveys of subduction zones are generally consistent with this picture, as they show zones of enhanced conductivity deep below volcanic arcs, which may be caused by the presence of conductive fluids or melts in the mantle wedge. However, the quantitative interpretation of these data used to be difficult, since electrical conductivity data for fluids were only available to low pressures < 1 GPa. The first contribution in this section of the annual report shows new conductivity measurements of aqueous NaCl-H_2O fluids to 5 GPa. These measurements were made possible by the development of a new conductivity cell for the piston cylinder apparatus, where the fluid is enclosed in the pore space of diamond powder between two electrodes. In general, high pressure is found to enhance conductivity due to enhanced ion dissociation. If applied to subduction zone conditions, the data suggest that already very low fractions of saline aqueous fluids may be able to account for the observed conductivity anomalies. Modelling the actual conductivity of a rock-fluid system, however, always critically depends on the connectivity of the fluid. Therefore, in a separate project, the conductivity of forsterite aggregates containing a small fraction of saline fluids was measured. With time, measured conductivities reached a constant value, indicating attainment of textural equilibrium. The relationship between bulk conductivity and fluid connectivity will be further studied by X-ray microtomography.

The following chapters in this section of the annual report look at the behaviour of water and carbon, the two most important volatile components in Earth's interior. Water in the ringwoodite phase of the transition zone has been a subject of considerable interest since the discovery of a ringwoodite grain inside a natural diamond, which contained about 1 wt. % of water. This seemed to be somewhat at odds with experimental data suggesting that at high temperatures in the mantle, water solubility in ringwoodite drops far below the 1 wt. % level. New experimental data presented here show that water solubility in ringwoodite does indeed decrease with temperature, but the effect is less pronounced than previously thought. The next two contributions look at the behaviour of carbon during early Earth history, when our planet was mostly molten and the metallic core segregated from a magma ocean. It is widely believed that during this process, most of the carbon on Earth ended up in the core. However, new data on the solubility of carbon monoxide (CO) in silicate melts suggest that under certain very reducing conditions, carbon solubility in the silicate melt may be very low, which in turn limits the amount of carbon that could be sequestered in the core. New data on carbon diffusion in liquid iron suggest relatively short timescales for the equilibration between metallic iron and the magma ocean.

The last two contributions in this section look at the dynamics of magmatic systems, very early in Earth's history and today. Measurements of the self-diffusion coefficient of Si, O,

Mg, and Ca to 25 GPa were used to estimate the viscosity profile in a deep magma ocean. A viscosity maximum at a depth of 250 km is observed. Another study looked at the kinetics of melt-rock interaction in the crust today, which appears to be controlled by a combination of diffusion and convection.

a. *Electrical conductivity of NaCl-H_2O fluids to 5 GPa (H. Guo and H. Keppler)*

Magnetotelluric studies often reveal zones of elevated electrical conductivity below active volcanoes, in the deep crust, and in the mantle wedge above subducted slabs. In principle, these anomalies could be caused by various conductive phases, in particular hydrous silicate melts or aqueous fluids. However, distinguishing between these possibilities used to be nearly impossible, because electrical conductivity data for fluids at high pressures were mostly limited to < 0.4 GPa. In order to overcome this problem, we developed a new electrical conductivity cell for piston cylinder experiments (Fig. 3.5-1). In this cell, the fluid is contained in the pore space of diamond powder between two electrodes. The cell was used for measurements up to 5 GPa. The cell constant was calibrated by measuring the resistance of the cell after recovery at ambient conditions.

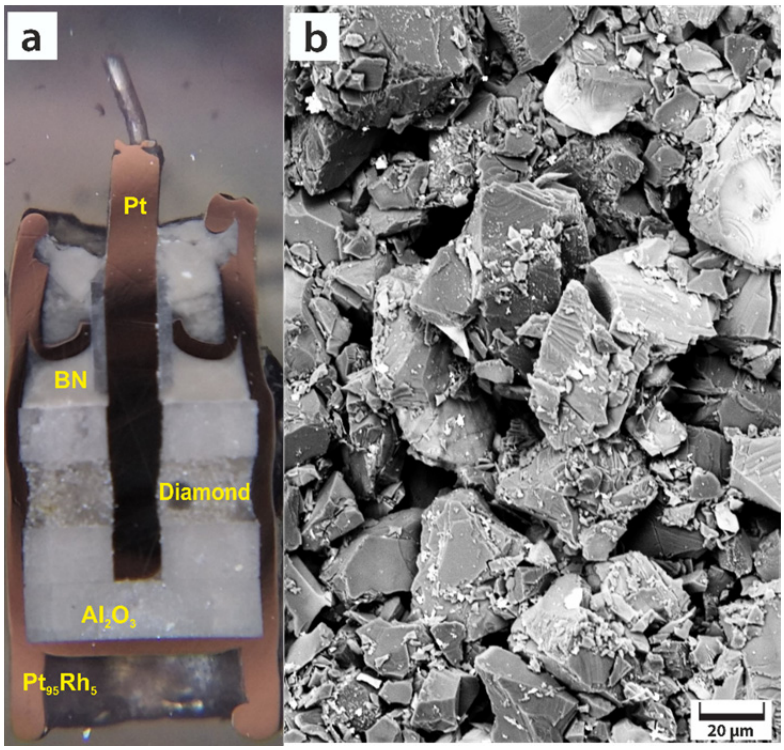

Fig. 3.5-1: (a) Cross section of a recovered capsule used for electrical conductivity measurements in the piston cylinder apparatus. The platinum rod in the center and the capsule itself are the two electrodes. The fluid is contained in the pores of diamond powder and sealed by alumna discs and boron nitride (BN). A SEM image of the diamond powder after the run is shown in (b).

Measured electrical conductivities for aqueous fluids with two different concentrations of NaCl are shown in Fig. 3.5-2. At mantle temperatures, conductivity increases greatly with pressure due to enhanced dissociation of NaCl. Only at low temperatures, the opposite effect is observed, which may be due to increasing viscosity of the fluid. Measured conductivities σ are very well reproduced by a numerical model

$$\log \sigma = - 0.919 - 872.5/T + 7.61 \log \rho + 0.852 \log c + \log \Lambda_0,$$

where σ is the conductivity in S/m, T is temperature in K, c is NaCl concentration in wt. %, ρ is the density of pure water (in g/cm^3) at given pressure and temperature, and Λ_0 is the molar conductivity of NaCl in water at infinite dilution (in S cm^2 mol^{-1}), Λ_0 =1573 - 1212 ρ + 537062/T - 208122721/T^2.

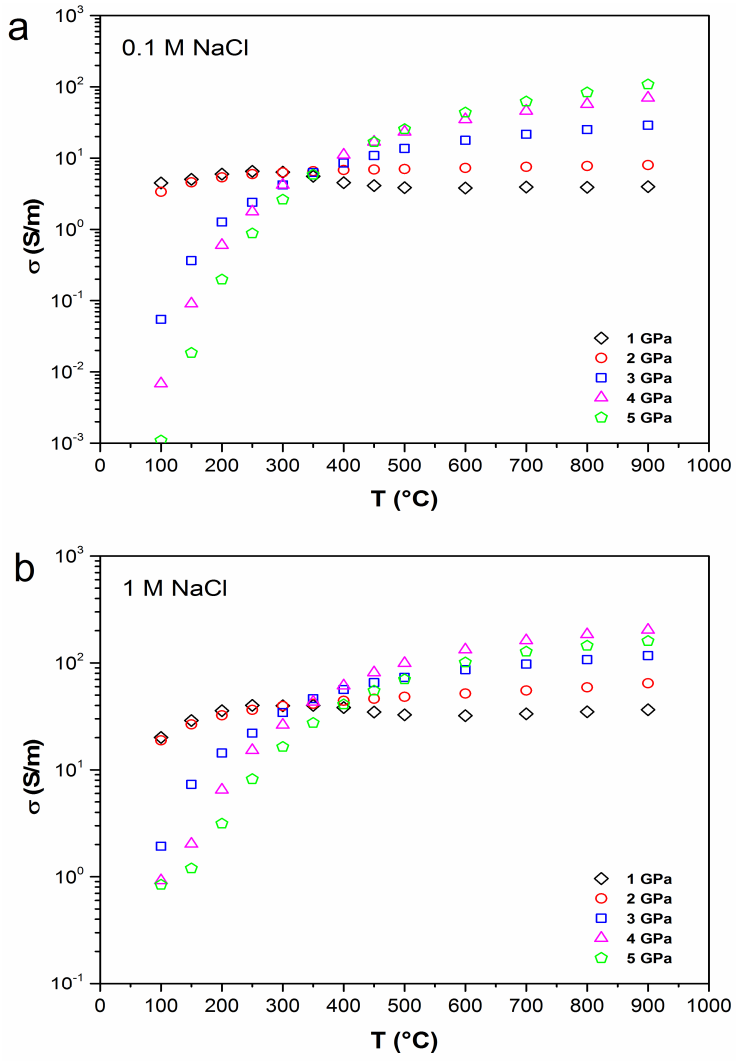

Fig. 3.5-2: Measured electrical conductivities of aqueous fluids containing different concentrations of NaCl (a: 0.1 M; b: 1 M; 1 M refers to 1 mol NaCl / liter at standard conditions). Note the strong enhancement of conductivity by pressure at high temperatures.

The new conductivity data can be used to estimate the fluid fraction that may be responsible for the observed conductivity anomaly in the mantle wedge of different subduction zones. Figure 3.5-3 shows the results of models assuming NaCl concentrations of 1, 5, and 10 wt. % in the fluid. The conductivity anomalies below Greece, New Zealand, and Mexico can be readily explained by the presence of a very small fraction of moderately saline aqueous fluid. On the other hand, the conductivities observed under Central Cascadia are so high that they would require unrealistically high fluid fractions and therefore, they are more likely related to the presence of silicate melts.

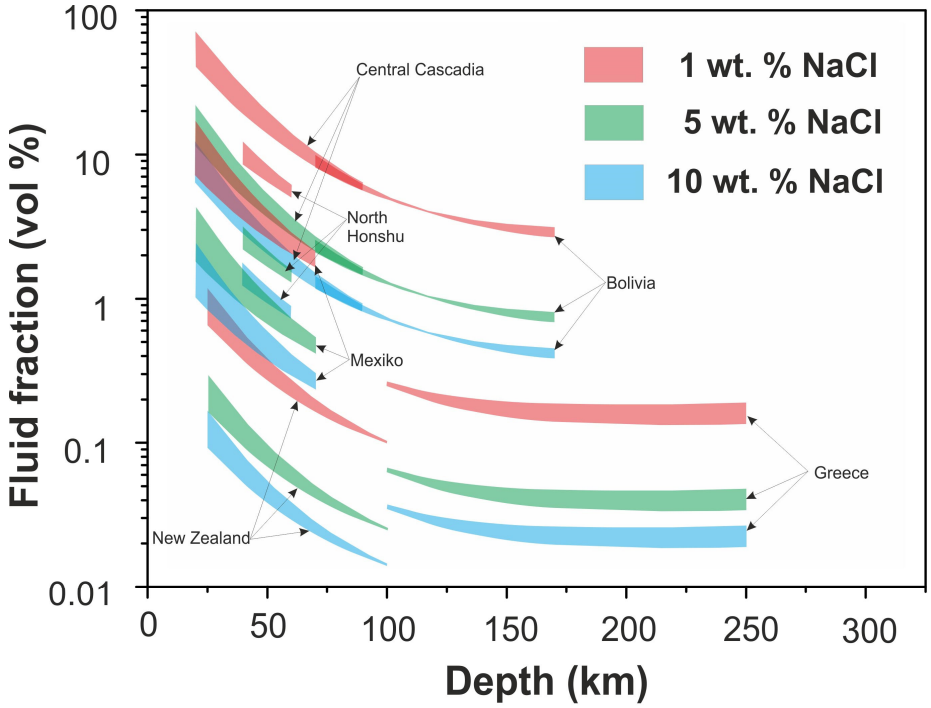

Fig. 3.5-3: Modelling results for the enhanced electric conductivity observed in the mantle wedge of various subduction zones. Most data may be explained by a rather small fraction of a moderately saline fluid. However, the conductivities below Central Cascadia would require unrealistically high fluid fractions; they are more likely de to the presence of silicate melts.

b. *Electrical conductivity of forsterite aggregates containing H_2O-NaCl fluids at 800 °C and 1 GPa (Y. Huang/Sendai, H. Guo, T. Nakatani/Sendai, M. Nakamura/Sendai and H. Keppler)*

Quantitative models of the effect of small fluid fractions on the electrical conductivity of the deep crust or the mantle wedge above subduction zones require data on fluid connectivity and fluid distribution in polyphase aggregates. Some previous studies of fluid-mineral (albite, quartz and plagioclase) systems demonstrated that the electrical conductivity increases with salinity and fluid fractions. However, the duration of those experiments may not have been

long enough to obtain an equilibrated microstructure. Data for fluids in olivine matrix are still lacking, which makes the construction of models for the electrical conductivity of the uppermost mantle in subduction zones difficult. The present study therefore investigated the electrical conductivity of texturally equilibrated aggregates in the system forsterite–H_2O–NaCl at 800 °C and 1 GPa to in order to better understand the origin of the high conductivity anomalies observed in subduction zones.

Forsterite was synthesized from iron-free gel powders and was ground to a grain size of 38 - 53 μm. The electrical conductivity was measured in a piston cylinder apparatus using a conductivity cell similar to that shown in Fig. 3.5-1. Forsterite powder and NaCl-bearing solutions (5 wt. % NaCl) with initial fluid fractions of 0.5, 2.5, 5.0, and 10.0 wt. % were sandwiched between two alumina disks (as insulating spacers) at the top and bottom of a $Pt_{95}Rh_5$ capsule. An inner platinum rod and the outer capsule served as electrodes. Experiments were run for 8 - 9 days at 800 °C and 1 GPa to assure attainment of equilibrium. The conductivity was measured every day. The recovered samples showed that the fluid was distributed along grain boundaries throughout the sample (Fig. 3.5-4).

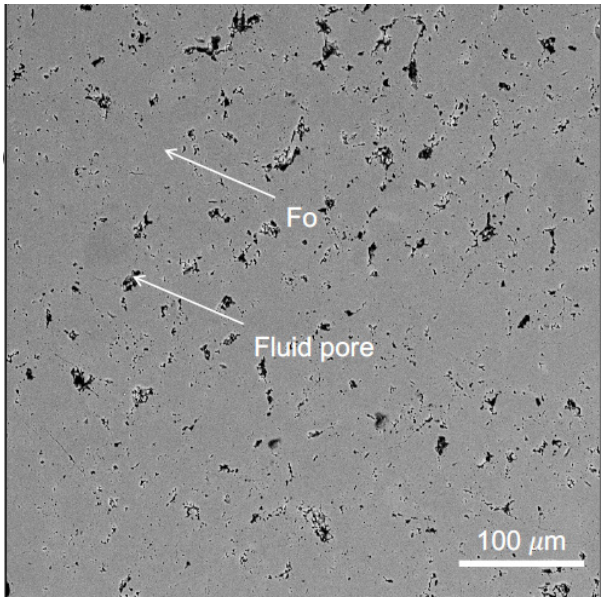

Fig. 3.5-4: Backscatter electron image of a polished section of the recovered sample in the forsterite–H_2O–NaCl system (at 800 ˚C and 1 GPa, after 9 days). Forsterite (Fo) is grey, fluid pores are black.

The conductivities rapidly decreased during the first day and then gradually reached a constant value (Fig. 3.5-5). This may be attributed to a change in the microstructure towards a textural equilibrium state. Figure 3.5-5 also shows that conductivity increases with the fraction of NaCl-bearing aqueous fluids. The bulk electrical conductivity in the forsterite–

H_2O–NaCl system is governed by the fluid connectivity and the total concentrations of dissolved ionic species in the aqueous fluids. The dominant connectivity paths depend on the geometrical distribution of aqueous fluids in a fluids-bearing rock system. For an interconnected fluid pathway, the circuit may approach the response of the grain interior and aqueous fluids in a parallel circuit. Without an interconnected fluids pathway, the circuit may be closer to the response of the grain interior and aqueous fluids in a series circuit. To understand the fluid fraction dependency in terms of microstructure, we are planning to constrain the fluid geometry using X-ray computer tomography (CT).

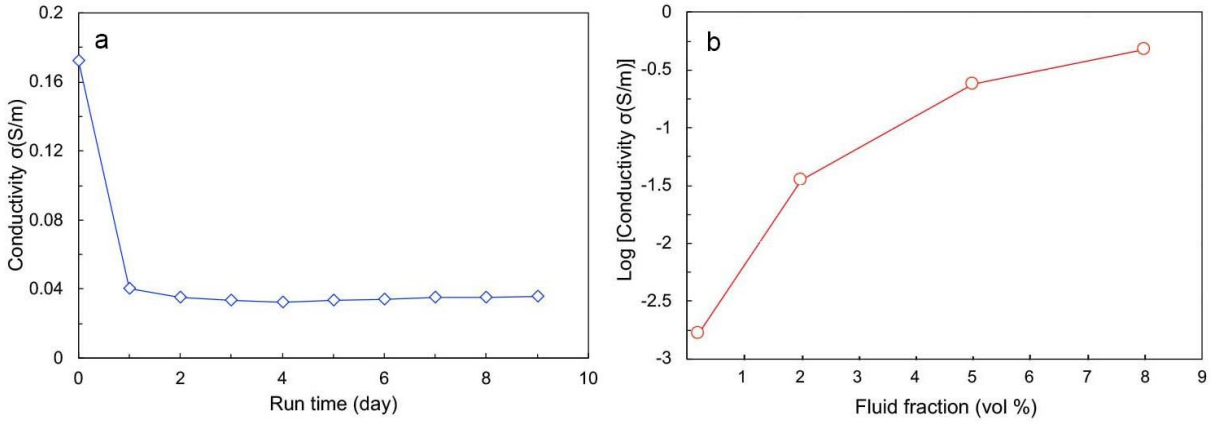

Fig. 3.5-5: Electrical conductivity of aggregates in the forsterite–H_2O–NaCl system at 800 °C and 1 GPa. (a) Electrical conductivity measured as a function of run duration. Fluid fraction is about 2 vol. %. (b) Electrical conductivity as a function of fluid fraction after textural equilibration (5 wt. % NaCl).

c. *Water solubility in ringwoodite at mantle transition zone temperatures (H. Fei and T. Katsura)*

The mantle transition zone, a potential water reservoir in the Earth's interior, is suggested to contain at least locally more than 1 wt. % of water, as indicated by a ringwoodite sample found as inclusion in a natural diamond. However, laboratory experiments suggested that the water solubility in ringwoodite significantly decreases with increasing temperature. Although ringwoodite may store up to 2.6 wt. % water at relatively low temperatures (~ 1600 K), under the realistic mantle transition zone condition at ~ 2000 K, the water solubility may be less than 0.3 wt. %, which is in obvious conflict with the idea of a water rich mantle transition zone.

To clarify the water storage capacity of ringwoodite in the mantle transition zone, we revisited the water solubility in both Fe-free and Fe-bearing ringwoodite. Mixtures of MgO, SiO_2, FeO, and $Mg(OH)_2$ powders with bulk compositions of Fo100, Fo90, and Fo75 and water were used as starting material. The mixtures were loaded in a PtRh capsule and

annealed at 23 GPa and 1600 - 2000 K, for over 40 min. The run products contained ringwoodite, hydrous melt, and akimotoite. The water contents in ringwoodite were analyzed by Fourier transform infrared (FTIR) spectroscopy.

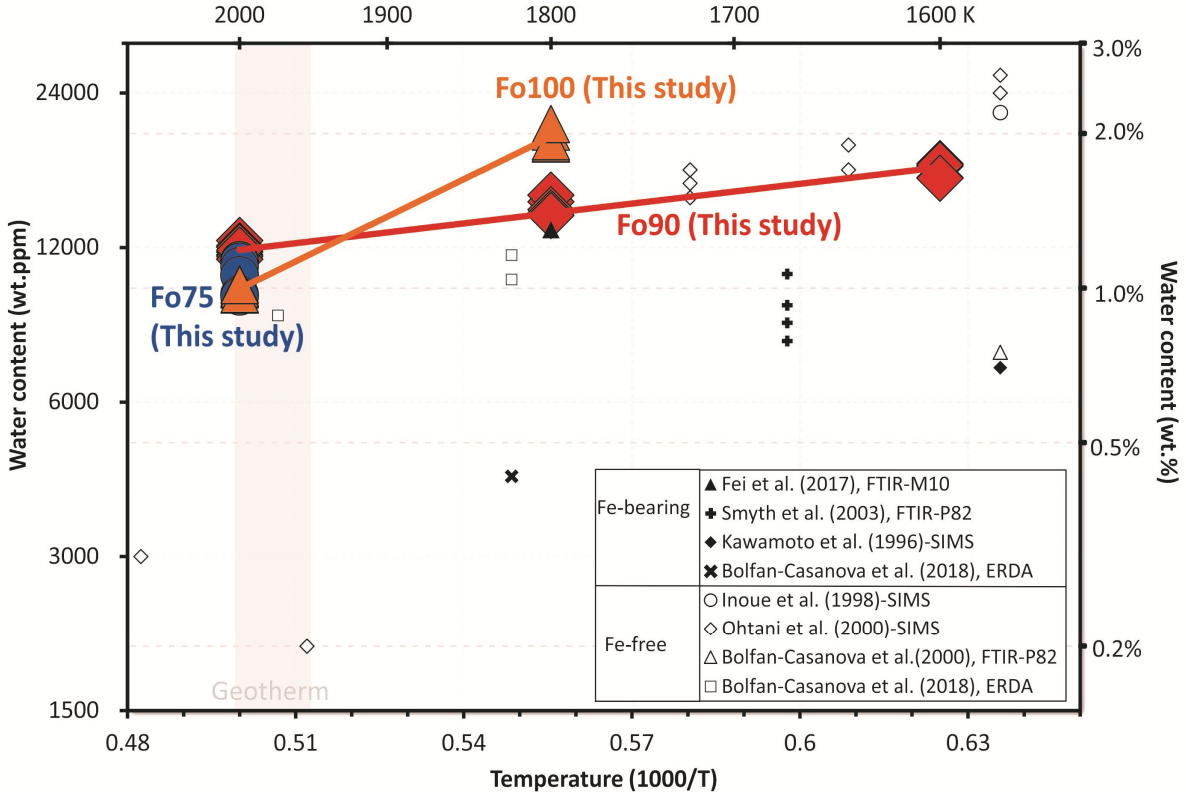

Fig. 3.5-6: Temperature dependence of water solubility in ringwoodite. Each data point from this study indicates C_{H2O}^{rw} from one single FTIR spectrum. SIMS: secondary ion mass spectrometry. FTIR-P82: FTIR with Paterson (1982, Bull. Miner. 105: 20) calibration. FTIR-M10: FTIR with Koch-Muller and Rhede (2010, Am. Min. 95: 770) calibration. ERDA: Elastic Recoil Detection Analysis. Database in the figure: Fei *et al.* (2017, Sci. Adv. 3: e1603024); Smyth *et al.* (2003, Am. Min. 88: 1402); Kawamoto *et al.* (1996, EPSL 142: 587); Bolfan-Casanova *et al.* (2018, Front. Earth Sci. 6: 75); Inoue *et al.* (1996, EPSL 160: 107); Ohtani *et al.* (2000, PCM 27: 533); Bolfan-Casanova *et al.* (2000, EPSL 182: 209).

The experimental results (Fig. 3.5-6) show that, although the water solubility in ringwoodite decreases with increasing temperature, even at 2000 K, both Fe-free and Fe-bearing ringwoodite can still store more than 1.0 wt. % water. The water solubility does not depend on Fe-content at 2000 K, whereas at lower temperatures, the solubility in Fe-free ringwoodite is much higher than for the Fe-bearing phase. The high water solubility at 2000 K is consistent with the water-rich mantle transition zone inferred from mineral viscosity data and from the analysis of a natural ringwoodite inclusion. The relatively low water content in ringwoodite reported in previous experimental studies may be due to disequilibrium with the SiO_2 buffer.

d. *Carbon solubility in silicate melts and the fate of carbon during terrestrial core formation (T. Yoshioka, D. Nakashima/Sendai, T. Nakamura/ Sendai, S. Shcheka, H. Keppler)*

The initial distribution of carbon in our planet was largely determined by the processes occurring during the solidification of a magma ocean, which was in equilibrium with a primordial atmosphere. It is widely believed that during the fractionation of the metal from the silicate melt, most of the carbon was sequestered into the core. The efficiency of this process, however, does not only depend on the metal/silicate partition coefficient of carbon and the relevant diffusion coefficients, but also on the equilibrium distribution of carbon between the silicate melt and the primordial atmosphere, where carbon was likely present as a mixture of CO and CO_2. We therefore experimentally studied the solubility of carbon in a silicate melt in equilibrium with graphite and a CO-CO_2 fluid phase. Experiments were carried out in an internally heated pressure vessel to 0.5 GPa and in a piston cylinder apparatus to 3 GPa. Bulk carbon contents in the run product glasses were determined by SIMS (secondary ion mas spectrometry), while the contents of oxidized carbon (CO_2 and carbonate) were measured by infrared spectroscopy (FTIR). By subtracting the two numbers, it was possible to estimate the solubility of reduced carbon (Fig. 3.5-7), which is interpreted as being due to carbon monoxide (CO).

Bulk carbon solubility in equilibrium with a CO-CO_2 fluid phase and graphite is not much different from the solubility of pure CO_2. This is because in the pressure and temperature range studied, the fluid phase is dominated by CO_2 and CO is only a minor component. However, if the solubility of CO alone is parameterized as a function of CO fugacity, it is about one order of magnitude smaller than that of CO_2, but comparable to that of argon, a noble gas of similar size. For example, the solubility of CO in MORB basalt melt may be described by the equation

$$\log c_{CO}^{MORB} = -5.83 + 0.98 \log f_{CO} \; (R^2 = 0.84),$$

where c_{CO} is the solubility of CO (expressed as wt. % carbon) and f_{CO} is CO fugacity.

The new CO solubility data presented here have some interesting consequences for the behaviour of carbon during core formation. If the magma ocean initially had an oxygen fugacity close to the iron wustite (IW) buffer, carbon in the atmosphere was mostly present as CO_2. In this case, the solubility in the silicate melt is rather high and most of the carbon will ultimately partition into the core. However, if at least during the early stages of core formation, the oxygen fugacity was four or five log units below the IW buffer, the gas phase will be dominated by CO. Moreover, graphite precipitation would limit the possible CO fugacity, such that only little carbon is dissolved in the silicate melt. This could be a plausible mechanism for limiting the partitioning of carbon into the core and for retaining a significant fraction of total carbon near the surface of the early Earth.

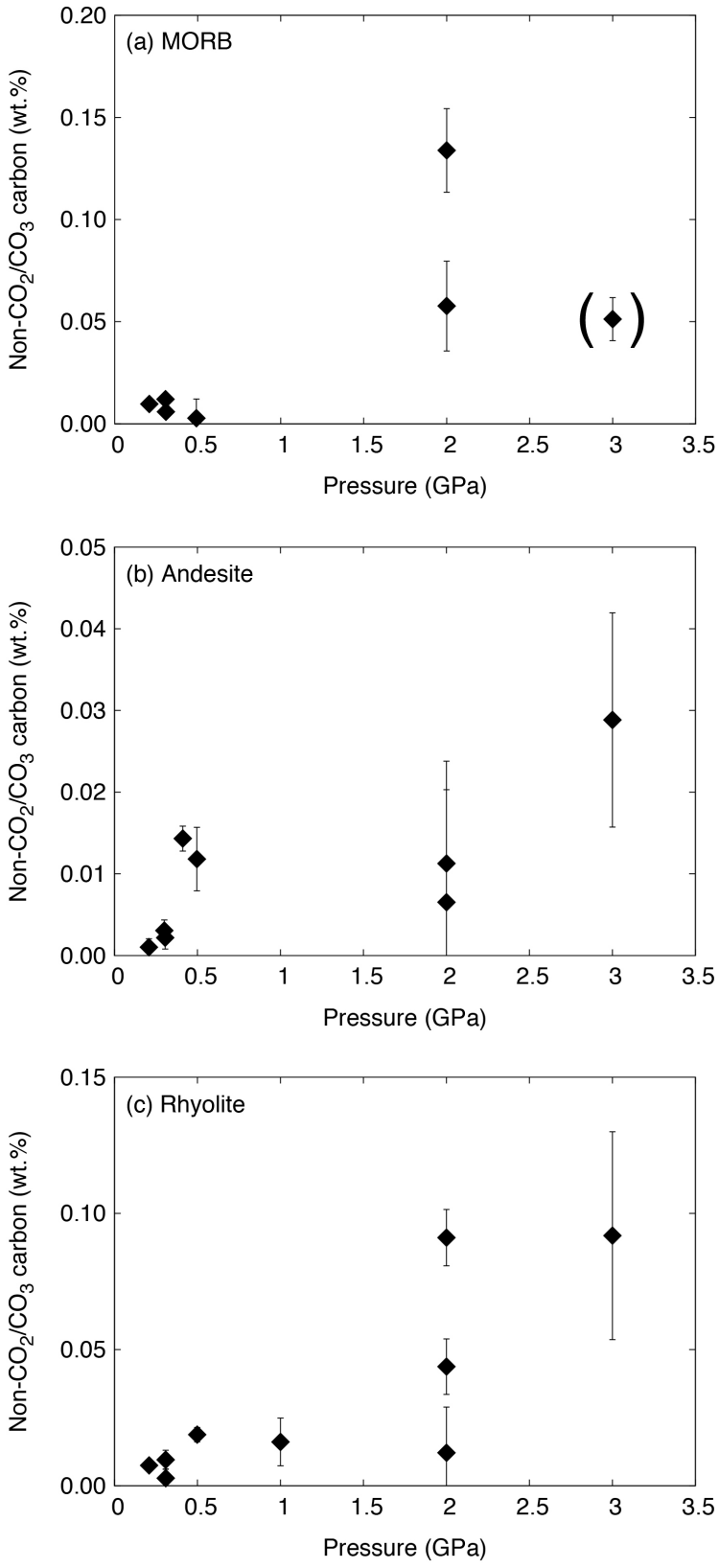

Fig. 3.5-7: Solubility of reduced carbon (CO) in MORB basalt, andesite, and rhyolite melt in equilibrium with graphite and a CO-CO_2 gas phase. Temperatures range from 1100 to 1600 ˚C. The one data point shown in brackets is probably unreliable due to a possible leak of the capsule.

e. *Experimental determination of carbon diffusion in liquid iron at high pressure (A.M. Rebaza, E.S. Posner, M. Thielmann, and D.C. Rubie)*

During the accretionary stages of Earth's formation, carbon and other atmophile elements fractionated between mantle-forming silicate melt and both atmosphere-forming vapor and core-forming metallic liquid. The presence of carbon and other light elements in the core also played an important role in the onset and existence of Earth's geodynamo, which shields the planet from harmful solar radiation and is considered requisite for planetary habitability. In this study, we investigated the effects of pressure (P) and temperature (T) on rates of chemical diffusion of carbon in molten iron that is required to constrain the length and timescale of chemical equilibration between silicate liquid and core-forming metallic melt during Earth's core formation.

Diffusion-couple experiments between pure Fe and Fe with 4 wt. % C were performed over a P-T range of 3-15 GPa and 1677-2474 K using a multianvil press and quenched carbon concentration profiles were measured by electron microprobe. All diffusion profiles obtained at the same pressure were simultaneously fitted to refine the activation enthalpy of diffusion using a least-squares minimization that accounts for diffusion that occurred prior to the reaching the target temperature. Typical concentration profiles and fitted curves are shown in Fig. 3.5-8, and an Arrhenian diagram of our results alongside previous studies is shown in Fig. 3.5-9.

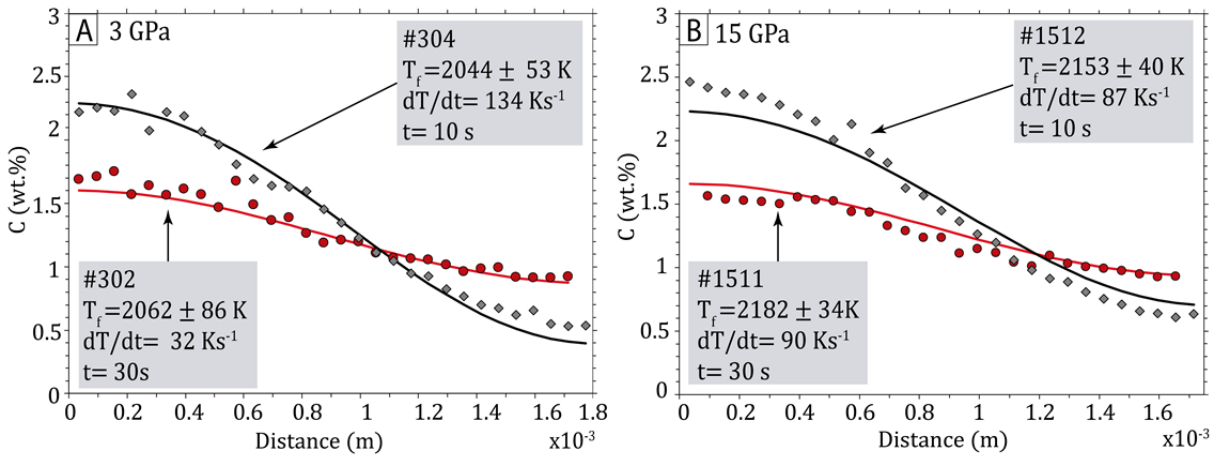

Fig. 3.5-8: Quenched carbon concentration profiles obtained at (a) 3 GPa and (b) 15 GPa. Both panels demonstrate that diffusion profiles flatten with increasing time at constant temperature. Fitted curves represent a global solution to all experiments conducted at the respective pressure interval.

Carbon diffusion rates vary from approximately 5×10^{-9} m^2 s^{-1} to 2×10^{-8} m^2 s^{-1} over the full range of P-T conditions of this study. Refined activation enthalpy values decrease with

pressure from 62 ± 5 kJ mol^{-1} at 3 GPa to 44 ± 4 kJ mol^{-1} at 8 GPa and to 31 ± 6 kJ mol^{-1} at 15 GPa. We observe a negligible *P* effect on carbon diffusion in liquid iron, similar to that reported for oxygen (Fig. 3.5-9), which is in better agreement with 1-bar experimental data than extrapolations based on diffusion parameters for carbon self-diffusion in liquid Fe_3C (Fig. 3.5-9). A negligible *P* effect on carbon diffusion likely coincides with the liquid structural change in liquid iron from bcc-like to fcc-like as determined from previously reported X-ray diffraction measurements of liquid Fe with 3.5 wt. % C, which may also influence its metal-silicate partition coefficient. The diffusivity of carbon in liquid iron is comparable to that of oxygen, and is 2-3 times faster than Si and Fe (Fig. 3.5-9). Timescales of C and O chemical equilibration between metallic liquid and silicate melt are therefore shorter and equilibration length scales are longer than those for Si. Further computational study is underway to compare with results obtained here and extend the experimental dataset to conditions of the Earth's outer core.

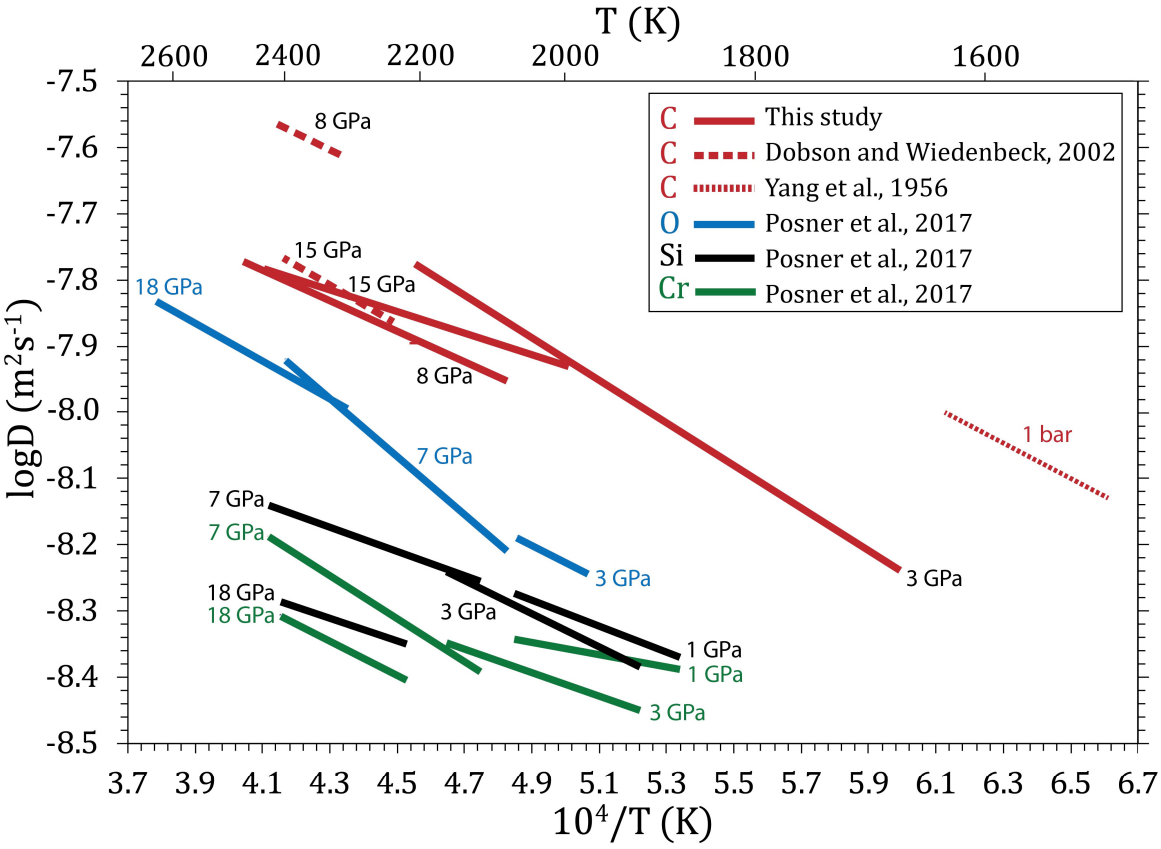

Fig. 3.5-9: Arrhenius diagram showing carbon chemical diffusion (red curves, this study) and self-diffusion (gray dashed curves, Dobson and Wiedenbeck, 2002, Geophys. Res. Lett. 29: 2006; gray dotted curves, Yang *et al.* 1956, Met. Soc. Am. 206: 1577). A smaller pressure effect on carbon diffusion is observed in this study compared to data reported by Dobson and Wiedenbeck (2002), similar to the behaviour reported for oxygen (blue curves, Posner *et al.* 2017, EPSL 464: 116). Carbon and oxygen diffuse ~ 2-3 times faster than Si (black) and Cr (green), the latter of which also decrease more strongly with pressure (Posner *et al.* 2017, GCA 203: 323).

f. *Mass transport properties of peridotite melt at high pressure and implications for magma ocean viscosities (E.S. Posner, B. Schmickler, and D.C. Rubie)*

The early differentiation of Earth is considered to have involved episodes of large-scale melting that resulted in the formation of one or more deep magma oceans during the late stages of accretion. Mass transport properties of peridotite melt at high pressure are therefore required to constrain the dynamics of a deep magma ocean (*e.g.*, rates of convection and cooling), differentiation processes through their effects on the kinetics of crystal growth and the physics of settling in a convecting magma ocean, as well as chemical equilibration between silicates and core-forming metal liquids. *In situ* falling-sphere viscometry experiments are currently limited to pressures below ~ 13 GPa for technical reasons, while diffusion experiments are feasible up to at least 18-25 GPa using a multianvil press. In order to take advantage of the larger pressure range of the latter approach, we investigated the self-diffusion of Si, O, Mg, and Ca and chemical-diffusion coefficients of Ni and Co up to 24 GPa and 2623 K in anhydrous peridotite liquid using a multianvil press. Isotope abundance (^{18}O, ^{30}Si, ^{25}Mg, ^{44}Ca) profiles along each sample length and perpendicular to the diffusion interface were analyzed by secondary ion mass spectrometry, and Ni and Co concentration profiles were measured by electron microprobe analysis.

Direct determination of the activation enthalpy (ΔH) of diffusion was not possible in this study due to rapid equilibration of the small liquid samples and thus limited temperature range above the peridotite liquidus. We therefore fitted a pre-exponential diffusion coefficient (D_0) for each quenched profile assuming a fixed ΔH value (100, 200, or 300 kJ mol^{-1}) using a finite difference algorithm set up to account for diffusion that occurred during heating, as employed in previous studies. Effects on the diffusion coefficient upon extrapolation to higher temperatures were evaluated using the refined D_0 for each ΔH value, as shown for each species in Fig. 3.5-10.

Our results indicate that the rates of self-diffusion of Si, O, Mg, Ca and chemical diffusion of Ni and Co decrease with increasing pressure from 4 to 8 GPa, where diffusivity reaches a minimum, and then increase with a further pressure increase to reach a maximum at ~ 12 GPa (Fig. 3.5-10). The effect of pressure on diffusion and viscosity in peridotite melt is small compared with the effect of temperature, which implies that viscosity along the melting curve decreases with depth. Predicted viscosities from self-diffusion coefficients for oxygen, obtained using the Eyring equation, are similar to viscosities measured by falling sphere viscometry, including the observed changes of the pressure dependence. We use diffusion parameters determined in this study to estimate the viscosity of a magma ocean with a depth of ~ 700 km, as shown in Fig. 3.5-11. The results indicate that the viscosity increases from ~ 10 mPa s near the surface to a reach a maximum of ~ 50 mPa s at a depth of ~ 250 km. At higher pressures the viscosity decreases to ~ 10 mPa s at a depth of ~ 300 km, below which it remains almost constant.

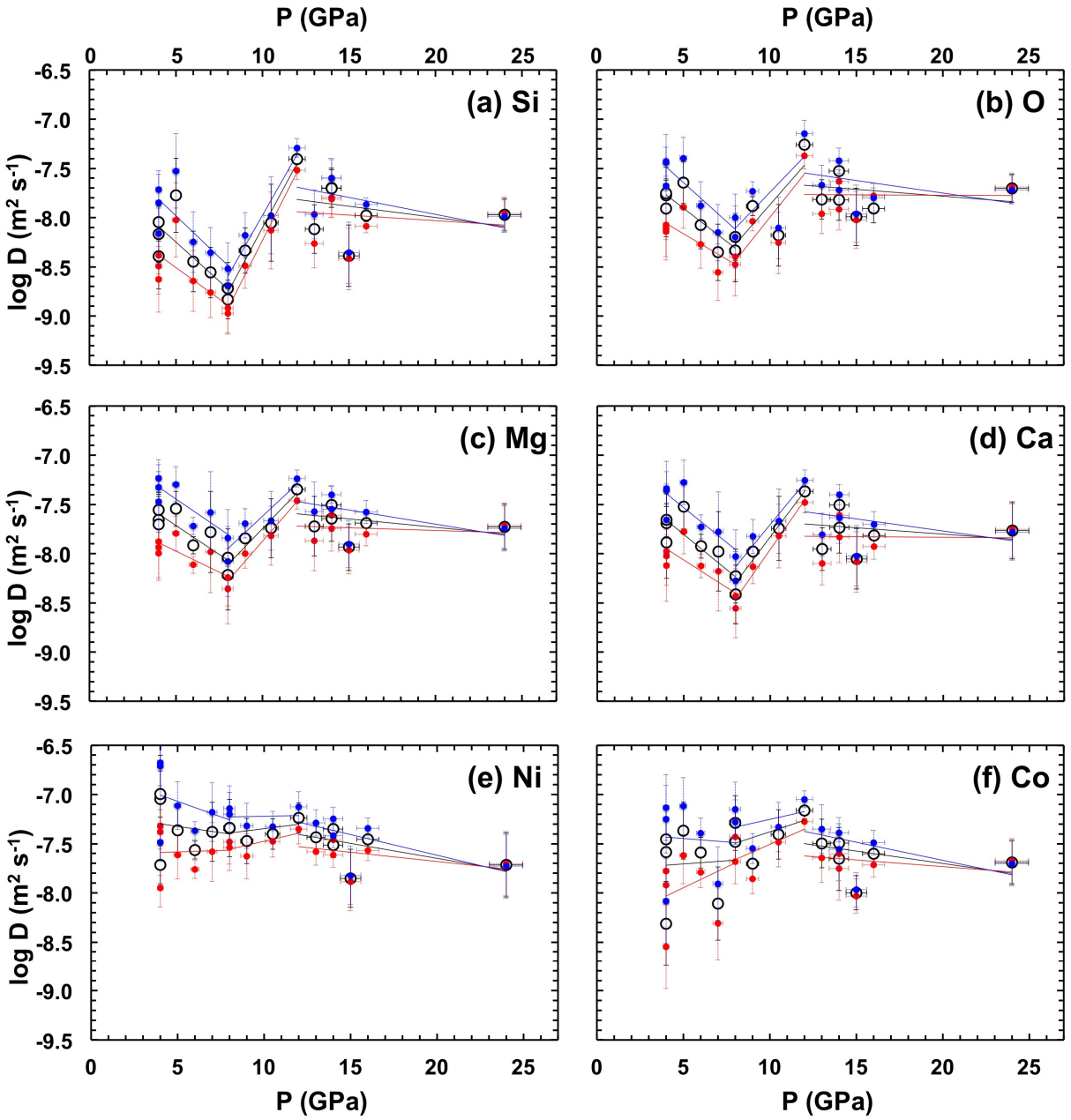

Fig. 3.5-10: Plots of $\log_{10}$ diffusivities as a function of pressure for the self-diffusion of (a) Si, (b) O, (c) Mg, and (d) Ca, and chemical diffusion of (e) Ni and (f) Co in anhydrous peridotite melt. The diffusion coefficients have been recalculated using fitted pre-exponential D_0 values to a temperature of 2600 K, using fixed ΔH values of 100 kJ mol^{-1} (red circles), 200 kJ mol-1 (unfilled circles), and 300 kJ mol^{-1} (blue circles), in order to show the pressure effect. (2600 K exceeds the liquidus temperatures over the experimental pressure range.) Error bars represent ±1σ. Scatter of the data using different ΔH values is larger at low pressure due to larger extrapolations to 2600 K. To illustrate the changes in the sign of the pressure dependence, linear fits to the data are shown in respective colors over intervals of (i) 4-8 GPa, (ii) 8-12 GPa, and (iii) 12-24 GPa. The data in panels (a)-(d) clearly show that diffusion coefficients decrease with pressure (*i.e.*, $\Delta V > 0$) in pressure interval (i), increase with pressure (*i.e.*, $\Delta V < 0$) in interval (ii), and weakly decrease with pressure in interval (iii).

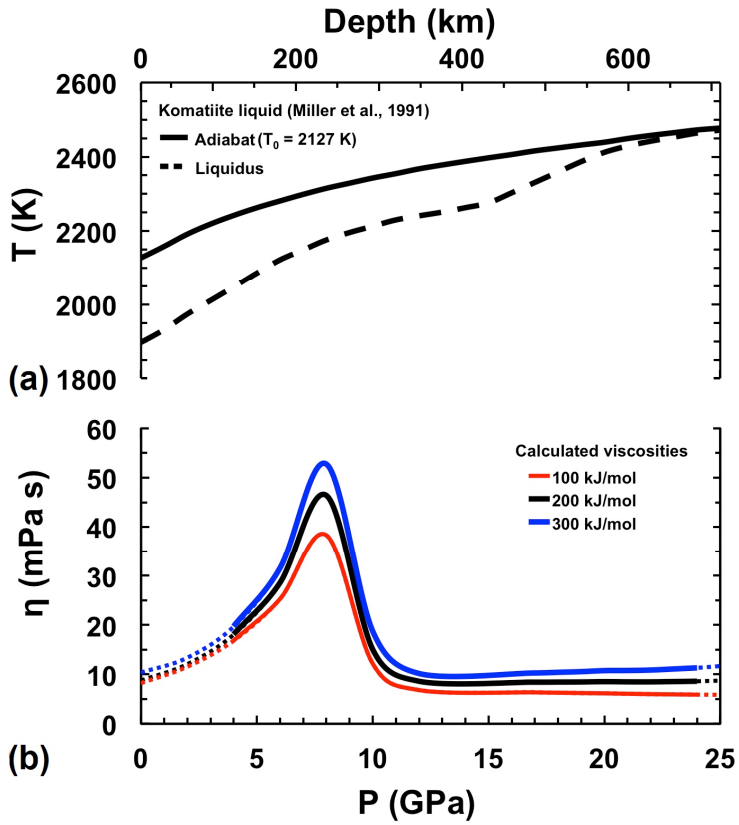

Fig. 3.5-11: (a) Adiabatic temperature gradient (solid curve) and liquidus (dashed curve) for komatiite liquid (Miller *et al.* 1991, J. Geophys. Res. 96: 849) as an analogue of the temperature of a magma ocean of ~ 700 km depth with a potential surface temperature of ~ 2127 K. Note that high-pressure liquidus temperatures are as much as 100 K lower than the peridotite liquidus. (b) Viscosities calculated according to the Eyring equation using diffusion parameters obtained from 4-8, 8-12, and 12-24 GPa datasets, activation enthalpy (ΔH) values of 100 kJ mol-1 (red curve), 200 kJ mol-1 (black curve), and 300 kJ mol-1 (blue curve), and an atomic jump distance of 4.4 Å. Dashed curves represent extrapolations beyond the pressure range of study.

g. *Experimental studies of melt-rock interaction in the crust (A.Y. Borisova/Toulouse, in cooperation with H. Keppler)*

Areas of volcanic activity such as hot spots (*e.g.*, Iceland, Hawaii, and Reunion) with predominantly basaltic crust are the most attractive targets for geothermal energy exploitation. Deep geothermal drilling installations sometimes may be stopped because of drilling into a magmatic chamber or into the partial melting zone of the hot surrounding rocks. Two major phenomena occur during reactions between magmas, fluids and rocks: (i) the metamorphism and partial melting of the rocks due to a thermal and hydrothermal source and (ii) the assimilation of the surrounding rocks by the infiltrating magma. These phenomena are still poorly constrained despite their crucial importance for the operation of deep geothermal stations. Experimental and thermodynamic studies on the interactions

demonstrated efficient partial melting of felsic, mafic and ultramafic crust. However, the existing data and models do not capture the behaviour of altered oceanic rocks, which are most common in geothermal areas.

To understand the processes of magma-rock-fluid interactions in regions of hot spots (*e.g.*, Iceland), which are most attractive for deep geothermal exploitation, we studied the interaction of altered crust (altered rhyolite from Krafla volcano) with a magma of plume mantle origin (picritic basalt from Eyjafjallajökull volcano). We performed high-temperature (1250 °C) experiments in an internally-heated pressure vessel at 0.2 GPa. A doubly-polished cylinder of altered rhyolite was placed in the upper part and basaltic glass powder in the bottom part of a $Au_{80}Pd_{20}$ capsule. Experiments with variable mass ratios of natural glass powder to natural rocks and different run durations up to 58 hours were performed.

Melting and dissolution of the altered rhyolite rock in the basaltic melt produced melts of intermediate composition (Fig. 3.5-12). Quantitative modeling of the observed concentration profiles suggests that they are caused by a combination of bulk melting, diffusion, and convection. The data will be used to produce quantitative models for melt-rock interaction that may predict the lithology and thermal structure in geothermal systems.

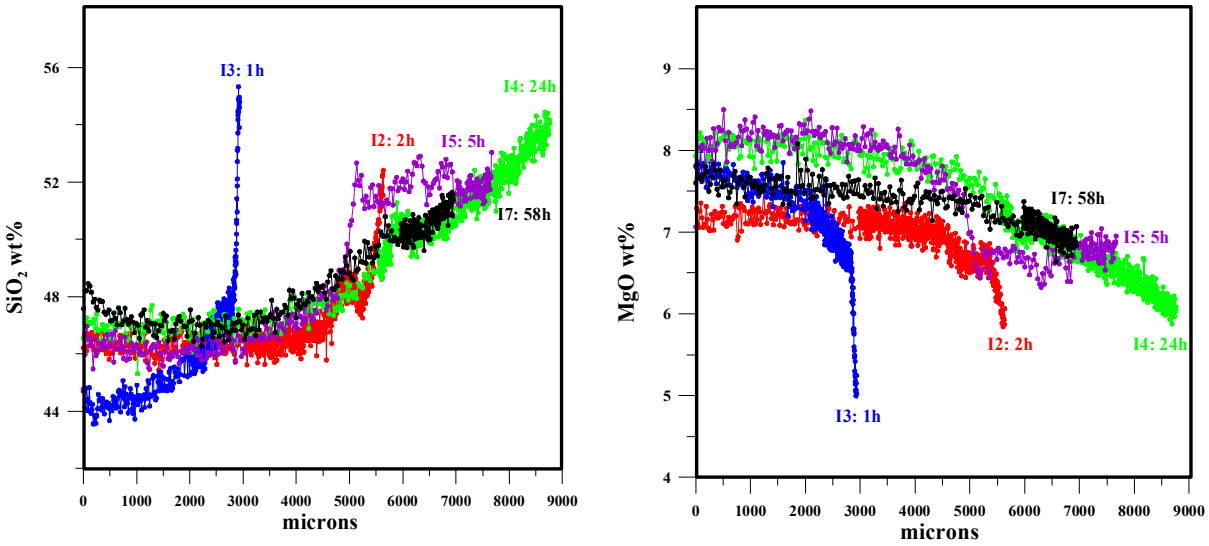

Fig. 3.5-12: SiO_2 and MgO concentration profiles from altered rhyolite-basalt interaction experiments at 1250 ˚C and 0.2 GPa. Numbers given are sample numbers and run durations. Initially, the basaltic liquid was on the left, the altered rhyolite on the right of the profile.

3.6 Rheology

Rheology in solid Earth science is investigation of flow properties of minerals and rocks under pressure and temperature conditions corresponding to the Earth's interior. Large-scale deformation processes such as global mantle convection are understood based on such knowledge. For these reasons, the Bayerisches Geoinstitut investigates rheology of mantle rocks by experimental, analytical and computational techniques. All contributions of 2018, however, made efforts to develop of analytical methods. The first contribution examined grain-boundary characteristics of torsion-deformed olivine aggregate by means of electron back-scattered electron diffraction. The second investigation by Bollinger *et al.* also observed grain boundaries of olivine aggregate, but using transmission electron microscopy with orientation mapping techniques. The third study by Sawa *et al.* investigated compaction of porous germanate olivine polycrystals by scanning and electron microscopy. Further development of these studies would provide useful information for investigation regarding dynamics of the Earth's interior.

a. *Grain boundary effects on olivine plastic deformation (F. Ferreira, K. Marquardt and L. Hansen/Oxford)*

Olivine is the major mineral phase of Earth's upper mantle. Therefore, olivine governs physical properties of the upper mantle and controls mantle flow. Deformation in some regions of the mantle is localized in narrow zones, where grain sizes are strongly reduced. In such regions, grain boundaries should influence on rock deformation and their effects must be better understood. To investigate effects of grain boundaries on deformation, we analyzed distributions of grain boundaries in torsion-deformed polycrystalline aggregates of olivine. In addition, the ease at which dislocations crosses grain boundaries was calculated using the m' factor, a geometric criterion for slip transmission. The grain boundaries were characterized by means of electron backscattered diffraction (EBSD). The changes in slip-system activities and m' factor with strain (Fig. 3.6-1) suggest that slip transmission should become easier with increasing strain until the total shear strain reaches $\gamma = 4$, and essentially remains unchanged for further strain increase. The rapid increase in the m' factor is correlated with increase of grains oriented in the soft direction by the (010)[100] slip system. At least 60 % of the grains are oriented in the glide direction of this slip system, when γ exceeds 4. On the other hand, we observed a constant change of the grain-boundary plane distribution (GBPD) up to the total strain of $\gamma = 10.9$ (Fig. 3.6-2). At the low strains ($\gamma = 0$ to 3.6), {hk0} planes are dominant. With increasing strain, clustering of grain-boundary planes close to {140} develops. At the highest strains ($\gamma = 7.3$ to 10.9), these planes are 3 times more abundant than the others. As deformation progresses, more grains are oriented in the soft orientations, with the ***b***-planes aligned parallel to the shear plane. This also means that slip systems of neighboring grains are closer to parallelism, characterizing a feedback process. We suggest occurrence of continuous grain-boundary formation, even after a steady-state deformation is achieved.

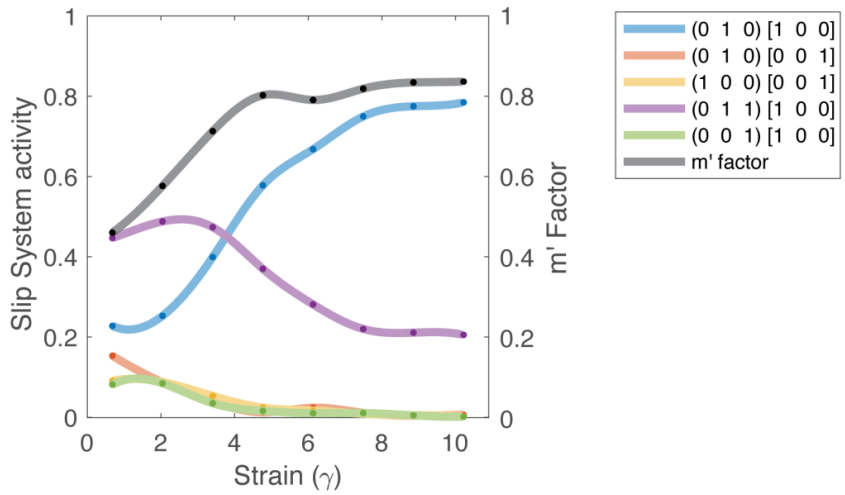

Fig. 3.6-1: Slip-system activity and *m′* factor evolution for increasing strain. These data are presented for 8 sections of equal area. The slip-system activity is given by the ratio between the number of grains in an easy to glide orientation for each slip system and the total number of grains. The *m′* factor is given for the calculated average of each section. The *m′* factor ranges from 0 for an impenetrable boundary, to 1 for a transparent boundary.

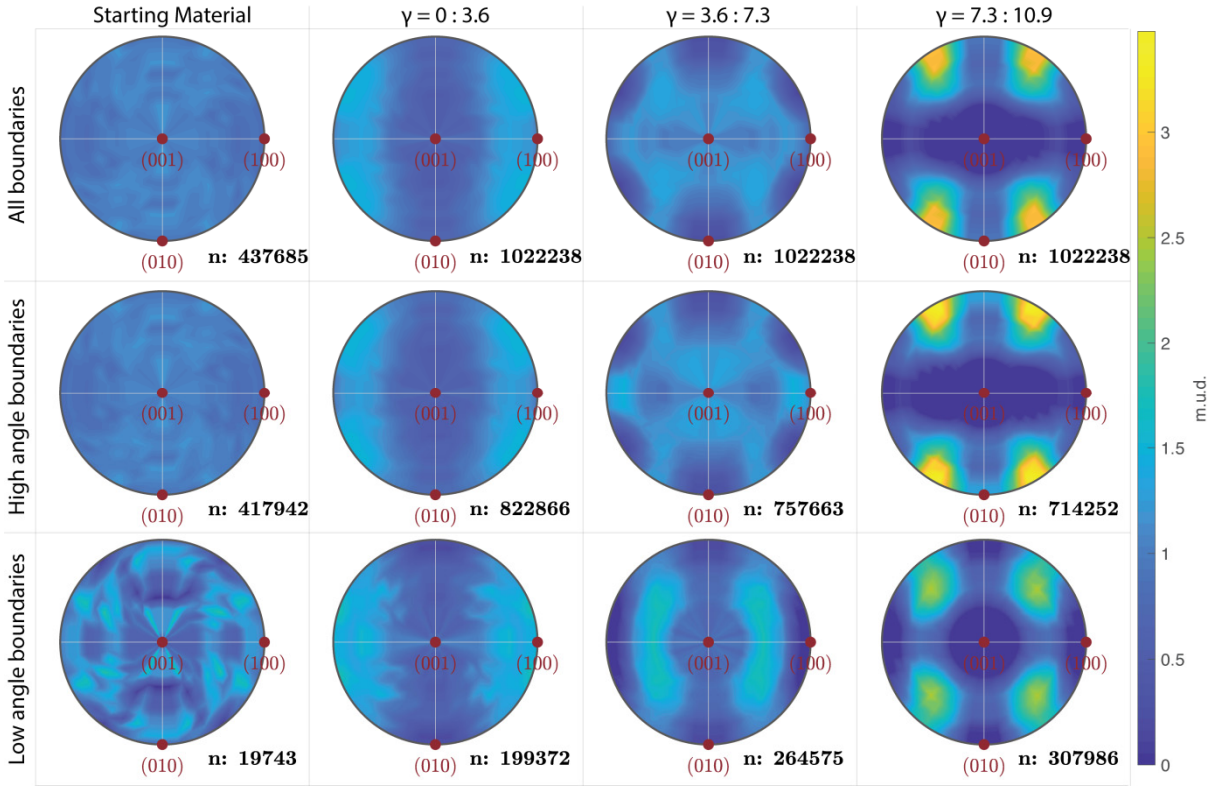

Fig. 3.6-2: The upper hemisphere projections of GBPD of olivine for all grains ("All boundaries", upper row), grains with misorientation angle higher than 20º ("High angle boundaries", middle row) and grains with misorientation angle between 2º and 20º ("Low angle boundaries", bottom row), with increasing strain from $\gamma = 0$ to $\gamma = 10.9$. The number of grain boundary segments (n) is given below each plot.

b. *Microstructural evidence for grain boundary migration and dynamic recrystallization in experimentally deformed forsterite aggregates (C. Bollinger; B.C. Nzogang, A. Mussi and J. Bouquerel/Lille, D.A. Molodov/Aachen and P. Cordier/Lille)*

Since $(Mg, Fe)_2SiO_4$ olivine is the main constituent of the upper mantle, understanding its plastic behaviour and deformation mechanisms is important in order to model the rheology of the mantle. Plastic deformation of peridotites accommodates large strains in the mantle. At relatively low temperatures, *e.g.*, in the lithospheric mantle, reaching large strains is possible, only when microstructure evolves to release stored energy through recrystallization, especially under the steady-state regime. The concept of recrystallization includes different mechanisms to lead to microstructural evolution during deformation. Formation of new grains is one of such mechanisms. Other recovery mechanisms such as dislocation annihilation by cross-slip or climb and grain-boundary migration can also contribute.

In this study, we focused on recovery mechanisms involving grain boundaries and recrystallization. We examined forsterite samples deformed at large strains at a temperature of 1100 °C, which is appropriate for lithosphere, and characterized their deformed microstructures using transmission electron microscopy with orientation mapping techniques (ACOM-TEM).

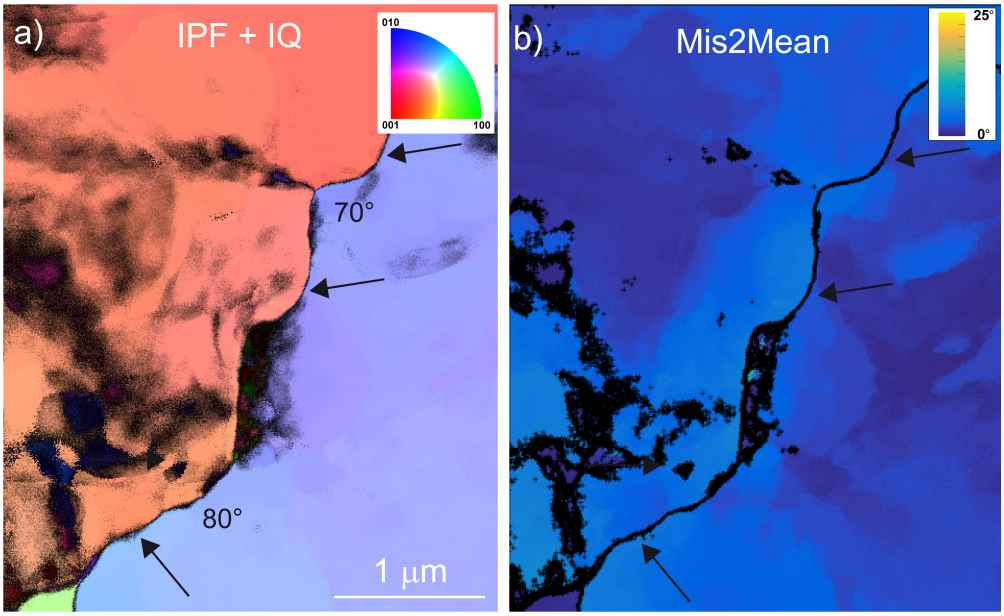

Fig. 3.6-3: Grain boundaries in the For70B sample, which was deformed at a temperature of 1100 °C, a pressure of 5 GPa and a strain rate of 1×10^{-5} s^{-1}) with a total strain of 40 %. a) An inversed pole figure (IPF) map superimposed with the indexation quality (IQ). The color code shows the directions of the *Pnma* symmetry. The grain boundaries indicated by the black arrows have misorientations of 70-80°. b) Mis2Mean, which indicates misorientations of measurement points from a reference of the mean orientation, map corresponding to a). Note that the deviation of misorientation is within 10°.

We observed serrated grain and sub-grain boundaries (GB and SGB, respectively) in a sample with 25 % strains (Fig. 3.6-3). We interpret these microstructural features as evidence of occurrence of grain-boundary migration mechanism. By evaluating the driving forces for grain/subgrain-boundary motion, we find that the interfacial tension drives boundary motion more than the strain energy. In a sample with larger strains of 40 %, we found pervasive evidence for discontinuous dynamic recrystallization with nucleation of new grains at grain boundaries (Fig. 3.6-4). The observations reveal that subgrain migration and grain boundary bulging contribute to the nucleation of new grains. These mechanisms are probably critical to allow deformation of peridotite with large strains under steady-state regimes in the lithospheric mantle.

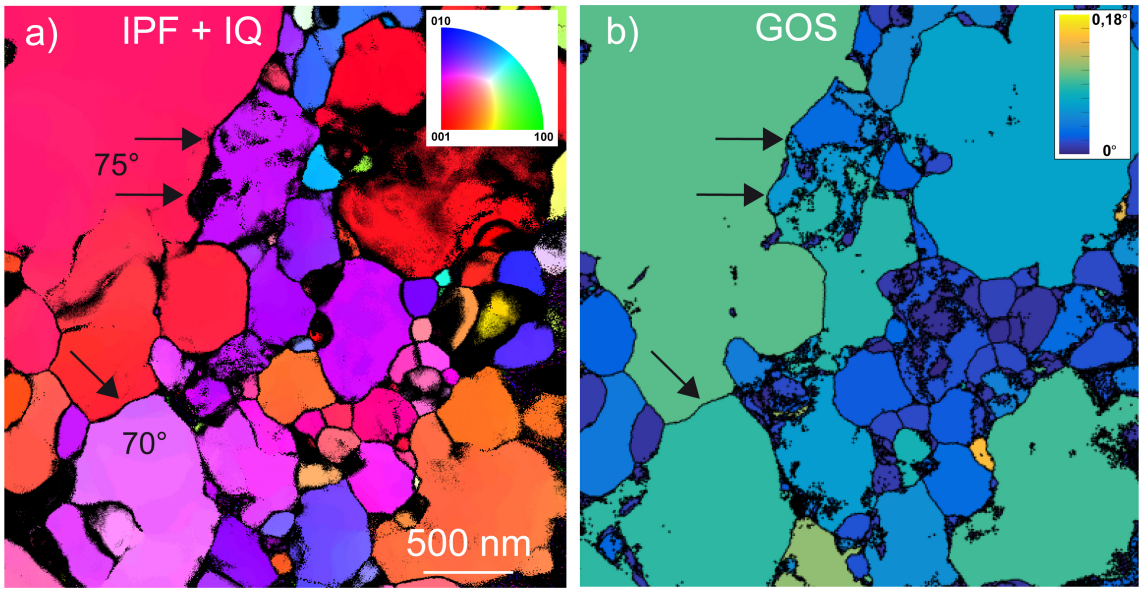

Fig. 3.6-4: Small grains in the For70B sample. a) An IPF map superimposed with IQ. The colour code shows the directions of the *Pnma* symmetry. The misorientation angles of some boundaries are indicated with arrows. b) The grain orientation spread (GOS) map, which indicates deviations of average misorientation of grains from the reference point, corresponding to a).

c. *Strain localization bands developed in experimentally created fine-grained aggregates (S. Sawa, J. Muto and H. Nagahama/Sendai; N. Miyajima)*

Strain localization bands are often observed in natural and experimentally-deformed porous rocks. Strain localization bands have finer grains than the other parts, because grains are crushed due to pore collapse during deformation. Previous studies pointed out that they form under stress conditions close to the transition regime from brittle faulting to cataclastic flow. However, samples in the majority of previous studies are natural porous sandstones, and there are only few studies using experimental fine-grained porous aggregates. We suggest a

possibility that strain localization in fine-grained porous samples, which influences the rheology of rocks, may occur at initial stages of deformation in laboratory experiments. Therefore, we conducted a deformation experiment to observe microstructures of such samples using a scanning electron microscope (SEM) and transmission electron microscope (TEM).

The deformation experiment was performed using germanate olivine powder with grain sizes less than 10 μm and porosity of 30 % as samples in a Griggs-type deformation apparatus. The samples were pressurized to 1.0 GPa and heated to 300 °C, and then were deformed by displacing a differential piston with a strain rate of 3.1×10^{-4} s^{-1}. Little after differential stresses started to be generated, the displacement of the differential piston was terminated to stop compaction of the samples, and the samples were recovered for SEM and TEM observations
The SEM observation showed a number of fine-grained bands (Fig. 3.6-5). They should be compaction shear bands, which are special cases of shear bands, based on a theoretical shear-band analysis of the bifurcation approach. Furthermore, the TEM observation revealed that coarse grains next to fine grains have a high dislocation density (Fig. 3.6-6). During compaction, grains should have rotated and have been crushed due to shear-strain localization to have high dislocation density.

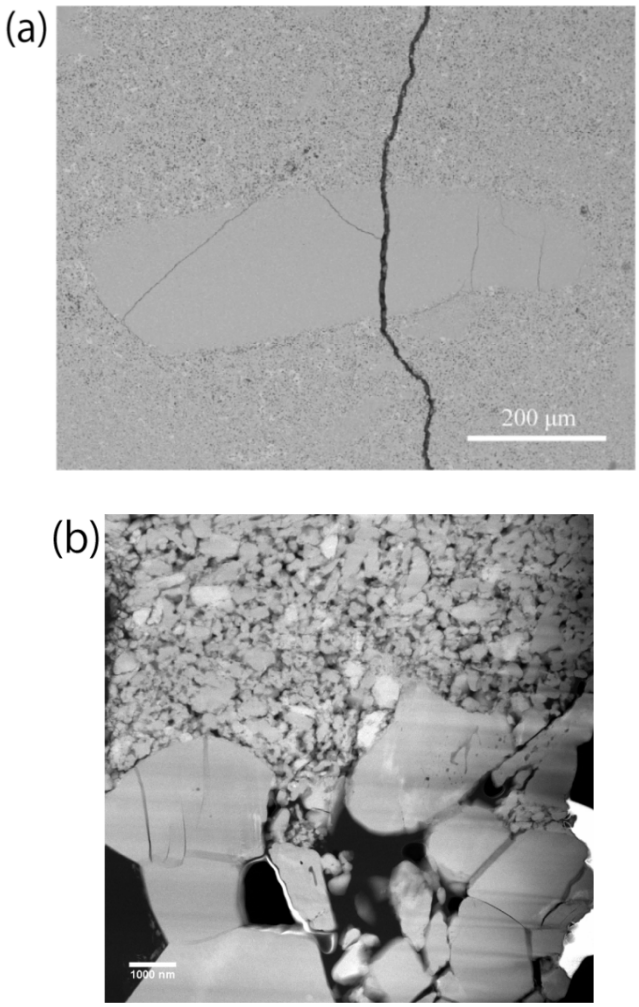

Fig. 3.6-5: Textures of a powdered germanate-olivine sample after compaction. (a) A back-scattered electron image. The compaction shear band is observed in the middle of the image. The grain size of coarse grains is 1-10 μm, whereas those of the fine grains in this band are less than 1 μm. (b) A high-angle annular dark field (HAADF) STEM image at the boundary of the compaction shear band. The gray and light gray minerals are germanate olivine and pyroxene, respectively.

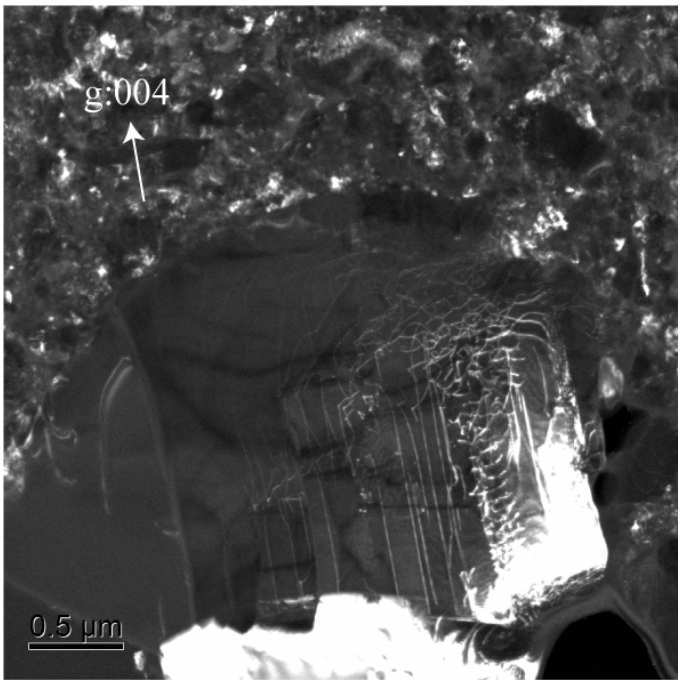

Fig. 3.6-6: A weak-beam dark-field TEM image with a diffraction vector of $\boldsymbol{g}$ = 004. The coarse grain has high-density [001] dislocations.

3.7 Materials Science

At Bayerisches Geoinstitut, unique expertise in high-pressure equipment, *in situ* technologies, and sample characterisation are available that allow us to address sophisticated and challenging research into the physics and chemistry of materials. In this section, we present results of studies of various classes of solids: complex oxides, nitrides, and yttrium aluminium garnet (YAG). The *in situ* demonstration of ultra-high-pressure chemical reactions between iron and nitrogen to form FeN_4 at 180 GPa is certainly a highlight in material science research at Bayerisches Geoinstitut this year.

Fe_4O_5, which was first synthesized and recovered from high-pressure experiments in 2011, continues to show interesting chemical and physical phenomena due to the mixed valence of Fe^{2+} and Fe^{3+} in the crystal, as evidenced by a continuing series of contributions to the annual report since 2012. This year, single crystal *in situ* data on high-pressure crystal structure and magnetic properties of Fe_4O_5 reveal that it undergoes a unique charge-ordering transition below 150 K that involves competing dimeric and trimeric ordering within chains of Fe ions. This transition also drives an intricate incommensurate distortion in its crystal structure.

Poly-nitrogen compounds like FeN_4, mentioned in the introductory paragraph, are the subject of the following three contributions. Nitrogen-based materials have been considered as potential high energy density materials for a long time as they can store and release large quantities of chemical energy through a transformation from single- to triple-bonded state in nitrogen. High-pressure studies provide a pathway to reinvigorate research in these materials that has stagnated for a long time using classical chemical methods. Generally, high nitrogen content and stability are mutually exclusive, making the synthesis of such materials challenging, but the energy input by high pressure can bridge this gap. By directly reacting N_2 with Fe, Re and S in the diamond anvil cell, researchers at Bayerisches Geoinstitut synthesized several novel nitrogen-bearing compounds, and the resulting crystalline materials FeN_4, $ReN_8{\cdot}xN_2$ and SN_2 are analyzed for their structure. The synthesis of $ReN_8{\cdot}xN_2$ in the megabar range is a unique example of the formation of a complex porous framework in a direct reaction between two elements, in which one of the reagents also plays the role of guest molecule that is essential for the stability of the synthesized compound.

Grain boundary diffusion and segregation are of fundamental interest in polycrystalline materials as they have a significant influence on many processes in engineering or geology. For laser ceramics, like yttrium aluminium garnet (YAG), their influences include the applicability and life-time. In a study presented here, the grain boundary diffusion of La, Fe, Mg, and Ti has been characterized for geometrically well-defined grain boundaries in YAG. Segregating elements along the grain boundary mutually influence their incorporation and therefore material properties.

a. *Pressure tuning of charge ordering in iron oxide, Fe_4O_5 (S.V. Ovsyannikov, M. Bykov, E. Bykova/Hamburg, K. Glazyrin/Hamburg, R.S. Manna/Augsburg, A.A. Tsirlin/Augsburg; V. Cerantola/Grenoble, I. Kupenko/Münster, A.V. Kurnosov, I. Kantor/Grenoble, A.S. Pakhomova/Grenoble, I. Chuvashova/Washington D.C., A.I. Chumakov/Grenoble, R. Rüffer/ Grenoble, C.A. McCammon and L.S. Dubrovinsky)*

A Verwey-type charge-ordering transition in magnetite (Fe_3O_4) at 120 K leads to the formation of linear units of three iron ions with one shared electron, called trimerons. The recently-discovered iron pentoxide (Fe_4O_5) comprising mixed-valent iron cations at octahedral chains, demonstrates another unusual charge-ordering transition at 150 K involving competing formation of iron trimerons and dimerons. In this work we found that pressure can tune the charge-ordering pattern in Fe_4O_5 and strongly affect ordering temperature. We report two charge-ordered phases, the first of which may comprise both dimeron and trimeron units, whereas the second exhibits an overall dimerization involving both the octahedral and trigonal-prismatic chains of iron in the crystal structure. We link the dramatic change in the charge-ordering pattern in the second phase to a redistribution of electrons between the octahedral and prismatic iron chains, and propose that the average oxidation state of iron cations can pre-determine a charge-ordering pattern.

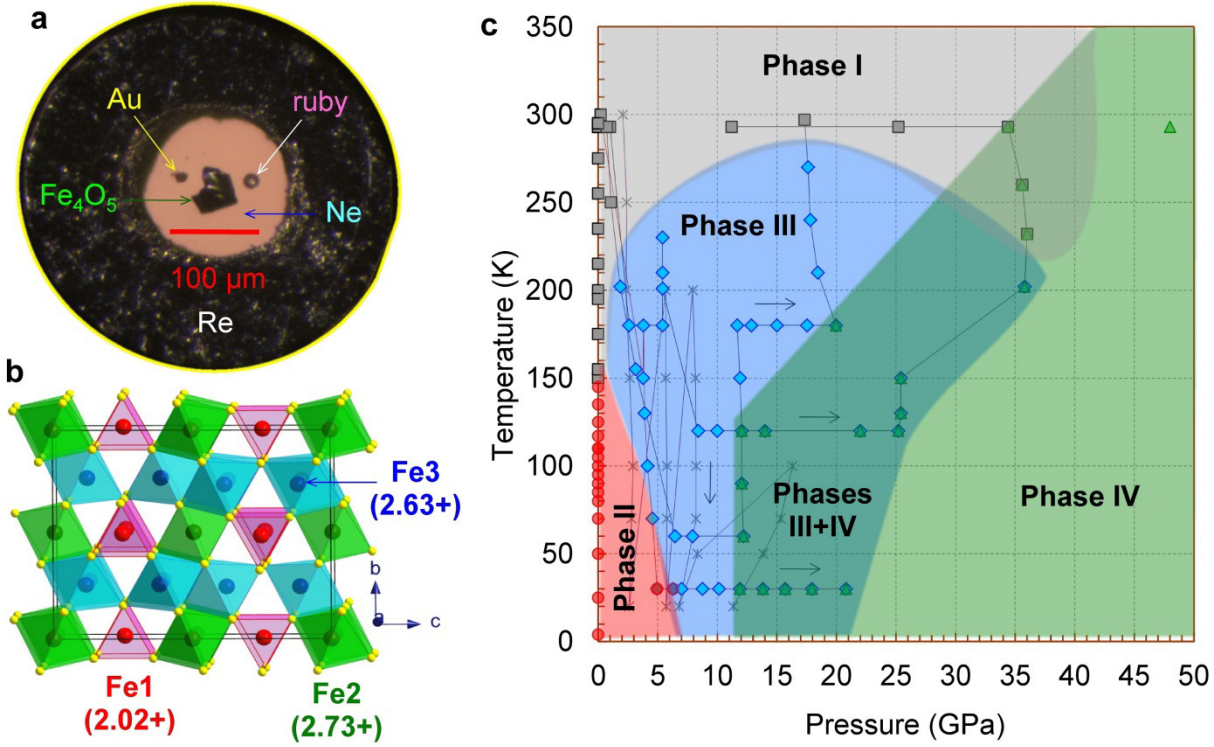

Fig. 3.7-1: (*a*) A diamond anvil cell with a single crystal of Fe_4O_5 and two pressure markers (ruby, Au) loaded in a neon pressure-transmitting medium in the sample chamber drilled inside rhenium gasket. (*b*) Crystal structure of Fe_4O_5 at ambient conditions (Fe_4O_5-I phase) and bond valence sums (BVS) values of different iron cations. (*c*) High-pressure, low-temperature phase diagram of Fe_4O_5.Shaded areas show proposed stability regions of the different phases discussed in the text.

We started the experiments from normal conditions (Fe_4O_5-I phase) and gradually decreased the temperature in a cryostat while monitoring the sample by X-ray diffraction. At about 200 K and 2 GPa, we observed the appearance of superlattice reflections, indicating the emergence of charge-ordering. We verified that the reflections do not belong to the earlier-reported charge-ordered Fe_4O_5-II phase, and termed this phase as Fe_4O_5-III. Upon heating at about 18 GPa, we could follow the superlattice reflections of Fe_4O_5-III up to at least 270 K (Fig. 3.7-1). The single-crystal diffraction patterns of Fe_4O_5-III are ambiguous and can be indexed equally well by two crystal structures: Fe_4O_5-III-a with a monoclinic $C2/m$ lattice and Fe_4O_5-III-b with an orthorhombic $C222_1$ unit cell.

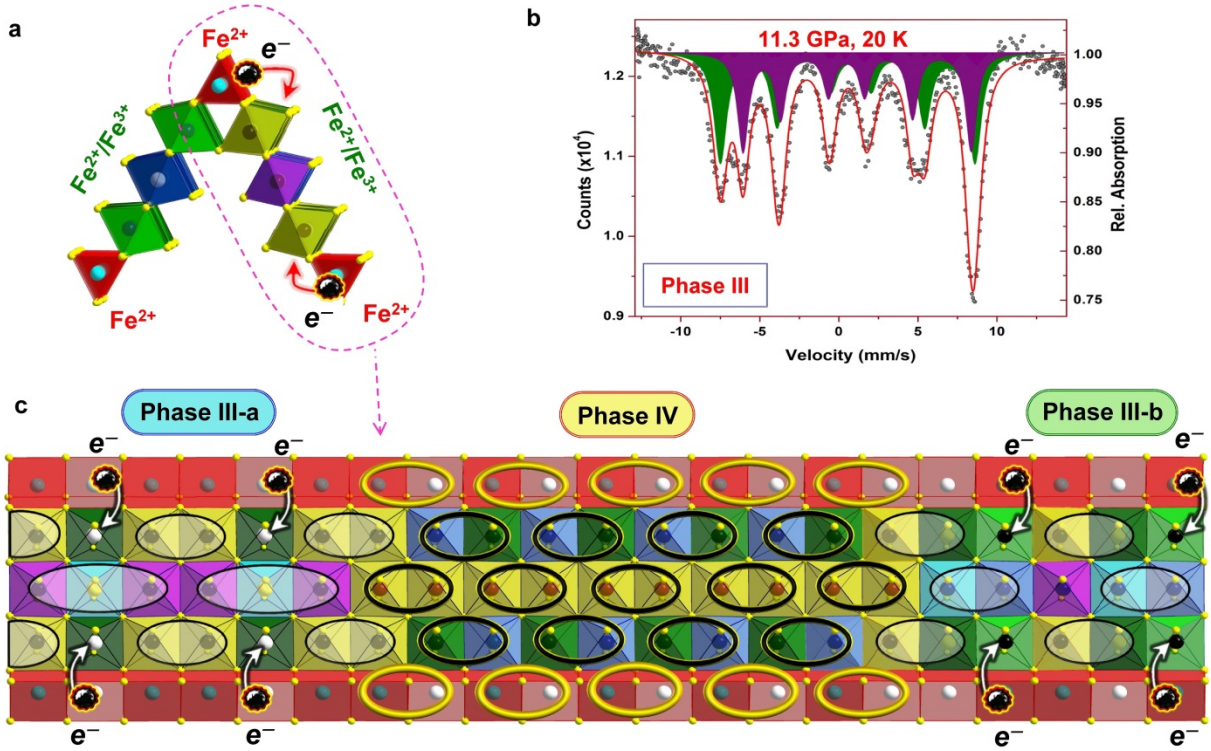

Fig. 3.7-2: (*a*) Edge-shared diagonal ribbons of prisms and octahedra in the crystal structure of Fe_4O_5-III phase provide "channels" for charge hopping between prisms and octahedra. (*b*) A representative Mössbauer spectrum of the Fe_4O_5-III phase. The spectrum exhibits a complex distribution of hyperfine fields that can be refined by superposition of sextets. (*c*) A model demonstrating the coexistence of several charge-ordered phases in a single crystal of Fe_4O_5. The electron transfer between the prisms and octahedra leads to a short-range reorganization of ordering.

The octahedral chains of Fe_4O_5-III occupied by mixed-valent iron cations show a pronounced shortening of distances between some neighboring Fe atoms, whereas the prismatic chains of are characterized by nearly equal Fe-Fe distances. The dramatic shortening suggests the formation of Fe dimers and trimers (Fig. 3.7-2). We analyzed the Fe-O bond lengths of all iron cations in both Fe_4O_5-III candidate structures using a common bond valence sum (BVS)

method. The BVS results reveal that the dimers consist of moderately overcharged valence-mixed $Fe^{2.5+}$ ions; similarly, compared to a combination of one Fe^{2+} and two Fe^{3+} ions, the trimers may be both strongly overcharged (+8.29) or strongly undercharged (+7.57).

Above 12 GPa and temperatures below 150 K, additional reflections appeared, suggesting the incipient transition to a further phase, Fe_4O_5-IV; at these low temperatures, the transition to Fe_4O_5-IV is nearly complete at 25 GPa. For Fe_4O_5-IV we determined a monoclinic $P2_1/m$ symmetry. This structure shows an overall dimerization, involving both octahedral and prismatic chains (Fig. 3.7-2). The calculated BVS values for the prismatic Fe1 atoms in this structure are found to be +2.26; average values of Fe in the octahedral chains are +2.63 and +2.554. These values are also consistent with dimeric ordering in the chain; they also suggest that Fe_4O_5 with a nominal average oxidation state of $Fe^{2.5+}$ tends to reach a state under pressure with more uniform charge distribution. The reduced distances between some iron atoms in the octahedral chains and the neighboring atoms in the prisms in both Fe_4O_5-III-a and Fe_4O_5-III-b structures appeared to be the most suitable channels for hopping of electrons from the prisms to the octahedral matrix (Fig. 3.7-2).

At ambient conditions the Mössbauer spectra of Fe_4O_5 can be well fitted by the superposition of a magnetic sextet and a paramagnetic doublet with relative areas of 80(2)% and 20(2)%, respectively. They can be assigned to octahedral Fe2 and Fe3 atoms and the prismatic Fe1 atoms, respectively. Mössbauer spectra collected in the charge-ordered phases, by contrast, show a superposition of several sextets. For instance, the spectrum acquired at 20 K and 11.3 GPa for the Fe_4O_5-III phase can be well described by two sextets with center shifts of δ_{CS}=0.66(3) and 0.82(3) mm/s (Fig. 3.7-2). These values corresponded to oxidation states of +2.7 and +2.45, respectively, in general agreement with the BVS results given above. This observation unambiguously demonstrates that the oxidation states of the octahedrally-coordinated iron in Fe_4O_5 do not split into integer Fe^{2+} and Fe^{3+} components, even at 20 K.

b. *Synthesis of FeN_4 at 180 GPa and its crystal structure from a submicron-sized grain (M. Bykov, S. Khandarkhaeva, T. Fedotenko/Bayreuth, P. Sedmak/Grenoble, N.A. Dubrovinskaia/ Bayreuth and L.S. Dubrovinsky)*

Polynitrogen compounds have attracted great interest because of their potential applications as high-energy-density materials. The synthesis of such materials usually requires high-pressure high-temperature conditions that are generated in a diamond anvil cell (DAC). With increasing pressures, synthesis and diffraction studies in DACs become more challenging, even at dedicated high-pressure stations of 3rd generation synchrotron facilities where the X-ray beam can be focused to 2-3 μm. At pressures above 150 GPa, the size of the sample does not exceed 10 μm, and single-crystalline grains of the reaction product(s) are often of submicron size which leads to a poor signal-to-noise ratio in single-crystal X-ray diffraction (SCXRD). In addition, contributions of parasitic diffraction from the gasket material increase with pressure as the sample chamber becomes smaller. Submicron focusing of the X-ray

beam, which is possible at some synchrotron beamlines, can provide suitable conditions to collect SCXRD data in the megabar pressure range.

In this study, a piece of iron powder was loaded inside a sample chamber of a BX90-type diamond anvil cell equipped with double-bevelled Boehler–Almax type diamonds (culet diameter 40 mm). Nitrogen was used as a pressure-transmitting medium and as a reagent for the synthesis. The sample was compressed to 180 GPa and laser-heated from both sides up to 2700(200) K. The X-ray beam was focused to 0.3×0.3 μm^2 at the synchrotron beamline ID11 at the ESRF in Grenoble which allowed us to collect SCXRD data from a FeN_4 grain with linear dimensions of ~ 0.5 μm. As a result of submicron beam focusing, the quality of the SCXRD data collected at 180 GPa turned out to be much better than our previous refinement at 135 GPa. This is evident from a comparison of important refinement indicators, such as the data-to-parameter ratio (7.1 vs 4.8), $\Delta\rho_{max}/\Delta\rho_{min}$ (0.76/-0.56 vs 0.98/-1.09 $e\cdot$Å^3) and $R_1[I > 2\sigma(I)]$ (0.040 vs 0.064). As a consequence, the precision of the bond lengths and angles is significantly improved (Table 3.7-1).

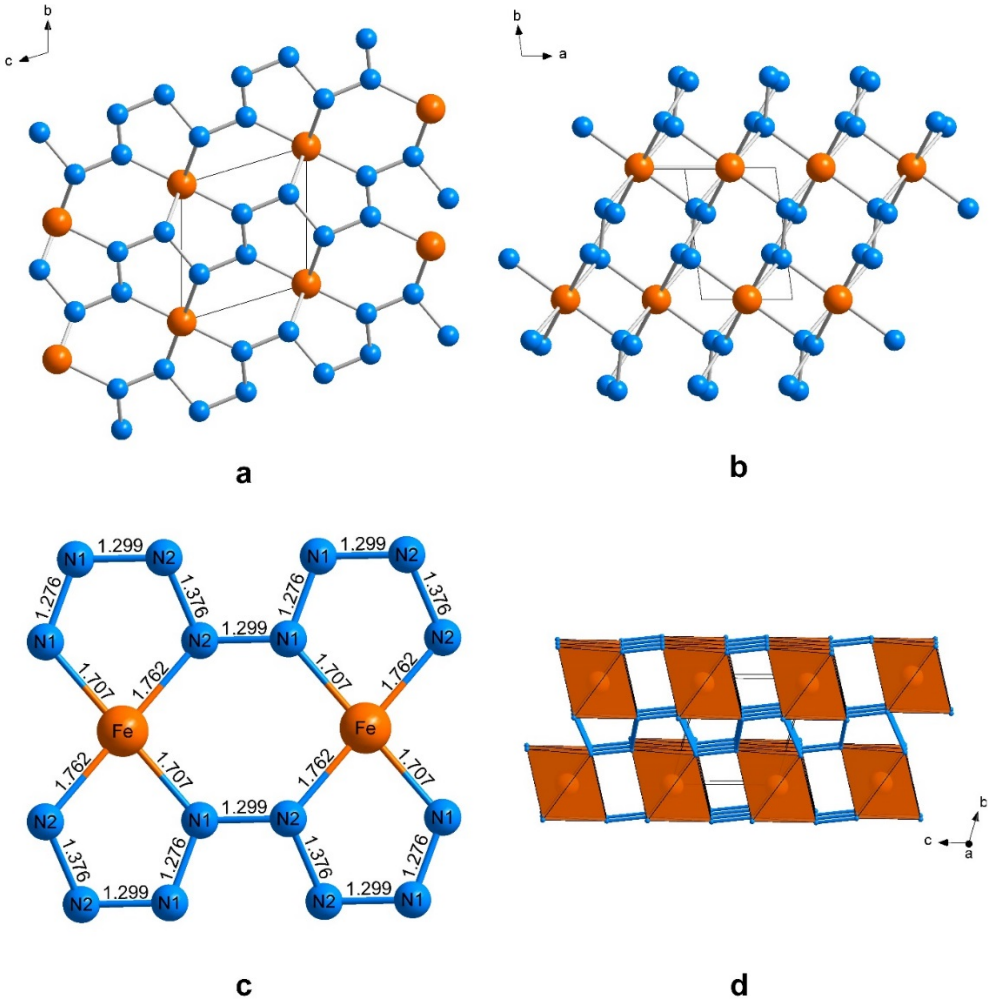

Fig. 3.7-3: Crystal structure of FeN_4 at 180 GPa. Projections of the crystal structure along [100] (a) and [001] (b), respectively and in polyhedral representation (d). (c) A fragment of the crystal structure showing the coordination of Fe atoms.

The crystal structure of FeN_4 at 180 GPa is presented in Fig. 3.7-3. The Fe1 atom occupies an inversion center of space-group type $P\bar{1}$ (Wyckoff position 1*d*), while the two nitrogen atoms N1 and N2 occupy general positions (2*i*). The iron atom is coordinated by six nitrogen atoms, forming a distorted octahedron (FeN_6). The FeN_6 octahedra share opposite edges, forming infinite chains along the [100] direction. These chains are interconnected through N-N bridges as shown in Fig. 3.7-3. The covalently bonded nitrogen atoms form infinite zigzag chains running along [001]. The N1 atom has a trigonal–planar coordination, while N2 is tetrahedrally coordinated, suggesting sp^2 and sp^3 hybridization, respectively. Therefore, the nitrogen atoms form catena-poly[tetraz-1-ene-1,4-diyl] anions $[–N–N–N=N–]_{\infty}$.

This study demonstrates that the experimental setups with submicron X-ray beam focusing open new perspectives for the accurate structural studies at multimegabar pressures that were thought as impossible before. This is extremely important for the advances in chemistry, physics, mineral and materials science.

Table 3.7-1: Comparison of the structure refinements and structural parameters of FeN_4 based on the datasets, collected with different focus size of the X-ray beam.

	Microfocus	**Nanofocus**
Beam size, μm^2	3 × 3	0.3 × 0.3
Pressure, GPa	135	180
R_1	0.064	0.040
$\Delta\rho_{max}/\Delta\rho_{min}$, $e\cdot Å^{-3}$	0.98/-1.09	0.76/-0.56
Data/parameter ratio	4.8	7.1
Interatomic distances, Å:		
Fe – N1	1.73(2)	1.707(11)
Fe – N2	1.81(3)	1.783(14)
N1 – N1	1.29(5)	1.277(14)
N1 – N2	1.30(3)	1.298(8)
N2 – N2	1.43(4)	1.37(3)

c. *High-pressure synthesis of a nitrogen-rich inclusion compound $ReN_8{\cdot}xN_2$ with conjugated polymeric nitrogen chains (M. Bykov, E. Bykova/Hamburg, E. Koemets, T. Fedotenko/ Bayreuth, G. Aprilis/Bayreuth, K. Glazyrin/Hamburg, H.-P. Liermann/Hamburg, A. Ponomareva/Moscow, J. Tidholm/Linköping, F. Tasnádi/Linköping, I.A. Abrikosov/ Linköping, N.A. Dubrovinskaia/Bayreuth and L.S. Dubrovinsky)*

Polynitrogen compounds have attracted great interest because of their potential applications as high-energy-density materials. High nitrogen content and stability are mutually exclusive, making the synthesis of such materials challenging. One way to stabilize such compounds is the application of high pressure. In the present work we have synthesized a novel compound $ReN_8{\cdot}N_2$ via direct reaction between rhenium and nitrogen in a laser-heated diamond anvil cell.

A piece of rhenium powder was placed inside a BX90 diamond anvil cell (DAC) equipped with Boehler-Almax type diamonds. The sample chamber was filled with nitrogen which served both as a pressure-transmitting medium and reagent. The DAC was compressed to 105 GPa and the sample was laser-heated up to 2300 K. Although the initial reagents were powders, the chemical reaction led to the formation of numerous good-quality single-crystal domains of the new compound, such that the diffraction data from the quenched material could be treated using well-established methods of single-crystal data analysis. Indexing revealed a body-centered orthorhombic unit cell with the lattice parameters $a = 3.4475(7)$, $b = 6.491(11)$, and $c = 6.048(3)$ Å, and symmetry *Immm*. The initial structure solution suggested the chemical formula ReN_8 (Fig. 3.7-4) and a structure in which Re atoms occupy the 2*a* (0,0,0) site and nitrogen atoms N1 occupy the site 16*o* (-0.320(3), 0.178(3), 0.1874(16)). Each Re atom is a member of two mutually perpendicular quasi-planar ReN_8 spiro-cycles, lying in the (011) and (0-11) planes (Fig. 3.7-4). Along the *a*-axis, nitrogen atoms are connected to each other by forming infinite zigzag chains, and Re and N1 atoms form a framework containing square-shaped channels. The size of the voids is sufficiently large to accommodate nitrogen molecules. We were able to detect a residual electron density, which can be explained by placing another nitrogen atom N2 at the partially occupied site 4*f* (*x*,1/2,0), with a N2-N2 distance of 1.1(1) Å corresponds to the N≡N triple bond. The structure at 134 GPa was ultimately refined with a chemical composition $ReN_8 \cdot 0.7(2)N_2$.

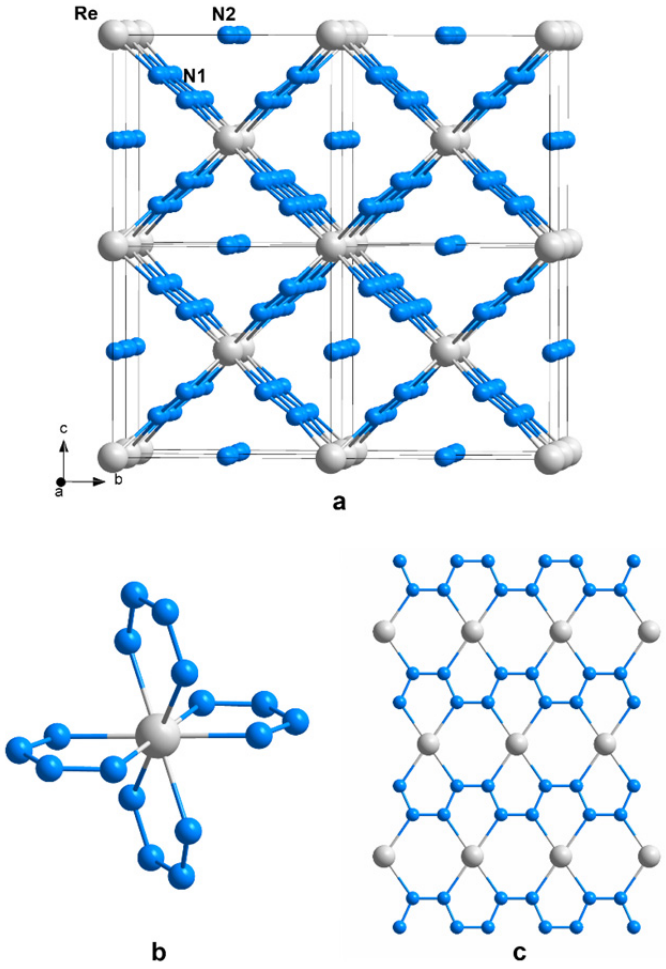

Fig. 3.7-4: (a) Crystal structure of $ReN_8 \cdot xN_2$ at 134 GPa. Re and N1 atoms form a framework with rectangular-shaped channels, which accommodate N2 atoms. N atoms are shown in blue, Re in gray. b) Fragment of the crystal structure showing the coordination of Re atoms: only Re and N1 atoms are shown. c) Atoms in the lattice plane (0 1 -1). Out-of plane atoms are not shown.

The geometry of the nitrogen chains and the interatomic distances provide can be used to analyze bonding in this compound. All of the N1 atoms have planar triangular coordination, suggesting sp^2 hybridization; N1-N1 distances are 1.24(2) and 1.30(4) Å, intermediate between double- and single-bonded N-N units at this pressure. Nitrogen chains in $ReN_8 \cdot xN_2$ are therefore described as polydiazenediyl $[-N=N-]_\infty$, which is a nitrogen analogue of polyacetylene and polythiazyl $(SN)_x$.

The synthesis of $ReN_8 \cdot xN_2$ is a unique example of the formation of a complex porous framework in a direct reaction between two elements, in which one of the reagents also is the guest molecule that is essential for the stability of the synthesized compound.

d. *High-pressure synthesis of novel nitrides in the S-N_2 and Mg-N_2 systems (D. Laniel/ Bayreuth, M. Bykov, N.A. Dubrovinskaia/Bayreuth and L.S Dubrovinsky)*

The pursuit of novel sources of energy is one of the key challenges of this century. Advancing high energy density materials (HEDM) using classical chemical methods, however, has stagnated over the past half-century. The high-pressure synthesis of materials provides a promising alternative to produce solids that contain single-bonded nitrogen arrangements which can store and release the largest quantities of chemical energy through the transformation from single- to triple-bonded states in nitrogen. Poly-nitrogen ions synthesized at high pressure could be employed as building blocks for a single-bonded nitrogen-only salt, metastable at ambient conditions, the ultimate green HEDM.

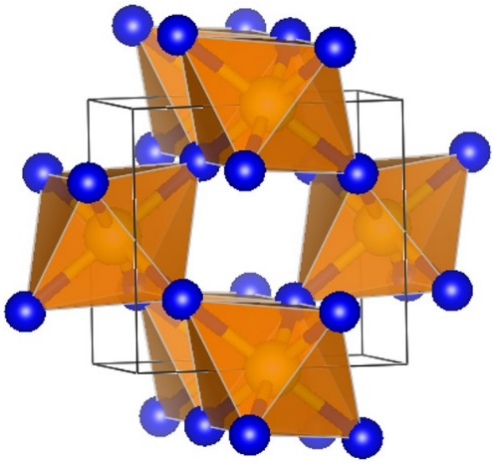

Fig. 3.7-5: Structure of the novel SN_2 compound, determined by single crystal X-ray diffraction, synthesized under high pressure and temperature. The blue and yellow spheres represent N and S atoms, respectively.

The main goal of this research was to synthesize and characterize novel cationic and anionic poly-nitrogen complexes relevant for the design of improved HEDM. Preliminary experiments on S-N_2 and Mg-N_2 samples were performed at high pressures and temperatures.

In both systems, characterization of the quenched laser-heated solids by Raman spectroscopy and/or X-ray diffraction revealed the signature of a chemical reaction between the elements and the formation of previously unobserved compounds. For S-N_2 samples, we were able to resolve the structure of the obtained stoichiometric compound (SN_2) by single-crystal X-ray diffraction measurements. As illustrated in Fig. 3.7-5, this novel solid is comprised of S-N bonds, where six N atoms coordinate each S atom to produce a close-to perfect octahedron, with bond lengths varying between 1.65 Å to 1.66 Å, indicative of a S-N bond order of about one. Raman spectra support this notion as the SN_2 solid was detected to have a vibrational mode at a frequency of 1120 cm^{-1}, typically for single-bonded S-N atoms.

In the case of the Mg-N_2 system, observations suggest the synthesis of a novel Mg-N solid following the sample laser heating at high pressures. As illustrated in Fig. 3.7-6, the magnesium piece significantly grew in size following laser heating, indicative of diffusion of nitrogen atoms into it. Moreover, new Raman modes at frequencies typical of covalently bonded N-N atoms with a bond order of about 1.5 were detected on the heated portions of the sample. Upcoming X-ray diffraction experiments will allow to confirm these preliminary measurements and resolve the novel compound's crystalline structure.

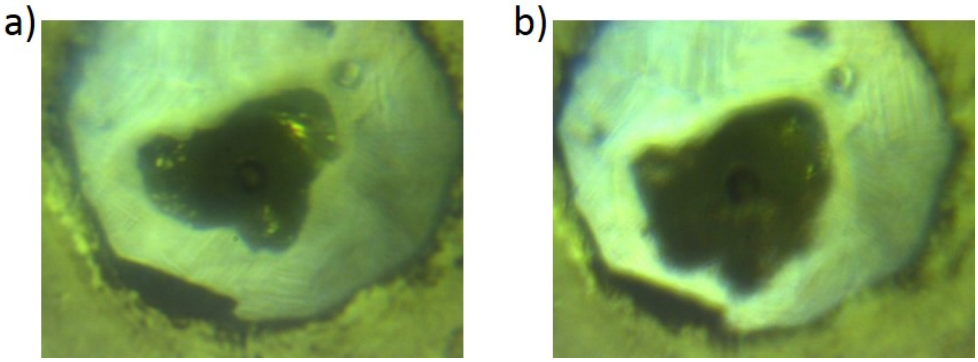

Fig. 3.7-6: Microphotograph of a Mg-N_2 sample inside a diamond anvil cell before (a) and after (b) laser heating. The magnesium piece drastically increases in size, suggesting the diffusion of nitrogen atoms into it and the formation of a previously unknown Mg-N solid.

e. *Grain boundary diffusion and its relation to segregation of multiple elements in YAG (J. Polednia, R. Dohmen/Bochum and K. Marquardt)*

We studied grain boundary diffusion and segregation of La, Fe, Mg, and Ti in a geometrically well-defined grain boundary (GB) of pure yttrium aluminium garnet (YAG). Determining GB diffusion and segregation coefficients in YAG GBs will help both in developing industrial materials and understanding certain geological issues. YAG is one of the most extensively-used laser medium for high power lasers – either as single crystals or a polycrystalline ceramic. In addition, as a garnet-structured material, YAG serves as a model material for

geologically relevant materials, and our study contributes to understanding fundamental GB processes occurring in garnet-rich rocks, such as garnetites.

Bicrystals of YAG were synthesized by the direct wafer bonding method. Perpendicular to the GB, a $La_{3.60}Al_{4.40}O_{12}$ thin-film was pulse-laser deposited as a diffusion source. Minor elements were added through a gas phase in the furnace during the experiment. Diffusion anneals were performed at 1000 and 1450 °C and element concentrations were mapped using energy dispersive X-ray (EDX) spectroscopy in scanning transmission electron microscopy (STEM) mode. The volume and GB diffusion coefficients are determined by fitting a numerical diffusion model to the data. Our model is able to separate the segregation coefficient, s, from the GB diffusion coefficient, $D_{gb,}$ and the GB width, δ. The presented TEM-EDX maps are relatively large, resulting in pixel sizes larger than the physical width of the GB. Such convolution effects result in a range of possible segregation coefficients. The products sD_{gb} for La, Fe, Mg and Ti are at least 8 orders of magnitude faster than their respective volume diffusion, with a minimum diffusivity of 9×10^{-11} m^2/s at 1450 °C. We predict that bulk diffusion of these elements is controlled by sD_{gb} for grain sizes ranging from 0.1 µm - 10 m. We further conclude that segregating elements can influence each other's incorporation and therefore material properties.

3.8 Methodological Developments

An important goal at Bayerisches Geoinstitut is to pursue methodological developments that will benefit and enhance research in the Earth, planetary and material sciences. One obvious aim is to increase the range of extreme conditions that can be reached experimentally, such as the maximum achievable conditions of pressure and temperature. Equally important is the development of experimental techniques for accurately measuring physical parameters in high-pressure experiments and for probing the structure, composition and other properties of samples under extreme conditions. Additional areas include the development of methods for analyzing the chemical compositions of very small samples and for characterizing the microstructures of deformed minerals and other materials. Finally, methodological developments that improve the results of numerical models are of considerable importance, for example for understanding the convection dynamics of the interiors of the Earth and other planets. The ten contributions of this section cover many of these aspects.

The first five contributions of this section are concerned with developments of the diamond anvil cell (DAC), an apparatus that is used for achieving pressures greater than those that are possible with the multianvil apparatus. When combined with laser-heating, the DAC allows pressure-temperature conditions that prevail at the centre of the Earth to be achieved and it is therefore indispensable for experimental studies that concern the Earth's deep mantle and core. The first contribution describes ground-breaking developments that enable the structure of very small samples at high pressure in a diamond anvil cell to be investigated using nuclear magnetic resonance (NMR) spectroscopy. NMR is an important technique that has been used routinely in the Earth sciences to study the structure of minerals and glasses under ambient conditions. Normally quite large samples are required but, based on the developments described here, very small samples can now be studied *in situ* at extremely high pressures. Another problem with the small size of DAC samples (typically only 3-4 μm at pressures above 200 GPa) is that laser heating can often affect a region that is much larger that the sample. The second contribution below describes developments to obtain a highly focused beam that is only 5 μm in diameter – which will result in a much improved accuracy when measuring the sample temperature. The following contribution is concerned with studying water ices at high temperatures in the diamond anvil cell in order to understand the mantles of the giant planets Uranus and Saturn. Such experiments are difficult because H_2O reacts with the metallic gaskets in DAC experiments and releases hydrogen that can cause the diamond anvils to fail. A solution to this problem, as described below, is to compress and heat the sample rapidly while at the same time collecting X-ray diffraction data from the sample. Another problem with the DAC is that the cell needs to be rotated in some types of experiments (such as single crystal X-ray diffraction) which causes misalignment of the sample with respect to X-rays and laser beams. This problem has been overcome by redesigning the diamond anvils with a round table (DART anvils).

Oxygen fugacity (the chemical potential of oxygen) is a critical parameter that determines the outcome of many experiments on iron-bearing systems. It is therefore essential to be able to

determine the oxygen fugacity in experiments at high pressures and temperatures and two contributions below describe new methods for doing this. In the first case, the method depends on including a metallic Fe-Ir alloy in a DAC sample because the composition of the alloy is determined by oxygen fugacity. In the second case, oxygen fugacity has been determined as a function of pressure and temperature when Ru and RuO_2 coexist in equilibrium.

Technical developments that enable concentrations of the elements sulphur and chlorine to be analyzed in small melt inclusions using laser-ablation inductively-coupled-plasma mass spectrometry (LA-ICP-MS) are described. Other analytical methods typically require large homogeneous samples when analyzing these elements and are therefore unsuitable for melt inclusions. The next contribution concerns research into the rheology of Earth-forming minerals. The use of a combination of several techniques is described for preparing samples of deformed minerals for examination in the transmission electron microscope (TEM). This approach results in the ability to select very specific microstructures for TEM investigations.

The final two contributions describe some developments in numerical modelling. The first is concerned with determining the permeability of low-porosity rocks using a numerical approach (permeability is very difficult to measure+ experimentally when porosities are low). In the second (and final contribution of this section) the effects of varying grid resolution and geometry on the results of numerical models of mantle convection and coupled plate tectonics are investigated.

a. *Development of novel techniques for high-pressure NMR in diamond anvil cells (T. Meier, S. Khandarkhaeva, S. Petitgirard and L.S. Dubrovinsky)*

Implementing Nuclear Resonance Spectroscopy (NMR) in diamond anvil cell experiments promises enormous benefits for both high-pressure research and experimental geophysics, as it locally probes chemical and electronic environments of matter with unprecedented accuracy. Furthermore, one of the most NMR sensitive nucleii turns out to be hydrogen, which is the least detectable element using other methods. Therefore, developing novel NMR resonators for NMR spectroscopy has remained a high priority within the BGI in 2018.

At the beginning of the year, we were able to develop a more sophisticated resonator structure using the recently introduced sensing of the faint nuclear induction signal due to the precession of an excited spin system by means of so-called Lenz lenses. These novel NMR resonators are almost two dimensional flux transformers, allowing for an enhancement of the radio-frequency magnetic fields within the sample cavity. These new resonators are built by the combination of physical and chemical vapour deposition techniques and focused ion beam (FIB) cutting (see Fig. 3.8-1).

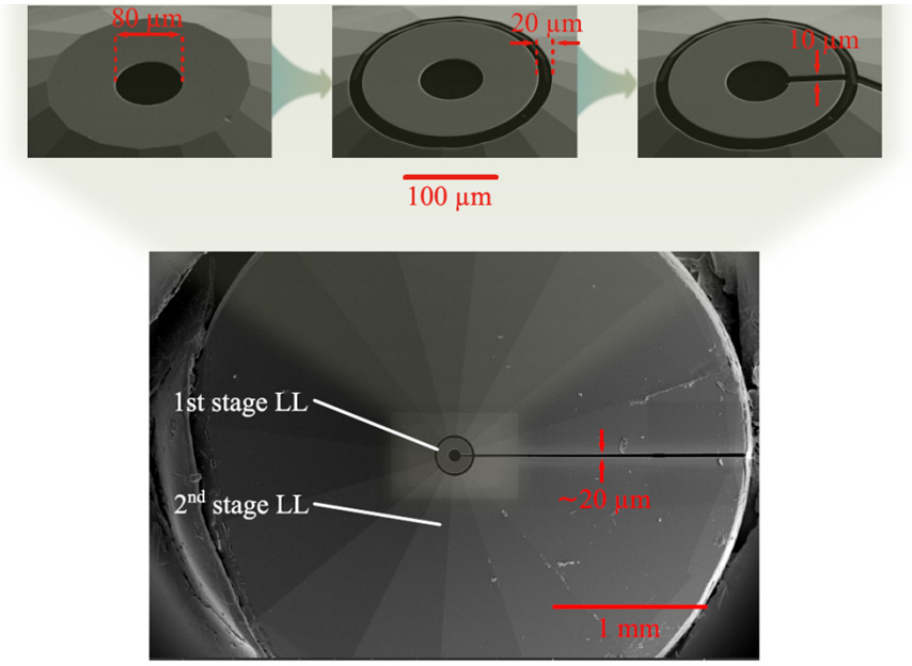

Fig. 3.8-1: Scanning electron microscope (SEM) images of the NMR resonator structure. The complete anvil can be seen in the bottom image, incorporating both 1st and 2nd stage Lenz lenses. The close ups (top) show the 2nd stage LL in detail at different fabrication steps.

We were able to demonstrate that this novel approach can lead to a significant enhancement of the NMR sensitivity in diamond anvil cells, opening up the possibility of its use at pressures well into the megabar range. Figure 3.8-2 shows a proton spectrum of iron monohydride synthesized *in situ* in a DAC and pressurized up to 190 GPa.

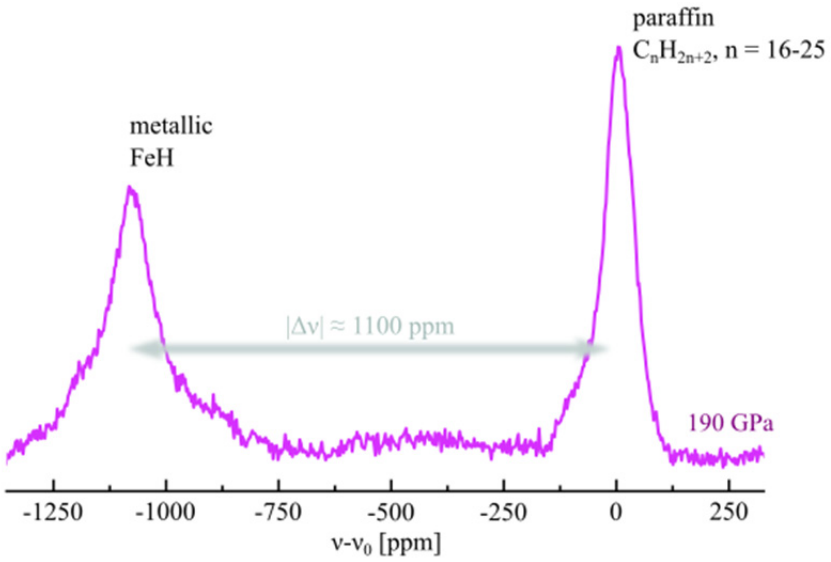

Fig. 3.8-2: ^{1}H-NMR spectrum of metallic iron monohydride and paraffin oil at 190 GPa.

b. *Compact laser heating setup for ultra-high pressure applications (T. Fedotenko and G. Aprilis/Bayreuth; E. Koemets and L.S. Dubrovinsky; N.A. Dubrovinskaia/Bayreuth)*

Laser heating of samples in diamond anvil cells (DACs) has been already in use for more than five decades. There are many examples of its applications in geosciences for simulating conditions of deep Earth and planetary interiors, studies of physical and chemical processes at extreme conditions, and the synthesis of novel materials.

In conventional laser-heating experiments the diameter of a laser beam ranges from 15 to 50 μm FWHM. In ultra-high pressure diamond anvil cells experiments (using bevelled anvils with small culet sizes, double-stage, or toroidal-type anvils, for example), the size of the studied samples is usually much smaller than 10 μm. Typically samples have a diameter of 3-4 μm at pressures above 200 GPa. Such a small size requires tighter laser beam focusing, higher magnification, and better optical resolution of the laser heating set up.

We have developed a portable double-sided laser-heating setup for ultra-high pressure applications. It is designed to improve the accuracy of temperature measurements, to decrease the size of the laser spot focused on the sample, and to get higher magnification imaging for precise heating of DAC samples at pressures above 200 GPa. The system consists of two identical parts (for heating from both sides of a DAC), one of which is schematically shown in Fig. 3.8-3. Each of the parts includes the following modules: laser, power control, focusing and shaping optics, visual observation, and temperature collection. As the laser source, we use a SPI pulsed fiber laser with a maximum power of 200W, and a central wavelength of 1064 nm. The output collimated laser beam is focused to a diameter of about 5 μm by a Focal-π Shaper (Focal-π Shaper 9 1064 by AdlOptica GmbH) and Mitutoyo 20x lens (Mitutoyo infinity corrected M plan apo B 20x). We use a Focal-π Shaper to expand the laser beam and additionally convert its initially Gaussian distributed intensity to a flat-top distribution that stays invariable over a long distance. For imaging the sample, we use high-resolution EYE © CCD cameras, while the sample is illuminated by the LED. The image of the sample is obtained in transmission mode, if the material in the sample chamber of a DAC is at least partially transparent, and/or in reflected mode. The light passes through a set of lenses into the zoom objective and projects the image of the sample on the matrix of the CCD camera. The short pass filter with cut-off at 800 nm is set in front of the zoom objective to protect the CCD camera from laser radiation.

Installed on the observation path, the 50/50 beam splitter (Thorlabs BSW10) reflects half of the light intensity for the temperature measurement by means of spectroradiometry. Thermal radiation focused on the optical fiber is guided into a IsoPlane SCT 320 spectrometer with a 1024x256 PI-MAX 4 detector. To prevent saturation of the detector by diffuse laser radiation we employ a blocking notch filter with the central wavelength of 1064 nm. For precise temperature measurements above 4500K, a long-pass filter with the edge at 450 nm is installed to avoid contamination of thermal-emitted spectra by second-order UV reflections.

The laser heating setup was successfully tested in experiments with DACs having culet sizes of 40 µm (pressure chambers are about 10 to 20 µm in diameter, with characteristic sample sizes of about 5 µm) at pressures above 250 GPa. As an example, Fig. 3.8-4 shows an image of the DAC pressure chamber during laser heating of NiO in a Ne pressure medium at 230(±5) GPa and 2500(±150) K.

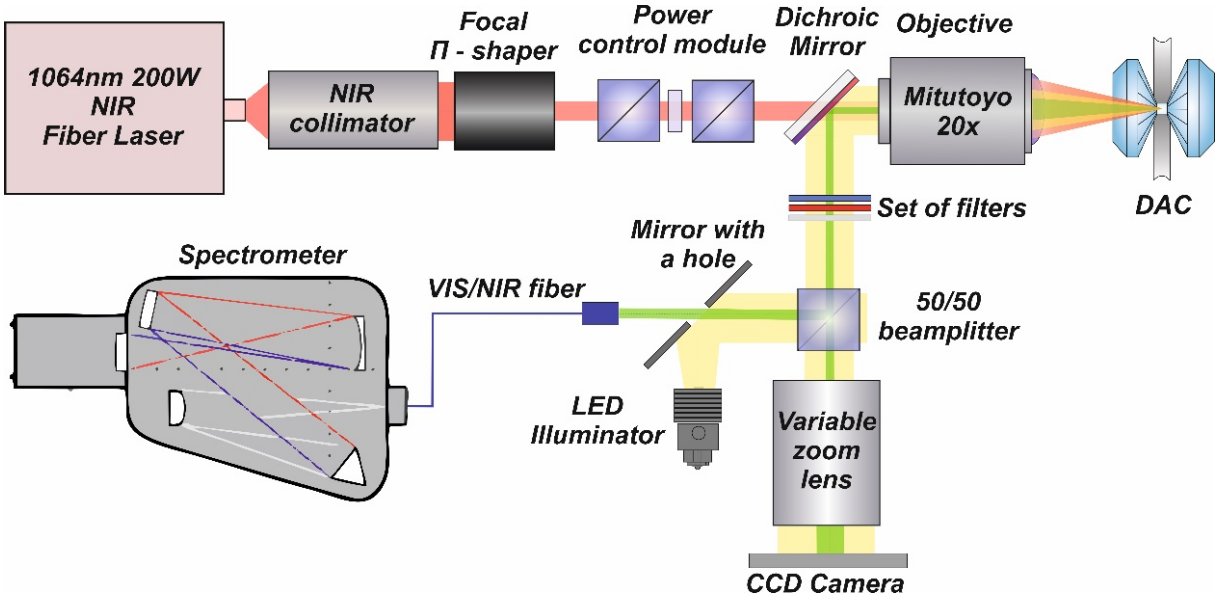

Fig. 3.8-3: Compact laser heating setup for ultra-high pressure applications (only one of two identical parts is shown here).

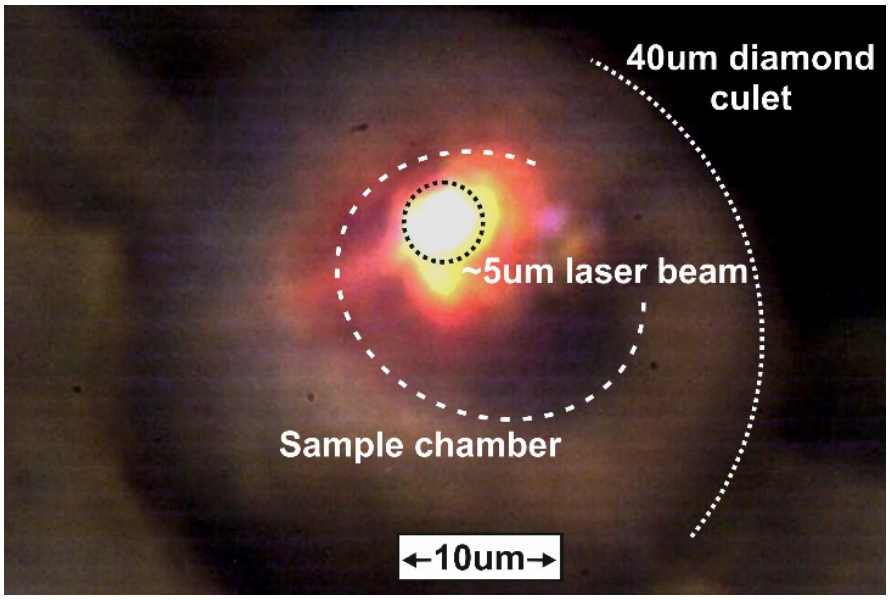

Fig. 3.8-4: Image of the sample chamber during laser heating of NiO in Ne pressure-transmitting medium at 230 GPa and 2700 K. Beveled diamond anvils have a culet size of 40 µm diameter.

c. *A dynamic DAC setup for high temperature time-resolved XRD experiments on planetary H_2O ice (A.S.J. Méndez, H. Marquardt/Oxford; M. Wendt, I. Schwark, A. Ehnes, K. Glazyrin and R. Husband/Hamburg; A. Kurnosov, A.S. Pakhomova/Hamburg, K. Schulze, N. Satta, J. Buchen/Pasadena and H.-P. Liermann/Hamburg)*

Theoretical models predict that high-pressure H_2O ices are subjected to very high temperatures in the mantles of the giant icy planets Uranus and Neptune, as well as in mini-Neptune exoplanets. In addition to the complexity of the phase diagram of H_2O ices, generating high temperature and high-pressure conditions in the laboratory is extremely difficult. One of the main difficulties of working with water at high temperature is that it becomes very reactive. A chemical reaction between water and the gasket material in a diamond anvil cell (DAC, will lead to water dissociation, then diffusion of H_2 and diamond anvil failure. This experimental challenge can potentially be overcome by conducting fast compression experiments in which pressure-temperature conditions are reached for short times. On this basis, we are implementing a dynamic resistance-heated diamond anvil cell (dRHDAC) at the Extreme Conditions Beamline at PETRA III to perform rapid compression on H_2O at high temperature. A time-resolved characterization of our samples is possible by X-ray diffraction measurements employing GaAs LAMBDA detectors that are optimized for high energy diffraction. First experiments on H_2O have been carried out across the cubic to tetragonal transition of ice VII at room temperature, 673 K, 773 K, 873 K and 973 K employing different compression rates. The cubic-tetragonal transition has been observed by static compression experiments as a subtle splitting of the diffraction lines of ice VII at around 14 GPa (as reported in the literature). Our diffraction data reveal the splitting of the Ice VII (110) peak at higher pressures when increasing temperature (Fig. 3.8-5). Further data analysis is needed to understand the nature of this lattice distortion in ice VII and its influence on the H-bond symmetrisation that leads to the formation of different polymorphs at higher pressures.

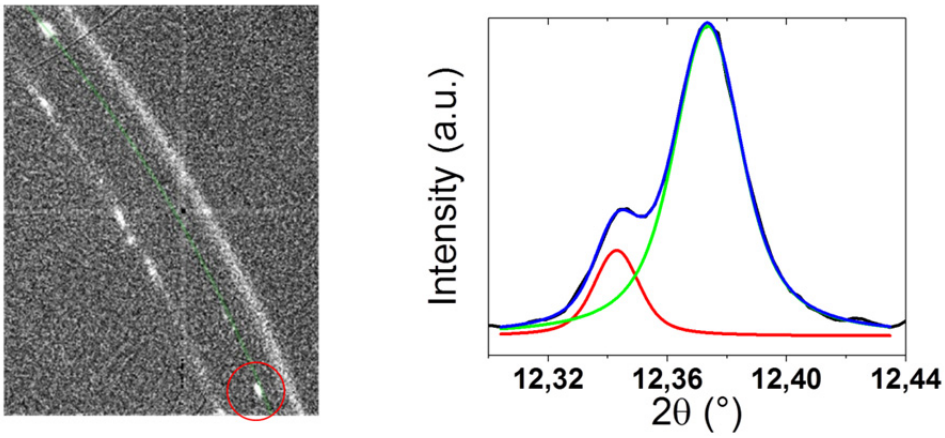

Fig. 3.8-5. Left: Diffraction data collected at 873 K showing the diffraction image on one detector. The green line indicates the position of the intensity maximum of the 110 line of ice VII at 13 GPa. The red circle shows diffraction spots next to the main peak. Right: Integrated diffraction pattern that shows a clear splitting of the 110 line of ice VII.

d. *Diamond anvils with a round table (DART-anvils) and conical crown (L.S. Dubrovinsky, and E. Koemets; N.A. Dubrovinskaia/Bayreuth)*

Diamond anvils are obviously the most important components of a diamond anvil cell (DAC). With the development of new analytical techniques used to study materials at extreme conditions, the design of anvils has evolved as well. Many of novel and rapidly-developing methods of *in situ* investigations of materials under pressure (single-crystal X-ray diffraction, inelastic X-ray scattering, Brillouin spectroscopy, etc.) require DACs to be moved with respect to the electromagnetic radiation beam (*e.g.*, X-rays and/or laser), which is used for heating, exciting, or probing materials properties at extreme pressures and variable temperature conditions.

Conventional anvils have a "flat plate" geometry, and rotation of the cell at any angle with respect to the stationary beam leads to strong refraction, as diamond is a material with a high refractive index (n = 2.425 at 532 nm). This destroys the alignment of the sample with respect to the optical beam. Special procedures (sometimes quite complicated, time- and labour-consuming) are required to maintain the alignment with respect to X-rays and optical systems, but still certain types of experiments, which involve DAC rotation, cannot be performed while keeping lasers or optical components stationary. For example, immobile laser heating of a sample in a DAC with conventional (flat-table) anvils during single-crystal X-ray diffraction data collection is impossible, as the sample moves out of the focus of the laser beam upon rotation of the cell.

A solution has been found by manufacturing anvils with a new design, the Diamond Anvil with a Round Table (DART), which enables a number of the problems associated with the use of conventional anvils in DACs to be eliminated. The major feature of the new DART-anvil design is a spherical shape of both the crown and the table of a diamond with the centre of the culet located exactly in the centre of the sphere (Fig. 3.8-6, left). Initially, DART anvils were produced by making diamond spheres of an appropriate diameter, cutting them in half, and forming (polishing) the pavilion and the culet. This approach has two disadvantages: (1) the crystallographic orientation of the culet is arbitrary (not an optimal (100)-oriented as in commonly-used anvils), and (2) the spherical shape of the crown needs to be very precise so that it exactly matches the shape of the seat, which is difficult to achieve.

In order to overcome these problems we have developed and produced (at Dutch Diamond Technologies BV) DARTs with a conical crown (Fig. 3.8-6, right). The girdle diameter of the new anvils is equal to 3.1 mm, and the cone angle is 60°, so that the DARTs with the conical crown may be implemented in the BX90-type DACs with the seats that are conventional in Almax-EasyLab Boehler-type anvils. With anvils having 250 μm culet diameters, we performed experiments at pressures up to 75 GPa without any damage to the DARTs.

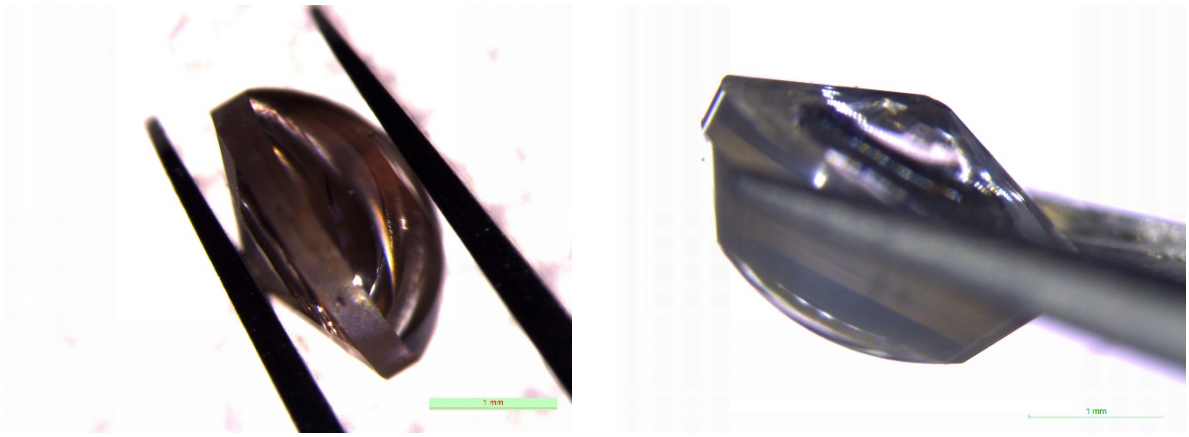

Fig. 3.8-6: Microscope images of the DART-anvils (held by tweezers) with spherical (left) and conical (right) crowns.

e. *Probing oxygen fugacity through diamond anvil cell experiments (S. Dominijanni, C.A. McCammon, L.S. Dubrovinsky, N. Miyajima and D.J. Frost)*

Oxygen fugacity (fO_2) is a thermodynamic parameter that indicates the chemical potential of oxygen in redox reactions. This parameter can significantly affect the stabilities and physical-chemical properties of minerals and melts and it plays a key role in many geological processes including magma genesis and metasomatism. In experiments, fO_2 is frequently controlled by a metal–oxide fO_2 buffer (*e.g.*, Ni-NiO, Fe-FeO, Re-ReO, etc.), or calculated using noble metal alloys (Fe-Ir, Fe-Pt, Fe-Pd) as sliding redox sensors during high-pressure and high-temperature experiments in large volume apparatus (such as multianvil or piston cylinder presses). Recent experimental studies on the stability field of carbonates at high pressure, performed in diamond anvil cells (DAC), show contradictory results that might be attributed to different redox conditions during the experiments. Therefore, we have investigated the oxygen fugacity conditions during DAC experiments.

We used a mixture of 95 mol.% ferropericlase $(Mg_{0.75}Fe_{0.25})O$ plus 5 mol.% of pure iridium powder in order to crystallize an Fe-Ir alloy and use it as a sliding redox sensor to calculate fO_2. The starting powder was compressed into a pellet and loaded in a DAC with Boehler Almax type diamonds of 250 μm culet size. Ne was used as a pressure-transmitting medium. Powder diffraction data were collected at beamlines ID15b and ID27 at the European Synchrotron Radiation facility (Grenoble, France) and at the Advanced Photon Source (Chicago, USA). A double-sided laser heating system was used to heat the sample at ~ 2000 K. Our preliminary results from synchrotron powder X-ray diffraction show that after heating, an Fe-Ir metal alloy indexed in the Fm-3m space group is formed by the reaction of pure Ir and Fe from ferropericlase (Fig. 3.8-7) according to the reaction:

$$(Mg,Fe)O + Ir \rightarrow (Mg,Fe)O + (Fe,Ir)$$

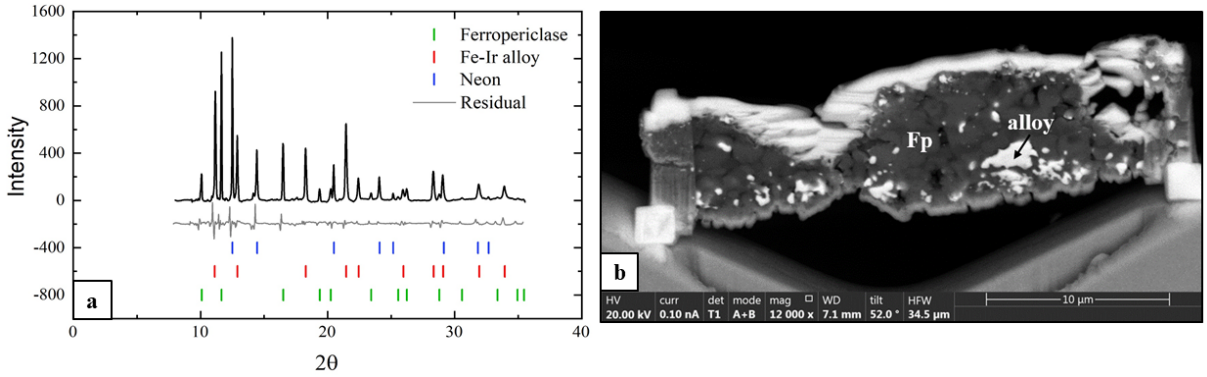

Fig. 3.8-7: a) XRD pattern obtained after heating $Mg_{0.75}Fe_{0.25}O$ + Ir at 2000 K and 36 GPa. Three phases are identified: Fe-Ir metal alloy, ferropericlase and solid neon. Le Bail refinement was performed using the Jana software package; b) BSE image of a lamella cut with the focused ion beam (FIB) from the center of the sample. The bright areas are Fe-Ir metal alloy while the grey areas are ferropericlase.

The redox conditions were assessed based on the composition determined from the cell parameters of the Fe-Ir alloy and a thermodynamic model. The estimated fO_2 is close to that of the iron-wustite (IW) buffer. Further chemical analyses and additional experiments are ongoing to quantify the oxygen fugacity in a laser-heated DAC.

f. *Equations of state, phase relations and oxygen fugacity of the Ru-RuO_2 buffer at high pressures and temperatures (K. Armstrong, N. Siersch, T. Boffa Ballaran and D.J. Frost)*

Experimental studies of transition zone and lower mantle minerals show that ferric iron components are increasingly stabilized with depth in the mantle. To fully characterize the thermodynamic stability of such components, however, it is crucial to be able to measure their concentrations at a known oxygen fugacity. Imposing an oxygen fugacity on an experimental charge can be accomplished by adding pure buffer phases, such as Ni+NiO or Fe+FeO directly into the capsule. Significant uncertainties can arise, however, if the buffer phases react extensively with the sample. In addition, thermal equation of state properties of both phases must be known at high pressures to accurately determine the oxygen fugacity imposed by the buffer.

The metal-oxide pair Ru+RuO_2 is ideal as an internal oxygen fugacity buffer. Both phases remain solid to high temperatures and react minimally with silicates, only exchanging oxygen. Additionally, the imposed fO_2 is relatively high, such that Fe loss into Pt capsules is minimal and ferric iron is present in sufficient concentrations to be accurately measured. Previous studies have examined the thermal expansion of both phases at ambient pressure, as well as compressibility at room temperature, however, no previous studies have investigated both simultaneously. More importantly, RuO_2 has been observed to undergo a series of phase transformations. At ambient conditions, RuO_2 has a tetragonal, rutile-type structure. At room temperature and increasing pressure, it first undergoes a second-order ferroelastic phase

transformation to an orthorhombic $CaCl_2$-type structure, and at higher pressures transforms to a cubic pyrite-type structure. The phase transformations influence the calculated oxygen fugacity but can be accounted for by deriving expressions to describe the Gibbs free energies of the high-pressure phases by fitting data on the phase relations and the volumes.

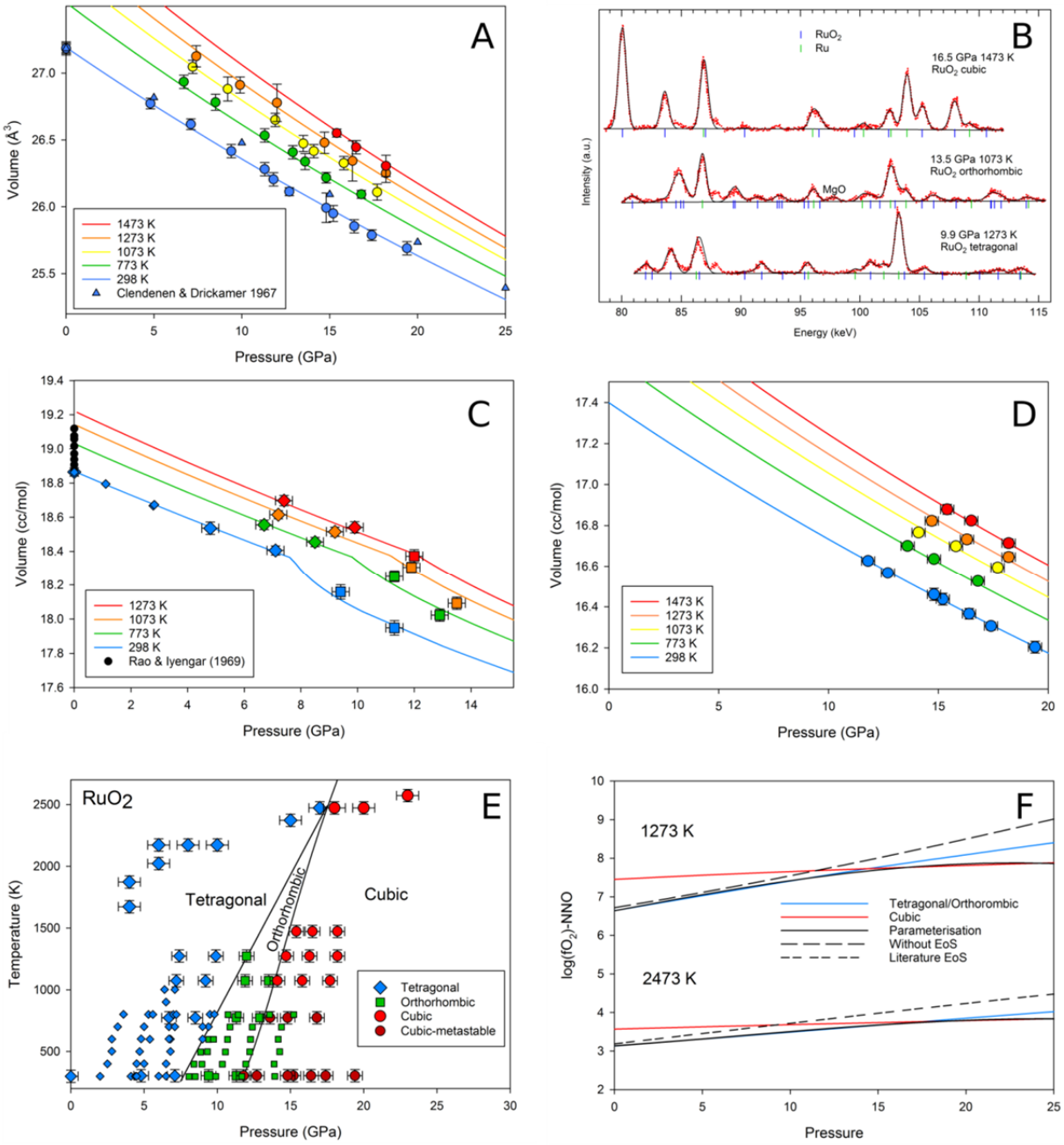

Fig. 3.8-8: (A) Data and calculated isotherms for Ru metal. (B) Diffraction patterns for the three phases of RuO_2 encountered in this study. (C) Data and calculated isotherms for RuO_2 tetragonal and orthorhombic phases. (D) Data and calculated isotherms for cubic RuO_2 phase. (E) Phase relations of RuO_2 between 0-25 GPa and 298-2500 K. (F) Calculated oxygen fugacity of the Ru+RuO_2 buffer assemblage, relative to the Ni-NiO buffer, at two different temperatures. Results are also shown that do not account for phase changes or equation of state parameters.

We have collected synchrotron X-ray diffraction data on Ru and RuO_2 to 19.4 GPa and 1473 K, with which we have determined phase relations of the RuO_2 phases and derived thermal equation of state (EoS) parameters for both Ru and RuO_2 (Fig. 3.8-8A-E). Further, we have derived a continuous Gibbs free energy expression for the tetragonal and orthorhombic phases of RuO_2, by fitting the second-order phase transition boundary and P-V-T data for both phases, using a model based on Landau theory combined with the modified Tait EoS (Fig. 3.8-8C). The transition between the orthorhombic and cubic phases was then used along with EoS data for both phases to determine a Gibbs free energy expression for the cubic phase. We have used these data to calculate the oxygen fugacity of the $Ru + O_2 = RuO_2$ equilibrium, which we have parameterised as a single polynomial across the stability fields of all three phases of RuO_2. The expression is valid from 0-25 GPa and 773-2500 K, with an estimated uncertainty of 0.2 log units. Our calculated fO_2 is shown (Fig. 3.8-8F) to be between 0.5-2 log units lower than estimates that use data obtained at ambient-conditions, which demonstrates the importance of accurately determining the high-pressure/-temperature behaviour of oxygen fugacity buffer phases.

g. In situ *quantification of chlorine and sulphur in glasses, minerals and melt inclusions by LA-ICP-MS (B. Rottier and A. Audétat)*

In situ analysis of sulfur and chlorine in geological materials is typically conducted by electron probe micro-analysis or secondary-ion mass spectrometry. Both of these methods require a homogeneous material that is exposed at the surface, which is commonly not the case for silicate melt inclusions. To overcome this problem, the accuracy and precision of sulfur and chlorine quantification by laser-ablation inductively-coupled-plasma (quadrupole) mass spectrometry (LA-ICP-MS) were investigated for melt inclusions and also for glasses and minerals. Samples with known sulfur and/or chlorine concentrations were analyzed using suitable external standards. Representative LA-ICP-MS signals are shown in Fig. 3.8-9. The main limitation for chlorine and sulfur quantification in geological materials by LA-ICP-MS is a contamination effect resulting in excess Cl and S signals during ablation of any material. This contamination results from the mobilization of chlorine and sulfur impurities attached to the walls of the sample chamber and the gas transport tubes. In the case of Cl accurate results can be obtained for Cl concentrations of few hundred of ppm after applying a simple correction formula that relates the magnitude of the excess Cl signal to the quantity of produced aerosol, which is approximated by sensitivity. In the case of S the application of a similar correction formula does not suffice, and a second correction formula that relates the calculated sulfur content to the actual sulfur content needs to be applied. The newly-developed combined approach allows accurate quantification of S in minerals and glasses down to a concentration of ~ 600 µg/g. For unexposed silicate melt inclusions the numerical host correction automatically removes the excess Cl related to the amount of produced aerosol, hence Cl concentrations turn out accurate without any correction. Due to counting statistics and uncertainties in the host correction, a minimum melt inclusion size of 30 µm is required to accurately quantify Cl in melt inclusions containing ~ 1,500 µg/g Cl. Sulfur concentrations, on the other hand, can be accurately quantified down to 700 µg/g even in

small (15 µm) melt inclusions. In summary, chlorine and sulfur can be accurately and precisely quantified by LA-ICP-MS in glasses, minerals, and melt inclusions down to concentrations of several hundreds of µg/g, provided that an ICP-MS instrument with a relatively low background on Cl and S is available and that instrument-specific correction equations are established on a set of samples with known Cl and S contents.

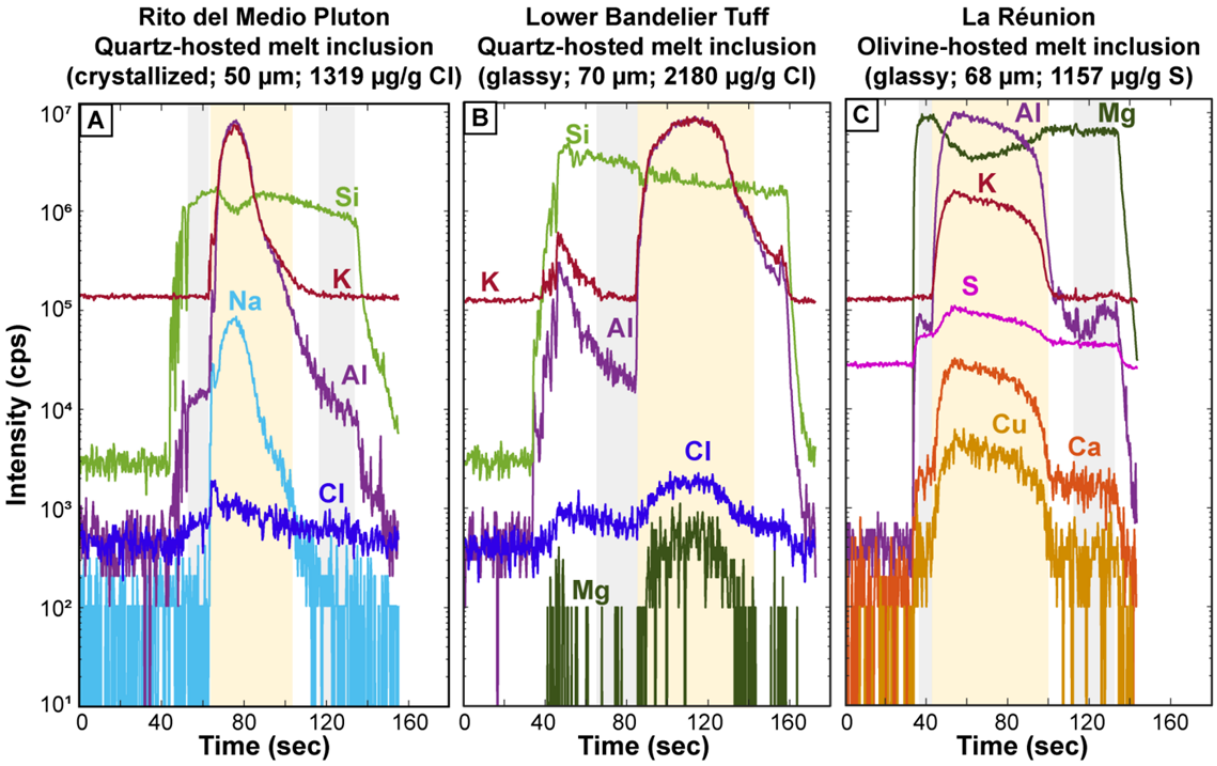

Fig. 3.8-9: LA-ICP-MS signals of melt inclusions. A) Crystallized melt inclusion in quartz from a miarolitic cavity in the Rito del Medio Pluton; B) Glassy melt inclusion in a magmatic quartz phenocryst from the Lower Bandelier Tuff. The high Al and K signals at the beginning of the quartz ablation reflect surface pollution due to a previous melt inclusion analysis nearby. C) LA-ICP-MS signal of a glassy, olivine-hosted melt inclusion from La Réunion island. The shaded grey bands are the parts of the signal used for the host correction, and the shaded yellow bands are the integration windows used for the melt inclusions. When two sections of the signal were selected for the host composition, the weighted average signal was used for the host correction.

h. *Combining ECCI and FIB milling techniques to prepare site-specific TEM samples from a deformed pyrope at high pressure and temperature (N. Miyajima, T. Mandolini, F. Heidelbach and C. Bollinger)*

The investigation of the microstructures and textures of rocks is essential for understanding micro- and macroscale deformation and its relation to the rheology of the Earth's mantle. Currently we are applying *electron channeling contrast imaging* (ECCI) to rock-forming minerals, such as olivine, pyroxene and ferropericlase, to observe individual dislocations in

the bulk rock specimens. Diffraction contrast imaging in the transmission electron microscope (TEM) is optimal for observing individual crystal defects such as dislocations and stacking faults. Orientation-controlled/optimized-electron channeling contrast imaging in the scanning electron microscope (SEM) is also an alternative technique for the characterization of microstructures such as subgrain boundaries and individual dislocations.

These two electron microscopy techniques have respective advantages for sample preparation and spatial resolution. SEM can be used to examine multi-grain textures containing dislocations in a surface-polished bulk sample, while dislocation characterizations in TEM are performed on a thin foil. In TEM, dislocation microstructures, such as partial dislocations with stacking faults, can be characterized intensively in a limited area of the TEM foil. On the other hand, for SEM observations it is relatively easy to prepare a specimen simply by surface-polishing. The characterization using back-scattered electrons is very powerful for investigating rock sample fabrics that preserve the original defects including the grain boundaries.

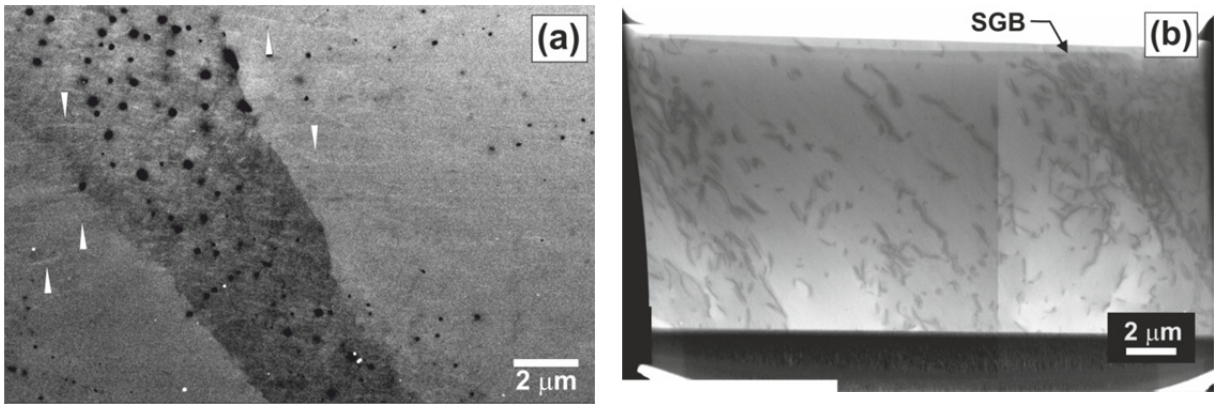

Fig. 3.8-10: (a) Orientation-optimized ECCI of a deformation band in a sample of garnet (#M643). Some "dislocation-like" contrasts are indicated by arrowheads. (b) Scanning TEM bright-field image of a TEM lamella from the deformation band area of (a). A high density of dislocations in the deformation band forms a subgrain boundary (SGB). A vertical line in the center part of the image is an artefact caused by joining two scanning images.

In order to maximize the above-mentioned respective advantages, focused ion milling (FIB) techniques play an important role in site-specific TEM sample preparation of deformed specimens. Here we propose combining ECCI and FIB milling techniques to prepare site-specific TEM samples for dislocation analysis of a deformed single crystal of pyrope-rich garnet. The site-specific characterizations from ECCI to TEM, with assistance of FIB, can provide a new approach to investigate dislocation microstructures of materials that have been deformed at high pressures and temperatures.

In the orientation-optimized ECCI method, we successfully observed individual dislocations across subgrain boundaries in low-atomic number minerals, such as forsterite and pyrope-rich

garnet (averaged Z-numbers ~ 10). In the ECCI on the single crystal garnet, polysynthetic deformation bands consisting of dislocations, unusual contrasts in stripes and inhomogeneous distributions of sub-micrometer-sized pores were found (Fig. 3.8-10a). Further site-specific TEM observations on the deformation band revealed a high density of partial dislocations and stacking fault ribbons (Fig. 3.8-10b). Currently, characterization of these defects and fluid-bearing pores is in progress. The analytical procedure from ECCI to the site specific FIB-sampling should become a standard technique when characterizing individual dislocations in the TEM.

i. *Stencil rescaling: A new method for permeability computation of porous media (P. Eichheimer, W. Fujita/Sendai, M. Thielmann, A. Popov/Mainz, G.J. Golabek and B.J.P. Kaus/Mainz)*

Modeling water transport into the Earth's mantle requires a detailed knowledge about the permeability of the Earth's crust and lithosphere for a large range of porosities. While experiments provide permeability measurements for most conditions, they tend to become inaccurate in the case of low porosities. In this case, digital rock physics (DRP) allows the permeability and related geometric factors across different scales to be computed using numerical methods. Micro permeabilities on pore-scale for example can be evaluated by using micro-CT data as an input for fluid flow simulations. When computing the overall fluid flow, care is required when defining boundary conditions at the interfaces between fluid and solid phases, otherwise additional errors can result.

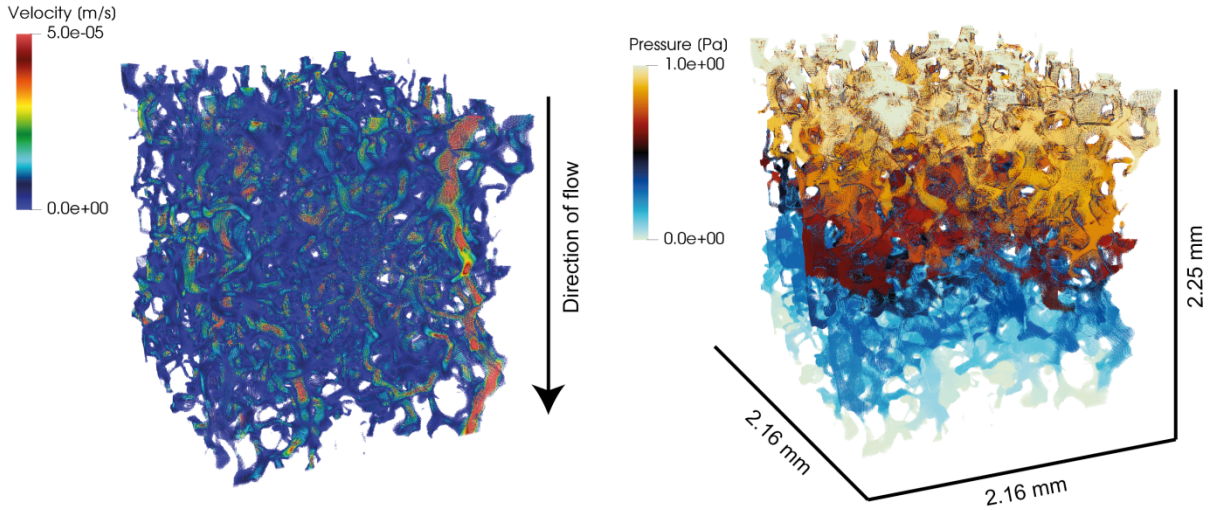

Fig. 3.8-11: Computed fluid flow velocities and pressure in a sample of Fontainebleau sandstone.

In this work we present the new method of stencil rescaling employed in the 3D finite difference code LaMEM. To test the accuracy of the method, we performed several benchmark tests. The performed benchmarks use both analytical solutions for simplified

geometries as well as results from other numerical approaches for more complicated, but also more realistic geometries. The results of the computed Fontainebleau sandstone (Fig. 3.8-11) are in good agreement with other recent numerical studies. We show that the stencil rescaling method allows for higher accuracy at no additional computational cost.

j. *Effect of grid resolution on tectonic regimes in global-scale convection models (E. Marzotto, M. Thielmann and G.J. Golabek)*

Global-scale mantle convection models that are based on a visco-plastic rheology usually show different tectonic regimes: plate-like, episodic or stagnant lid (Fig. 3.8-12). In the plate-like regime, the lid is continuously subducting into the mantle. The episodic lid regime is characterized by the stability of the lid until sufficiently large lithospheric stresses break it, causing rapid resurfacing. Finally the stagnant lid regime is defined by an unbreakable lid that does not participate in convection.

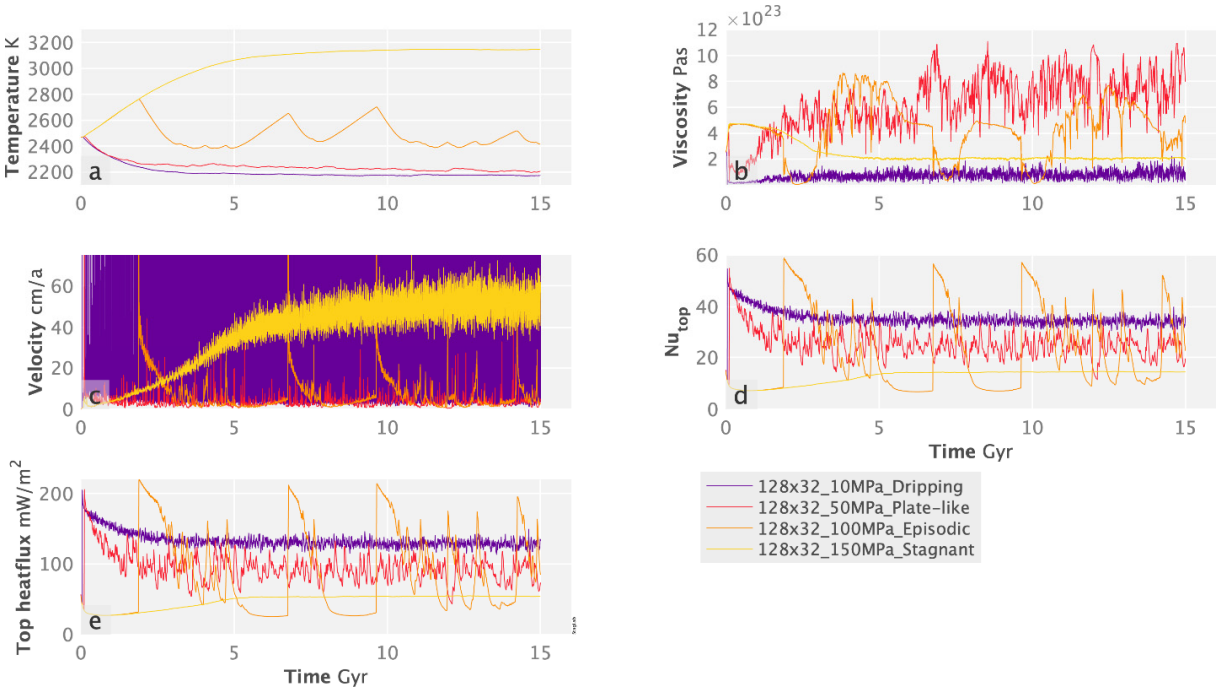

Fig. 3.8-12: The evolution of different lid regimes with time: Dripping (purple), plate-like (red), episodic (orange) and stagnant (yellow). Each panel shows the parameter evolution profile: (a) temperature, (b) viscosity, (c) whole mantle velocity, (d) surface Nusselt number, and (e) surface heat flux. The surface temperature is set at 300 K in all cases.

In numerical simulations the yield stress is a key parameter as it sets the stress necessary for the cold surface regions to yield. A high yield stress will result in a stagnant lid. On the other hand, a low yield stress causes a weak lid that is constantly broken and sinks into the mantle.

In addition to the key importance of physical parameters, numerical modelling parameters also have an effect on the tectonic regime, and different outcomes can result simply by changing the grid resolution. Here we use the code StagYY in a 2D spherical annulus geometry (as described in published literature) to determine the resolution-dependent tectonic regime for different yield stresses in global-scale convection models. To assess the effect of grid resolution on lid behaviour we tested resolutions ranging from 128x32 to 1024x128 grid points keeping all physical parameters unchanged. To ensure that steady state has been reached, each simulation is run for 15 Gyrs.

Our results show that there is a correspondence between low radial resolution and mobile lid regime and that low aspect ratio cells (azimuthal to radial grid spacing) favor a plate-like mobile lid, while for large aspect ratios the episodic lid regime is persistent (Fig. 3.8-13).

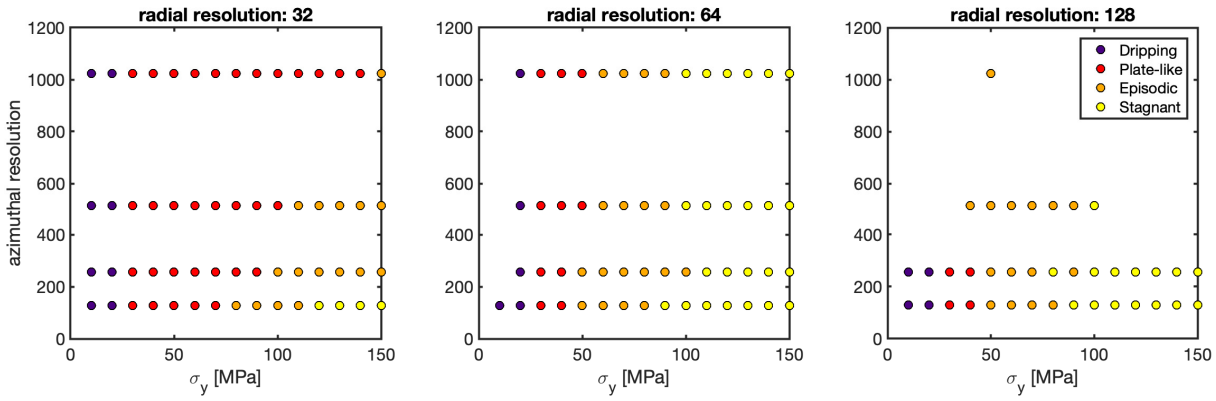

Fig. 3.8-13: Lid regimes obtained for various yield stresses. Each symbol represents a simulation where the controlling parameters are radial resolution, azimuthal resolution and yield stress. In each box the radial resolution is kept constant (32, 64 and 128 nodes) whereas the azimuthal resolution is changed to test the effect of grid resolution on the lid behaviour, over a range of 15 different yield stresses (from 10 to 150 MPa). The different regimes are color coded as in Fig. 3.8-12: dripping (purple), plate-like (red), episodic (orange) and stagnant lid (yellow).

4. International Research and Training Group – "Deep Earth Volatile Cycles" (DFG GRK 2156/1)

The International Research and Training Group (IRTG) "Deep Earth Volatile Cycles" is funded by the *Deutsche Forschungsgemeinschaft* (DFG). This graduate school for doctoral studies started in April 2016 for a period of 4.5 years. It is a cooperation between the Bayerisches Geoinstitut (BGI) and the Department of Earth Sciences at Tohoku University, Sendai/Japan. The IRTG is chaired by Dan Frost/Bayreuth and Michihiko Nakamura/Sendai.

The objective of this collaborative research effort is to study the cycling of volatile elements through the deep interior of the Earth. Using mainly experimental and computational methods the group's goal is to quantify how volatile elements such as carbon, hydrogen and nitrogen are transported, stored and expelled from the interior as a result of plate tectonic processes. Doctoral researchers receive training in modern experimental and modelling techniques employed in solid Earth geosciences in a structured learning programme. At the same time they pursue independent research into geochemical and geophysical aspects of the internal volatile cycle. Doctoral researchers from the BGI spend between 6 to 12 months at Tohoku University as part of a complementary research exchange that sees scientists from Tohoku University spending time at the BGI.

In 2018 the following PhD students were enrolled in the IRTG at BGI:

Sumith Abeykoon (M.Sc. 2018, Bayreuth) since May	*Oxybarometry and thermobarometry based on accessory phases.* Supervisor: Prof. D. Frost, Dr. A. Audetat
Serena Dominijanni (M.Sc. 2018, Roma) since May	*Probing mantle oxygen fugacity through experiments and natural samples.* Supervisor: PD Dr. C. McCammon
Laura Cialdella (M.Sc. 2018, Padua) since June	*Nitrogen solubility and partitioning in magmas.* Supervisor: Prof. Dr. H. Keppler

IRTG Activities in 2018:

High pressure short course: In February twenty-nine doctoral and master students took part in a five-day high pressure short course at Bayerisches Geoinstitut. Seven doctoral students from Tohoku University joined the course along with IRTG members from the BGI and participants from nine countries in total. The students received a practical introduction into high pressure and temperature experiments as well as numerous related analytical techniques. The course was very well received and fostered exchange and collaboration between participants and lecturers.

Participants and lecturers of the DMG short course "*High-Pressure Experimental Techniques and Applications to the Earth's Interior*" at BGI.

Introduction to Japanese culture by Professor Menkhaus (Meiji University, Tokyo):

On March 26 Professor Menkhaus from Meiji University in Tokyo was invited to BGI to hold a lecture with following discussion about Japanese culture and history in order to prepare IRTG-students for their research exchange stay at Tohoku University. Professor Menkhaus teaches law at Meiji University in Tokyo and has lived and worked in Japan for over 30 years. He is the Chairman of the Association of Former Fellows of the *Japanese Society for the Promotion of Science (JSPS)*. In his entertaining lecture he gave the students a vivid impression of the cultural similarities and differences between Europe and Japan.

EBSD Workshop: In July an IRTG sponsored course "Texture and interface analyses using EBSD" was organized at BGI consisting of lectures and practicals and introducing the main measuring and analysis tools in the field of grain boundary characterization with electron backscattering diffraction (EBSD). For this course a number of leading experts in this field (Marc de Graef and Gregory Rohrer (Carnegie Mellon University, U.S.A.), Pamela Burnley (University of Nevada), Vivian Tong (Imperial College, London), Luis Morales (ETH Zürich), Matteo Demurtas (University of Otago, New Zealand)) were invited to Bayreuth. With 29 participants (6 of them from Tohoku) the course was very well attended and received.

Lecturers and participants of the IRTG sponsored short course *Texture and interface analyses using EBSD* at BGI.

IRTG field trip: On September 26 the IRTG students from BGI visited the German research reactor FRM II at Garching near Munich, where neutron scattering experiments are performed in a variety of experimental setups. Among them is also the multianvil press SAPHiR, which has been installed there on the initiative of BGI and will be used for *in situ* HP-HT neutron diffraction experiments. On the return to Bayreuth a stop was made at the world famous paleontological site of Solnhofen, where most of the existing fossils of the feathered dinosaur Archaeopteryx were discovered.

The IRTG visitor group at the FRM II reactor in Garching.

Humboldt research award for Professor Eiji Ohtani from Tohoku University:

Professor Ohtani from Tohoku University received the prestigious Research Award of the Alexander von Humboldt Foundation for his achievements in experimental high pressure Earth sciences. As part of the award he spent three months in late 2018 at BGI, where he started several projects with BGI colleagues and IRTG students. He will return to Bayreuth for a number of times over the next years to further strengthen the ties between BGI and Tohoku University.

In 2018 several staff members and students of the two participating institutes made visits to the collaborating institutions for discussion of projects, presentations, experiments and internships:

Tohoku colleagues visiting BGI in 2018:

Name	Period	Name	Period
Maeda, Fumiya	04.01.-16.01.	Muranushi, Miki	17.08.-01.09.
Sawa, Sando	17.02.-02.03.	Nakajima, Ayano	17.08.-01.09.
Ohtani, Eiji, Prof.	23.02.-03.03.	Maeda, Fumiya	20.08.-27.09.
Hirano, Naoto, Prof.	08.03.-13.03.	Ohtani, Eiji, Prof.	01.09.-30.11.
Sato, Yuki	08.03.-13.03.	Suzuki, Akio, Prof.	09.09.-19.09.
Yutani, Taku	08.03.-28.02.19	Muranushi, Miki	09.09.-19.09.
Okumura, Satoshi	18.03.-28.03.	Nakajima, Ayano	09.09.-19.09.
Liang, Yuan	23.04.-18.05.	Nakamura, Michihiko, Prof.	09.10.-12.10.
Huang, Yongsheng	01.07.-30.09.	Hirano, Naoto, Prof.	05.11.-10.11.
Sawa, Sando	10.07.-18.07.	Maeda, Fumiya	09.12.-29.12.
Araya, Naoki	16.07.-27.07.	Suzuki, Akio, Prof.	22.12.-14.01.19
Suzuki, Akio, Prof.	17.08.-01.09.	Ohashi, Tomonori	22.12.-14.01.19

BGI colleagues visiting Tohoku in 2018:

Name	Period	Name	Period
Rustioni, Greta	27.02.-15.06.	Frost, Dan, Prof.	18.05.-01.06.
Eichheimer, Philipp	27.02.-14.09.	Koemets, Egor	04.06.-16.07.
Putak Juricek, Marija	17.05.-26.08.	Golabek, Gregor, Prof.	29.07.-06.08.

5. Publications, Conference Presentations, Seminars

5.1 Publications (published)

Supplement to **2017** (papers published at the end of 2017):

CHUST, T.C.; STEINLE-NEUMANN, G.; DOLEJŠ, D.; SCHUBERTH, B.S.A.; BUNGE, H.-P. (2017): MMA-EoS: A computational framework for mineralogical thermodynamics. Journal of Geopysical Research – Solid Earth 122, 9881-9920

2018

AKAOGI, M.; KAWAHARA, A.; KOJITANI, H.; YOSHIDA, K.; ANEGAWA, Y.; ISHII, T. (2018): High-pressure phase transitions in $MgCr_2O_4$·Mg_2SiO_4 composition: Reactions between olivine and chromite with implications for ultrahigh-pressure chromitites. American Mineralogist 103, 161-170

AKSENOV, S.M.; BYKOVA, E.; RASTSVETAEVA, R.K.; CHUKANOV, N.V.; MAKAROVA, I.P.; HANFLAND, M.; DUBROVINSKY, L. (2018): Microporous crystal structure of labuntsovite-Fe and high-pressure behavior up to 23 GPa. Acta Crystallographica Section B: Structural Science, Crystal Engineering and Materials 74, 1-11

ALÉON, J.; MARIN-CARBONNE, J.; MCKEEGAN, K.D.; EL GORESY, A. (2018): O, Mg, and Si isotope distributions in the complex ultrarefractory CAI Efremovka 101.1: Assimilation of ultrarefractory, FUN, and regular CAI precursors. Geochimica et Cosmochimica Acta 232, 48-81

AUDÉTAT, A.; ZHANG, L.; NI, H. (2018): Copper and Li diffusion in plagioclase, pyroxenes, olivine and apatite, and consequences for the composition of melt inclusions. Geochimica et Cosmochimica Acta 243, 99-115

BADRO, J.; AUBERT, J.; HIROSE, K.; NOMURA, R.; BLANCHARD, I.; BORENSZTAJN, S.; SIEBERT, J. (2018): Magnesium partitioning between Earth's mantle and core and its potential to drive an early exsolution geodynamo. Geophysical Research Letters 45, 13240-13248

BEYER, C.; ROSENTHAL, A.; MYHILL, R.; CRICHTON, W.A.; YU, T.; WANG, Y.; FROST, D.J. (2018): An internally consistent pressure calibration of geobarometers applicable to the Earth's upper mantle using *in situ* XRD. Geochimica et Cosmochimica Acta 222, 421-435

BIANCHI, F.; WITTEL, F.K.; THIELMANN, M.; TRTIK, P.; HERRMANN, H.J. (2018): Tomographic study of internal erosion of particle flows in porous media. Transport in Porous Media 16(13), 1-16

BIANCHI, F.; THIELMANN, M.; DE ARCANGELIS, L.; HERRMANN, H.J. (2018): Critical bursts in filtration. Physical Review Letters 120(3), 034503

BINDER, B.; WENZEL, T.; KEPPLER, H. (2018): The partitioning of sulfur between multicomponent aqueous fluids and felsic melts. Contributions to Mineralogy and Petrology 173, 18

BUCHEN, J.; MARQUARDT, H.; SPEZIALE, S.; KAWAZOE, T.; BOFFA BALLARAN, T.; KURNOSOV, A. (2018): High-pressure single-crystal elasticity of wadsleyite and the seismic signature of water in the shallow transition zone. Earth and Planetary Science Letters, 498, 77-87

BUCHEN, J.; MARQUARDT, H.; SCHULZE, K.; SPEZIALE, S.; BOFFA BALLARAN, T.; NISHIYAMA, N.; HANFLAND, M. (2018): Equation of state of polycrystalline stishovite across the tetragonal-orthorhombic phase transition. Journal of Geophysical Research: Solid Earth 123, 7347-7360

BYKOV, M.; BYKOVA, E.; KOEMETS, E.; FEDOTENKO, T.; APRILIS, G.; GLAZYRIN, K.; LIERMANN, H.-P.; PONOMAREVA, A.V.; TIDHOLM, J.; TASNÁDI, F.; ABRIKOSOV, I.A.; DUBROVINSKAIA, N.; DUBROVINSKY, L. (2018): High-pressure synthesis of a nitrogen-rich inclusion compound $ReN_8 \cdot xN_2$ with conjugated polymeric nitrogen chains. Angewandte Chemie International Edition 57, 9048-9053

BYKOV, M.; BYKOVA, E.; APRILIS, G.; GLAZYRIN, K.; KOEMETS, E.; CHUVASHOVA, I.; KUPENKO, I.; MCCAMMON, C.; MEZOUAR, M.; PRAKAPENKA, V.; LIERMANN, H.-P.; TASNADI, F.; PONOMAREVA, A.V.; ABRIKOSOV, I.A.; DUBROVINSKAIA, N.; DUBROVINSKY, L. (2018): Fe-N system at high pressure reveals a compound featuring polymeric nitrogen chains. Nature Communications 9, 2756-2766

BYKOV, M.; KHANDARKHAEVA, S.; FEDOTENKO, T.; SEDMAK, P.; DUBROVINSKAIA, N.; DUBROVINSKY, L. (2018): Synthesis of FeN_4 at 180 GPa and its crystal structure from a submicron-sized grain. Acta Crystallographica Section E 74, 1392-1395

BYKOVA, E.; BYKOV, M.; ČERNOK, A.; TIDHOLM, J.; SIMAK, S.; HELLMAN, O.; BELOV, M.; ABRIKOSOV, I.; LIERMANN, H.-P.; HANFLAND, M.; PRAKAPENKA, V.; PRESCHER, C.; DUBROVINSKAIA, N.; DUBROVINSKY, L. (2018): Metastable silica high pressure polymorphs as structural proxies of deep Earth silicate melts. Nature Communications 9, 4789-4797

CAPITANI, G.; MIYAJIMA, N.; SULPIZIO, R.; D'ADDABBO, M.; GALIMBERTI, L.; GUIDI, M.; ANDREOZZI, G.B. (2018): Iron release in aqueous environment by fresh volcanic ash from Mount Etna (Italy) and Popocatépetl (Mexico) volcanoes. Environmental Earth Sciences 77(13), 521-536

CAVALCANTE, C.; LAGOEIRO, L.; FOSSEN, H.; EGYDIO-SILVA, M.; MORALES, L.F.; FERREIRA, F.; CONTE, T. (2018): Temperature constraints on microfabric patterns in quartzofeldsphatic mylonites, Ribeira belt (SE Brazil). Journal of Structural Geology 115, 243-262

CHANG, J.; AUDÉTAT, A. (2018): Petrogenesis and metal content of hornblende-rich xenoliths from two Laramide-age magma systems in southwestern USA: insights into the metal budget of arc magmas. Journal of Petrology 59, 1869-1898

CHANG, J.; LI, J.W.; AUDÉTAT, A. (2018): Formation and evolution of multistage magmatic-hydrothermal fluids at the Yulong porphyry Cu-Mo deposit, eastern Tibet: Insights from LA-ICP-MS analysis of fluid inclusions. Geochimica et Cosmochimica Acta 232, 181-205

CHARITON, S.; CERANTOLA, V.; ISMAILOVA, L.; BYKOVA, E.; BYKOV, M.; KUPENKO, I.; MCCAMMON, C.; DUBROVINSKY, L. (2018): The high-pressure behavior of spherocobaltite ($CoCO_3$): A single crystal Raman spectroscopy and XRD study. Physics and Chemistry of Minerals 45, 59-68

COLLINGS, I.; BYKOV, M.; BYKOVA, E.; HANFLAND, M.; VAN SMAALEN, S.; DUBROVINSKY, L.; DUBROVINSKAIA, N. (2018): Disorder–order transitions in the perovskite metal–organic frameworks $[(CH_3)_2NH_2][M(HCOO)_3]$ at high pressure. CrystEngComm 20, 3512-3521

COLLINGS, I.E.; MANNA, R.S.; TSIRLIN, A.A.; BYKOV, M.; BYKOVA, E.; HANFLAND, M.; GEGENWART, P.; VAN SMAALEN, S.; DUBROVINSKY, L.; DUBROVINSKAIA, N. (2018): Pressure dependence of spin canting in ammonium metal formate antiferromagnets. Physical Chemistry Chemical Physics 20, 24465-24476

COMBONI, D.; LOTTI, P.; GATTA, G.D.; MERLINI, M.; LIERMANN, H.-P.; FROST, D.J. (2018): Pargasite at high pressure and temperature. Physics and Chemistry of Minerals 45, 259-278

CONG, J.; ZHAI, K.; CHAI, Y.; SHANG, D.; KHALYAVIN, D.D.; JOHNSON, R.D.; KOZLENKO, D.P.; KICHANOV, S.E.; ABAKUMOV, A.M.; TSIRLIN, A.A.; DUBROVINSKY, L.; XU, X.; SHENG, Z.; OVSYANNIKOV, S.V.; SUN, Y. (2018): Spin-induced multiferroicity in the binary perovskite manganite Mn_2O_3. Nature Communications 9, 2996-3005

DANG, N.T.; ZAKHVALINSKII, V.S.; KOZLENKO, D.P.; PHAN, T.-L.; KICHANOV, S.E.; TRUKHANOV, S.V.; TRUKHANOV, A.V.; NEKRASOVA, YU. S.; TARAN, S.V.; OVSYANNIKOV, S.V.; JABAROV, S.G.; TRUKHANOVA, E.L. (2018): Effect of Fe doping on structural, magnetic and electrical properties of $La_{0.7}Ca_{0.3}Mn_{0.5}Fe_{0.5}O_3$. Ceramics International 44, 14974-14979

DANG, N.T.; ZAKHVALINSKII, V.S.; KOZLENKO, D.P.; PHAN, T.-L.; KICHANOV, S.E.; TRUKHANOV, S.V.; TRUKHANOV, A.V.; NEKRASOVA, YU.S.; TARAN, S.V.; OVSYANNIKOV, S.V.; JABAROV, S.G. (2018): Effect of Fe doping on structure and magnetotransport properties of perovskite manganite. European Physical Journal Plus 133, 296

DUBROVINSKAIA, N.; DUBROVINSKY, L. (2018): Crystallography taken to the extreme. Physica Scripta 93, 062501-06518

FEI, H.; KOIZUMI, S.; SAKAMOTO, N.; HASHIGUCHI, M.; YURIMOTO, H.; MARQUARDT, K.; MIYAJIMA, N.; KATSURA, T. (2018): Pressure, temperature, water content, and oxygen fugacity dependence of Mg grain-boundary diffusion coefficient in forsterite. American Mineralogist 103, 1354-1361

FEI, H.; KOIZUMI, S.; SAKAMOTO, N.; HASHIGUCHI, M.; YURIMOTO, H.; MARQUARDT, K.; MIYAJIMA, N.; KATSURA, T. (2018): Mg lattice diffusion in iron-free olivine and implications to conductivity anomaly in the oceanic asthenosphere. Earth and Planetary Science Letters 484, 204-212

FEI, H.; WIEDENBECK, M.; SAKAMOTO, N.; YURIMOTO, H.; YOSHINO, T.; YAMAZAKI, D.; KATSURA T. (2018): Negative activation volume of oxygen-self-diffusion in forsterite. Physics of the Earth and Planetary Interiors 275, 1-8

FU, S.; YANG, J.; ZHANG, Y.; LIU, J.; OKUCHI, T.; MCCAMMON, C.; KIM, H.-I.; LEE, S.K.; LIN, J.-F. (2018): Abnormal elasticity of Fe-bearing bridgmanite in the Earth's lower mantle. Geophysical Research Letters 45, 4725-4732

GARBER, J.M.; MAURYA, S.; HERNANDEZ, J.-A.; DUNCAN, M.S.; ZENG, L.; ZHANG, H.L.; FAUL, U.; MCCAMMON, C.; MONTAGNER, J.-P.; MORESI, L.; ROMANOWICZ, B.A.; RUDNICK, R.L.; STIXRUDE, L. (2018): Multi-disciplinary constraints on the abundance of diamond and eclogite in the cratonic lithosphere. Geochemistry, Geophysics, Geosystems 19, 2062-2086

GOLABEK, G.J.; EMSENHUBER, A.; JUTZI, M.; ASPHAUG, E.I.; GERYA, T.V. (2018): Coupling SPH and thermochemical models of planets: Methodology and example of a Mars-sized body. Icarus 301, 235-246

GORELOVA, L.A.; PAKHOMOVA, A.S.; APRILIS, G.; DUBROVINSKY, L.S.; KRIVOVICHEV, S.V. (2018): Pentacoordinated silicon in the high-pressure modification of datolite, $CaBSiO_4(OH)$. Inorganic Chemistry Frontiers 5, 1653-1660

GREENBERG, E.; LEONOV, I.; LAYEK, S.; KONOPKOVA, Z.; PASTERNAK, M.P.; DUBROVINSKY, L.; JEANLOZ, R.; ABRIKOSOV, I.A.; ROZENBERG G.Kh. (2018): Pressure-induced site-selective mott insulator-metal transition in Fe_2O_3. Physical Review X 8, 031059

GRÜNINGER, H.; SCHMUTZLER, A.; SIEGEL, R.; ARMSTRONG, K.; FROST, D.J.; SENKER, J. (2018): Quantitative description of H-1 SQ and DQ coherences for the hydroxyl disorder within hydrous ringwoodite. Physical Chemistry Chemical Physics 20, 15098-15105

GUO, H.; AUDÉTAT, A. (2018): Gold diffusion into and out of quartz-hosted fluid inclusions during re-equilibration experiments at 600-800 °C and 2 kbar. Chemical Geology 476, 1-10

GUO, H.; AUDÉTAT, A.; DOLEJS, D. (2018): Solubility of gold in oxidized, sulfur-bearing fluids at 500-850 °C and 200-230 MPa: a synthetic fluid inclusion study. Geochimica et Cosmochimica Acta 222, 655-670

HAKIM, K.; RIVOLDINI, A.; VAN HOOLST, T.; COTTENIER, S.; JAEKEN, J.; CHUST, T.; STEINLE-NEUMANN, G. (2018): A new *ab initio* equation of state of hcp-Fe and its implication on the interior structure and mass-radius relations of rocky super-Earths. Icarus 313, 61-78

HUNT, A.C.; COOK, D.L.; LICHTENBERG, T.; REGER, P.M.; EK, M.; GOLABEK, G.J.; SCHÖNBÄCHLER, M. (2018): Late metal-silicate separation on the IAB parent asteroid: Constraints from combined W and Pt isotopes and thermal modelling. Earth and Planetary Science Letters 482, 490-500

IMMOOR, J.; MARQUARDT, H.; MIYAGI, L.; LIN, F.; SPEZIALE, S.; MERKEL, S.; BUCHEN, J.; KURNOSOV, A.; LIERMANN, H.-P. (2018): Evidence for {100}<011> slip in ferropericlase in Earth's lower mantle from high-pressure/high-temperature experiments. Earth and Planetary Science Letters 489, 251-257

ISHII, T.; HUANG, R.; FEI, H.; KOEMETS, I.; LIU, Z.; MAEDA, F.; YUAN, L.; WANG, L.; DRUZHBIN, D.; YAMAMOTO, T.; BHAT, S.; FARLA, R.; KAWAZOE, T.; TSUJINO, N.; KULIK, E.; HIGO, Y.; TANGE, T.; KATSURA, T. (2018): Complete agreement of the post-spinel transition with 660-km seismic discontinuity. Scientific Reports 8, 6358

ISHII, T.; UENVER-THIELE, L.; WOODLAND, A.B.; ALIG, E.; BOFFA BALLARAN, T. (2018): Synthesis and crystal structure of Mg-bearing Fe_9O_{11}: New insight in the complexity of Fe-Mg oxides at conditions of the deep upper mantle. American Mineralogist 103, 1873-1876

ISHII, T.; SAKAI, T.; KOJITANI, H.; MORI, D.; INAGUMA, Y.; MATSUSHITA, Y.; YAMAURA, K.; AKAOGI, M. (2018): High-pressure phase relations and crystal structures of postspinel phases in MgV_2O_4, FeV_2O_4, and $MnCr_2O_4$: Crystal chemistry of AB_2O_4 postspinel compounds. Inorganic Chemistry 57, 6648-6657

ISHII, T.; KOJITANI, H; AKAOGI, M. (2018): Phase relations and mineral chemistry in pyrolitic mantle at 1600-2200 °C under pressures up to the uppermost lower mantle: Phase transitions around the 660-km discontinuity and dynamics of upwelling hot plumes. Physics of the Earth and Planetary Interiors 274, 127-137

KEIM, M.F.; STAUDE, S.; MARQUARDT, K.; BACHMANN, K.; OPITZ, J.; MARKL, G. (2018): Weathering of Bi-bearing tennantite. Chemical Geology 499, 1-25

KHALYAVIN, D.D.; JOHNSON, R.D.; MANUEL, P.; TSIRLIN, A.A.; ABAKUMOV, A.M.; KOZLENKO, D.P.; SUN, Y.; DUBROVINSKY, L.; OVSYANNIKOV, S.V. (2018): Magneto-orbital texture in the perovskite modification of Mn_2O_3. Physical Review B 98, 014426

KISEEVA, E.S.; VASIUKOV, D.M.; WOOD, B.J.; MCCAMMON, C.; STACHEL, T.; BYKOV, M.; BYKOVA, E.; CHUMAKOV, A.; CERANTOLA, V.; HARRIS, J.W.; DUBROVINSKY, L. (2018): Oxidized iron in garnets from the mantle transition zone. Nature Geoscience 11, 144-147

KOROBEINIKOV, I.V.; MOROZOVA, N.V.; LUKYANOVA, L.N.; USOV, O.A.; KULBACHINSKII, V.A.; SHCHENNIKOV, V.V.; OVSYANNIKOV, S.V. (2018): Stress-controlled thermoelectric module for energy harvesting and its application for the significant enhancement of the power factor of Bi_2Te_3-based thermoelectrics. Journal of Physics D: Applied Physics 51, 025501

KUDRYAVTSEV, D.A.; KUTCHEROV, V.G.; DUBROVINSKY, L.S. (2018): Raman high-pressure study of butane isomers up to 40 GPa. AIP Advances 6, 115104-115109

KULIK, E.; MURZIN, V.; KAWAGUCHI, S.; NISHIYAMA, N.; KATSURA, T. (2018): Thermal expansion of coesite determined by synchrotron powder X-ray diffraction. Physics and Chemistry of Minerals 45, 873-881

KUTZSCHBACH, M.; GUTTMANN, P.; MARQUARDT, K.; WERNER, S.; HENZLER, K.; WILKE, M. (2018): Corrosion of silicate glasses at the nanometer scale: A TXM and XANES approach. Physics and Chemistry of Glasses – European Journal of Glass Science and Technology Part B 59, 11-26

LICHTENBERG, T.; GOLABEK, G.J.; DULLEMOND, C.P.; SCHÖNBÄCHLER, M.; GERYA, T.V.; MEYER, M.R. (2018): Impact splash chondrule formation during planetesimal recycling. Icarus 302, 27-43

MAHAN, B.; SIEBERT, J.; BLANCHARD, I.; BADRO, J.; SOSSI, P.; MOYNIER; F. (2018): Investigating Earth's formation history through copper & sulfur metal-silicate partitioning during core-mantle differentiation. Journal of Geophysical Research: Solid Earth 123, 8349-8363

MAHAN, B.; SIEBERT, J.; BLANCHARD, I.; BORENSZTAJN, S.; BADRO, J.; MOYNIER, F. (2018): Constraining compositional proxies for Earth's accretion and core formation through high pressure and high temperature Zn and S metal-silicate partitioning. Geochimica and Cosmochimica Acta 235, 21-40

MAJUMDER, M.; MANNA, R.S.; SIMUTIS, G.; ORAIN, J.C.; DEY, T.; FREUND, F.; JESCHE, A.; KHASANOV, R.; BISWAS, P.K.; BYKOVA, E.; DUBROVINSKAIA, N.; DUBROVINSKY, L.S.; YADAV, R.; HOZOI, L.; NISHIMOTO, S.; TSIRLIN, A.A.; GEGENWART, P. (2018): Breakdown of magnetic order in the pressurized kitaev iridate. Physical Review Letters 120, 7202-7206

MARQUARDT, H.; BUCHEN, J.; MENDEZ, A.S.J.; KURNOSOV, A.; WENDT, M.; ROTHKIRCH, A.; PENNICARD, D.; LIERMANN, H.-P. (2018): Elastic softening of $(Mg_{0.8}Fe_{0.2})O$ ferropericlase across the iron spin crossover measured at seismic frequencies. Geophysical Research Letters 45, 6862-6868

MARQUARDT, K.; FAUL, U. (2018): The structure and composition of olivine grain boundaries: 40 years of studies, status and current developments. Physics and Chemistry of Minerals, 45, 139-172

MASOTTA, M.; LAUMONIER, M.; MCCAMMON, C. (2018): Transport of melt and volatiles in magmas inferred from kinetic experiments on the partial melting of granitic rocks. Lithos 318-319, 434-447

MEIER, T. (2018): At its extremes: NMR at giga-pascal pressures. – In: WEBB, G. (Ed.): Annual Reports in NMR Spectroscopy 93, 1-74, Elsevier, London, front page article

MEIER, T. (2018): Journey to the centre of the Earth: Jules Vernes' dream in the laboratory from an NMR perspective. Progress in Nuclear Magnetic Resonance Spectroscopy 106-107, 26-36

MEIER, T.; KHANDARKHAEVA, S.; PETITGIRARD, S.; KÖRBER, T.; LAUERER, A.; RÖSSLER, E.; DUBROVINSKY, L. (2018): NMR at pressures up to 90 GPa. Journal of Magnetic Resonance 292, 44-47

MEIER, T.; PETITGIRARD, S.; KHANDARKHAEVA, S.; DUBROVINSKY, L. (2018): Observation of nuclear quantum effects and hydrogen bond symmetrisation in high pressure ice. Nature Communications 9, 2766

MIYAJIMA, N.; LI, Y.; ABEYKOON, S.; HEIDELBACH, F. (2018): Electron channelling contrast imaging of individual dislocations in geological materials using a field-emission scanning electron microscope equipped with an EBSD system. European Journal of Mineralogy 30(1), 5-15

MIYAJIMA, N. (2018): Electron channeling to achieve the full potential of MINERALOGY. American Mineralogist 103, 1173-1175

MONTEUX, J.; GOLABEK, G.J.; RUBIE, D.C.; TOBIE, G.; YOUNG, E.D. (2018): Water and the interior structure of terrestrial planets and icy bodies. Space Science Reviews 214, 39

MORBIDELLI, A.; NESVORNY, D.; LAURENZ, V.; MARCHI, S.; RUBIE, D.C.; ELKINS-TANTON, L.; JACOBSON, S. (2018): The timeline of the lunar bombardment: Revisited. Icarus 305, 262-276

MOROZOVA, N.V.; KOROBEINIKOV, I.V.; KUROCHKA, K.V.; TITOV, A.N.; OVSYANNIKOV, S.V. (2018): Thermoelectric properties of compressed titanium and zirconium trichalcogenides. Journal of Physical Chemistry C 122, 14362-14372

MYHILL, R.; OJWANG, D.O.; ZIBERNA, L.; FROST, D.J.; BOFFA BALLARAN, T.; MIYAJIMA, N. (2018): Correction to: On the *P-T-f*O_2 stability of Fe_4O_5, Fe_5O_6, and Fe_4O_5-rich solid solutions (Vol. 171, 51, 2016). Contributions to Mineralogy and Petrology, 173, 1

NÚÑEZ VALDEZ, M.; EFTHIMIOPOULOS, I.; TARAN, M.; MÜLLER, J.; BYKOVA, E.; MCCAMMON, C.; KOCH-MÜLLER, M.; WILKE, M. (2018): Evidence for a pressure-induced spin transition in olivine-type $LiFePO_4$ triphylite. Physical Review B 97, 184405-1-9

NZOGANG, B.C.; THILLIEZ, S.; MUSSI, A.; KAWAZOE, T.; MIYAJIMA, N.; BOUQUEREL, J.; CORDIER, P. (2018): Application of scanning precession electron diffraction in the Transmission Electron Microscope to the characterization of deformation in wadsleyite and ringwoodite. Minerals 8(4), 153

O'BRIEN, D.P.; RAYMOND, S.N.; RUBIE, D.C.; JACOBSON, S.A.; IZODORO, A. (2018): The delivery of water during terrestrial planet formation. Space Science Reviews 214, 47

OVSYANNIKOV, S.V.; BYKOV, M.; BYKOVA, E.; GLAZYRIN, K.; MANNA, R.S.; TSIRLIN, A.A.; CERANTOLA, V.; KUPENKO, I.; KURNOSOV, A.V.; KANTOR, I.; PAKHOMOVA, A.S.; CHUVASHOVA, I.; CHUMAKOV, A.; RÜFFER, R.; MCCAMMON, C.; DUBROVINSKY, L.S. (2018): Pressure tuning of charge ordering in iron oxide. Nature Communications 9, 4142

POMMIER, A.; KOHLSTEDT, D.L.; HANSEN, L.N.; MACKWELL, S.J.; TASAKA, M.; HEIDELBACH, F.; LEINENWEBER, K. (2018): Experimental investigation of the effect of shear on the electrical properties of polycrystalline olivine. Contributions to Mineralogy and Petrology 173, 41

POMMIER, A.; LAURENZ, V.; DAVIES, C.J.; FROST, D.J. (2018): Melting phase relations in the Fe-S and Fe-S-O systems at core conditions in small terrestrial bodies. Icarus 306, 150-162

POSNER E.S.; SCHMICKLER B.; RUBIE D.C. (2018): Self-diffusion and chemical diffusion in peridotite melt at high pressure and implications for magma ocean viscosities. Chemical Geology 502, 66-75

ROMANENKO, A.V.; RASHCHENKO, S.V.; KURNOSOV, A.; DUBROVINSKY, L.; GORYAINOV, S.V.; LIKHACHEVA, A.Y.; LITASOV, K.D. (2018): Single-standard method for simultaneous pressure and temperature estimation using Sm^{2+}:SrB_4O_7 fluorescence. Journal of Applied Physics 124, 165902-165907

ROTTIER, B.; KOUZMANOV, K.; CASANOVA, C.; WÄLLE, M.; FONTBOTÉ, L. (2018): Cyclic dilution of magmatic metal-rich hypersaline fluids by magmatic low-salinity fluid: A major process generating the giant epithermal polymetallic deposit of Cerro de Pasco, Peru. Economic Geology 113, 825-856

ROTTIER, B.; KOUZMANOV, K.; CASANOVA, C.; BOUVIER, A.-S.; BAUMGARTNER, L.; WÄLLE, M.; FONTBOTÉ, L. (2018): Mineralized breccia clasts: A window into hidden porphyry-type mineralization underlying the epithermal polymetallic deposit of Cerro de Pasco (Peru). Mineralium Deposita 1, 1-28

SCHULZE, K.; MARQUARDT, H.; KAWAZOE, T.; BOFFA BALLARAN, T.; MCCAMMON, C.; KOCH-MÜLLER, M.; KURNOSOV, A.; MARQUARDT, K. (2018): Seismically invisible water in Earth's transition zone? Earth and Planetary Sciences Letters 498, 9-16

SCHULZE, K.; PAMATO, M.G.; KURNOSOV, A.; BOFFA BALLARAN, T.; GLAZYRIN, K.; PAKHOMOVA, A.; MARQUARDT, H. (2018): High-pressure single-crystal structural analysis of $AlSiO_3OH$ phase egg. American Mineralogist 103, 1975-1980

SIEBERT, J.; SOSSI, P.; BLANCHARD, I.; MAHAN, B.; BADRO, J.; MOYNIER, F. (2018): Chondritic Mn/Na ratio and limited post-nebular volatile loss of the Earth. Earth and Planetary Science Letters 485, 130-139

SOLFERINO, G.F.D.; GOLABEK, G.J. (2018): Olivine grain growth in partially molten Fe-Ni-S: A proxy for the genesis of pallasite meteorites. Earth and Planetary Science Letters 504, 38-52

SORBADERE, F.; LAURENZ, V.; FROST, D.J.; WENZ, M.; ROSENTHAL, A.; MCCAMMON, C.; RIVARD, C. (2018): The behaviour of ferric iron during partial melting of peridotite. Geochimica et Cosmochimica Acta 239, 235-254

THIELMANN, M. (2018): Grain size assisted thermal runaway as a nucleation mechanism for continental mantle earthquakes: Impact of complex rheologies. Tectonophysics 746, 611-623

TRUKHANOV, S.V.; TRUKHANOV, A.V.; DANG, N.T.; ZAKHVALINSKII, V.S.; KOZLENKO, D.P.; PHAN, T.-L.; KICHANOV, S.E.; OVSYANNIKOV, S.V.; JABAROV, S.G.; TRUKHANOV, AN.V.; TRUKHANOVA, E.L.; VINNIK, D.A.; GUDKOVA, S.A. (2018): Magnetotransport properties and phase separation in iron substituted lanthanum-calcium manganite. Materials Research Express 5, 086108

UENVER-THIELE, L.; WOODLAND, A.B.; MIYAJIMA, N.; BOFFA BALLARAN, T.; FROST, D.J. (2018): Behaviour of Fe_4O_5-$Mg_2Fe_2O_5$ solid solutions and their relation to coexisting Mg-Fe silicates and oxide phases. Contributions to Mineralogy and Petrology 173, 20

VASIUKOV, D.M.; ISMAILOVA, L.; KUPENKO, I.; CERANTOLA, V.; SINMYO, R.; GLAZYRIN, K.; MCCAMMON, C.; CHUMAKOV, A.I.; DUBROVINSKY, L.; DUBROVINSKAIA, N. (2018): Sound velocities of skiagite–iron–majorite solid solution to 56 GPa probed by nuclear inelastic scattering. Physics and Chemistry of Minerals 45, 397-404

VOGEL, S.; BAUMANN, D.; NIKLAUS, R.; BYKOVA, E.; BYKOV, M.; DUBROVINSKAIA, N.A.; DUBROVINSKY, L.S.; SCHNICK, W. (2018): Stishovite's relative: A post-coesite form of phosphorus oxonitride. Angewandte Chemie International Edition 57, 6691-6695

VOGEL, A.K.; JENNINGS, E.S.; LAURENZ, V.; RUBIE, D.C.; FROST, D.J. (2018): The dependence of metal-silicate partitioning of moderately volatile elements on oxygen fugacity and Si contents of Fe metal: Implications for their valence states in silicate liquids. Geochimica et Cosmochimica Acta 237, 275-293

WAGLE, F.; STEINLE-NEUMANN, G.; DE KOKER, N. (2018): Saturation and negative temperature coefficient of electrical resistivity in liquid iron-sulfur alloys at high densities from first-principles calculations. Physical Review B 97, 094307

WAGLE, F.; STEINLE-NEUMANN, G. (2018): Electrical resistivity discontinuity of iron along the melting curve. Geophysical Journal International 213, 237-243

YOSHIOKA, T.; WIEDENBECK, M.; SHCHEKA, S.; KEPPLER, H. (2018): Nitrogen solubility in transition zone and lower mantle minerals. Earth and Planetary Science Letters 488, 134-143

YUAN, L.; OHTANI, E.; SHIBAZAKI, Y.; OZAWA, S.; JIN, Z.M.; SUZUKI, A.; FROST, D.J. (2018): The stability of anhydrous phase B, $Mg_{14}Si_5O_{24}$, at mantle transition zone conditions. Physics and Chemistry of Minerals 45, 523-531

ZAREI, A.; KLUMBACH; S.; KEPPLER. H. (2018): The relative Raman scattering cross sections of H_2O and D_2O, with implications for *in situ* studies of isotope fractionation. ACS Earth and Space Chemistry 2, 925-934

ZAREI, A.; LI, Y.; FEI, H.; KATSURA, T. (2018): A nearly zero temperature gradient furnace system for high pressure multi-anvil experiments. High Pressure Research 38, 243-249

ZHANG, D.; AUDÉTAT, A. (2018): Magmatic-hydrothermal evolution of the barren Huangshan Pluton, Anhui Province, China: a melt and fluid inclusions study. Economic Geology 113, 803-824

5.2 Publications (submitted, in press)

APRILIS, G.; KANTOR, I.; KUPENKO, I.; CERANTOLA, V.; COLLINGS, I.; PAKHOMOVA, A.; TORCHIO, R.; FEDOTENKO, T.; CHARITON, S.; BYKOV, M.; BYKOVA, E.; KOEMETS, E.; VASIUKOV, D.; MCCAMMON, C.; DUBROVINSKY, L.; DUBROVINSKAIA, N.: Comparative study of the influence of pulsed and continuous wave laser heating on mobilization of carbon and its chemical reaction with an iron sample in a diamond anvil cell. Journal of Applied Physics (submitted)

BEYER, Ch.; DOHMEN, R.; ROGALLA, D.; BECKER, H.-W.; MARQUARDT, K.; VOLLMER, C.; HAGEMANN, U.; HARTMANN, N.; CHAKRABORTY, S.: Lead diffusion in $CaTiO_3$: A combined study using Rutherford Backscattering and TOF-SIMS for depth profiling to reveal the role of lattice strain in diffusion processes. American Mineralogist (accepted)

BOLLINGER, C.; MARQUARDT, K.; FERREIRA, F.: Intragranular plasticity vs. grain boundary sliding (GBS) in forsterite: microstructural evidence at high pressures (3.5-5.0 GPa). American Mineralogist (in press)

BOLLINGER, C.; NZOGANG, B.C.; MUSSI, A.; BOUQUEREL, J.; MOLODOV, D.A.; CORDIER, P.: Microstructural evidence for grain boundary migration and dynamic recrystallization in experimentally deformed forsterite aggregates. Minerals (in press), doi: 10.3390/min9010017

CERANTOLA, V.; WILKE, M.; KANTOR, I.; ISMAILOVA, L.; KUPENKO, I.; MCCAMMON, C.; PASCARELLI, S.; DUBROVINSKY, L.S.: Experimental investigation of $FeCO_3$ (siderite) stability in the Earth's lower mantle using XANES spectroscopy. American Mineralogist (submitted)

CHARITON, S.; MCCAMMON, C.; VASIUKOV, D.; STEKIEL, M.; KANTOR, A.; CERANTOLA, V.; KUPENKO, I.; FEDOTENKO, T.; KOEMETS, E.; HANFLAND, M.; CHUMAKOV, A.; DUBROVINSKY, L.: Seismic detectability of carbonates in the deep Earth: A Nuclear Inelastic Scattering study. American Mineralogist (submitted)

DE MIN, A.; VELICOGNA, M.; ZIBERNA, L.; CHIARADIA, A.; MARZOLI, A.: Triassic magmatism in Southern Alps as an early phase of Pangea break-up. Lithos (submitted)

FEDORTCHOUK, Y.; LIEBSKE, C.; SCHMIDT, M.; MCCAMMON, C.: Diamond destruction and growth during mantle metasomatism: an experimental study of diamond resorption features. Earth and Planetary Science Letters (in press)

GUO, H.; KEPPLER, H.: Electrical conductivity of NaCl bearing aqueous fluids to 900 °C and 5 GPa. Journal of Geophysical Research (submitted)

HUANG, Y.; NAKATANI, T.; NAKAMURA, M.; MCCAMMON, C.: Shallow fluid circulation in mantle wedge inferred from the dihedral angle in an olivine-NaCl-H_2O system. Nature Communications (submitted)

HUECK, M.; STIPP BASEI, M.A.; WEMMER, K.; ORIOLO, S.; HEIDELBACH, F.; SIEGESMUND, S.: Evolution of the Major Gercino Shear Zone in the Dom Feliciano Belt, South Brazil, and implications for the assembly of Southwestern Gondwana. International Journal of Earth Sciences (accepted)

ISHII, T.; LIU, Z.; KATSURA, T.: A breakthrough in pressure generation by Kawai-type multi-anvil apparatus with tungsten carbide anvils. Engineering (submitted)

ISHII, T.; KOJITANI, H.; AKAOGI, M.: Phase relations of harzburgite and MORB up to the uppermost lower mantle conditions: Precise comparison with pyrolite by multi-sample cell high-pressure experiments with implication to dynamics of subducted slabs. Journal of Geophysical Research (submitted)

ISHII, T.; HUANG, R.; FEI, H.; KOEMETS, I.; LIU, Z.; MYHILL, R.; MAEDA, F.; YUAN, L.; WANG, L.; DRUZHBIN, D.; YAMAMOTO, T.; BHAT, S.; FARLA, R.; KAWAZOE, T.; TSUJINO, N.; KULIK, E.; HIGO, Y.; TANGE, Y.; KATSURA, T. (2018): Extremely narrow binary post-spinel transition explains the sharp 660-km discontinuity. Nature Geoscience (submitted)

JENNINGS, E.S.; RUBIE, D.C.; JACOBSON, S.A.; MORBIDELLI, A.; NAKAJIMA, Y.; VOGEL, A.K.; ROSE-WESTON, L.A.; FROST, D.J.: Accretionary core formation cannot fully explain the depletions of Mo and W in Earth's mantle. Geochimica et Cosmochimica Acta (submitted)

KORELL, J.-A.; FRENCH, M.; STEINLE-NEUMANN, G.; REDMER, R.: Paramagnetic-to-diamagnetic transition in dense liquid iron and its influence on electronic transport properties. Physical Review Letters (submitted)

KRESSALL, R.D.; FEDORTCHOUK, Y.; MCCAMMON, C.; ELLIOT, B.: Stability of chromite and ilmenite in a silicate melt at various fO_2 at 0.1 MPa: New insights into use of oxides as diamond indicator minerals in kimberlites. Journal of Petrology (submitted)

KULIK, E.; NISHIYAMA, N.; HIGO, Y.; GAIDA, N.; KATSURA, T.: Hardness of polycrystalline SiO_2 coesite. Journal of the American Ceramic Society (in press)

KUPENKO, I.; APRILIS, G.; VASIUKOV, D.M.; MCCAMMON, C.; CHARITON, S.; CERANTOLA, V.; KANTOR, I.; CHUMAKOV, A.I.; RÜFFER, R.; DUBROVINSKY, L.; SANCHEZ-VALLE, C.: Magnetism in cold subducting slabs at transition zone depths. Nature (submitted)

KURNOSOV, A.; MARQUARDT, H.; DUBROVINSKY, L.; POTAPKIN, V.: A waveguide-based flexible CO_2-laser heating system for diamond-anvil cell applications. Comptes Rendus Geoscience (in press)

KURNOSOV, A.; MARQUARDT, H.; FROST, D.J.; BOFFA BALLARAN, T.; ZIBERNA, L.: Reply to Comment on "High-pressure single crystal elasticity measurements of Al-Fe-bridgmanite support a Fe^{3+}-rich pyrolitic lower mantle". Nature (in press)

LICHTENBERG, T.; GOLABEK, G.J.; BURN, R.; MEYER, M.R.; ALIBERT, Y.; GERYA, T.V.; MORDASINI, C.A.: A water budget dichtomy of rocky protoplanets from ^{26}Al heating. Nature Astronomy (in press)

LICHTENBERG, T.; KELLER, T.; KATZ, R.F.; GOLABEK, G.J.; GERYA, T.V.: Magma ascent in planetesimals: control by grain size. Astrophysics (in press)

LIU, Z.; GREAUX, S.; CAI, N.; SIERSCH, N.; BOFFA BALLARAN, T.; IRIFUNE, T.; FROST, D.J.: Influence of aluminum on elasticity of majorite-pyrope garnets. American Mineralogist (submitted)

LIU, Z.; BOFFA BALLARAN, T.; FROST, D.J.; KATSURA, T.: Strong correlation of the oxygen vacancy component in bridgmanite with Mg/Si ratio. Earth and Planetary Science Letters (submitted)

LIU, Z.; AKAOGI, M.; KATSURA, T.: Increase of the oxygen vacancy component in bridgmanite with temperature. Earth and Planetary Science Letters (in press)

LIU, Z.; DUBROVINSKY, L.; CUI, Q.; SU, N.; MCCAMMON, C.; CHENG, J.; KATSURA, T.: A new weakly ferromagnetic $(Mg_{0.5}Fe_{3+0.5})(Si_{0.5}Al_{3+0.5})O_3$ $LiNbO_3$-type phase synthesized at high pressure and high temperature. Crystal Growth and Design (submitted)

MATROSOVA, E.A.; ISMAILOVA, L.; BOBROV, A.V.; BYKOVA, E.; BYKOV, M.; GLAZYRIN, K.; BINDI, L.; OVSYANNIKOV, S.V.; AKSENOV, S.M.; PUSHCHAROVSKY, D.Yu.; DUBROVINSKY, L.: Compressibility of two Na-rich clinopyroxenes: A synchrotron single-crystal X-ray diffraction study. American Mineralogist (submitted)

MCCAMMON, C.; BUREAU, H.; CLEAVES, H.J.; COTTRELL, E.; DORFMAN, S.M.; KELLOGG, L.H.; LI, J.; MIKHAIL, S.; MOUSSALLAM, Y.; SANLOUP, C.; THOMSON, A.; BROVARONE, A.V.: Deep Earth carbon reactions through time and space. American Mineralogist (submitted)

MCGOWAN, N.; GRIFFIN, W.L.; O'REILLY, S.Y.; CLARK, S.M.; ROQUE-ROSELL, J.; MARCUS, M.A.; MCCAMMON, C.A.; PEARSON, N.J.: The oxidation state of Fe in chromite by µ-XRD and K-edge µ-XANES: A record of deep Earth processes? Geochimica et Cosmochimica Acta (submitted)

MIYAJIMA, N.; MANDOLINI, T.; HEIDELBACH, F.; BOLLINGER, C.: Combining ECCI and FIB milling techniques to prepare site-specific TEM samples for crystal defect analysis of deformed minerals at high pressure. Comptes Rendues Geosciences (in press)

MOUSSALLAM, Y.; LONGPRÉ, M.-A.; MCCAMMON, C.; GOMEZ-ULLA, A.; ROSE-KOGA, E.F.; SCAILLET, B.; PETERS, N.; GENNARO, E.; PARIS, R.; OPPENHEIMER, C.: Mantle plumes are ultra-oxidized. Science (submitted)

PATRICK, M.; INDARES, A.; MCCAMMON, C.: The influence of ferric iron on phase stability in midpressure anatectic aluminous gneisses. Canadian Mineralogist (submitted)

PRESTON, T.R.; APPEL, K.; BRAMBRINK, E.; CHEN, B.; FLETCHER, L.B.; FORTMANN-GROTE, C.; GLENZER, S.H.; GRANADOS, E.; GÖDE, S.; KONOPKOVA, Z.; LEE, H.J.; MARQUARDT, H.; MCBRIDE, E.E.; NAGLER, B.; NAKATSUTSUMI, M.; SPERLING, P.; WITTE, B.B.L.; ZASTRAU, U.: Measurements of the momentum-dependence of plasmonic excitations in matter around 1 Mbar using an X-ray Free Electron Laser. Applied Physics Letters (submitted)

RABIA, K.; MENG, F.; THOMSON, M.D.; BYKOV, M.; MERLIN, R.; VAN SMAALEN, S.; ROSKOS, H.G.: Coherent photo-induced phonon emission in the charge-density-wave state of $K_{0.3}MoO_3$. New Journal of Physics (submitted)

RATERRON, P.; BOLLINGER, C.; MERKEL, S.: Olivine intergranular plasticity at mantle pressures and temperatures. Comptes Rendus Geoscience (accepted)

ROTTIER, B.; AUDÉTAT, A.: *In situ* quantification of chlorine and sulfur in glasses, minerals and melt inclusions by LA-ICP- MS. Chemical Geology (in press)

SATTA, N.; MARQUARDT, H.; KURNOSOV, A.; BUCHEN, J.; KAWAZOE, T.; MCCAMMON, C.; BOFFA BALLARAN, T.: Single-crystal elasticity of iron-bearing phase E by Brillouin spectroscopy and seismic detection of water in Earth's upper mantle. Journal of Geophysical Research (submitted)

SEROVAISKII, A.; MUKHINA, E.; DUBROVINSKY, L.; KOLESNIKOV, A.; MCCAMMON, C.; APRILIS, G.; KUPENKO, I.; CHUMAKOV, A.; RÜFFER, R.; HANFLAND, M.; KUTCHEROV, V.: Fate of hydrocarbons in iron-bearing mineral environments during subduction. Geology (submitted)

SINMYO, R.; NAKAJIMA, Y.; MCCAMMON, C.A.; MIYAJIMA, N.; PETITGIRARD, S.; MYHILL, R.; DUBROVINSKY, L.; FROST, D.J.: Effect of Fe^{3+} on subsolidus and melting phase relations under lower mantle conditions. Earth and Planetary Science Letters (submitted)

SIROTKINA, E.A.; ISMAILOVA, L.; BOBROV, A.V.; BYKOVA, E.; BYKOV, M.; GLAZYRIN, K.; BINDI, L.; OVSYANNIKOV, S.V.; AKSENOV, S.M.; PUSHCHAROVSKY, D.Yu.; DUBROVINSKY, L.: Compressibility of two Na-rich clinopyroxenes: A synchrotron single-crystal X-ray diffraction study. American Minerologist (submitted)

TRYBEL, F.; STEINLE-NEUMANN, G.; MEIER, T.: Proton dynamics in high-pressure ice-VII from density functional theory. Physical Research Letters (submitted)

VASIUKOV, D.M.; DUBROVINSKY, L.; KUPENKO, I.; CERANTOLA, V.; APRILIS, G.; ISMAILOVA, L.; BYKOVA, E.; MCCAMMON, C.; PRESCHER, C.; CHUMAKOV, A.I.; DUBROVINSKAIA, N.: Pressure-induced spin pairing transition of Fe^{3+} in oxygen octahedra. Physical Review B (submitted)

WAGLE, F.; STEINLE-NEUMANN, G.; DE KOKER, N.: Resistivity saturation in liquid iron-light-element alloys at conditions of planetary cores from first principles computations. Comptes Rendus Geoscience (in press)

WAGLE, F.; STEINLE-NEUMANN, G.: Liquid iron equation of state to the terapascal regime from *ab initio* simulations. Journal of Geophysical Research (submitted)

WANG, L.; MIYAJIMA, N.; KAWAZOE, T.; KASURA, T.: Activation of [100](001) slip system by water incorporation in olivine. American Mineralogist (in press)

YOSHIOKA, T.; NAKAJIMA, D.; NAKAMURA, T.; SHCHEKA, S.; KEPPLER, H.: Carbon solubility in silicate melts in equilibrium with a CO-CO_2 gas phase and graphite. Geochimica et Cosmochimica Acta (submitted)

5.3 Presentations at scientific institutions and at congresses

APRILIS, G.; KANTOR, I.; KUPENKO, I.; CERANTOLA, V.; COLLINGS, I.; PAKHOMOVA, A.; TORCHIO, R.; BYKOV, M.; BYKOVA, E.; VASIUKOV, D.; CHARITON, S.; SIMONOVA, D.; MCCAMMON, C.; DUBROVINSKY, L.; DUBROVINSKAIA, N.: 17.-21.06.2018, EMPG-XVI, Clermont-Ferrand, France[*A]: "Chemical interaction of iron with diamond anvils in pulsed and continuous wave laser heated diamond anvil cells"

ARMSTRONG, K.; CONDAMINÉ, P.; ABEYKOON, S.; BUREAU, H.; MCCAMMON, C.; FROST, D.: 10.-14.12.2018, AGU Fall Meeting, Washington D.C., USA[*B]: "Hydrogen partitioning between silicate melt and liquid sulfide: an early oxidation mechanism for the mantle?", Abstract DI42A-02

AUDÉTAT, A.: 01.03.2018, 3rd GOOD Meeting 2018, GeoZentrum Nordbayern, Erlangen, Germany: "The use of fluid inclusions and melt inclusions in ore deposit research"

AUDÉTAT, A.: 29.06.2018, University of Bern, Switzerland: "How LA-ICP-MS changed (and is still changing!) the world of inclusion research"

BLANCHARD, I.; JACOBSON, S.A.; RUBIE, D.C.: 17.-21.06.2018, EMPG-XVI, Clermont-Ferrand, France[*A]: "Behavior of sulfur during core-mantle differentiation of the Earth"

BLANCHARD, I.; JACOBSON, S.A.; RUBIE, D.C.: 21.-23.03.2018, General Meeting DFG SPP 1833 'Building a Habitable Earth', Göttingen, Germany: "Behavior of sulfur during core-mantle differentiation of the Earth"

BLANCHARD, I.; JACOBSON, S.A.; ABEYKOON, S.; LAURENZ, V.; VOGEL, A.K.; ROSE-WESTON, L.A.; RUBIE, D.C.: 10.-14.12.2018, AGU Fall Meeting, Washington D.C., USA[*B]: "Behavior of sulfur during core-mantle differentiation of the Earth", Abstract DI11B-0002

BLUNDY, J.; MELEKHOVA, E.; ULMER, P.; PICHAVANT, M.; HUMPHREYS, M.; ZIBERNA, L.; CERANTOLA, V.; BROOKER, R.; MCCAMMON, C.: 17.-21.06.2018, EMPG-XVI, Clermont-Ferrand, France[*A]: "Iron redox equilibria in hydrous basaltic melts and Fe^{2+}-Mg exchange between olivine and melt"

BOFFA BALLARAN, T.: 22.-27.08.2018, The 31st European Crystallographic Meeting (ECM31), Oviedo, Spain (*invited*): "Crystallography applied to the Earth's lower mantle"

BOFFA BALLARAN, T.: 26.10.2018, Institut de Minéralogy, de Physique de Matériaux et de Cosmochimie, Paris, France: "Elastic behavior of minerals of the transition zone"

BOLLINGER, C.; MARQUARDT, K.; FERREIRA, F.; NZOGANG, B.C.; MUSSI, A.; MOLODOV, D.A.; CORDIER, P.: 10.-14.12.2018, AGU Fall Meeting, Washington D.C., USA[*B]: "On the role of grain boundary processes and mobility on the rheology of forsterite: Microstructural evidences", Abstract MR43C-0130

BONECHI, B.; STAGNO, S.; KONO, Y.; ZIBERNA, L.; PERINELLI, C.; GAETA, M.: 17.-21.06.2018, EMPG-XVI, Clermont-Ferrand, France[*A]: "Rheology of primitive alkaline basalts: constraints on the pre-eruptive system of Campi Flegrei (Naples, Italy)"

BUCHEN, J.; MARQUARDT, H.; SCHULZE, K.; KURNOSOV, A.; BOFFA BALLARAN, T.; SPEZIALE, S.; KAWAZOE, T.: 08.-13.04.2018, European Geosciences Union General Assembly 2018, Vienna, Austria: "Tracing water in the transition zone: From wadsleyite single-crystal elasticity to seismic observables", Geophysical Research Abstracts 20, EGU2018-18438, 2018

BUCHEN, J.; MARQUARDT, H.; SCHULZE, K.; KURNOSOV, A.; CHAUDHARI, A.; BOFFA BALLARAN, T.; SPEZIALE, S.; NISHIYAMA, N.: 08.-13.04.2018, European Geosciences Union General Assembly 2018, Vienna, Austria: "Stiffer than expected: high-pressure elasticity of polycrystalline stishovite questions seismic signature of deep silica", Geophysical Research Abstracts 20, EGU2018-18910, 2018

BUCHEN, J.; MARQUARDT, H.; SCHULZE, K.; SPEZIALE, S.; KURNOSOV, A.; CHAUDHARI, A.; BOFFA BALLARAN, T.; NISHIYAMA, N.: 17.-21.06.2018, EMPG-XVI, Clermont-Ferrand, France[*A]: "High-pressure elasticity of polycrystalline stishovite and seismic scattering in Earth's lower mantle"

BUCHEN, J.; MARQUARDT, H.; SCHULZE, K.; SPEZIALE, S.; KURNOSOV, A.; CHAUDHARI, A.; BOFFA BALLARAN, T.; NISHIYAMA, N.: 02.-06.09.2018, GeoBonn 2018 'Living Earth', Bonn, Germany: "The high-pressure elasticity of polycrystalline stishovite and seismic scattering in Earth's lower mantle"

BUCHEN, J.; SCHULZE, K.; KURNOSOV, A.; BOFFA BALLARAN, T.; SPEZIALE, S.; KAWAZOE, T.; KOCH-MÜLLER, M.; MARQUARDT, H.: 02.-06.09.2018, GeoBonn 2018 'Living Earth', Bonn, Germany: "Tracing water in the transition zone: from single-crystal elasticity to seismic observables"

BUCHEN, J.; MARQUARDT, H.; SCHULZE, K.; SPEZIALE, S.; KURNOSOV, A.; CHAUDHARI, A.; BOFFA BALLARAN, T.; NISHIYAMA, N.: 10.-14.12.2018, AGU Fall Meeting, Washington D.C., USA[*B]: "The ferroelastic phase transition in polycrystalline stishovite and seismic scattering in Earth's lower mantle", Abstract DI31C-0030

CERANTOLA, V.; SAHLE, C.; BYKOVA, E.; PETITGIRARD, S.; WILKE, M.; CHARITON, S.; KUPENKO, I.; MERLINI, M.; MCCAMMON, C.; CHUMAKOV, A.I.; CHECCHIA, S.; MICHIEL, M.D.; KANTOR, I.; SVITLYK, V.; HANFLAND, M.; MEZOUAR, M.; PRESCHER, C.; RÜFFER, R.; PRAKAPENKA, V.; DUBROVINSKY, L.: 02.-07.09.2018, 56th EHPRG Meeting, Aveiro, Portugal: "Structure and properties of carbonates and carbonatitic melts at extreme conditions"

CHARITON, S.; BYKOVA, E.; BYKOV, M.; CERANTOLA, V.; APRILIS, G.; MCCAMMON, C.; DUBROVINSKY, L.: 05.-08.03.2018, 26th Annual Meeting of the German Crystallographic Society (DGK) 2018, Essen, Germany: "The crystal chemistry of calcite-type structure carbonates at extreme conditions"

CHARITON, S.; BYKOVA, E.; BYKOV, M.; CERANTOLA, V.; VASIUKOV, D.; STEKIEL, M.; APRILIS, G.; KUPENKO, I.; KOEMETS, E.; MCCAMMON, C.; DUBROVINSKY, L.: 17.-22.06.2018, Gordon Research Conference – Deep Carbon Science, Smithfield, USA: "Looking for carbonates in the deep Earth: An experimental approach at extreme conditions"

COUPER, S.; SPEZIALE, S.; MARQUARDT, H.; LIERMANN, H.-P.; MIYAGI, L.: 10.-14.12.2018, AGU Fall Meeting, Washington D.C., USA[*B]: "Texture development and slip system activities of bridgmanite during high temperature deformation of a lower mantle assemblage in a resistively heated diamond anvil cell", Abstract MR32A-05

DUBROVINSKY, L.S.; DUBROVINSKAIA, N.A.: 05.-08.03.2018, 26th Annual Meeting of the German Crystallographic Society (DGK), Essen, Germany (*Plenary lecture*): "Crystallography taken to the extreme"

DUBROVINSKY, L.S.: 26.-30.08.2018, 7th EuCheMS Chemistry Congress, Liverpool, U.K. (*invited*): "Inorganic synthesis and crystal chemistry at multimegabar pressures"

DUBROVINSKY, L.S.; DUBROVINSKAIA, N.A.: 10.-14.12.2018, AGU Fall Meeting, Washington D.C., USA[*B] (*invited*): "Structural studies of minerals and compounds at pressures above 200 GPa", Abstract MR14A-03, 2018

EICHHEIMER, P.; THIELMANN, M.; GOLABEK, G.J.: 20.-24.05.2018, Japan Geoscience Union Meeting (JpGU2018), Chiba, Japan: "Towards modelling of water in Earth's mantle"

FEDORTCHOUK, Y.; CHINN, I.; LIEBSKE, C.; MCCAMMON, C.: 12.-17.08.2018, Goldschmidt 2018, Boston, USA: "Mantle metasomatism as recorded in diamond dissolution features"

FEI, H.: 09.02.2018, Chinese Academy of Sciences, Institute of Geochemistry, Guiyang, P.R. China: "The effect of water on mantle rheology and estimation of water content in the mantle transition zone"

FEI, H.; DRUZHBIN, D.; KATSURA, T.: 17.-21.06.2018, EMPG-XVI, Clermont-Ferrand, France[*A]: "Ionic conductivity in natural olivine"

FEI, H.: 21.-24.10.2018, Annual Meeting of Chinese Geoscience Union (CGU), Beijing, P.R. China (*invited talk*): "Water-enhanced ionic conductivity in olivine"

FEI, H.: 21.-24.10.2018, Annual Meeting of Chinese Geoscience Union (CGU), Beijing, P.R. China (*invited talk*): "Water solubility of ringwoodite under mantle transition zone conditions"

FEI, H.: 25.10.2018, Beijing University, School of Earth and Space Sciences, Beijing, P.R. China: "Water in the mantle transition zone"

FEI, H.; DRUZHBIN, D.; KATSURA, T.: 10.-14.12.2018, AGU Fall Meeting, Washington D.C., USA[*B]: "Olivine ionic conduction accounts for the high electrical conductivity layers in the asthenosphere", Abstract DI43C-0038, 2018

FERREIRA; K.; MARQUARDT, K.: 17.-21.06.2018, EMPG-XVI, Clermont-Ferrand, France[*A]: "Transmission of dislocations across olivine grain boundaries"

FROST, D.; ARMSTRONG, K.; RUBIE, D.; MCCAMMON, C.; BOFFA BALLARAN, T.; SIERSCH, N.; WANG, Y.: 12.-17.08.2018, Goldschmidt 2018, Boston, USA: "Silicate melt ferric/ferrous iron speciation and the redox state of a deep magma ocean"

GOLABEK, G.J.; SOLFERINO, G.F.D.; NIMMO, F.; SCHMIDT, M.X.; JUTZI, M.; EMSENHUBER, A.; GERYA, T.V.; ASPHAUG, E.I.: 16.01.2018, LMU München, Germany: "Modelling the early evolution of terrestrial bodies"

GOLABEK, G.J.; ROZEL, A.B.; JAIN, C.; TACKLEY, P.J.; GERYA, T.V.: 02.03.2018, University of California San Diego, Scripps Institution of Oceanography, San Diego, USA: "Modelling crust formation on Archean Earth"

GOLABEK, G.J.; SOLFERINO, G.F.D.: 03.04.2018, Frankfurt-Mainz-Bayreuth Geodynamics Workshop, Frankfurt/M., Germany: "New laboratory and numerical experiments on pallasite formation"

GOLABEK, G.J.; JUTZI, M.; EMSENHUBER, A.; GERYA, T.V.; ASPHAUG, E.I.: 19.04.2018, Workshop on 'Giant Collisions and their Effects on the Thermochemical Evolution of Planets', Berlin, Germany: "Coupling giant impacts and longer-term evolution models"

GOLABEK, G.J.; ROZEL, A.B.; JAIN, C.; TACKLEY, P.J.; GERYA, T.V.: 03.05.2018, TU Berlin, Germany: "Modelling continental crust formation on Archean Earth"

GOLABEK, G.J.; ROZEL, A.B.; JAIN, C.; TACKLEY, P.J.; GERYA, T.V.: 31.05.2018, University of Oslo, Norway: "Modelling continental crust formation on Archean Earth"

GOLABEK, G.J.; ROZEL, A.B.; JAIN, C.; TACKLEY, P.J.; GERYA, T.V.: 03.08.2018, Tohoku University, Sendai, Japan: "Modelling continental crust formation on Archean Earth"

GOLABEK, G.J.; LICHTENBERG, T.; BURN, R.; MEYER, M.R.; ALIBERT, Y.; GERYA, T.V.; MORDASINI, C.A.: 19.-22.08.2018, German-Swiss Geodynamics Workshop, Noer, Germany: "Gradual desiccation of rocky protoplanets from ^{26}Al-heating"

GOLABEK, G.J.; ROZEL, A.B.; JAIN, C.; TACKLEY, P.J.; GERYA, T.V.: 18.10.2018, University of Oxford, U.K.: "Modelling continental crust formation on Archean Earth"

GOLABEK, G.J.; LICHTENBERG, T.; BURN, R.; MEYER, M.R.; ALIBERT, Y.; GERYA, T.V.; MORDASINI, C.A.: 10.-14.12.2018, AGU Fall Meeting, Washington D.C., USA[*B]: "Gradual desiccation of rocky protoplanets from ^{26}Al-heating", Abstract P31D-3738

GOLABEK, G.J.; NIMMO, F.; GERYA, T.V.; SCHENK, P.; PLATTNER, A.: 10.-14.12.2018, AGU Fall Meeting, Washington D.C., USA[*B]: "3D numerical models of thermal convection inside Triton's icy shell", Abstract P33E-3881

HUANG, Y.; NAKATANI, T.; NAKAMURA, M.; MCCAMMON, C.: 27.-29.05.2018, Earth, Sea and Sky III: International Joint Graduate Program Workshop in Earth and Environmental Sciences, Sendai, Japan: "Experimental constraints on the dihedral angles in the system of olivine-multicomponent aqueous fluids at 800-1100 °C and 1-4 GPa"

HUANG, R.; BOFFA BALLARAN, T.; MCCAMMON, C.; MIYAJIMA, N.; FROST, D.J.: 17.-21.06.2018, EMPG-XVI, Clermont-Ferrand, France[*A]: "The speciation of Fe and Al in bridgmanite as a function of composition and oxygen fugacity"

HUANG, R.; BOFFA BALLARAN, T.; MCCAMMON, C.; MIYAJIMA, N.; FROST, D.: 10.-14.12.2018, AGU Fall Meeting, Washington D.C., USA[*B]: "Speciation of Fe and Al in bridgmanite as a function of composition and oxygen fugacity", Abstract DI24A-06

HUANG, Y.; NAKATANI, T.; NAKAMURA, M.; MCCAMMON, C.: 10.-14.12.2018, AGU Fall Meeting, Washington D.C., USA[*B]: "Shallow fluid circulation in mantle wedge inferred from dihedral angle between olivine and NaCl-bearing aqueous fluid", Abstract MR43C-0128

ISHII, T.; HUANG, R.; FEI, H.; KOEMETS, I.; LIU, Z.; MAEDA, F.; YUAN, L.; WANG, L.; DRUZHBIN, D.; YAMAMOTO, T.; BHAT, S.; FARLA, R.; KAWAZOE, T.; NORIYOSHI, T.; KULIK, E.; HIGO, Y.; TANGE, Y.; KATSURA, T.: 08.-13.04.2018, European Geosciences Union General Assembly 2018, Vienna, Austria: "The pressure and thickness of the post-spinel transition in $(Mg,Fe)_2SiO_4$ explaining the sharp 660-km discontinuity", Geophysical Research Abstracts 20, EGU2018-6995, 2018

ISHII, T.; OHIRA, I.; KAWAZOE, T.; BOFFA BALLARAN, T.; SUZUKI, A.; OHTANI, E.: 20.-24.05.2018, Japan Geoscience Union Meeting (JpGU2018), Chiba, Japan: "Single crystal X-ray structure study of δ-phase $AlOOH$-$FeOOH$-$MgSiO_2(OH)_2$"

ISHII, T.; KATSURA, T.: 01.-02.10.2018, The Large Volume Press beamline workshop, Hamburg, Germany: "Determination of phase relations under deep mantle conditions using multi-anvil presses in combination with *in situ* X-ray diffraction: current capability and future development"

ISHII, T.; LIU, Z.; BONDAR, D.; NAKAJIMA, A.; YANG, B.; TANG, H.; HIGO, Y.; TANGE, Y.; KATSURA, T.: 10.-14.12.2018, AGU Fall Meeting, Washington D.C., USA[*B]: "Experimental redetermination of the post-spinel transition boundary in Mg_2SiO_4 by means of *in situ* X-ray diffraction in a multi-anvil press", Abstract DI31C-0032

JENNINGS, E.S.; BLANCHARD, I.; PETITGIRARD, S.; FRANCHI, I.A.; ZHAO, X.; JACOBSON, S.A.; RUBIE, D.C.: 10.-14.12.2018, AGU Fall Meeting, Washington D.C., USA[*B]: "Fate of carbon during the formation of Earth's core", Abstract DI11B-0018

JESUS-RYDIN, C.; ROMANOWICZ, B.; MCCAMMON, C.: 10.-14.12.2018, AGU Fall Meeting, Washington D.C., USA[*B]: "European Research Council (ERC) funding opportunities", Abstract TH25F

KATSURA, T.: 19.-20.02.2018, Graduate School of Science, Tohoku University, Sendai, Japan: "Basic Lecture on Earth and Planetary Materials III", "Basic Theory on Earth and Planetary Materials III"

KATSURA, T.: 20.02.2018, Tohoku University, Graduate School of Science, Sendai, Japan: "Binary phase relations between ringwoodite and bridgmanite + ferropericlase: implication for sharpness of the 660-km discontinuity"

KATSURA, T.: 21.-24.02.2018, Ehime University, Geodynamic Research Center, Matsuyama, Japan: "Physics and Chemistry of the Earth's mantle"

KATSURA, T.: 24.02.2018, Ehime University, Geodynamic Research Center, Matsuyama, Japan: "Binary phase relations between ringwoodite and bridgmanite + ferropericlase: implication for sharpness of the 660-km discontinuity"

KATSURA, T.: 13.-14.03.2018, Deep Volatiles, Energy & Environments Summit (DVEES 2018), Shanghai, P.R. China (*invited)*: "The $MgAlO_{2.5}$ contents in bridgmanite as a function of pressure and bulk composition based on defect chemistry and its applications to volatile storage capacity in the lower mantle"

KATSURA, T.: 27.06.2018, Center for High Pressure Science and Technology Advanced Research, Beijing, P.R. China: "Development of advanced multi-anvil technology and its application to investigation of mantle dynamics"

KATSURA, T.: 02.08.2018, Hiroshima Institute of Plate Convergence Region Research, Higashi-Hiroshima, Japan: "Binary phase relations of the postspinel transition in the system $(Mg,Fe)_2SiO_4$-interpretation of extremely thin 660-km seismic discontinuity"

KATSURA, T.: 11.09.2018, Chinese Academy of Science, Institute for Geology and Geophysics, Beijing, P.R. China: "Water-enhanced olivine ionic conduction accounts for the upper-mantle conductivity anomaly"

KATSURA, T.: 13.09.2018, Institute for Geochemistry, Guiyang, P.R. China: "Binary phase relations between ringwoodite and bridgmanite + ferropericlase: Implication for sharpness of the 660-km discontinuity"

KATSURA, T.; LIU, Z.; WANG, B.; FEI, H.; ISHII, T.; HUANG, R.; WANG, L.; CHANYSHEV, A.; MCCAMMON, C.; DUBROVINSKY, L.; FROST, D.; BOFFA BALLARAN, T.: 10.-14.12.2018, AGU Fall Meeting, Washington D.C., USA[*B]: "Pressure, temperature and composition dependence of the oxygen-vacancy components in bridgmanite under mid-mantle conditions: implications to mantle viscosity variation and volatile transport", Abstract DI31C-0029

KOROBEINIKOV, I.V.; MOROZOVA, N.V.; OVSYANNIKOV, S.V.: 23.-27.07.2018, Joint 18th International Conference on High Pressure Semiconductor Physics & 2nd International Workshop on High Pressure Study of Superconductors, Barcelona, Spain: "Thermoelectric properties of compressed germanium", Book of Abstracts, We4.9-P17

KUPENKO, I.; APRILIS, G.; VASIUKOV, D.; MCCAMMON, C.; CHARITON, S.; CERANTOLA, V.; KANTOR, I.; CHUMAKOV, A.I.; RÜFFER, R.; DUBROVINSKY, L.; SANCHEZ-VALLE, C.: 17.-21.06.2018, EMPG-XVI, Clermont-Ferrand, France[*A]: "Magnetic hematite at depths of the Earth's transition zone"

LAUBIER, M.; BOLFAN-CASANOVA, N.; GABORIEAU, M.; MCCAMMON, C.: 12.-17.08.2018, Goldschmidt 2018, Boston, USA: "On the use of experimentally derived redox sensors in olivine-hosted melt inclusions"

LEE, K.; GU, T.; CREASY, N.; LI, M.; MCCAMMON, C.; GIRARD, J.: 12.-17.08.2018, Goldschmidt 2018, Boston, USA: "Aiding atmosphere oxidation through mantle convection"

LICHTENBERG, T.; KELLER, T.; KATZ, R.F.; GOLABEK, G.J.; GERYA, T.V.: 08.-13.04.2018, European Geosciences Union General Assembly 2018, Vienna, Austria: "Magma ascent in planetesimals controlled by grain size", Geophysical Research Abstracts 20, EGU2018-8262, 2018

MAEDA, F.; KAMADA, S.; MIYAJIMA, N.; PETITGIRARD, S.; HIRAO, N.; MCCAMMON, C.; FROST, D.; SAKAMAKI, T.; SUZUKI, A.: 27.-29.05.2018, Earth, Sea and Sky III: International Joint Graduate Program Workshop in Earth and Environmental Sciences, Sendai, Japan: "Stability of $MgCO_3$ under iron-rich lower mantle conditions"

MAEDA, F.; KAMADA, S.; MIYAJIMA, N.; PETITGIRARD, S.; HIRAO, N.; SAKAMAKI, T.; MCCAMMON, C.; FROST, D.J.; OHISHI, Y.; SUZUKI, A.: 02.-07.09.2018, 56th EHPRG Meeting, Aveiro, Portugal: "Reaction of $MgCO_3$ high-pressure carbonate and metallic iron in the deep lower mantle"

MAEDA, F.; KAMADA, S.; MIYAJIMA, N.; HIRAO, N.; KAWAGUCHI, S.; PETITGIRARD, S.; MCCAMMON, C.; FROST, D.; SAKAMAKI, T.; SUZUKI, A.: 26.-28.11.2018, The 59th High Pressure Conference of Japan, Okayama, Japan: "Stability of $MgCO_3$ under H_2O and Fe-rich lower mantle conditions"

MARQUARDT, H.: 13.11.2018, University College London, U.K.: "Experimental exploration of Earth's mantle"

MARQUARDT, K.: 21.03.2018, Universität Innsbruck, Austria: "Transmission electron microscopy to understand geomaterials"

MARQUARDT, K.: 10.05.2018, Imperial College London, U.K.: "Interfaces in ceramics of the deep Earth Interfacial network characteristics – aiming to link structure to property"

MARQUARDT, K.: 23.-25.05.2018, EBSD 2018, Ann Arbor, USA (*keynote lecture*): "Interfacial networks characteristics obtained from EBSD analyses"

MARQUARDT, K.: 06.06.2018, GeoForschungsZentrum Potsdam, Germany: "Studying Earth materials interfaces by electron microscopy"

MARQUARDT, K.: 27.06.2018, TU Berlin, Germany: "Studying Earth materials interfaces by electron microscopy: An attempt to relate structure to property"

MARQUARDT, K.: 02.07.2018, University College London, U.K.: "Interfaces in rocks of the deep Earth"

MCCAMMON, C.A.: 15.-16.02.2018, Kick-Off Meeting of the FOR2125/2, Hamburg, Germany: "A new frontier: Oxygen fugacity in the diamond anvil cell"

MCCAMMON, C.A.: 15.-16.02.2018, Kick-Off Meeting of the FOR2125/2, Hamburg, Germany: "Prospects for detecting carbonates in the mantle from seismic data"

MCCAMMON, C.A.: 22.-23.03.2018, Earth in Five Reactions Workshop, Washington D.C., USA: "Who cares about deep carbon sequestration?"

MCCAMMON, C.; WINKLER, B.: 17.-22.06.2018, Gordon Research Conference – Deep Carbon Science, Smithfield, USA: "CarboPaT continues! Past and future exploration of carbonates at extreme conditions"

MCCAMMON, C.A.: 13.-17.08.2018, XXII Meeting of the International Mineralogical Association, Melbourne, Australia: "Deep electron transfer between iron and carbon"

MCCAMMON, C.A.: 22.08.2018, University of New South Wales, Canberra, Australia: "Remote sensing our own planet or how deep does the carbon cycle really go?"

MCCAMMON, C.A.: 27.08.2018, Monash University, Clayton, Australia: "Deep carbon: Fact or fiction, and where could it be hiding?"

MCCAMMON, C.A.: 28.08.2018, Australian Synchrotron, Clayton, Australia: "Novel synchrotron applications involving iron"

MCCAMMON, C.A.: 15.-17.11.2018, 9th TOYOTA RIKEN International Workshop on Mössbauer Spectroscopy, Nagoya, Japan: "Mössbauer spectroscopy with high spatial resolution: Spotlight on geoscience"

MCCAMMON, C.A.: 10.-14.12.2018, AGU Fall Meeting, Washington D.C., USA^{*B}: "What makes waves in some parts of the rocks inside our world go fast?", Abstract ED21B-06

MEIER, T.; KHANDARKHAEVA, S.; PETITGIRARD, S.; DUBROVINSKY, L.S.: 22.03.2018, University of Edinburgh, Center for Science at Extreme Conditions (CSEC), Edinburgh, U.K.: "On the way to NMR at mega-bar pressures – Observation of proton tunneling in ice up to 90 GPa"

MEIER, T.; KHANDARKHAEVA, S.; PETITGIRARD, S.; DUBROVINSKY, L.S.: 01.-05.07.2018, EUROMAR 2018, Nantes, France: "On the way to NMR at mega-bar pressures: Observation of hydrogen bond symmetrisation in high pressure ices"

MEIER, T.; KHANDARKHAEVA, S.; PETITGIRARD, S.; DUBROVINSKY, L.: 29.07.-02.08.2018, International Union of Crystallography Workshop on High Pressure (IUCr-HP), Honolulu, Hawaii, USA (*invited*): "On the way to NMR at mega-bar pressures – Challenges and new horizons"

MEIER, T.: 02.-07.09.2018, 56th EHPRG Meeting, Aveiro, Portugal (*award lecture*): "On the way to NMR at mega-bar pressures: Past and future challenges"

MÉNDEZ, A.S.J.; MARQUARDT, H.; LIERMANN, H.-P.; BUCHEN, J.: 17.-21.06.2018, EMPG-XVI, Clermont-Ferrand, France^{*A}: "Time-resolved X-ray diffraction study of the spin crossover of (MgFe)O under dynamic compression"

MÉNDEZ, A.S.J.; MARQUARDT, H.; WENDT, M.; SCHWARK, I.; EHNES, A.; GLAZYRIN, K.; HUSBAND, R.; KURNOSOV, A.; PAKHOMOVA, A.; SCHULZE, K.; SATTA, N.; BUCHEN, J.; LIERMANN, H.-P.: 10.-14.12.2018, AGU Fall Meeting, Washington D.C., USA^{*B} (*invited*): "A dynamic Diamond Anvil Cell (dDAC) setup for time-resolved high-temperature X-ray diffraction experiments under dynamic compression", Abstract MR14A-04

MÉNDEZ, A.S.J.; MARQUARDT, H.; BUCHEN, J.; KURNOSOV, A.; WENDT, M.; ROTHKIRCH, A.; PENNICARD, D.; LIERMANN, H.-P.: 10.-14.12.2018, AGU Fall Meeting, Washington D.C., USA[*B]: "Direct measurements of the bulk modulus softening in (Mg,Fe)O across the iron spin change measured at seismic frequencies in a dynamic DAC using time-resolved XRD, Abstract MR33B-0101

MIYAJIMA, N.; HUANG, R.; SORBADÈRE, F.; BOFFA BALLARAN, T.; MCCAMMON, C.; FROST, D.J.: 17.-21.06.2018, EMPG-XVI, Clermont-Ferrand, France[*A]: "Quantitative determination of iron oxidation states in minerals using electron energy loss near-edge structure spectroscopy: a geochemical application of Fe L2,3-edge ELNES revisited"

MIYAJIMA, N.; LI, Y.; SUMITH A.; MANDOLINI, T.; HEIDELBACH, F.: 23.-27.07.2018, EBSD Workshop organized by K. Marquardt, BGI, Bayreuth, Germany: "Electron channeling contrast imaging of individual dislocations and stacking faults in geological materials using a field emission scanning electron microscope"

MIYAJIMA, N.; UENVER-THIELE, L.; WOODLAND, A.B.; SINMYO, R.; ISHII, T.; BOFFA BALLARAN, T.; FROST, D.J.: 13.-17.08.2018, XXII Meeting of the International Mineralogical Association, Melbourne, Australia: "Antiphase domain boundaries in magnetite: A key feature of unseen high-pressure mixed-valence iron oxides"

MIYAJIMA, N.; MANDOLINI, T.; HEIDELBACH, F.: 02.-06.09.2018, GeoBonn 2018 'Living Earth', Bonn, Germany: "Partial dislocations and stacking fault ribbons in deformed pyrope at high pressure and temperature: Combining ECCI and FIB milling techniques to prepare site-specific TEM samples"

MOROZOVA, N.V.; KOROBEINIKOV, I.V.; KUROCHKA, K.V.; TITOV, A.N.; OVSYANNIKOV, S.V.: 23.-27.07.2018, Joint 18th International Conference on High Pressure Semiconductor Physics & 2nd International Workshop on High Pressure Study of Superconductors, Barcelona, Spain: "Thermoelectric properties of MX_3 (M – Ti, Zr, X – S, Se, Te) under high pressure", Book of Abstracts, Th4.8-P16

MOROZOVA, N.V.; KOROBEINIKOV, I.V.; KUROCHKA, K.V.; TITOV, A.N.; OVSYANNIKOV, S.V.: 02.-07.09.2018, 56th EHPRG Meeting, Aveiro, Portugal: "Thermoelectric properties of MX_3 (M – Ti, Zr, X – S, Se, Te) under high pressure", Book of Abstracts, 291

MOROZOVA, N.V.; KOROBEINIKOV, I.V.; KUROCHKA, K.V.; TITOV, A.N.; OVSYANNIKOV, S.V.: 30.09.-03.10.2018, The 9th Asian Conference on High Pressure Research (ACHPR9), Singapore: "2D titanium and zirconium trichalcogenides (TiS_3, ZrS_3, $ZrSe_3$ and $ZrTe_3$) under high pressure: thermoelectric and electrical properties", Book of Abstracts, 211

OVSYANNIKOV, S.V.: 23.-27.07.2018, Joint 18th International Conference on High Pressure Semiconductor Physics & 2nd International Workshop on High Pressure Study of Superconductors, Barcelona, Spain (*invited*): "High pressure high temperature synthesis and phase transitions in simple oxides", Book of Abstracts, Th2.1

OVSYANNIKOV, S.V.; BYKOV, M.; BYKOVA, E.; GLAZYRIN, K.; TSIRLIN, A.A.; MANNA, R.S.; KOZLENKO, D.P.; KICHANOV, S.E.; ABAKUMOV, A.M.; VASIUKOV, D.; CHUVASHOVA, I.; PAKHOMOVA, A.S.; KURNOSOV, A.V.; CERANTOLA, V.; KUPENKO, I.; MCCAMMON, C.; DUBROVINSKY, L.S.: 02.-07.09.2018, 56th EHPRG Meeting, Aveiro, Portugal (*invited*): "High-pressure effects on the charge-ordering transitions in iron oxides", Book of Abstracts, 188-189

OVSYANNIKOV, S.V.; CONG, J.; ZHAI, K.; CHAI, Y.; SHANG, D.; KHALYAVIN, D.D.; JOHNSON, R.D.; KOZLENKO, D.P.; KICHANOV, S.E.; ABAKUMOV, A.M.; TSIRLIN, A.A.; KARKIN, A.E.; MOROZOVA, N.V.; XU, X.; SHENG, Z.; SUN, Y.; DUBROVINSKY, L.S.: 02.-07.09.2018, 56th EHPRG Meeting, Aveiro, Portugal: "High-pressure synthesis and properties of perovskite-type Mn_2O_3", Book of Abstracts, 292-293

OVSYANNIKOV, S.V.; BYKOV, M.; BYKOVA, E.; GLAZYRIN, K.; TSIRLIN, A.A.; MANNA, R.S.; KOZLENKO, D.P.; KICHANOV, S.E.; ABAKUMOV, A.M.; VASIUKOV, D.; CHUVASHOVA, I.; PAKHOMOVA, A.S.; KURNOSOV, A.V.; CERANTOLA, V.; KUPENKO, I.; MCCAMMON, C.; DUBROVINSKY, L.S.: 30.09.-03.10.2018, The 9th Asian Conference on High Pressure Research (ACHPR9), Singapore (*invited*): "High-pressure perspectives on the charge ordering in iron oxides", Book of Abstracts, 74

OVSYANNIKOV, S.V.; BYKOV, M.; BYKOVA, E.; GLAZYRIN, K.; PAKHOMOVA, A.S.; KURNOSOV, A.V.; CERANTOLA, V.; KUPENKO, I.; MCCAMMON, C.; DUBROVINSKY, L.S.: 10.-12.10.2018, 7th Joint Workshop on High Pressure, Planetary, and Plasma Physics (HP4), Berlin, Germany: "High-pressure behavior of Fe_4O_5 at low and high temperatures"

PEIFFER, S.; WAN, M.; MCCAMMON, C.; SCHRÖDER, C.: 18.-22.03.2018, 255th American Chemical Society National Meeting & Exposition, New Orleans, USA: "Metastable sulphur species at iron mineral surfaces"

PELLETER, A.A.; ROSENTHAL, A.; MCCAMMON, C.; LAURENZ, V.; LAPORTE, D.; BOLFAN-CASANOVA, N.: 17.-21.06.2018, EMPG-XVI, Clermont-Ferrand, France[*A]: "Variations in Fe^{3+}/Fe_{total} ratios in sediment-derived silicic melts at sub-arc depths"

POLEDNIA, J.; BUCHEN, J.; MARQUARDT, K.: 10.-14.12.2018, AGU Fall Meeting, Washington D.C., USA[*B]: "Anisotropic thermal expansion and thermal fracturing of olivine bicrystals: Pathways for magma flux at mid-ocean ridges", Abstract DI43C-0044

POSNER, E.S.; RUBIE, D.C.; FROST, D.J.; STEINLE-NEUMANN, G.: 11.-16.03.2018, Winter School at the Ecole de Physique des Houches, Les Houches, France: "Mass transport and structural properties of light elements in liquid iron at high pressure"

POSNER, E.S.: 21.-23.03.2018, General Meeting DFG SPP 1833 'Building a Habitable Earth', Göttingen, Germany: "Fate of carbon during early differentiation of the Earth"

POSNER, E.S.: 25.-28.06.2018, Origin of the Earth-Moon System, TRR 170 'Late Accretion onto Terrestrial Planets' Summer School, Trechtingshausen, Germany: "Chemical aspects of core formation"

POSNER, E.S.: 25.-28.06.2018, Origin of the Earth-Moon System, TRR 170 'Late Accretion onto Terrestrial Planets' Summer School, Trechtingshausen, Germany: "Constraints on the Earth's final magma ocean"

PRESTON, T.R.; SPERLING, P.; APPEL, K.; CHEN, B.; FLETCHER, L.; GLENZER, S.H.; GÖDE, S.; KONOPKOVA, Z.; LEE, H.J.; MARQUARDT, H.; MCBRIDE, E.E.; NAGLER, B.; NAKATSTSUMI, M.; WITTE, B.B.L.; ZASTRAU, U.: 02.-06.07.2018, The 45th European Physical Society Conference on Plasma Physics, Prague, Czech Republic: "High resolution measurement of the momentum-dependent plasmonic excitations at 1 Mbar matter"

REDMER, R.; KORELL, J.-A.; FRENCH, M.; STEINLE-NEUMANN, G.: 10.-12.10.2018, 7th Joint Workshop on High Pressure, Planetary, and Plasma Physics (HP4), Berlin, Germany: "Paramagnetic-to-diamagnetic transition in dense liquid iron and its influence on electronic transport properties"

ROSENTHAL, A.; MCCAMMON, C.; CRICHTON, W.; CERANTOLA, V.; CHUMAKOV, A.; VASILYEV, P.; LAUBIER, M.; ANDRAULT, D.; JACOB, D.; YAXLEY, G.; WOODLAND, A.; FOLEY, S.; PEARSON, G.; LAPORTE, D.; NJUL, R.; SCHULZE, H.: 13.-17.08.2018, XXII Meeting of the International Mineralogical Association, Melbourne, Australia: "Determination of the oxidation state of iron in natural peridotitic and eclogitic garnets by synchrotron Mössbauer spectroscopy"

RUBIE, D.C.: 17.-22.06.2018, Gordon Research Conference – Deep Carbon Science, Smithfield, USA: "The behaviour of the volatile elements sulfur and carbon in the early solar system: From condensation to planetary differentiation"

RUSTIONI, G.; AUDÉTAT, A.; KEPPLER, H.: 20.-24.05.2018, Japan Geoscience Union Meeting (JpGU2018), Chiba, Japan: "The effect of chlorine on the transport of trace elements in subduction zones"

RUSTIONI, G.; AUDÉTAT, A.; KEPPLER, H.: 17.-21.06.2018, EMPG-XVI, Clermont-Ferrand, France[*A]: "Experimental constraints on trace element mobility in subduction zone fluids"

SATTA, N.; MARQUARDT, H.; KURNOSOV, A.; BOFFA BALLARAN, T.; BUCHEN, J.; MCCAMMON, C.; KAWAZOE, T.: 17.-21.06.2018, EMPG-XVI, Clermont-Ferrand, France[*A]: "Single-crystal elasticity of iron-rich phase E"

SATTA, N.; MARQUARDT, H.; KURNOSOV, A.; BOFFA BALLARAN, T.; BUCHEN, J.; MCCAMMON, C.; KAWAZOE, T.: 02.-06.09.2018, GeoBonn 2018 'Living Earth', Bonn, Germany: "Single-crystal elasticity of iron-bearing phase E by Brillouin spectroscopy and seismic detection of water in Earth's upper mantle"

SAWA, S.; MIYAJIMA, N.; MUTO, J.; NAGAHAMA, H.: 26.-28.11.2018, The 59th High Pressure Conference of Japan, Okayama, Japan: "Study of mechanism responsible for deep-focus earthquakes by a Griggs type piston-cylinder apparatus"

SCHULZE, K.; BOFFA BALLARAN, T.; PAMATO, M.G.; KURNOSOV, A.; GLAZYRIN, K.; MARQUARDT, H.; PAKHOMOVA, A.: 17.-21.06.2018, EMPG-XVI, Clermont-Ferrand, France[*A]: "High pressure single-crystal structural analysis of $AlSiO_3OH$ phase egg"

SCHULZE, K.; BOFFA BALLARAN, T.; PAMATO, M.G.; KURNOSOV, A.; GLAZYRIN, K.; PAKHOMOVA, A.; MARQUARDT, H.: 02.-06.09.2018, GeoBonn 2018 'Living Earth', Bonn, Germany: "A high-pressure structural analysis of $AlSiO_3OH$ Phase Egg"

SIERSCH, N.C.; BOFFA BALLARAN, T.; LIU, Z.; KURNOSOV, A.; ISHII, T.; CRINITI, G.; YU, T.; WANG, Y.; FROST, D.: 10.-14.12.2018, AGU Fall Meeting, Washington D.C., USA[*B]: "Elastic Wave Velocities of Mg, Fe- and Al-bearing akimotoite by means of ultrasonic measurements and Brillouin spectroscopy", Abstract MR33B-0104

SOLFERINO, G.F.D.; GOLABEK, G.J.: 08.-13.04.2018, European Geosciences Union General Assembly 2018, Vienna, Austria: "The formation of pallasite meteorites: A combined experimental and numerical study", Geophysical Research Abstracts 20, EGU2018-3849, 2018

STEINLE-NEUMANN, G.; WAGLE, F.: 10.-12.10.2018, 7th Joint Workshop on High Pressure, Planetary, and Plasma Physics (HP4), Berlin, Germany: "P-V-T equation-of-state of liquid Fe from *ab initio* simulations to the TPa regime"

STEINLE-NEUMANN, G.: 10.-14.12.2018, AGU Fall Meeting, Washington D.C., USA[*B]: "Inner rocks of our world in the computer", Abstract ED21B-11

STEINLE-NEUMANN, G.; WAGLE, F.: 10.-14.12.2018, AGU Fall Meeting, Washington D.C., USA[*B]: "P-V-T equation-of-state of liquid Fe from *ab initio* simulations to the TPa regime", Abstract DI43B-0019

THIELMANN, M.; DURETZ, T.; KAUS, B.J.P.; ROZEL, A.; RICARD, Y.: 25.01.2018, Séminaire de Mécanique d'Orsay, Orsay, France: "Ductile strain localization: the key for plate tectonics on a convective planet"

THIELMANN, M.; DURETZ, T.; KAUS, B.J.P.; ROZEL, A.; RICARD, Y.: 22.03.2018, Erdwissenschaftliches Kolloquium Universität Wien, Austria: "Earthquakes, shear zones and plate tectonics: the importance of ductile weakening mechanisms"

THIELMANN, M.; DURETZ; T.: 08.-13.04.2018, European Geosciences Union General Assembly 2018, Vienna, Austria: "Earthquakes below the brittle-ductile transition: The role of grain size assisted thermal runaway", Geophysical Research Abstracts 20, EGU2018-13732, 2018

THIELMANN, M.; DURETZ, T.: 20.-24.05.2018, Japan Geoscience Union Meeting (JpGU2018), Chiba, Japan: "Intermediate depth earthquakes due to grain size assisted thermal runaway: What are the odds?"

THIELMANN, M.; DURETZ, T.; KAUS, B.J.P.; ROZEL, A.; RICARD, Y.: 27.-29.05.2018, Earth, Sea and Sky III: International Joint Graduate Program Workshop in Earth and Environmental Sciences, Sendai, Japan: "From ductile shear zones to earthquakes"

THIELMANN, M.; MARQUARDT, H.; GOLABEK, G.J.G.: 01.-04.10.2018, GeoMod 2018, Barcelona, Spain: "Deformation in two-phase rocks: a look through the statistical lens"

TRYBEL, F.; STEINLE-NEUMANN, G.: 06.-07.08.2018, Workshop on 'Low-Mass Planets', Rostock, Germany: "GPU accelerated *ab initio* calculations"

TRYBEL, F.; STEINLE-NEUMANN, G.; MEIER, T.: 10.-12.10.2018, 7th Joint Workshop on High Pressure, Planetary, and Plasma Physics (HP4), Berlin, Germany: "Proton dynamics in high-pressure ice-VII from density functional theory"

UENVER-THIELE, L.; WOODLAND, A.B.; BOFFA BALLARAN, T.; FROST, D.J.: 17.-21.06.2018, EMPG-XVI, Clermont-Ferrand, France[*A]: "Phase relations between $(Mg,Fe)_2Fe_2O_5$ and Mg-Fe silicates like garnet and phase B"

WEIS, C.; SAKROWSKI, R.; SPIEKERMANN, G.; ELBERS, M.; CERANTOLA, V.; FOROV, Y.; HARDER, M.; YAVAŞ, H.; VANKÓ, G.; SAHLE, C.J.; MCCAMMON, C.; TOLAN, M.; WILKE, M.; STERNEMANN, C.: 22.-27.07.2018, 17th International Conference on X-ray Absorption Fine Structure, Kraków, Poland: "Fe spin transition in Earth's mantle minerals – Insights from a combination of X-ray Raman scattering and X-ray emission spectroscopy"

YAO, J.; FROST, D.J.; STEINLE-NEUMANN, G.; LIU, Z.; FEI, H.; ZIBERNA, L.: 21.-23.03.2018, General Meeting DFG SPP 1833 'Building a Habitable Earth', Göttingen, Germany: "Towards melting relations in the MgO-FeO-SiO_2 system at lower mantle conditions from multi-anvil experiments"

YOSHIOKA, T.; NAKAJIMA, D.; NAKAMURA, T.; SHCHEKA, S.; KEPPLER, H.: 02.-06.09.2018, GeoBonn 2018 'Living Earth', Bonn, Germany: "Carbon solubility in silicate melts coexisting with graphite and a CO-CO_2 gas phase"

YUTANI, T.; CONDAMINÉ, P.; SATO, Y.; MCCAMMON, C.; HIRANO, N.; FROST, D.: 10.-14.12.2018, AGU Fall Meeting, Washington D.C., USA[*B]: "An experimental study on the genesis of petit-spot Lavas", Abstract V23L-0210

ZIBERNA, L.; CERANTOLA, V.; MILANI, S.; MELAI, C.; FACCINCANI, L.; STAGNO, V.; ISMAILOVA, L.; BULANOVA, G.; SMITH, C.; CHUMAKOV, A.; FROST, D.; MCCAMMON, C.: 05.-07.02.2018, European Synchrotron Radiation Facility User Meeting 2018, Grenoble, France: "Synchrotron Mössbauer spectroscopy applied to mantle xenoliths and inclusions in diamonds from the Murowa kimberlite, Zimbabwe"

ZIBERNA, L.; CERANTOLA, V.; SMITH, C.; BULANOVA, G.; FROST, D.: 09.-14.06.2018, Conference on 'The Problems of Magmatic and Metamorphic Petrology, Geodynamics and Genesis of Diamonds', Novosibirsk, Russia (*invited*): "The oxidation state of ultra-refractory mantle peridotites from Murowa, Zimbabwe"

ZIBERNA L.; CERANTOLA, V.; MILANI, S.; SMITH C.; BULANOVA, G.; MELAI, C.; FACCINCANI, L.; ISMAILOVA, L.; STAGNO, V.; MCCAMMON, C.; FROST D.: 12.-14.09.2018, SGI-SIMP Congress on 'Geosciences for the Environment, Natural Hazard and Cultural Heritage', Catania, Italy: "Oxidation state of Fe in highly refractory mantle peridotites"

[*A] **EMPG-XVI: Sixteenth International Symposium on Experimental Mineralogy, Petrology and Geochemistry, 17.-21.06.2018, Clermont-Ferrand, France**

[*B] **AGU: American Geophysical Union Fall Meeting, 10.-14.12.2018, Washington D.C., USA**

5.4 Lectures and seminars at Bayerisches Geoinstitut

ARMSTRONG, Katherine, Bayerisches Geoinstitut, Bayreuth, Germany: "Redox evolution of the early Earth's mantle", 27.11.2018

AULBACH, Sonja, Johann Wolfgang Goethe-Universität, Petrologie und Geochemie, Frankfurt/M., Germany: "Fe redox state and oxygen fugacity of mantle eclogites: Implications for lithospheric and sublithospheric processes", 31.10.2018

BRUNE, Sascha, GFZ Helmholz-Zentrum Potsdam, Geodynamische Modellierung, Potsdam, Germany: "Impact of continental rifting on plate motions and paleoclimate", 18.01.2018

BUCHEN, Johannes, Bayerisches Geoinstitut, Bayreuth, Germany: "High-pressure single-crystal elasticity of wadsleyite and seismic remote sensing of water in Earth's mantle", *Academy Commission Business Meeting*, 26.04.2018

DÖHMANN, Maximilian, GFZ Helmholz-Zentrum Potsdam, Geodynamische Modellierung, Potsdam, Germany: "Strain localization and weakening processes in viscously deforming rocks: Numerical modeling based on laboratory torsion experiments", 18.01.2018

FAUL, Ulrich, Massachusetts Institute of Technology, Department of Earth, Atmospheric and Planetary Sciences, Cambridge, USA: "Seismic and rheological properties of olivine: The influence of water and redox state", 11.07.2018

JACKSON, Jennifer, California Institute of Technology, Seismological Laboratory, Pasadena, USA: "Multi-scale structures and anisotropy at Earth's core-mantle boundary", 06.06.2018

ISHII, Takayuki, Bayerisches Geoinstitut, Bayreuth, Germany: "The pressure and thickness of the post-spinel transition in $(Mg,Fe)_2SiO_4$ explaining the sharp 660-km seismic discontinuity", *Academy Commission Business Meeting*, 26.04.2018

KHAN, Amir, ETH Zürich, Institute of Geophysics, Zurich, Switzerland: "InSights on the internal structure, composition, and origin of Mars", 05.07.2018

KOHN, Matt, Boise State University, Department of Geosciences, Boise, USA: "Shear heating controls mineralogy, seismicity, and convection in subduction zones", 07.05.2018

KUBIK, Edith, Institut de Physique du Globe de Paris, France: "Tracing Earth's volatile delivery with tin", 05.04.2018

KUFNER, Sofia-Katerina, GFZ Helmholz-Zentrum Potsdam, Dynamik der Lithosphäre, Potsdam, Germany: "Anatomy of a continental subduction zone – what drives the Pamir-Hindu Kush intermediate depth seismicity", 07.06.2018

LANDEAU, Maylis, Institut de Physique du Globe de Paris, France: "Earth formation in the lab: Metal-silicate equilibration and core stratification following large planetary collisions", 29.11.2018

LI, Jie, University of Michigan, Earth and Invironmental Sciences, Ann Arbor, USA: "Redox dehydration of Earth's deep mantle", 02.10.2018

LIN, Jung-Fu, The University of Texas at Austin, Department of Geological Sciences, Austin, USA: "Iron partitioning and fractionation in the lower mantle", 02.10.2018

MEIER, Thomas, Bayerisches Geoinstitut, Bayreuth, Germany: "On the way to NMR at mega-bar pressures – Observation of nuclear quantum effects and hydrogen bond symmetrisation in high pressure ice", *Academy Commission Business Meeting*, 26.04.2018

MEIERHENRICH, Uwe, Université Nice Sophia-Antipolis, Bioanalytical Chemistry and Natural Fragrances, Nice, France: "A 3D presentation – Rosetta's identification of organic molecules in a comet nucleus", 06.12.2018

NISHIDA, Keisuke, The University of Tokyo, Department of Earth and Planetary Science, Tokyo: "Effect of pressure, temperature and sulfur content on sound velocity in liquid Fe-S", 21.06.2016

NOACK, Lena, FU Berlin, Institut für Geologische Wissenschaften, Berlin, Germany: "Mineral physics of Earth and exoplanets: Predictions for long-term evolution of rocky planets", 28.06.2018

ORLANDINI, Omero Felipe, University of Colorado at Boulder, Department of Geological Sciences, Boulder, USA: "Petrology, rheology, and seismic anisotropy of a deep-crustal mechanical anomaly", 22.11.2018

PISTONE, Mattia, Université de Lausanne, Institut des Sciences de la Terre, Lausanne, Switzerland: "Magmatic fluid transport from the Earth's crust to volcanoes", 20.11.2018

POTTS, Nicola, The University of Edinburgh, School of GeoSciences, Edinburgh, U.K.: "Constraining the volatile storage capacity of the lunar interior", 12.07.2018

RUH, Jonas, ICTJA Barcelona, Structure and Dynamics of the Earth and Crystallography, Barcelona, Spain: "Importance of fluid overpressure for the structural evolution of the Makran accretionary wedge", 14.11.2018

SCHULZE, Kirsten, Bayerisches Geoinstitut, Bayreuth: "Hydration in the transition zone – elasticity studies on ringwoodite and phase egg", 03.05.2018

SECCO, Richard, Western University, Department of Earth Sciences, London, Canada: "Resistivity experiments on transition metals as applied to heat flow in cores of terrestrial bodies", 29.08.2018

SOSSI, Paolo, Institut de Physique du Globe de Paris, France: "Evaporation of moderately volatile elements from silicate melts: Experiments and theory", 30.05.2018

SPEICH, Laura, University of Bristol, Department of Earth Sciences, Bristol, U.K.: "Platelet evolution in diamond as a new thermometer for the lithospheric mantle", 17.05.2018

SPEZIALE, Sergio, GFZ Helmholz-Zentrum Potsdam, Chemie und Physik der Geomaterialien, Potsdam, Germany: "What do we know about the elastic anisotropy of minerals?", 06.03.2018

VALENCIA, Diana, University of Toronto, Scarborough, Physical and Environmental Sciences Department, Toronto, Canada: "Super-Earth compositions as a signature of planet formation", 03.08.2018

WAGLE, Fabian, Bayerisches Geoinstitut, Bayreuth: "Structure and transport properties of iron and its alloys at planetary core conditions", 24.05.2018

WÜNNEMANN, Kai, Museum für Naturkunde, Leibniz-Institut für Evolutions- und Biodiversitätsforschung Berlin, Germany: "The role of impacts processes in planetary evolution", 08.11.2018

YOSHIOKA, Takahiro, Bayerisches Geoinstitut, Bayreuth: "Experimental studies on the deep geochemistry of carbon and nitrogen", 18.10.2018

ZHANG, Zhou, University of California San Diego, Institute of Geophysics and Planetary Physics, La Jolla, USA: "The effects of sulfur on Fe-Ni alloy precipitation depth and deep diamond formation", 15.11.2018

5.5 Conference organization

08.-13.04.2018, European Geosciences Union General Assembly 2018, Vienna, Austria: "Terrestrial Planet Evolution: Deep Carbon Cycle and Interior/Exterior coupling" (S. ZAHIROVIC, C. GILLMANN, M. PISTONE, L. PURKAMO, N. BELLOT, G. GOLABEK, V. STAGNO)

18.-19.04.2018, Workshop on "Giant Collisions and their Effects on the Thermochemical Evolution of Planets", Berlin, Germany (G. GOLABEK)

23.-27.07.2018, PhD Short Course "Texture and interface analyses using EBSD", Bayerisches Geoinstitut, Universität Bayreuth, Germany (K. MARQUARDT)

13.-17.08.2018, International Mineralogical Association Meeting, Melbourne, Australia: Session "Unseen but Integral to the Earth's Interior: How Minerals Determine Properties and Processes (P. COMODI, T. INOUE, C.A. MCCAMMON, E. OHTANI, J. WYKES)

02.-06.09.2018, GeoBonn 2018, Bonn, Germany: "Materials, structure and dynamics of Earth's deep interior" (M. WILKE, H. MARQUARDT)

26.-27.10.2018, 109. Sitzung des Forschungskollegiums Physik des Erdkörpers (FKPE), Bayreuth, Germany (G. GOLABEK)

10.-14.12.2018, American Geophysical Union Fall Meeting, Washington D.C., USA: Session MR33B: "Elastic Properties of Earth Materials and Their Application in Seismology and Geodynamics" (J. BUCHEN, S. ZHANG, S. STACKHOUSE, H. MARQUARDT)

10.-14.12.2018, American Geophysical Union Fall Meeting, Washington D.C., USA: Session DI010: "Emerging Methods in Diamond Anvil Cell Research" (T. MEIER, K. GLAZYRIN)

6. Visiting scientists

6.1 Visiting scientists funded by the Bayerisches Geoinstitut

BRUNE, Sascha, GFZ Helmholz-Zentrum Potsdam, Geodynamische Modellierung, Potsdam, Germany: 17.-19.01.2018

CHAKRABORTY, Sumit, Ruhr-Universität Bochum, Ruhr-Universität Bochum, Institut für Geologie, Mineralogie und Geophysik, Bochum, Germany: 15.-16.04.2018

DÖHMANN, Maximilian, GFZ Helmholz-Zentrum Potsdam, Geodynamische Modellierung, Potsdam, Germany: 17.-19.01.2018

DOLEJŠ, David, Universität Freiberg, Institut für Geo- und Umweltnaturwissenschaften, Freiberg, Germany: 19.-23.02.2018

GREEN, Eleanor, ETH Zurich, Institute of Geochemistry and Petrology, Zurich, Switzerland: 27.-28.09.2018

NISHIDA, Keisuke, The University of Tokyo, Department of Earth and Planetary Science, Tokyo: 19.-23.06.2018

KHAN, Amir, ETH Zurich, Institute of Geophysics, Zurich, Switzerland: 04.-06.07.2018

KOHN, Matt, Boise State University, Department of Geosciences, Boise, USA: 06.-09.05.2018

KRUMREIN, Nikolaus, Universität Tübingen, Geowissenschaften, Tübingen, Germany: 17.02.-01.04.2018

KUFNER, Sofia-Katerina, GFZ Helmholz-Zentrum Potsdam, Dynamik der Lithosphäre, Potsdam, Germany: 07.-08.06.2018

LANDEAU, Maylis, Institut de Physique du Globe de Paris, France: 28.-30.11.2018

NOACK, Lena, FU Berlin, Institut für Geologische Wissenschaften, Berlin, Germany: 27.-29.06.2018

ORLANDINI, Omero Felipe, University of Colorado at Boulder, Department of Geological Sciences, Boulder, USA: 20.-23.11.2018

POTTS, Nicola, The University of Edinburgh, School of GeoSciences, Edinburgh, U.K.: 11.-13.07.2018

RUH, Jonas, ICTJA Barcelona, Structure and Dynamics of the Earth and Crystallography, Barcelona, Spain: 13.-15.11.2018

SCHMALHOLZ, Stefan, Université de Lausanne, Institut des Sciences de la Terre, Lausanne, Switzerland: 29.-30.01.2018

SOSSI, Paolo, Institut de Physique du Globe de Paris, France: 28.-31.05.2018

VLASOV, Kirill, Moscow State University, Geology Department, Moscow, Russia: 22.-25.04.2018

WALTE, Nico, TU München, Forschungs-Neutronenquelle Heinz Maier-Leibnitz (FRM II), Garching, Germany: 19.-21.02.2018

WÜNNEMANN, Kai, Museum für Naturkunde, Leibniz-Institut für Evolutions- und Biodiversitätsforschung, Berlin, Germany: "The role of impacts processes in planetary evolution", 08.11.2018

6.2 Visiting scientists supported by other externally funded BGI projects

AULBACH, Sonja, Johann Wolfgang Goethe-Universität, Petrologie und Geochemie, Frankfurt/M., Germany: 31.10.-01.11.2018 (IRTG[*D])

BURNLEY, Pamela, High Pressure Science and Engineering Center (HiPSEC), Department of Geoscience, Las Vegas, USA: 22.-28.07.2018 (IRTG[*D])

CHUST, Thomas, Ludwig-Maximilians-Universität, Department für Geo- und Umwelt-wissenschaften, München, Germany: 25.-27.06.2018 (DFG[*B])

DE GRAEF, Marc, Carnegie Mellon University, Department of Materials Science and Engineering, Pittsburgh, USA: 22.-27.07.2018 (DFG[*B])

DEMURTAS, Matteo, University of Otago, Geology Department, Dunedin, New Zealand: 25.-.27.07.2018 (DFG[*B])

DE KLOE, René, AMETEK BV, Tilburg, The Netherlands: 23.-26.07.2018 (DFG[*B])

FAUL, Ulrich, Massachusetts Institute of Technology, Earth, Atmospheric and Planetary Sciences, Cambridge, USA: 05.-27.07.2018 (IRTG[*D]), 06.11.-02.12.2018 (ERC[*C])

JACKSON, Jennifer, California Institute of Technology, Seismological Laboratory, Pasadena, USA: 05.-07.06.2018 (IRTG[*D])

MEIERHENRICH, Uwe, Université Nice Sophia-Antipolis, Bioanalytical Chemistry and Natural Fragrances, Nice, France: 06.12.2018 (DFG[*B])

MENKHAUS, Heinrich, Meiji Universität, Faculty of Law, Tokyo, Japan: 26.-27.03.2018 (IRTG[*D])

MORALES, Luiz, ETH Zurich, Department of Earth Sciences, Zurich, Switzerland: 23.-25.07.2018 (DFG[*B])

ROHRER, Gregory S., Carnegie Mellon University, Department of Materials Science and Engineering, Pittsburgh, USA: 22.-27.07.2018 (DFG[*B])

SECCO, Richard, Western University, Department of Earth Sciences, London, Canada: 28.08.-01.09.2018 (DFG[*B])

SPEZIALE, Sergio, GFZ Helmholz-Zentrum Potsdam, Chemie und Physik der Geomaterialien, Potsdam, Germany: 05.-07.03.2018 (DFG[*B])

TONG, Vivian, Imperial College London, Faculty of Engineering, Department of Materials, London, U.K.: 22.-27.07.2018 (DFG[*B])

WALTE, Nico, TU München, Forschungs-Neutronenquelle Heinz Maier-Leibnitz (FRM II), Garching, Germany: 31.01.-02.02.2018, 11.-12.10.2018, 18.-19.12.2018 (BMBF[*A])

ZHANG, Zhou, University of California San Diego, Institute of Geophysics and Planetary Physics, La Jolla, USA: 12.-16.11.2018 (IRTG[*D])

[*A)] BMBF: Bundesministerium für Bildung und Forschung

[*B)] DFG: Deutsche Forschungsgemeinschaft

[*C)] ERC: European Research Council

[*D)] IRTG: International Research Training Group "Deep Earth Volatile Cycles" (DFG)

6.3 Visiting scientists supported by the DFG Core Facility programme

ALLABAR, Anja, Eberhard Karls Universität Tübingen, Experimentelle Mineralogie, Tübingen, Germany: 05.-09.03.2018, 22.03.2018

BERKELS, Dennis, Ruhr-Universität Bochum, Institut für Geologie, Mineralogie und Geophysik, Bochum, Germany: 19.-29.03.2018, 08.-12.10.2018

BEYER, Christopher, Ruhr-Universität Bochum, Institut für Geologie, Mineralogie und Geophysik, Bochum, Germany: 05.-14.01.2018

BORISOVA, Anastassia, Géosciences Environnement Toulouse, France: 04.-11.03.2018, 10.-17.12.2018

COMODI, Paola, Università degli Studi di Perugia, Dipartimento di Fisica e Geologia, Perugia, Italy: 05.-09.11.2018

DE LIGNY, Dominique, Universität Erlangen-Nürnberg, Department Werkstoff-wissenschaften, Lehrstuhl für Glas und Keramik, Erlangen, Germany: 04.06.2018

ENDER, Christopher, Max-Planck-Institut für Polymerforschung, Mainz, Germany: 23.-27.07.2018

FRIEBEL, Jonas, Max-Planck-Institut für Polymerforschung, Mainz, Germany: 23.-27.07.2018

FULFORD, Luke, University of Edinburgh, School of Engineering, Edinburgh, U.K.: 21.01.-01.02.2018

GRÜTZNER-HANDKE, Tobias, Universität Münster, Institut für Mineralogie, Münster, Germany: 14.-20.10.2018

KUBIK, Edith, Institut de Physique du Globe de Paris, France: 02.-09.04.2018

MATJUSCHKIN, Vladimir, Johann Wolfgang Goethe-Universität, Physikalisch-Chemische Mineralogie, Frankfurt/M., Germany: 04.-09.03.2018, 29.04.-06.05.2018

MORROW, Ryan, IFW Dresden, Institut für Festkörperforschung, Dresden, Germany: 10.-16.09.2018, 05.-09.11.2018, 02.-08.12.2018

MOUTAABBID, Hicham, Sorbonne Université, Institut de minéralogie, de physique des matériaux et de cosmochimie, Paris, France: 22.-28.04.2018

MORTIMER, Patrick, University of Edinburgh, School of Engineering, Edinburgh, U.K.: 21.01.-01.02.2018

MYHILL, Robert, University of Bristol, School of Earth Sciences, Bristol, U.K.: 05.-13.01.2018

NOVELLA, Davide, University of Cambridge, Department of Earth Sciences, Cambridge, U.K.: 06.-19.02.2018

OTTERSBERG, Niklas, Ruhr-Universität Bochum, Institut für Geologie, Mineralogie und Geophysik, Bochum, Germany: 07.-13.01.2018

PRIMOCERIO, Jennifer, Ruhr-Universität Bochum, Institut für Geologie, Mineralogie und Geophysik, Bochum, Germany: 17.02.-17.03.2018

SIEBERT, Julien, Institut de Physique du Globe de Paris, France: 02.-06.04.2018

UENVER-THIELE, Laura, Johann Wolfgang Goethe-Universität, Physikalisch-Chemische Mineralogie, Frankfurt/M., Germany: 04.-09.03.2018, 29.04.-06.05.2018

WERR, Ferdinand, Universität Erlangen-Nürnberg, Department Werkstoffwissenschaften, Lehrstuhl für Glas und Keramik, Erlangen, Germany: 04.06.2018

WOOD, Marisa, University College London, Department of Earth Sciences, London, U.K.: 12.-23.02.2018

WOODLAND, Alan, Johann Wolfgang Goethe-Universität, Physikalisch-Chemische Mineralogie, Frankfurt/M., Germany: 08.-12.10.2018

YUSIM, Wenjamin, Universität Erlangen-Nürnberg, Department Werkstoffwissenschaften, Lehrstuhl für Glas und Keramik, Erlangen, Germany: 04.06.2018

ZAPATA, Todd, Max-Planck-Institut für Polymerforschung, Mainz, Germany: 23.-27.07.2018

ZUCCHINI, Azzurra, Università degli Studi di Perugia, Dipartimento di Fisica e Geologia, Perugia, Italy: 04.-12.11.2018

6.4 Visitors (externally funded)

ADAMS, Andrea, UC San Diego, Scripps Institution of Oceanography, La Jolla, USA: 20.-21.09.2018

ANGEL, Ross, Università degli Studi di Pavia, Dipartimento di Scienze della Terra e dell'Ambiente, Pavia, Italy: 01.-09.02.2018

ANZOLINI, Chiara, Università degli Studi di Padova, Dipartimento di Geoscienze, Padova, Italy: 09.-21.01.2018

ARAYA, Naoki, Tohoku University, Department of Earth Science, Sendai, Japan: 16.-27.07.2018

BALLANTYNE, Harry, Universität Bern, Space Research & Planetary Sciences (WP), Bern, Switzerland: 07.-09.11.2018

BINCK, Jannes, Goethe-Universität Frankfurt/M., AG Kristallographie/Mineralogie, Frankfurt/M., Germany: 05.-09.11.2018

BRETON, Helene, University of Edinburgh, Department of Earth and Planetary Science, Edinburgh, U.K.: 14.-16.08.2018

CHAUDHARI, Alok, Monash University, School of Earth, Atmosphere & Environment, Clayton, Australia: 06.-10.09.2018

CORDIER, Patrick, Université Lille 1, UMET - Unité Matériaux et Transformation, CNRS, Villeneuve d'Ascq, France: 22.-23.01.2018

DU, Jingguo, China University of Geosciences, Department of Earth Sciences and Resources, Beijing, P.R. China: 01.01.-24.01.2018

ELAZAR, Oded, The Hebrew University of Jerusalem, Fredy & Nadine Herrmann Institute of Earth Sciences, Jerusalem, Israel: 16.-19.09.2018

FUJITA, Wakana, Tohoku University, Division of Earth and Planetary Materials Science, Sendai, Japan: 01.01.-12.02.2018

GLAZYRIN, Konstantin, Deutsches Elektronen-Synchrotron, PETRA III, Hamburg, Germany: 29.-30.01.2018

GORELOVA, Liudmila, Petersburg University, Department of Crystallography, Saint Petersburg, Russia: 11.-16.02.2018

GOTO, Ken-ichi, Tohoku University, Department of Earth Science, Sendai, Japan: 01.-16.01.2018

HIRANO, Naoto, Tohoku University, Center for Northeast Asian Studies, Sendai, Japan: 08.-13.03.2018, 05.-10.11.2018

HUANG, Yongsheng, Tohoku University, Division of Earth and Planetary Materials Science, Sendai, Japan: 23.07.-24.09.2018

ISKRINA, Anastasiya, Lomonosov Moscow State University, Department of Petrology, Moscow, Russia: 01.07.-31.08.2018

JACOBSEN, Steven, Northwestern University, Department of Earth and Planetary Sciences, Evanston, USA: 07.06.-02.07.2018

KOMABAYASHI, Tetsuya, University of Edinburgh, Department of Earth and Planetary Science, Edinburgh, U.K.: 14.-16.08.2018

KUDRYAVTSEV, Daniil, Gubkin Russian State University of Oil and Gas, Moscow, Russia: 17.02.-13.04.2018

LANDI, Anna Irene, Università degli Studi di Firenze, Dipartimento di Scienze della Terra, Firenze, Italy: 05.11.-31.12.2018

LI, Jie, University of Michigan, Earth and Invironmental Sciences, Ann Arbor, USA: 01.-04.10.2018

LI, Yuan, Chinese Academy of Sciences, Guangzhou Institute of Geochemistry, Guangzhou, P.R. China: 21.08.-16.09.2018

LIN, Jung-Fu, The University of Texas at Austin, Department of Geological Sciences, Austin, USA: 01.-04.10.2018

MAEDA, Fumiya, Tohoku University, Earth and Planetary Material Physics Research Group, Sendai, Japan: 04.-16.01.2018, 22.08.-01.09.2018, 08.-27.09.2018, 09.-29.12.2018

MURANUSHI, Miki, Tohoku University, Department of Earth Science, Sendai, Japan: 17.08.-01.09.2018, 08.-19.09.2018

NAKAJIMA, Ayano, Tohoku University, Department of Earth Science, Sendai, Japan: 17.08.-01.09.2018, 08.-19.09.2018

NAKAMURA, Michihiko, Tohoku University, Graduate School of Science, Department of Earth Science, Sendai, Japan: 09.-12.10.2018

NAVON, Oded, The Hebrew University of Jerusalem, Fredy & Nadine Herrmann Institute of Earth Sciences, Jerusalem, Israel: 05.-06.02.2018

NOWAK, Marcus, Eberhard Karls Universität Tübingen, Experimentelle Mineralogie, Tübingen, Germany: 22.03.2018

OHASHI, Tomonori, Tohoku University, Department of Earth Science, Sendai, Japan: 22.-31.12.2018

OHTANI, Eiji, Tohoku University, Earth and Planetary Material Physics Research Group,

OKUMURA, Satoshi, Tohoku University, Graduate School of Science, Department of Earth Science, Sendai, Japan: 18.-28.03.2018

OUYANG, Hegen, Chinese Academy of Geological Sciences, Institute of Mineral Resources, Beijing, P.R. China: 15.05.-11.08.2018

PAMATO, Martha, University College London, Department of Earth Sciences, London, U.K.: 06.-19.02.2018

PELLETER, Anne-Aziliz, Laboratoire Magmas et Volcans, Aubière, France: 26.-29.03.2018

PLATTNER, Alain, California State University, Department of Earth & Environmental Sciences, Fresno, USA: 28.-29.05.2018

PISTONE, Mattia, Université de Lausanne, Institut des Sciences de la Terre, Lausanne, Switzerland: 19.-25.11.2018

PRIMOCERIO, Jennifer, Ruhr-Universität Bochum, Institut für Geologie, Mineralogie und Geophysik, Bochum, Germany: 06.07.-03.08.2018, 07.-14.12.2018

RASHCHENKO, Sergey, Novosibirsk State University, Novosibirsk, Russia: 30.10.-05.11.2018

SATO, Yuki, Tohoku University, Center for Northeast Asian Studies, Sendai, Japan: 08.-13.03.2018

SAWA, Sando, Tohoku University, Department of Earth Science, Sendai, Japan: 17.02.-02.03.2018, 10.-18.07.2018

SCHIERJOTT, Jana, ETH Zurich, Institut für Geophysik, Zurich, Switzerland: 21.-23.11.2018

SCHÖLMERICH, Markus, European XFEL, Schenefeld, Germany: 12.-15.06.2018

SMYTH, Joseph R., University of Colorado at Boulder, Department of Geological Sciences, Boulder, USA: 05.-16.02.2018, 19.-29.06.2018

SPEICH, Laura, University of Bristol, Department of Earth Sciences, Bristol, U.K.: 16.-18.05.2018

SPIVAK, Anna, Institute of Experimental Mineralogy, Chernogolovka, Moscow region, Russia: 01.06.-31.07.2018

STAGNO, Vincenzo, Università degli Studi di Roma "La Sapienza", Dipartimento di Scienze della Terra, Roma, Italy: 12.-15.06.2018

SUZUKI, Akio, Tohoku University, Earth and Planetary Material Physics Research Group, Sendai, Japan: 01.-08.01.2018, 17.08.-01.09.2018, 08.-19.09.2018, 22.-31.12.2018

VALENCIA, Diana, University of Toronto, Scarborough, Physical and Environmental Sciences Department, Toronto, Canada: 02.-04.08.2018

VOGEL, Sebastian, Ludwig-Maximilians-Universität, Department of Chemistry, Inorganic Solid-State Chemistry, München, Germany: 25.-28.09.2018

WEI, Chen, University of Chinese Academy of Sciences, Beijing, P.R. China: 30.11.-31.12.2018

YUAN, Liang, Tohoku University, Department of Earth and Planetary Material Sciences, Sendai, Japan: 23.04.-18.05.2018

YUTANI, Taku, Tohoku University, Center for Northeast Asian Studies, Sendai, Japan: 08.03.-31.12.2018

ZAFFIRO, Gabriele, Università degli Studi di Pavia, Dipartimento di Scienze della Terra e dell'Ambiente, Pavia, Italy: 02.05.-01.06.2018

ZAKHARCHENKO, Egor, Institute of Experimental Mineralogy, Chernogolovka, Moscow region, Russia: 01.06.-31.07.2018

ZAKHAROV, Boris, Institute of Solid State Chemistry and Mechanochemistry, Novosibirsk, Russia: 13.-27.05.2018

ZHANG, Daohan, China University of Geosciences, Faculty of Earth Resources, Wuhan, P.R. China: 24.09.-23.12.2018

7. Additional scientific activities

7.1 Habilitation/Theses

Habilitation

MARQUARDT, Hauke: Neues aus dem unteren Erdmantel: Wie die Forschung unser Verständnis der tiefen Erde revolutioniert.
STEINLE-NEUMANN, Gerd: Transport properties of liquid metals at high pressure and temperature – Geophysical significance for planetary cores.

Ph.D. theses

ARMSTRONG, Katherine: Redox evolution of the early Earth's mantle.
BUCHEN, Johannes: The elastic properties of wadsleyite and stishovite at high pressures – tracing deep Earth material cycles.
SCHULZE, Kirsten: Hydration in the transition zone – elasticity studies on ringwoodite and phase egg.
WAGLE, Fabian: Structure-property relations for resistivity of iron alloys at planetary core conditions.
WANG, Lin: Temperature, pressure and water content dependence of dislocation mobility in olivine.
YOSHIOKA, Takahiro: Experimental studies on the deep geochemistry of carbon and nitrogen.

M.Sc. theses

ABEYKOON, Sumith: Solubility of oxygen in mantle sulfides.
KOEMETS, Iuliia: High pressure crystal chemistry of Fe,Al-rich bridgmanite.
MANDOLINI, Tommaso: Plastic deformation of garnet single crystals at high temperature and pressure.
MISRA, Sourav Kumar: Oxybarometry of a carbon bearing-eclogite from Roberts Victor, South Africa.
URGESE, Matteo: Compressibility study of Fe^{2+}-bearing bridgmanite.

7.2 Honours and awards

AUDÉTAT, Andreas	Silver Medal of the Society of Economic Geologists
KATSURA, Tomoo	American Geophysical Union Fellow 2018
MARQUARDT, Katharina	EMU Research Excellence Medal

MEIER, Thomas	European High Pressure Research Group (EHPRG) Award, September 2018 2018 Early Career Scientist Travel Award from the International Union of Crystallography (IUCr) Commission on High Pressure, July 2018 2018 Laureate of "Germany, Land of Ideas: Excellent Places", patroned by the German Federal Government and the Federal Association of German Industry (BDI), June 2018
POSNER, Esther	American Geophysical Union (AGU) Mineral and Rock Physics Graduate Research Award

7.3 Editorship of scientific journals

DUBROVINSKY, Leonid	Member, Editorial Board of the Journal of High Pressure Research
KEPPLER, Hans	Editorial Board "Contributions to Mineralogy and Petrology" Editorial Board "ACS Earth and Space Chemistry"
MCCAMMON, Catherine	Chief Editor and Managing Editor "Physics and Chemistry of Minerals"
MIYAJIMA, Nobuyoshi	Associate Editor "European Journal of Mineralogy"

7.4 Membership of scientific advisory bodies

BOFFA BALLARAN, Tiziana	Member of the Review Panel for allocation of beam-time at the Advanced Light Source, Berkeley Member, Dana Medal Committee, American Mineralogical Society
DUBROVINSKY, Leonid	Member, Review Panel of Canadian Light Source Chair, Subcomission on Spectroscopy, Diffraction, and new Instrumentations in Mineral Physics of the International Mineralogical Association Member, Deep Carbon Observatory Scientific Steering Committee Member, Review Panel of PETRA III Member, Review Panel of Research Council of Lithuania

FROST, Dan	Chair of the Executive Committee for Elements Magazine Member, German National Academy of Sciences (Leopoldina) Elected member of the Bavarian Academy of Sciences Member of the selection committee for Alexander von Humboldt Professorships
KEPPLER, Hans	Member, Abraham Gottlob Werner Medal Committee, German Mineralogical Society (DMG) Member, German National Academy of Sciences (Leopoldina) Member, Bavarian Academy of Sciences Member, Deep Carbon Observatory Scientific Steering Committee Member, Alexander von Humboldt Foundation Selection Panel for Humboldt Awardees Member, Committee CE31 "Subatomic physics, sciences of the universe, structure and history of the Earth", Agence Nationale de la Recherche, Paris Member, Advisory Board, Dachverband Geowissenschaften
MCCAMMON, Catherine	Member, Starting Grant Panel PE10, European Research Council Member, Council, International Mineralogical Association Member, Council, Deutsche Mineralogische Gesellschaft Member, Governance Committee of the American Geophysical Union Member, Steering Committee Deep Carbon 2019 Chair, Sub-committee "Earth's Deep Interior" of the Commission of the Physics of Minerals, International Mineralogical Association Member, IASPEI/IAVCEI/IAGA Commission on Physics and Chemistry of Earth Materials

8. Scientific and Technical Personnel

Name		Position	Duration in 2018	Funding source
ABEYKOON, Sumith	B.Sc.	Student. Hilfskraft	to 30.04.	IRTG
		Wiss. Mitarbeiter	from 01.05.	IRTG
ARMSTRONG, Katherine	M.Sc.	Wiss. Mitarbeiterin	to 28.02.	IRTG
			01.03.-30.11.	DFG
AUDÉTAT, Andreas	Dr.	Akad. Oberrat		BGI
BAUER, Gerald	Dipl.-Ing. (FH)	Techn. Angestellter	from 01.02.	BGI
BHAT, Shrikant	Dr.	Wiss. Mitarbeiter		BMBF
BLANCHARD, Ingrid	Dr.	Wiss. Mitarbeiterin		DFG
BÖHM, Ulrich		Mechaniker		BGI
BOFFA BALLARAN, Tiziana	Dr.	Akad. Oberrätin		BGI
BOLLINGER, Caroline	Dr.	Wiss. Mitarbeiterin	to 31.03.	UBT[1]
BONDAR, Dmitry	M.Sc.	Wiss. Mitarbeiter		IRTG
BUCHEN, Johannes	Dipl.-Min.	Wiss. Mitarbeiter	to 30.04.	IRTG
			01.05.-30.09.	DFG
BUCHERT, Petra		Fremdsprachen-sekretärin		BGI
BYKOV, Maxim	Dr.	Wiss. Mitarbeiter		DFG
CHANG, Jia	M.Sc.	Stipendiat	to 10.10.	CSC
CHANYSHEV, Artem	M.Sc.	Wiss. Mitarbeiter	from 07.07.	DFG
CHARITON, Stella	M.Sc.	Wiss. Mitarbeiterin		DFG
CIALDELLA, Laura	M.Sc.	Wiss. Mitarbeiterin	from 15.07.	IRTG
CONDAMINE, Pierre	Dr.	Wiss. Mitarbeiter	to 31.07.	Leibniz
CRINITI, Giacomo	B.Sc.	Student. Hilfskraft		DFG
DOMINIJANNI, Serena	M.Sc.	Wiss. Mitarbeiter	from 01.05.	IRTG
DRUZHBIN, Dmitry	M.Sc.	Wiss. Mitarbeiter		DFG
DUBROVINSKY, Leonid	Apl. Prof. Dr.	Akad. Direktor		BGI
EBERHARD, Lisa	M.Sc.	Wiss. Mitarbeiterin		IRTG
EICHHEIMER, Philipp	M.Sc.	Wiss. Mitarbeiter		IRTG
FEI, Hongzhan	Dr.	Wiss. Mitarbeiter		DFG
FERREIRA, Filippe	M.Sc.	Wiss. Mitarbeiter	to 31.01.	IRTG
			from 01.02.	DFG
FISCHER, Heinz		Mechaniker		BGI
FISCHER, Nicole	RAmtfr	Verwalt. Beamtin		BGI
FLANIGAN, Michaela	M.Sc.	Wiss. Mitarbeiterin	to 30.09.	Leibniz
FROST, Daniel	Prof. Dr.	Leiter	to 30.09.	BGI
		Stellvertr. Leiter	from 01.10.	

GOLABEK, Gregor	Prof. Dr.	Professor		BGI
GUO, Haihao	Dr.	Wiss. Mitarbeiter	to 14.10.	DFG
HEIDELBACH, Florian	Dr.	Wiss. Mitarbeiter		BGI
HUANG, Rong	M.Sc.	Wiss. Mitarbeiterin	to 28.02.	AvH
			from 01.03.	Leibniz
IMMOOR, Julia	Dipl.-Geol.	Wiss. Mitarbeiterin	to 31.08.	DFG
ISHII, Takayuki	Dr.	Forschungsstipendiat		AvH
JENNINGS, Eleanor	Dr.	Wiss. Mitarbeiterin	to 07.01.	EU
JOCHUM, Johanna	Dr.	Wiss. Mitarbeiterin	from 01.05.	BMBF
KATSURA, Tomoo	Prof. Dr.	Stellvertr. Leiter	to 30.09.	BGI
		Professor	from 01.10.	
KEPPLER, Hans	Prof. Dr.	Professor	to 30.09.	BGI
		Leiter	from 01.10.	
KHANDARKHAEVA, Saiana	M.Sc.	Wiss. Mitarbeiterin		DFG
KISON-HERZING, Lydia		Sekretärin	to 28.02.	BGI
KLUMBACH, Steffen	Dr.	Wiss. Mitarbeiter	to 31.03.	DFG
KOEMETS, Egor	M.Sc.	Wiss. Mitarbeiter		IRTG
KOEMETS, Iuliia	B.Sc.	Student. Hilfskraft	to 31.10.	IRTG
		Wiss. Mitarbeiterin	from 01.11.	DFG
KRAUßE, Detlef	Dipl.-Inform. (FH)	Techn. Angestellter		BGI
KRIEGL, Holger		Haustechniker		BGI
KULIK, Eleonora	Dipl.-Physik-ingenieurin	Wiss. Mitarbeiterin	to 30.06.	DFG
KURNOSOV, Alexander	Dr.	Wiss. Mitarbeiter	to 21.08.	DFG
			from 15.10.	DFG
LAURENZ-HEUSER, Vera	Dr.	Wiss. Mitarbeiterin	to 30.04.	EU
LINHARDT, Sven		Elektrotechniker		BGI
LIU, Zhaodong	Dr.	Wiss. Mitarbeiter	to 30.11.	BGI/VP
MA, Ning	B.Sc.	Student. Hilfskraft	from 01.10.	DFG
MAKOWSKA, Malgorzata	Dr.	Wiss. Mitarbeiterin	to 31.03.	BMBF
MALLIK, Ananya	Dr.	Forschungsstipendiatin	to 31.01.	AvH
MANDOLINI, Tommaso	B.Sc.	Student. Hilfskraft	to 14.10.	IRTG
MARQUARDT, Hauke	Dr.	Nachwuchs-gruppenleiter	to 31.03.	DFG
MARQUARDT, Katharina	Dr.	Akad. Rätin		BGI
MARZOTTO, Enrico	M.Sc.	Wiss. Mitarbeiter		IRTG
MCCAMMON, Catherine	Privatdozentin Dr.	Akad. Direktorin		BGI
MEIER, Thomas	Dr.	Wiss. Mitarbeiter		BGI/VP
MELAI, Caterina	M.Sc.	Wiss. Mitarbeiterin		IRTG
MISRA, Sourav	B.Sc.	Student. Hilfskraft	to 03.05.	IRTG

MIYAJIMA, Nobuyoshi	Dr.	Akad. Oberrat		BGI
NISHIDA, Keisuke	Dr.	Wiss. Mitarbeiter	from 01.10.	DFG
NJUL, Raphael		Präparator		BGI
OHTANI**,** Eiji	Prof.	Forschungspreisträger	09.09.-03.12.	AvH
OVSYANNIKOV, Sergey	Dr.	Wiss. Mitarbeiter	to 28.02.	DFG
			from 27.08.	DFG
PETIGIRARD, Sylvain	Dr.	Wiss. Mitarbeiter	to 31.08.	DFG
POLEDNIA, Joana	M.Sc.	Wiss. Mitarbeiterin		DFG
POSNER, Esther	M.Sc.	Wiss. Mitarbeiterin	to 19.10.	UBT[1]
POTZEL, Anke		Chem.-Techn. Assistentin		BGI
POTZEL, Janina		Sekretärin	from 01.06.	BGI
PUTAK JURIČEK, Marija	M.Sc.	Wiss. Mitarbeiterin		IRTG
RAMMING, Gerd		Elektroniker		BGI
RAUSCH, Oliver		Mechaniker		BGI
REBAZA MORILLO, Anna Mireia	B.Sc.	Student. Hilfskraft	to 05.10.	IRTG
			from 06.10.	DFG
ROTHER, David Alexander		Präparator		BGI
ROTTIER, Bertrand	Dr.	Stipendiat		SNSF
RUBIE, David C.	Prof. Dr.	Professor		EU
RUSTIONI, Greta	M.Sc.	Wiss. Mitarbeiterin		IRTG
SAN JOSÉ MÉNDEZ, Alba	M.Sc.	Wiss. Mitarbeiterin	to 31.10.	DFG
SATTA, Niccolò	M.Sc.	Wiss. Mitarbeiter		IRTG
SCHARFENBERG, Romina	B.Sc.	Sekretärin		BGI
SCHULZE, Hubert		Präparator		GIF
SCHULZE, Kirsten	M.Sc.	Wiss. Mitarbeiterin	to 30.09.	DFG
SHCHEKA, Svyatoslav	Dr.	Wiss. Mitarbeiter		DFG
SIERSCH, Nicki	M.Sc.	Wiss. Mitarbeiterin		Leibniz
SILVA SOUZA, Danielle	B.Sc.	Student. Hilfskraft	from 09.10.	DFG
SIMONOVA, Dariia	M.Sc.	Wiss. Mitarbeiterin		DFG
STEINLE-NEUMANN, Gerd	Dr.	Akad. Oberrat		BGI
SZLACHTA, Victoria	B.Sc.	Student. Hilfskraft	01.10.-30.11.	HiWi
			from 01.12.	DFG
THIELMANN, Marcel	Dr.	Wiss. Mitarbeiter		BGI/VP
TRENZ, Ulrike		Biol.-Techn. Assistentin		BGI
TRYBEL, Florian	M.Sc.	Wiss. Mitarbeiter	to 14.08.	IRTG
			from 15.08.	DFG
ÜBELHACK, Stefan		Mechaniker		BGI
URGESE, Matteo	B.Sc.	Student. Hilfskraft	to 14.10.	IRTG
VLASOV, Kirill	M.Sc.	Wiss. Mitarbeiter	from 01.07.	DFG

WAGLE, Fabian	M.Sc.	Wiss. Mitarbeiter	15.03.-14.07.	DFG
WANG, Biao	B.Sc.	Student. Hilfskraft		DFG
WANG, Lin	M.Sc.	Wiss. Mitarbeiter	to 24.09.	DFG
WIESNER, Dorothea		Techn. Assistentin		BGI
XIE, Longjian	Dr.	Wiss. Mitarbeiter	from 01.10.	EU
YAO, Jie	M.Sc.	Wiss. Mitarbeiter		DFG
YOSHIOKA, Takahiro	M.Sc.	Wiss. Mitarbeiter	to 31.10.	DFG
ZIBERNA, Luca	Dr.	Forschungsstipendiat		AvH

Abbreviations/explanations:

AvH	Alexander von Humboldt Foundation
BGI	Staff Position of Bayerisches Geoinstitut
BGI/VP	Visiting Scientists' Program of Bayerisches Geoinstitut
BMBF	Federal Ministry of Education and Research
CSC	Chinese Science Council
DFG	German Science Foundation
EU	European Union
GIF	German-Israeli Foundation for Scientific Research and Development
HiWi	Hilfskraftmittel BGI
IRTG	International Research Training Group "Deep Earth Volatile Cycles"
Leibniz	Leibniz-Preis der Deutschen Forschungsgemeinschaft Prof. Frost
SNSF	Swiss National Science Foundation
UBT	Universität Bayreuth

[1] freie Stellenmittel

Index